AD-A280 631

DTIC
S ELECTE
JUN 2 4 1994
G D

AN AERODYNAMIC AND STATIC-STABILITY
ANALYSIS OF THE HYPERSONIC APPLIED
RESEARCH TECHNOLOGY (HART) MISSILE

DISSERTATION

Kenneth John Moran
Captain, USAF

AFIT/DS/AA/94-3

94-19380

AFIT/DS/AA/94-3

AN AERODYNAMIC AND STATIC-STABILITY ANALYSIS OF THE HYPERSONIC APPLIED RESEARCH TECHNOLOGY (HART) MISSILE

DISSERTATION

Presented to the Faculty of the Graduate School of Engineering

of the Air Force Institute of Technology

Air University

In Partial Fulfillment of the

Requirements for the Degree of

Doctor of Philosophy

Kenneth John Moran, B.S., M.S.

Captain, USAF

April, 1994

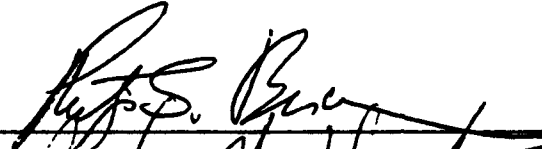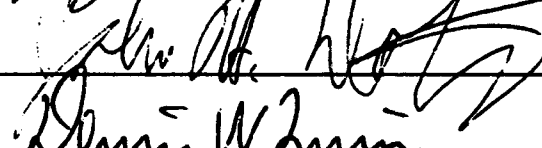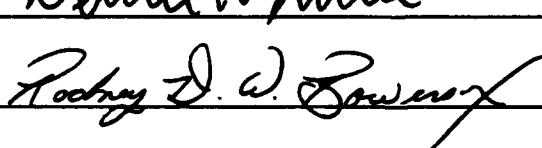| Accesion For		
NTIS CRA&I		☒
DTIC TAB		☐
Unannounced		☐
Justification		
By		
Distribution /		
Availability Codes		
Dist	Avail and / or Special	
A-1		

Approved for public release; distribution unlimited

AN AERODYNAMIC AND STATIC-STABILITY
ANALYSIS OF THE HYPERSONIC APPLIED
RESEARCH TECHNOLOGY (HART) MISSILE

Kenneth John Moran, B.S., M.S.

Captain, USAF

Approved:

_____ 26 May 94

_____ 26 May 94

_____ 26 MAY 94

_____ 26 May 94

_____

J. S. Przemienicki

Senior Dean

Acknowledgments

I dedicate this dissertation to my late father. It was always his desire to see me fulfill my dream of becoming an aeronautical scientist. Although he is not here to share this moment, his memory will always give my accomplishments meaning. His efforts and sacrifices made it all possible.

I am grateful to many people and several organizations for their assistance during my research. In particular, my advisor Dr. Philip Beran gave me the liberty to pursue my own goals and the guidance to realize them. I am forever in his debt. I would also like to thank the other committee members, Dr. Dennis Quinn, Captain John Doty, Dr. Rodney Bowersox, and my sponsor Dr Bruce Simpson. I am indebted to Dr Simpson on two counts, first for suggesting the research topic and second for providing invaluable computing resources without which this work could not have been done. Likewise, I owe thanks to the Avionics Directorate of Wright Laboratory whose Convex C220 came to reside at AFIT and became a computational work horse. Also, I would like to acknowledge the DoD National High Performance Computing Shared Resource Centers who provided some additional computing resources.

My wife, Tracy, deserves special recognition. Her tireless support and limitless understanding gave me sustenance and strength in ways I am only now beginning to realize.

<div align="right">Kenneth John Moran</div>

Table of Contents

iv

vi

List of Figures

List of Tables

xvii

List of Symbols

Symbol

A^+	=	near wall region length parameter
C_a	=	axial force coefficient
C_d	=	total drag coefficient
C_{d_b}	=	base drag coefficient
C_{d_f}	=	friction drag coefficient
C_{d_p}	=	pressure drag coefficient
C_{d_w}	=	wave drag coefficient
C_l	=	lifliftt coefficient
C_{m_α}	=	pitching-moment coefficient $\left(\frac{\partial C_m}{\partial \alpha}\right)$
C_n	=	normal force coefficient
D	=	body diameter
e_t	=	total energy per unit volume
$\vec{E}_{i+\frac{1}{2}jk}$	=	numerical flux at the $(i+\frac{1}{2}, j, k$ interface
$\vec{F}$	=	flux vector of a conserved quantity, U, (per unit area per unit time)
g^l	=	limiter for the lth wave field
J	=	flux Jacobian
$\bar{J}$	=	Jacobian of the transformation (2D)
k	=	thermal conductivity
L	=	body length
$L_\eta,\ L_\xi,\ L_\zeta$	=	operators for strang-type fractional-step method
$\hat{n}_x,\ \hat{n}_y,\ \hat{n}_z$	=	unit normals in the Cartesian coordinate directions
N	=	turbulence model pressure gradient function
p	=	pressure
p_l	=	pressure on the fin lower surface
p_{le}	=	pressure along the fin's leading edge

p_u	=	pressure on the fin upper surface
p_{t_2}	=	impact pressure (total pressure behind a normal shock wave)
P^+	=	Clauser-like pressure gradient function (inner formulation)
Pr	=	Prandtl number
Pr_t	=	turbulent Prandtl number
$q_x,\ q_y,\ q_z$	=	heat fluxes in Cartesian coordinate directions
r	=	radial coordinate
R_N	=	nosetip radius
R_B	=	body radius
$\hat{R}$	=	eigenvector due to diagonilation of flux Jacobian
Re	=	Reynolds number per unit length
Re_L	=	Reynolds number based on length
s	=	distance from nosetip along surface
$S(x)$	=	cross-sectional area at x
S_f	=	fin planform area
S_w	=	wetted area
S_B	=	base area
T	=	temperature
$u,\ v,\ w$	=	Cartesian velocity components
U	=	conserved quantity (per unit volume)
V	=	cell volume
x_{cg}	=	center of gravity
x_{cp}	=	center of pressure
$x,\ r,\ \theta$	=	cylindrical coordinates
$x,\ y,\ z$	=	Cartesian coordinates
$\hat{x}$	=	distance from nosetip in axial direction
y^+	=	nondimensioonal distance normal to surface ($\left[\frac{y^2 \rho_w |\omega_w|}{\mu_w}\right]^{1/2}$)
Z	=	turbulence model compressibility function

α	=	angle of attack
$\alpha_{i+\frac{1}{2}jk}$	=	vector of characteristic variables at the $(i + \frac{1}{2}, j, k$ interface
β	=	shock-wave angle
β^{*}	=	Clauser-like pressure gradient function (outer formulation)
δ	=	boundary-layer thickness
Δt	=	time step in numerical integration
ϵ	=	coefficient in entropy function
γ	=	ratio of specific heats
λ	=	eigenvalue due to diagonalization of flux Jacobian
$\hat{\lambda}$	=	entropy corrected eigenvalue
Λ	=	fin leading-edge sweep angle
μ	=	first coefficient of viscosity (molecular viscosity)
μ_t	=	eddy viscosity
ν	=	Courant number ($\frac{A\Delta t}{\Delta x}$)
ϕ	=	azimuthal angle (also potential perturbation variable)
Φ	=	upwind function
ρ	=	density
$\tau_{xx},\ \tau_{yy},\ \tau_{zz},$		
$\tau_{xy},\ \tau_{xz},\ \tau_{yz}$	=	viscous stresses

AFIT/DS/AA/94-3

Abstract

The flow about the complete Hypersonic Applied Research Technology (HART) missile is simulated for inviscid, laminar, and turbulent conditions and Mach numbers from 2 to 6. An explicit, second-order-accurate, flux-difference-splitting, algorithm is implemented and employed to solve the Navier-Stokes equations. The formulation models turbulence with the zero-equation, Baldwin-Lomax turbulence model, accounting for pressure-gradient and compressibility effects. The equations are solved using a finite-volume methodology.

In the first part of the study, numerical experiments are performed using an *infinitely thin-fin* approximation. The aerodynamic and static-stability characteristics are investigated to determine if conventional supersonic missile configurations can be flown at Mach numbers higher than 5. The effects of nosetip blunting and boundary-layer condition are demonstrated. In addition, many unresolved issues from experimental testing of the HART missile are addressed. In the second part of the study, the effects of fin thickness and cross section are explored. A comparison is made between thin-fin results and thick-fin results to assess the impact on missile stability.

The structure of the flow near the fins is significantly affected by the turbulent transport of momentum in regions of blocked cross flow. Turbulence and the blockage phenomenon cause bleeding around the fin leading edges. Ultimately, this results in lower fin effectiveness and reduced static stability. In addition, the strength and extent of the flow structures that develop in the blocked regions appear to be enhanced by fin thickness.

The aerodynamic characteristics of the HART missile are predicted at Mach numbers beyond the experimental free-flight testing capabilities. The current predictions indicate that the pitching-moment coefficient decreases with increasing Mach number much less than previous numerical computations. The present results also suggest that the clipped-delta-fin configuration is stable beyond Mach 7.

AN AERODYNAMIC AND STATIC-STABILITY
ANALYSIS OF THE HYPERSONIC APPLIED
RESEARCH TECHNOLOGY (HART) MISSILE

1. Introduction

This chapter presents a review of previous research, a description of the purpose for the present study, and an overview of the scope of the work. It begins with some background into Air Force high-speed-missile research as motivation for the current investigation. Additionally, some background is provided on the fin/body interaction problem. The scope of the present study relies on previous work in this area. Finally, an overview of the dissertation is made to lay a foundation for the chapters which follow.

1.1 Background on Missile Research

There have been many calculations for both axisymmetric and finned projectiles. Several studies have been made to assess the effect of nose bluntness on surface pressure, boundary-layer development, and magnus characteristics [44, 13, 83]. Sturek [81, 82, 85] has looked extensively at the aerodynamics of spinning shells (with and without fins). His work has concentrated on the influence of shell geometry and yawing on the magnus effect at supersonic speeds. Weinacht, et al. [98] have conducted PNS computations for much lower fineness-ratio, spinning and fin-stabilized projectiles in supersonic flow. The literature is replete with studies of turbulent boundary layers in supersonic flow; [30, 84] are just two examples. Investigations of un-spinning, very high fineness-ratio finned bodies, with respect to modeling turbulent boundary-layer development and stability performance at very low angle of attack are rare. In fact, no information could be found outside the Air Force program to be discussed shortly.

To realize the tactical advantages associated with increasing missile speeds, the Air Force Armament Laboratory (now the Wright Laboratory Armament Directorate) initiated an in-house program to investigate potential methods to extend

flight regimes for future air-to-air missiles. The first phase of this program involved a detailed investigation and documentation of the flow physics affecting the static stability of missiles. The goals of this phase were to predict, substantiate, and understand the static-stability characteristics of a generic missile configuration. A corollary goal was to begin identifying key missile geometry parameters that will effectively increase the stability envelope.

The Aeroballistics Section of the Wright Laboratory Armament Directorate developed a configuration that would most dramatically exhibit the static-stability limitations of current missile designs. This configuration was intended to provide the baseline characteristics from low supersonic to hypersonic velocities. It was a generic high fineness-ratio (length to diameter), tail-controlled missile, and was named the Hypersonic Applied Research Technology (HART) missile. The model consisted of an ogive nose, cylindrical body, and one four-fin group located near the extreme aft end of the projectile (shown in Figure 1 with a sharp nosetip and delta fins).
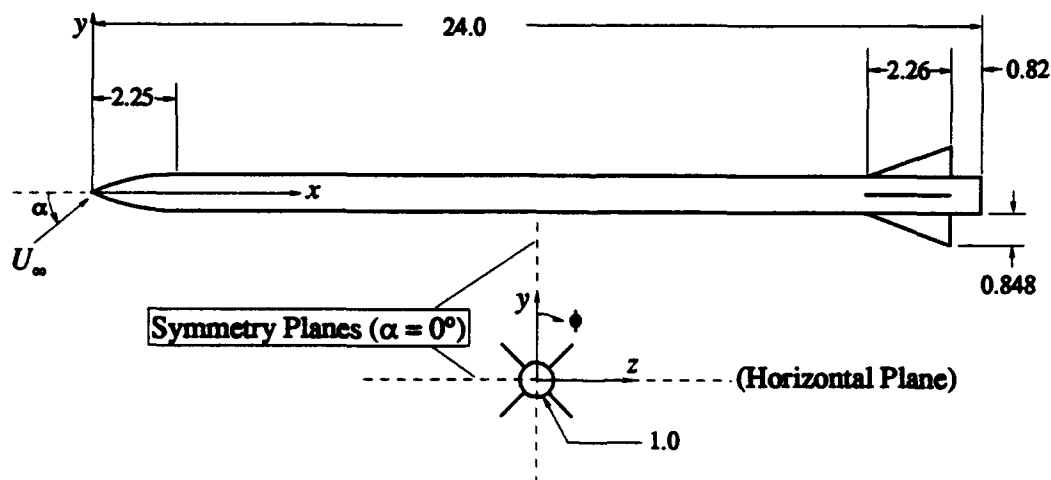
Figure 1. Hypersonic Applied Research Technology (HART) baseline model

Experimental testing, which began in 1987, and continues to date, has concentrated on varying geometry parameters like nosetip shape and fin shape. The variations to the baseline model of Figure 1 will be discussed in the following sections together with the experimental and numerical results.

1.1.1 Experimental Testing. Free-flight tests were conducted at the USAF Aeroballistic Research Facility (ARF), Eglin AFB, FL. The ARF is an enclosed concrete structure used to examine the exterior ballistics of various munitions while in unrestrained flight [45]. The instrumented section of the ARF is 207 meters long. There are 131 locations available as instrumentation sites, and used to obtain orthogonal photographs of the model's shadow during flight (called shadowgrams or shadowgraphs). These are subsequently used to determine the spatial position and angular orientations of the projectile at each of the shadowgraph stations.

At the time the baseline model was tested, a model with smaller delta fins was also investigated to confirm that the loss in static stability can create an unstable situation at high Mach numbers. For the small fins, neutral stability was predicted and confirmed to occur at about $M_\infty = 2.2$ [22]. In contrast, the baseline model showed a decreasing but still stable (negative) pitching moment up to the highest Mach numbers tested ($M_\infty \approx 4.5$) [22].

In 1989 and 1990, three additional models were tested [93]. A clipped-delta-fin configuration was fabricated with the same fin area as the baseline model, while maintaining the fin span of the small delta-fin model. In addition, an inverted-delta-fin model was constructed with the same area and span constraints described above. It was expected that the static stability would be improved by moving more of the fin outside the boundary layer [93]. In addition to fin modifications, the nosetip shape was modified with blunting. The sharp and blunt clipped-delta-fin models are shown in Figure 2, and are identical to the configurations analyzed in this study.

1.1.2 Analytical and Numerical Testing. The Aeroballistic Section of the Wright Laboratory Armament Directorate made use of several prediction techniques, including analytical, empirical, and numerical, to corroborate experimental findings. The analytical tool is entitled "Missile DATCOM" [94, 95]. It uses the Newtonian Flow Method [2] and the Second Order Shock Expansion Method [2] to calculate flow parameters. The empirical predictions were made with the Projectile Design Analysis System (PRODAS) [36]. PRODAS is an interactive program which allows the engineer to create a projectile, which is compared to similar configurations. The program then interpolates an extensive data base to provide aerodynamic estimates. Two numerical methods were utilized. First, an inviscid, space-marching Euler code was used. The code was developed by the Naval Surface Warfare Center and called

3
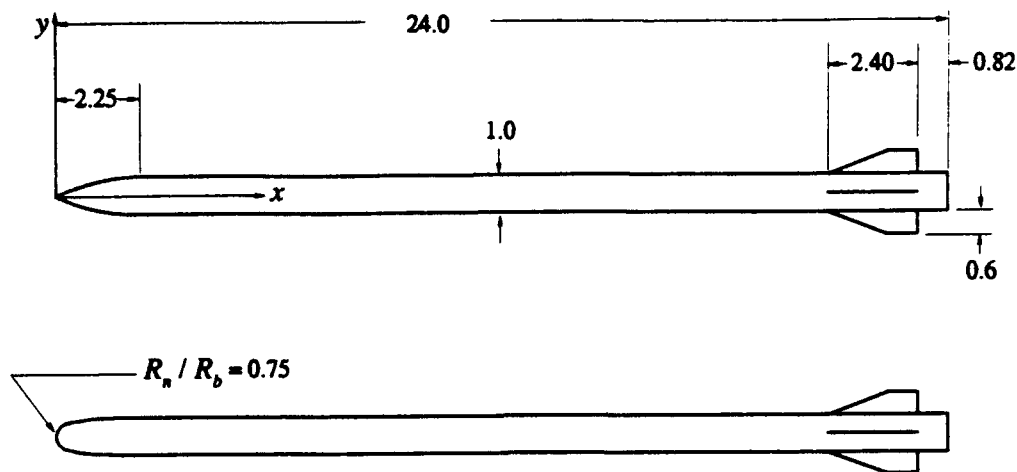
Figure 2. HART models with modified nosetip and clipped delta fins

the Zonal Euler Solver (ZEUS) [97]. Finally, a multiblock, implicit, steady-state Euler solver was used. This solver actually comprises a family of programs called the Eglin Arbitrary Geometry Implicit Euler (EAGLE) Code [50, 87, 88, 60]. The EAGLE solver constructs a multiblock grid, then solves the steady-state Euler equations.

Unless otherwise stated, the following options, pertaining to the EAGLE solver, were selected for all data presented in this document [68, 69] (see Section 3.5 for a discussion of the construction of a computational grid):

- Roe flux differencing

- Characteristic surface boundary conditions

- 40 points from the outer domain to the body

- Grid spacing clustered near the body with a minimum spacing of $0.004D$

- 19 points for the azimuthal half-plane

- Equal azimuthal angular spacing of $10°$

- Grid conformed to the fin leading edge through block structure

- Fin was treated as *infinitely thin*

Solutions were computed for the baseline HART model (delta fins), and the HART model with two other fin configurations (clipped-delta fins and inverted-delta

4

fins). For each of these configurations a solution was calculated at seven different Mach numbers for $\alpha = 0°$ and $\alpha = 0.5°$ [68]. Since EAGLE is an inviscid solver, only the forebody wave drag can be obtained. The other components were calculated empirically. The following were used for base drag and skin-friction drag [68]:

$$C_{d_b} = \frac{K}{M_\infty^2}, \tag{1}$$

$$C_{d_f} = \frac{.455}{[\log{(\mathrm{Re}_L)}]^{2.58}} \left(\frac{S_w}{S_b} \right). \tag{2}$$

where S_w is the wetted area, and S_b is the base area. The resulting total drag appears in [68] as well as [93]. The pitching moment is directly output from the EAGLE code. The drag and moment results are tabulated with the results from the present study in Chapter 4.

1.1.3 Summary of Previous Results. To date, experimental, empirical, and computational analyses of the HART missile have had varying degrees of agreement. In particular, four unexplained discrepancies materialized out of the previous combined experimental/computational work. First, the observed drag exhibited larger than expected scatter over the Mach number range tested (1.5-4.5), particularly above Mach 3.2 [93]. Further, the numerically predicted drag did not correlate well with the experimental drag. Second, free-flight testing showed an unusual trend in the pitching moment; the clipped-delta-fin and inverted-delta-fin missiles appeared to become more stable in the high-supersonic regime ($M_\infty \approx 4.0$) [93]. This was not expected and not resolved by the researchers of [93]. Third, ZEUS and EAGLE predictions of the pitching-moment coefficient differed significantly above Mach 5. The EAGLE solver computed a greater decrease in C_{m_α} with increasing M_∞ and much lower stability margins. Again, this was not resolved. Finally, differences between results for the modified geometry and the baseline model tested in 1987 were not addressed in [93]. These are the central questions to be addressed in this document.

The results from prior testing on the baseline model are presented to highlight a couple of these problems. The drag coefficients and pitching-moment coefficients obtained from experiment are plotted with the numerical results in Figure 3 and Figure 4. The experimental data is depicted with open symbols in both figures. The numerical drag prediction (EAGLE) in Figure 3 is empirically corrected for base drag and skin-friction drag. The poor correlation between the experimental and

5

numerical drag is evident as Mach number increases. In Figure 4, the experimental and numerical (EAGLE and ZEUS) pitching-moment coefficients agree at the lower Mach numbers, but the disagreement between the numerical predictions becomes large at higher Mach numbers.

1.2 Background on Fin/Body Interaction Problem

In general, there are very complicated flow structures associated with a blunt fin attached to a body in supersonic flow. The fin's bow shock interacts with a growing boundary layer on the body, and can involve the formation of strong horse-shoe vortices [80]. The interaction weakens dramatically, however, as the fin sweep angle increases. Price and Stallings [64] reported the effects of sweep as long ago as 1967. Recently, Hussain [41] studied blunted fins at sweep angles up to 75 degrees. He confirms the benefit of sweep in reducing the level and extent of the disturbed pressure field.

Although Hussain found clear evidence (oil flow pictures) that separation occurs up to the highest sweep tested at $M_\infty = 2.45$, some questions remain as to whether separation occurs for severely swept fins at higher Mach numbers. Price and Stallings [64] and Winkleman [99] experimentally found no disturbance ahead of a 75 degree swept fin at either $M_\infty = 3.71$ or $M_\infty = 5$. McMaster and Shang [55] used a McCormack method with the Baldwin-Lomax turbulence model to simulate a blunt fin on a flat plate at $M_\infty = 2.98$. They found that the flow remained attached for sweep angles exceeding 68 degrees. To the best of the author's knowledge, nobody has investigated turbulent, supersonic flow past a swept, flat-faced fin. Thus, the flow structure which should be predicted for this fin geometry is not entirely clear.

1.3 Purpose for Present Research

There are three main purposes for the present study. First, develop an efficient computational tool to simulate accurately the myriad of flow structures associated with high-speed-missile flight. Next, investigate the unexpected variations in the aerodynamic coefficients obtained from experimental testing (explained in Section 1.1.3), while substantiating the aerodynamic traits of the HART missile. Third, quantify the effects due to nosetip shape, base region, fin thickness, viscosity, and turbulence.
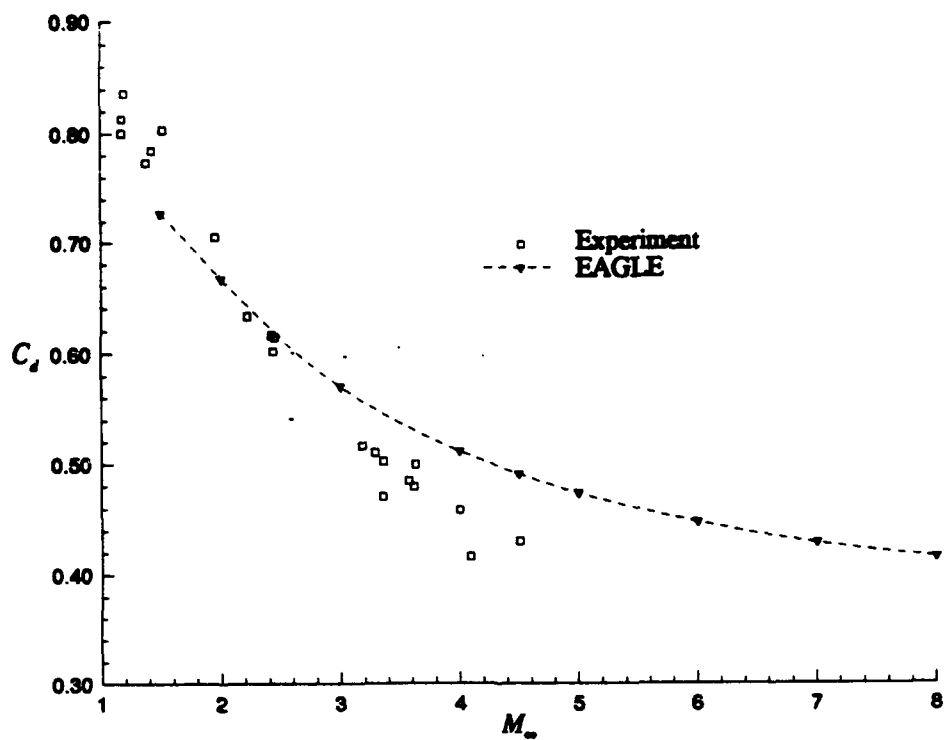
Figure 3. Axial-force coefficient (drag) for HART baseline model
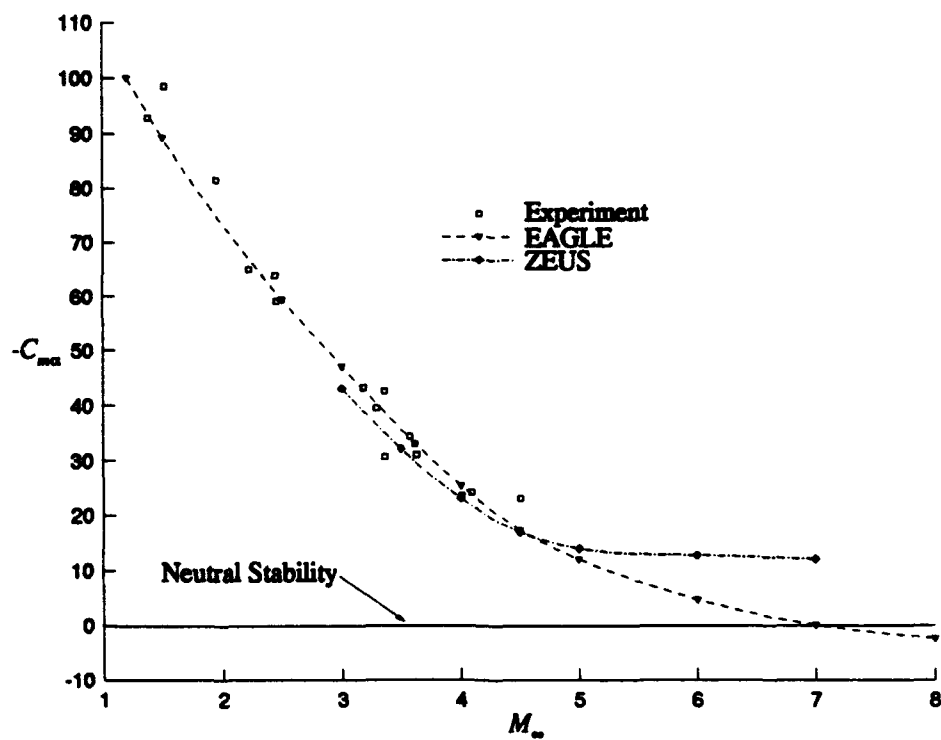
Figure 4. Pitching-moment coefficient for HART baseline model

7

The development of an accurate and efficient computational model is essential for the above investigations, and provides the means to study the flow physics and missile performance of future tests with greater detail than obtainable from free-flight testing. As discussed in Section 1.1.1, free-flight experiments are conducted in the Aeroballistic Research Facility (ARF) at Eglin AFB, Florida. Computationally, we can explore configurations and conditions beyond the practical limits of ARF testing. For example, flight model failure currently occurs during launch at Mach numbers above 4.5 [93]. Also, future configurations may fly at higher angles of attack and possess different center-of-gravity locations, requiring accommodations for larger variations in the trajectory and potentially unstable or very dynamic tests.

Clearly, the present research is driven by the results of the prior testing, and is aligned with the previously mentioned Air Force research program. Therefore, this work will address all of the previous testing in the course of the investigation. The intent is to substantiate the aerodynamic traits of the HART missile, and further the understanding of the fluid-dynamic mechanism affecting missile stability at higher Mach numbers. In combination with the experimental data, the results and analyses from this research will be used by missile designers to predict weapon performance characteristics in the hypersonic flight regime.

1.4   Overview of Dissertation

Simulation of a complete configuration is demanding (minimally requiring $O[100K]$ grid points). When the simulation involves turbulent boundary layers and wakes, supersonic flow and shocks, and shock/boundary-layer interactions, accurate results require sophisticated modeling techniques and many more grid points: $O[250K]$ points. For configurations which have length scales that differ by several orders of magnitude, $O[1000K]$ grid points are usually necessary. Since high-speed-missile research entails accurately predicting each flow structure mentioned above, and the ratio of missile length to fin thickness for the HART missile is about 500:1, the grids here could easily be millions of points.

To overcome the staggering memory implications, a tradeoff in algorithm performance for memory efficiency could have been pursued, but a different approach was attempted because this would have drastically reduced the scope of the investigation. The scope would be undesirably impacted because the run time for each

8

numerical test increases with this type of tradeoff. The alternate approach is to reduce the grid requirement, while maintaining high algorithm performance.

Lowering the grid requirement is achieved with two assumptions or approximations. In Part I, an *infinitely thin-fin* approximation was made. The fins are treated as having no thickness, and so they are merely boundary conditions within the computational domain. In regards to computational analysis, this is not an example of Keller's principle: "Something for nothing is worthless." The assumption relies on the premise that fin thickness is second-order to fin impermeability. This can be confirmed quite adequately on a reduced scale. In Part II, the actual thickness of the fin is modeled, but, owing to the projected grid refinement, the complete configuration is not reinvestigated.

1.4.1 Scope of Thin-fin Investigation (Part I). Computations are made for the sharp-nosetip and blunt-nosetip, clipped-delta-fin HART missiles (Figure 2) using the infinitely thin-fin approximation. Although most grid refinement issues are addressed prior to testing these shapes (see Appendices A and B), a limited grid refinement and sensitivity study is made with the thin fins to evaluate the variation of drag and pitching moment with azimuthal grid spacing, and sensitivity of C_{m_α} to α. After this sensitivity study, and using the thin-fin approximation, numerical experiments are undertaken to determine the aerodynamic coefficients for the two geometric variations of the HART missile.

Parametric Mach number studies ($M_\infty = 2 - 6$) are conducted for $\alpha = 0°$ and $\alpha = 5°$ under inviscid, laminar, and turbulent conditions for the sharp-nosetip model shown in Figure 2. The drag is broken down by component to facilitate various comparisons to the trends with Mach number predicted by theory and other results. Several semi-empirical corrections are proposed to account for the lack of fin cross section. The effect of the fins on base drag is also explored. Stability is investigated over the Mach range with the emphasis on the impact of viscosity, the effect of turbulence, and the influence of the base flow.

The analysis is formulated to address discrepancies that developed out of previous combined experimental/computational work on these configurations (Section 1.1.3). Also, the analysis is extended to higher Mach numbers than obtained in free-flight tests. For high Mach numbers, the current computations are qualitatively compared to the computational results of the two inviscid solvers used on the baseline model. Recall that these results differed significantly above Mach 4.0 (Figure 4).

The aerodynamics of the blunt-nosetip model are also determined with a parametric Mach number study. This study addresses several questions relevant to the blunt models: Is the dependence of the pitching moment on angle of attack affected by nosetip geometry? Does the lower total pressure associated with the normal portion of the bow shock wave affect pressure near the fins? Does delayed transition associated with the high entropy layer on blunted bodies impact the HART missile's pitching characteristics?

A discrepancy in the sharp-nosetip experimental models is documented, and its impact assessed. In addition, computations are made using the modified geometry to further document the experimental discrepancy.

The aerodynamics of the clipped-delta-fin HART models are contrasted with the baseline model in an attempt to address the goals of Air Force hypersonic missile research. As previously stated, the goals are to substantiate the stability characteristics of high fineness-ratio missiles, and identify key missile geometry parameters affecting the stability envelope.

1.4.2 Scope of Thick-fin Investigation (Part II). The accuracy, and thereby validity, of the thin-fin approximation made in Part I is addressed in this part of the research. A boundary for incipient separation at the fin leading edge/body junction was suggested by Stollery [80], and is explored with a parametric Mach number study. First, the structure of the flow is examined to determine if fin thickness significantly affects the interaction at the fin/body junction. The flow structure is directly compared to the structure from the thin-fin computations. Next, fin drag is compared to results from the thin-fin computations. Finally, the impact of fin thickness on static stability is addressed.

10

Part I: Investigation Using "Infinitely Thin Fin" Approximation

2. Governing Equations and Supporting Theory

The equations of fluid mechanics that are fundamental to the present research are outlined in this chapter along with important principles for the fin/body problem, inviscid drag on a slender body, and the pitching moment on a finned body. First, the flow structure near a fin/body junction is discussed. In particular, the relation between the extent of a shock/boundary-layer interaction and leading-edge bluntness, sweep angle, and incidence angle is highlighted. Next, inviscid theories for drag and pitching moment are examined. The introduction of fins onto a forebody is a departure from the validation models (axisymmetric bodies), therefore, linear theory is used to provide a bridge between the simpler validation computations and HART missile computations. Finally, the governing equations are presented with a brief discussion of boundary conditions and turbulence. The fluid equations are presented in full, three-dimensional form, and turbulence is accounted for with the Boussinesq [101] eddy viscosity concept. Eddy viscosity is invoked to achieve closure of the Reynolds equations for turbulent flow.

2.1 Flow Structure Near Fin

Glancing interactions include situations where the shock wave generated by one body cuts across the boundary layer growing over another, and the intersection line is swept. Figure 5 shows the geometry of a swept thin fin; the fin is swept at an angle Λ, and inclined to the freestream at an angle α. In the simplest interactions, the only shock wave of interest is that formed by the shock generator (fin), and the only boundary layer of interest is the one affected by the glancing impingement (i.e., on missile body). The generated shock and the boundary layer of interest are shown in Figure 5. Stollery [80] gives an excellent review of glancing shock/boundary-layer interactions.

2.1.1 Shock Wave Shape. Figure 6 is taken from [80] (with permission) to illustrate the shock-wave shape expected. Figure 6 shows a relationship between the shock-wave angle and a series of delta wings. The delta wings are wedge shaped with a wedge deflection angle indicated by α in Figure 6. In general, the deflection angle depends on the cross-sectional shape and the incidence angle. The deflection
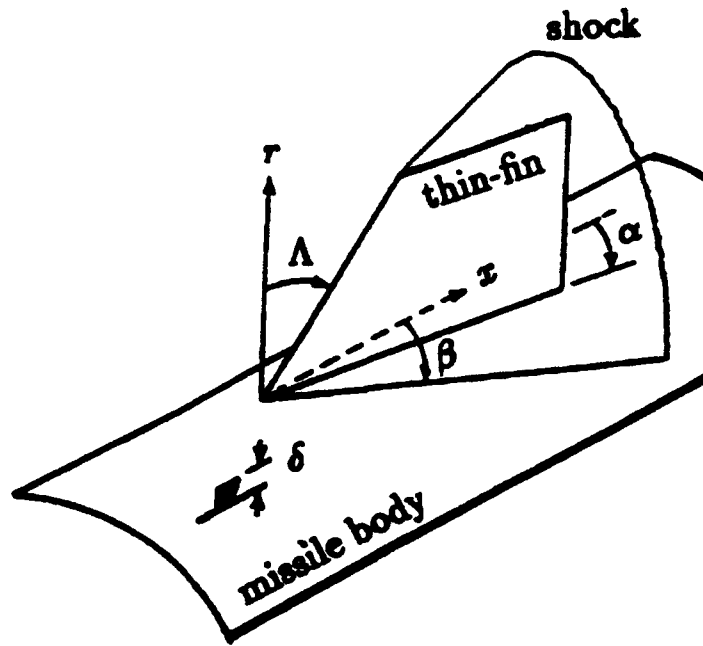
Figure 5. Swept thin fin geometry

angle for a thin fin, however, is exactly equal to the incidence angle. This is usually taken to be the angle of attack, but in this investigation it is somewhat less, since the fins are placed at 45 degrees relative to the horizontal (Figure 1). It is particularly interesting to note that the shock-wave angle should be very close to the Mach angle (μ in Figure 6) for the typical HART missile fin shape ($\Lambda \approx 70°$) at low angle of attack.

2.1.2 Shock/Boundary-layer Interaction. Figure 7 is also taken from [80] (with permission) to establish a basis for discussing the interactions. Streamsurface and vortex skeleton patterns are shown for *attached*, *separated*, and *secondary separation* flows. In the vortex skeleton representations, S is a separation line, A is an attachment line, and V is the core of a vortical structure.

The strength of the shock/boundary-layer interaction depends on the fin's leading edge radius of curvature, sweep (Λ), and orientation (α), [80]. Each of the following, therefore, reduces the extent of the interaction: reducing the leading-edge bluntness, increasing the sweep angle, and reducing the fin's inclination to the oncoming flow. In turn, the associated vortices lose strength or do not develop at all. In this study, the thin-fin assumption eliminates the radius of curvature at the leading edge. In addition there is a very low incidence angle ($\alpha \leq 5°$), and a very high

13
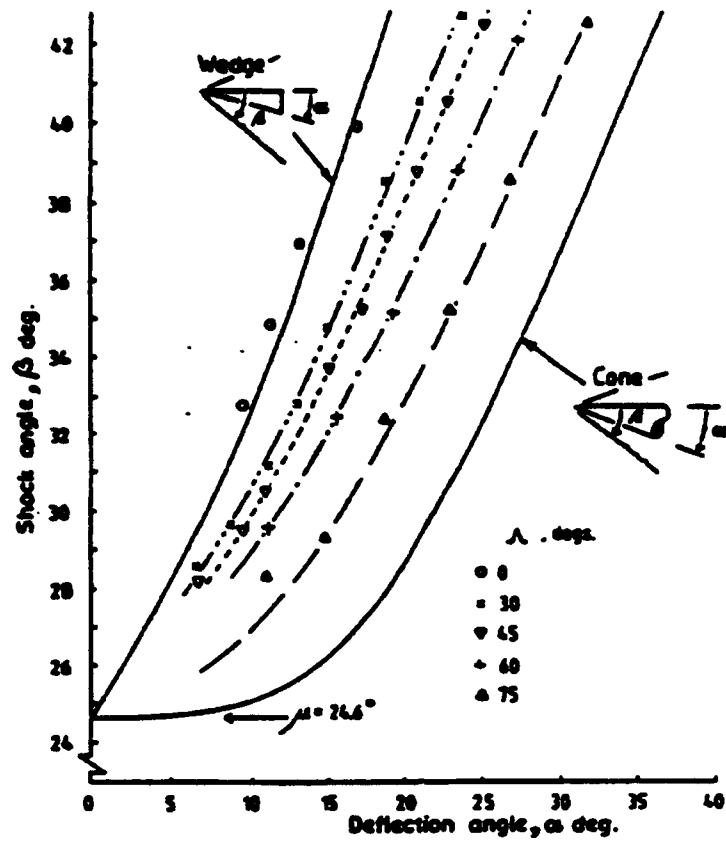
Figure 6.   Shock-wave angles measure from the centerline of a delta wing (from [80] with permission)
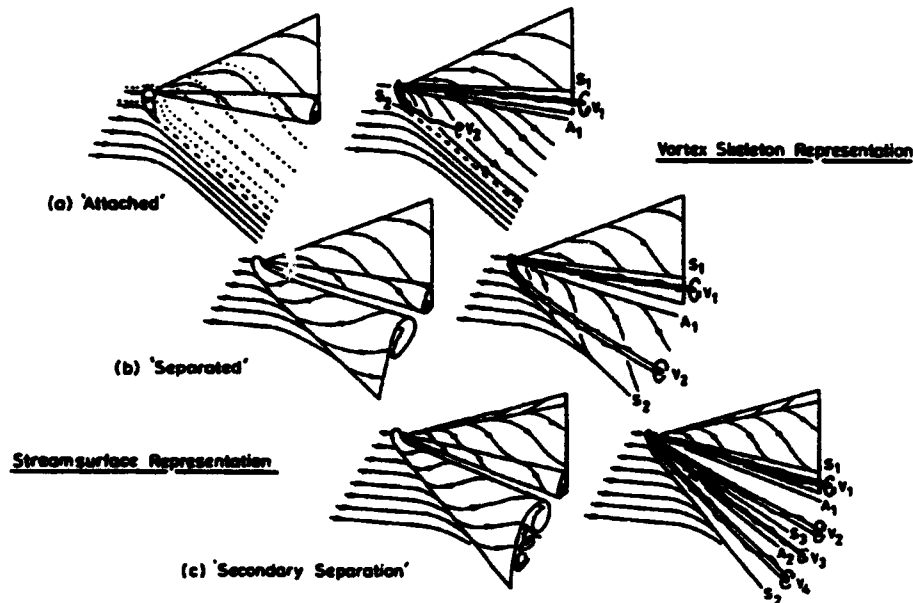
Figure 7.   Suggested flow patterns for swept-sharp-fin/sidewall-boundary-layer interactions (from [80] with permission)

14

sweep angle ($\Lambda \approx 70°$). Thus, the flow pattern should agree most closely with the *attached* representation of Figure 7.

2.2 Inviscid Theory for Drag and Pitching Moment

Inviscid theory provides a suitable comparison for computational results. By examining simple theoretical expressions for wave drag, an appropriate baseline can be established by which inviscid and viscous computations can be interpreted. In addition, by using theoretical aerodynamics for the fins, the pitching-moment trends with Mach number and angle of attack are formulated. These qualitative baseline trends are used to interpret and understand the computational results.

2.2.1 Theoretical Forebody Wave Drag.

The pressure drag acting on a body in supersonic flow can be thought of as composed of three parts: the wave drag, the vortex drag, and the base drag; the drag coefficients are C_{d_w}, C_{d_v}, and C_{d_b}, respectively. The vortex drag arises from the momentum carried away by vortices trailing from a lifting body [4]. No vortices exist for the HART missile configuration at the angles of attack examined herein. A theoretical solution to the base drag is not available, so empirical relations are often used of the form

$$C_{d_b} = \frac{K}{M_\infty^2}, \tag{3}$$

where K is an experimentally measured function of the freestream Mach number, M_∞, [56]. The wave drag results from the momentum carried away by the pressure waves set up by a body as it travels faster than the speed of sound [4].

Slender-body theory [4] provides an expression for wave drag in terms of a body's profile of cross-sectional area, $S(x)$, and the solution to a perturbation potential equation. By virtue of the smallness of the disturbance (slender body), a perturbation is introduced into the full potential equation (FPE). A linearized equation is derived to govern the perturbation potential (see [4]). The solution to this linearized equation provides ϕ and $g(x)$ in the following expression for wave drag:

$$\frac{D - D_b}{\rho_\infty U_\infty^2} = \int_0^L \ddot{S}(x)g(x)dx - \frac{1}{2}\dot{S}(L)g(L) - \frac{1}{2}\oint_{C_b} \phi\frac{\partial\phi}{\partial n}ds. \tag{4}$$

In (4), L is the length of the body, and C_b represents a contour around the base.

15

Introducing the solution to the perturbation potential equation for an axisymmetric body, and recognizing that for a body which ends in a cylindrical portion parallel to the freestream, $\partial\phi/\partial n$ and $\dot{S}$ vanish, yields

$$\frac{D - D_b}{\rho_\infty U_\infty^2} = -\frac{1}{2\pi}\int_0^L \tilde{S}(x)dx \int_0^x \tilde{S}(x_1)\ln(x - x_1)dx_1, \tag{5}$$

or

$$C_{d_b} = -\frac{1}{\pi S(L)}\int_0^L \tilde{S}(x)dx \int_0^x \tilde{S}(x_1)\ln(x - x_1)dx_1. \tag{6}$$

The most striking aspect about (6) is the absence of Mach number. This agrees fairly well with experimentally determined wave drag on very thin bodies of revolution [56]; wave drag on these bodies shows very mild Mach number dependence.

The HART missile has a 2.25 caliber tangent-ogive nose (Figure 1). Drew and Jenn [15] numerically evaluated (6) using the cross-sectional area distribution for this nose shape. They found $C_{d_w} = 0.232$. This value is somewhat high compared to experimentally determined wave drag [56], ranging from 10% high at $M_\infty \approx 1.5$ to 50% high when $M_\infty > 6$. The overprediction is a result of the relative bluntness of the nose. Slender-body theory performs better for fineness ratios exceeding 3.

The error associated with the slenderness assumption can be overcome by using a higher-order analysis, or by an empirical correction, and the Mach number dependence can be interjected by using the frontal projection area of a modified cross section. The new cross section is created by intersecting the body with a plane at the associated Mach angle. This is Whitcomb's area rule [100]. Both Mach number and fineness ratio were accounted for by Drew and Jenn [15]. At $M_\infty = 2$, they calculated the wave drag at approximately 0.166. (This is in reasonable agreement with the current calculations shown in Chapter 4.)

2.2.2 Pitching Moment From Linear Theory. Fin-stabilized configurations are known to exhibit decreasing static stability with increasing Mach number. The reason can be traced to a loss in the fin effectiveness associated with compressibility. This basic principle is clear from thin-airfoil theory. For a flat plate, at angle of attack, in supersonic flow, the lift coefficient determined from thin-airfoil theory is [4]

$$C_l = \frac{4\alpha}{\sqrt{M_\infty^2 - 1}}. \tag{7}$$

16

From (7), at a fixed angle of attack, as Mach number increases, the lift created by a flat plate decreases. Since the fins are treated as swept flat plates, the lift from the fins also decreases. Although boundary layers exist, and shock interactions affect the solution, this underlying principle dominates.

In contrast to thin-airfoil theory, slender-body theory predicts that the lift from the missile body is independent of Mach number [4].

$$C_l = 2\alpha. \tag{8}$$

Thin-airfoil theory can be modified to account for the azimuthal locations of the fins, and combined with slender-body theory to predict the lifting and pitching characteristics of a missile. Basically the more or less constant lift associated with the un-finned missile surface produces a nearly constant destabilizing moment. From (7), as Mach number rises, lift from the fins decreases. The lift from the fins is modified to account for the non-horizontal placement of the fins on the body ($\phi_{\text{fin}} \neq 90°$), and normalized to the missile base cross-sectional area, S_b. The ratio of the HART model's clipped-delta-fin area, S_f, to base area is 1.2223. Because the fins are aft of the center of gravity, less lift means the restoring moment decreases. Thus, the static margin or pitching-moment coefficient approaches neutral stability. The functionality of the pitching-moment relationship is obtained by using (7) and (8) with appropriate moment arms. The moment arm for the lift created by the body is the distance between the center of pressure for the body alone, x_{cp_1}, and the center of gravity for the total configuration (body with fins), x_{cg}. The moment arm for the lift generated by the fins is the distance between this same center of gravity and the center of pressure for the fins alone, x_{cp_2}. The pitching-moment coefficient becomes

$$C_{m_\alpha} = c_1 - \frac{c_2}{\sqrt{M_\infty^2 - 1}}, \tag{9}$$

where c_1 and c_2 are

$$c_1 = 2\left(\frac{x_{cg} - x_{cp_1}}{D}\right), \quad \text{and} \quad c_2 = 4\left(\frac{x_{cp_2} - x_{cg}}{D}\right)\left(\frac{4S_f}{S_b}\right)\left(\left|\cos\phi_{\text{fin}}\right|\right). \tag{10}$$

The constants c_1 and c_2 are calculated to correspond to the center of gravity at 43.5% of length. The center of pressure for a fin is taken to be its centroid. Therefore,

17

$x_{cp_2} - x_{cg} = 11.906D$. The center of pressure for the body is calculated using the experiments of Butler, et al. [9] and Dolling and Gray [13] on tangent-ogive cylinders. Butler, et al. and Dolling and Gray tested much shorter bodies than the HART missile body, but all results showed that for small angles of attack, surface pressure had equilibrated within six diameters downstream of the ogive section. Therefore, pressure was assumed constant over the remaining length of the HART missile body, and $x_{cp_1} - x_{cg} = -8.440D$. Figure 8 is a graph of (9).
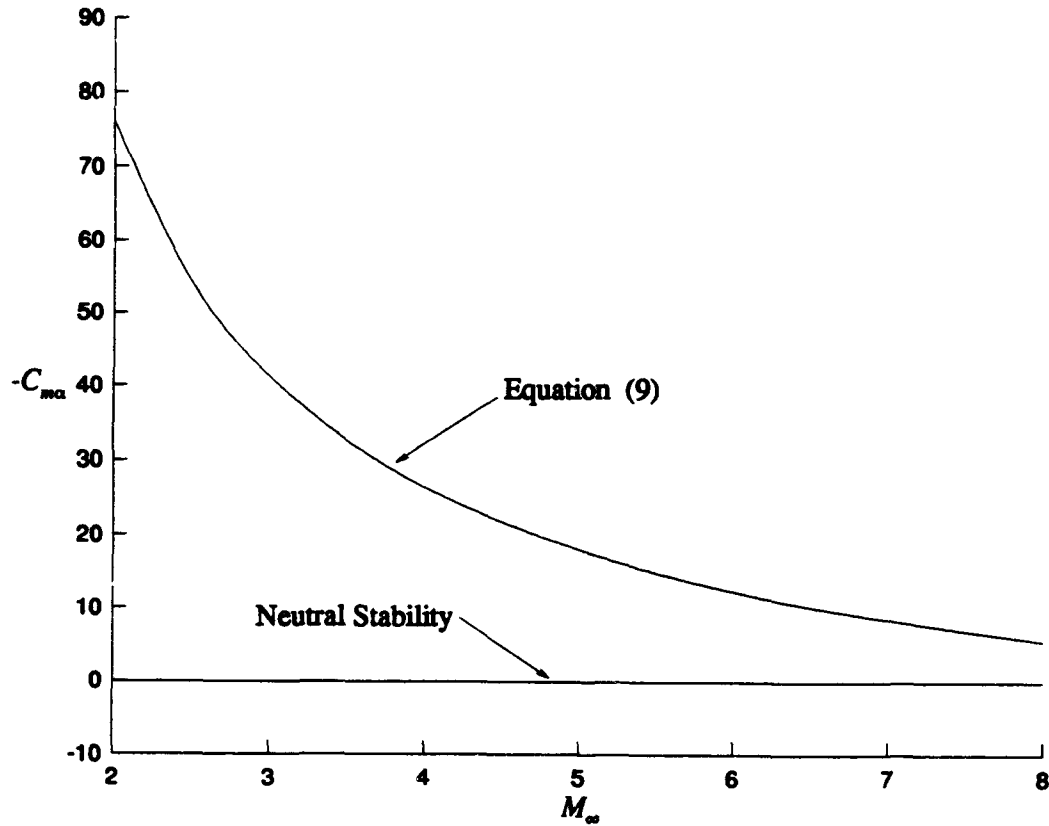
Figure 8. Pitching moment using thin-airfoil and slender-body theories

2.3 Governing Equations and Boundary Conditions

Equations are presented throughout in nondimensional form. The velocity and density scales are the freestream velocity and density, U_∞ and ρ_∞, respectively; pressure is nondimensionalized by $\rho_\infty U_\infty^2$. The length scale is the missile body diameter, D; and time is nondimensionalized by the aerodynamic time scale, D/U_∞.

18

The appropriate governing equations for a perfect gas are the Navier-Stokes equations. The integral form of the Navier-Stokes equations is written as

$$\frac{d}{dt}\int_V U\ dV + \oint_S \hat{n}\cdot\vec{F}\ dS = 0, \tag{11}$$

where U is a conserved variable (per unit volume), and $\vec{F}$ is the flux of U (per unit area per unit time). The volume of the region over which (11) is applied is V, and the surface of that region is S. Only modest assumptions are involved in (11). First, a continuum is required. Next, all variables are assumed continuous in time. Finally, conserved quantities cannot be produced internal to S, as with a chemical reaction for example.

Newton's assumption that a linear relationship exists between fluid stress and strain is assumed. Also, Stoke's hypothesis is used for the second coefficient of viscosity to yield the following flux definitions in each Cartesian direction [1]:

$$\hat{n}_x \cdot \vec{F} = E = \begin{bmatrix} \rho u \\ \rho u^2 + p - \mathrm{Re}^{-1}\tau_{xx} \\ \rho u v - \mathrm{Re}^{-1}\tau_{xy} \\ \rho u w - \mathrm{Re}^{-1}\tau_{xz} \\ (e_t + p)u - \mathrm{Re}^{-1}\left(u\tau_{xx} + v\tau_{xy} + w\tau_{xz} - \frac{q_x}{(\gamma-1)M_\infty^2}\right) \end{bmatrix},$$

$$\hat{n}_y \cdot \vec{F} = F = \begin{bmatrix} \rho v \\ \rho u v - \mathrm{Re}^{-1}\tau_{xy} \\ \rho v^2 + p - \mathrm{Re}^{-1}\tau_{yy} \\ \rho v w - \mathrm{Re}^{-1}\tau_{yz} \\ (e_t + p)v - \mathrm{Re}^{-1}\left(u\tau_{xy} + v\tau_{yy} + w\tau_{yz} - \frac{q_y}{(\gamma-1)M_\infty^2}\right) \end{bmatrix}, \quad (12)$$

$$\hat{n}_z \cdot \vec{F} = G = \begin{bmatrix} \rho w \\ \rho u w - \mathrm{Re}^{-1}\tau_{xz} \\ \rho v w - \mathrm{Re}^{-1}\tau_{yz} \\ \rho w^2 + p - \mathrm{Re}^{-1}\tau_{zz} \\ (e_t + p)w - \mathrm{Re}^{-1}\left(u\tau_{xz} + v\tau_{yz} + w\tau_{zz} - \frac{q_z}{(\gamma-1)M_\infty^2}\right) \end{bmatrix}.$$

The Reynolds number, Re, represents the ratio of convective to dissipative forces. The viscous stresses are defined as follows [1]:

$$
\begin{aligned}
\tau_{xx} &= \mu \left[\frac{4}{3}\frac{\partial u}{\partial x} - \frac{2}{3}\left(\frac{\partial v}{\partial y} + \frac{\partial w}{\partial z}\right) \right], \\
\tau_{yy} &= \mu \left[\frac{4}{3}\frac{\partial v}{\partial y} - \frac{2}{3}\left(\frac{\partial u}{\partial x} + \frac{\partial w}{\partial z}\right) \right], \\
\tau_{zz} &= \mu \left[\frac{4}{3}\frac{\partial w}{\partial z} - \frac{2}{3}\left(\frac{\partial u}{\partial x} + \frac{\partial v}{\partial y}\right) \right], \\
\tau_{xy} &= \mu \left(\frac{\partial u}{\partial y} + \frac{\partial v}{\partial x} \right), \\
\tau_{xz} &= \mu \left(\frac{\partial u}{\partial z} + \frac{\partial w}{\partial x} \right), \\
\tau_{yz} &= \mu \left(\frac{\partial v}{\partial z} + \frac{\partial w}{\partial y} \right).
\end{aligned}
\tag{13}
$$

In (13), μ is the the first coefficient of viscosity. The components of the heat-flux vector, q are defined as

$$
q_x = -k\frac{\partial T}{\partial x}, \qquad q_y = -k\frac{\partial T}{\partial y}, \qquad \text{and} \qquad q_z = -k\frac{\partial T}{\partial z}.
\tag{14}
$$

In nondimensional form the coefficient of thermal conductivity, k, is equivalent to μ/Pr; $\mathrm{Pr} = 0.71$. Viscosity and thermal conductivity are nondimensionalized by their freestream values. The freestream values are referenced to the freestream temperature, T_∞, which is taken to be the standard sea-level temperature. The equation of state for a perfect gas defines pressure (nondimensional):

$$
p = (\gamma - 1)e = (\gamma - 1)(e_t - \frac{1}{2}\rho \, \vec{u} \cdot \vec{u})
\tag{15}
$$

For inviscid calculations, those terms preceded by Re^{-1} are set to zero. For laminar viscous computations, μ is determined using Sutherland's formula [1]:

$$
\mu = T^{\frac{3}{2}}\left(\frac{1 + c_s}{T + c_s}\right) = \mu_l,
\tag{16}
$$

where $c_s = (110.4K)/T_\infty$. The subscript l denotes that (16) represents the molecular

viscosity for *laminar* flow. Recall, the governing equations are used in nondimensional form.

Equations (11)–(14) do not directly govern a turbulent flow. However, if the Reynolds-averaged Navier-Stokes equations are cast in nondimensional form, and eddy viscosity, μ_t, is invoked to achieve closure, then (11)–(14) still apply with minor alterations [101]. Then,

$$\mu = \mu_l + \mu_t, \qquad k = \frac{\mu_l}{\text{Pr}} + \frac{\mu_t}{\text{Pr}_t},$$

and μ_l is still calculated with (16). The turbulent Prandtl number, Pr_t, for air is assumed to be is 0.9 [101].

A location is selected along the missile length to separate laminar and turbulent portions of the boundary layer, and a fully turbulent condition is assumed for the wake region. Consequently, μ_t is calculated only in the turbulent regions. The Baldwin-Lomax algebraic model [5] is used to compute μ_t on the turbulent portion of the forebody because of its relatively low computational cost and ease of application. An empirical model is used to calculate μ_t in the wake. The turbulence models and the location of the laminar to turbulent *switch* are described in Section 3.4.

The computational domain is illustrated in Figure 9 where each boundary is given a number. Due to the supersonic condition at both the inflow and outflow boundaries, the associated boundary conditions are relatively straightforward; at the inflow (surface 1 in Figure 9), freestream conditions are applied, and at the outflow (surface 2 in Figure 9), extrapolation is employed. For the body (surface 3 in Figure 9), base (surface 4 in Figure 9), and fin surfaces, impermeability and no slip (viscous only) are enforced. Also, on the body, base, and fin surfaces, zero normal pressure gradient and an adiabatic wall are enforced. Since the HART missile is bisymmetric, and the model was inclined within one of the planes of symmetry, calculations were made around only half the circumference of the missile. Symmetry is then enforced at the azimuthal boundaries (surfaces 5 and 6 in Figure 9). For $\alpha = 0°$, axisymmetry is applied to surfaces 7 and 8 in Figure 9. Otherwise extrapolations give necessary data at those boundaries. More details are provided for these boundary conditions in Section 3.6.
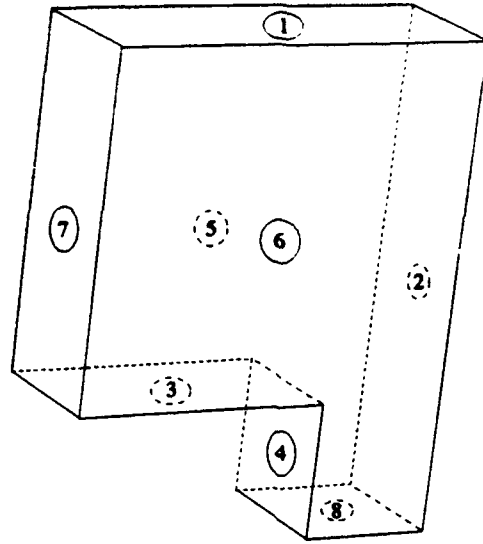
Figure 9. Computational domain showing boundary conditions

2.4 Aerodynamic Coefficients

Both static and dynamic first-order force and moment coefficients were obtained from free-flight experiments of the HART missile configuration [22, 93]. Additionally, some second-order coefficients were determined (e.g., the change in zero-yaw-drag coefficient with Mach number, $C_{d_{0_M}}$, and the change in pitching-moment coefficient with Mach number, $C_{m_{\alpha_M}}$). The present computational study provides only axial and normal force coefficients and the first-order pitching-moment coefficient; derivative coefficients are calculated numerically. The experimental and computational methodologies are explained in the following two sections.

2.4.1 Drag Coefficient, C_d.

The forces acting on the missile can be separated into pressure and viscous contributions. In terms of a drag coefficient this takes the following form:

$$C_d = C_{d_p} + C_{d_v}.$$

The pressure drag can be further separated into a wave drag and a base drag. Now the drag coefficient becomes:

$$C_d = C_{d_w} + C_{d_b} + C_{d_v},$$

where the fins and the missile body each have a wave, viscous, and base drag contribution. Therefore,

$$C_d = \left(C_{d_w} + C_{d_b} + C_{d_v}\right)_{\text{body}} + \left(C_{d_w} + C_{d_b} + C_{d_v}\right)_{\text{fins}}. \qquad (17)$$

The body forces are well modeled with the current technique, but due to insufficient grid resolution and lack of fin cross section, fin forces are not well modeled. (See Chapter 3 for a description of the present methodology and grid limitations.) Unfortunately, fin drag is not negligible [56]. To make any quantitative comparison with experimental data meaningful, fin drag must be accounted for. Therefore, semi-empirical corrections are proposed to obtain estimates of the fin components.

2.4.1.1 Fin wave drag. This portion of the drag is not directly computable due to the thin-fin approximation. Previous EAGLE computations were also made with the thin-fin assumption, but no correction was added to account for the wave drag created by the fins. The following steps are used with the current calculations to obtain a value for fin wave drag.

1. Assume that the pressure is constant across the flat-faced leading edge.

2. Numerically determine the local impact pressure, P_{t_2}, along the leading edge. Impact pressure is the total pressure behind a normal shock wave sitting in front of an imaginary numerical probe inserted into the flow.

3. Obtain the pressure along the fin's leading edge, p_{le}, by using the relation between fin sweep angle and impact pressure [64]. For $\Lambda \approx 70°$,

$$p_{le} = 0.2P_{t_2},$$

4. Use (18) with p_{le} and the actual thickness of the fin to determine fin wave drag.

This method relies on an accurate prediction of local impact pressure. The accuracy of the current algorithm is shown in Appendix A.

2.4.1.2 Fin base drag. Fin base drag is determined by correlating the local Mach number and pressure near the fin trailing edge with the pressure for

23

two-dimensional airfoils with flat bases [10]. The following relation determines the
nondimensional fin base pressure, p_{bf}:

$$p_{bf} = \left(\frac{0.675}{M_\infty}\right)\left(\frac{p_l + p_u}{2}\right),$$

where p_l and p_u are the surface pressures on the lower and upper surfaces of the fin
just upstream of the fin's base. As above for the leading edge, it is assumed that p_{bf}
is constant across the base and (18) is used with with p_{bf} to determine drag.

2.4.2 Pitching-moment Coefficient, C_{m_α}.

2.4.2.1 Experimental Methodology Using Trajectories and Six Degree-of-Freedom Analysis.
After missile models are fired through a test range, the time
history, position, and mass properties are used to determine the aerodynamic coef-
ficients and derivatives. This is done with the Aeroballistic Research Facility Data
Acquisition System (ARFDAS) [19]. This program utilizes linear theory to get pre-
liminary results. These data are passed to a routine that numerically integrates the
six degree-of-freedom (6DOF) theoretical equations of motion. An iteration process
is used to match the theoretical trajectory to the measured trajectory. The theo-
retical equations of motion are provided by Etkin [18] for a general vehicle. They
simplify considerably for a vehicle with fixed control surfaces, and still further for a
bisymmetric one. ARFDAS uses multiple flights in order to obtain a determination
of Mach number dependence. The analysis of multiple trajectories also gives better
angle dependency.

The 6DOF routine incorporates the Maximum Likelihood Method (MLM) to
match the theoretical trajectory to the experimentally measured trajectory. The
MLM is an iterative procedure that adjusts the aerodynamic coefficients to max-
imize a likelihood function. According to [35], the use of this likelihood function
eliminates the inherent assumption in least squares theory that the magnitude of
the measurement noise must be consistent between dynamic parameters.

2.4.2.2 Computational Methodology Using Discrete Data.
The forces
acting on a body by a fluid can be separated into pressure and viscous contributions.

24

The decomposed forces acting in the $\hat{i}$-direction (x-direction in Figure 1) are

$$F_{p_i} = -\int_S (p - p_\infty)\,\hat{n}_i \cdot d\vec{S}, \tag{18}$$

$$F_{v_i} = \int_S \left(\tau_{ji}\hat{n}_j \cdot d\vec{S} + \tau_{ki}\hat{n}_k \cdot d\vec{S}\right). \tag{19}$$

where $\hat{n}_i \cdot d\vec{S}$, $\hat{n}_j \cdot d\vec{S}$, and $\hat{n}_k \cdot d\vec{S}$ relate directly to the surface grid, and represent the projection of a surface area element into the three Cartesian directions. For finite-volume methodologies, they are already known as the projections of grid cell interfaces (Section 3.3).

For a bisymmetric computation, only two forces and one moment are non-trivial: the axial and normal forces and the pitching moment. The axial and normal force coefficient are denoted by, C_a and C_n, respectively. They are calculated here such that the axial direction is aligned with the x-direction, and the normal direction is aligned with the y-direction (see Figure 1). The aerodynamic forces can also be expressed in terms of lift and drag coefficients:

$$C_d = C_a \cos\alpha + C_n \sin\alpha, \tag{20}$$

$$C_l = C_n \cos\alpha - C_a \sin\alpha. \tag{21}$$

The pitching-moment coefficient is easily calculated from (18)–(19) by including the appropriate local moment arm:

$$\begin{aligned} M = &\int_S (y)\left(\tau_{ji}\hat{n}_j \cdot d\vec{S} + \tau_{ki}\hat{n}_k \cdot d\vec{S} - (p - p_\infty)\hat{n}_i \cdot d\vec{S}\right) \\ &+ \int_S (x_{cg} - x)\left(\tau_{ij}\hat{n}_i \cdot d\vec{S} + \tau_{kj}\hat{n}_k \cdot d\vec{S} - (p - p_\infty)\hat{n}_j \cdot d\vec{S}\right). \end{aligned} \tag{22}$$

Unlike the experiments, derivative coefficients are derived from computation using steady-state discrete data and finite-difference expressions. Solutions are calculated for $\alpha = 0°$ and $\alpha = 5°$, and the resulting normal-force and moment coefficients are used to compute c_{n_α} and c_{m_α}:

$$C_{n_\alpha} \doteq \frac{C_n(\alpha = 5°) - C_n(\alpha = 0)}{\Delta\alpha}, \tag{23}$$

$$C_{m_\alpha} \doteq \frac{C_m(\alpha = 5°) - C_m(\alpha = 0)}{\Delta\alpha}. \tag{24}$$

25

3. Methodology for the Thin-fin Investigation

This chapter details the method used to investigate the HART missile with the thin-fin approximation. First, the philosophy of the thin-fin analysis is discussed through a hierarchy of geometric and aerodynamic effects. Following this general discussion, details regarding the approximation and the computational techniques are described, including turbulence modeling. Finally, the grid structure and boundary conditions are explained.

3.1 Hierarchy of Effects

To systematically analyze the stability of the HART missile, a hierarchy of fin characteristics and phenomenon is used. The fin traits are categorized here as primary, secondary, and tertiary. The primary characteristic is fin impermeability. The size, shape, location, and orientation of a fin will dominate its pitching capability. Secondary traits include: no-slip fin surface, amount of fin submerged in missile boundary layer, fin proximity to base, and fin cross-sectional shape (thickness and leading-edge radius of curvature). Turbulent transport of momentum influencing the flow in the finned region is also considered a secondary effect. The properties of the boundary layer on the fin are deemed tertiary. Only primary and secondary traits are modeled or simulated in this research.

Previous computational efforts have been confined to the primary category described above. These methods have used Euler equations, with an infinitely thin-fin assumption, and without a base-flow region. Using the Navier-Stokes equations (Reynolds-averaged for turbulent flow), (11)-(14), makes it possible in the present research to study the influence of many secondary fin traits and phenomenon.

3.2 Description of the Thin-fin Approximation

The main reason for imposing an assumption about fin thickness is computational efficiency when studying complex flow structures. High-speed-missile research requires the accurate simulation of shocks, turbulent boundary layers and wakes, and shock/boundary-layer interactions. It typically takes many grid points to computationally analyze full configurations experiencing these phenomena. The HART missile length makes it even more demanding to predict these structures accurately

due to the disparity between length scales for a turbulent boundary layer and the length scale associated with the complete configuration. In general, the problem of extreme scale variation is encountered in all three dimensions. By assuming the fins to be infinitely thin, the azimuthal grid requirements are dramatically reduced. This is because the radius of curvature associated with the fin leading-edge is removed. The supposition is that dominant interactions in those directions can be calculated accurately without modeling the exact fin cross section, and without extensive grid refinement. This is the subject of Part II where no approximation is made, and a limited number of calculations are done over a subdomain around the fin group.

A fin without thickness is quite straightforward to model. It simply is represented by a discrete set of grid points that are coplanar. Since each point must represent at least two surfaces, some special care must be taken when using them in the numerical algorithm. Spatially coincident but distinct data are calculated on each fin surface. Additionally, the flow solver is restrained from obtaining information through any fin. In essence, each fin surface is a boundary embedded in the interior of the computational domain.

This technique neglects effects due to the radius of curvature associated with the fin leading edge. Nonetheless, the leading edge does exist, albeit without cross-sectional thickness or curvature. Therefore, any point coincident with the leading edge was handled differently than other points on the fin. Information at these points was extracted only from upstream coplanar data. The numerical implementation is discussed in Section 3.3. For fins which are very thin and highly swept, this is expected to be a reasonable approximation [80].

3.3 Computational Approach

3.3.1 Overview of the Development of the Flowfield Solver. There are several solvers that were developed by other researchers to study full configurations in supersonic flow. One example is the Langley Aerothermodynamic Upwind Relaxation Algorithm (LAURA). This is a point implicit shock-capturing code constructed by Gnoffo, et al. at NASA Langley [25]. It has been used extensively on reentry problems, including the Space Shuttle and the Aeroassisted Orbital Transfer Vehicle (AOTV) [23, 24].

These other techniques could have been modified for this work, but this was not the approach taken, for three reasons. The first relates to the anticipated grid

27

requirements. The finest grids required over 1 million points. There is a very limited availability of resources capable of handling the memory requirements implicit solvers demand for this number of points. Therefore, an explicit solver was sought. Second, the validation computing requirement would have been much higher. As will be explained later, the tact taken was to develop an axisymmetric geometry solver first, then expand this solver for full three-dimensional configurations. In this way, many numerical and grid related issues were settled at a reduced computational cost. Third, modification of an unfamiliar computer code without the benefit of *in-house* corporate knowledge may not proceed smoothly and efficiently. This is especially true for codes that are many tens of thousands of lines long. Additionally, unanticipated anomalies would prove harder to diagnose and correct.

Like other supersonic flowfield solvers for full configurations, the current technique had to be applied to a high Mach number and high Reynolds number combination, which is physically complicated and computationally demanding. The complexity arises from the development of strong curved shock waves, the associated vorticity which is generated, and interaction of this vorticity with the boundary layer. Turbulent transition and fin structures further complicate the interaction. Additional complexity is added by embedded subsonic flow that quickly expands to supersonic flow. Finally, the missile's flat base (see Figure 1) results in sudden flow separation, as well as a large mixing layer and recompression shock in the wake. Each of these phenomenon adds to the computational demands. Strong shocks and boundary-layer interactions make the correct amount of numerical dissipation uncertain. The subsonic flow involves a type change in the governing equations (from hyperbolic to elliptic), and turbulent boundary layers and mixing layers require very fine grid spacing to resolve steep gradients. Given this overall complexity, a computational methodology was developed that is sufficiently general to compute accurately a wide variety of flow structures.

This methodology or procedure by which the governing equations, (11)–(14), are solved is described in the following sections. The main aspects include three-dimensional or axisymmetric equations, explicit time integration, time-accurate calculations or steady-state calculations using local time stepping, and high-accuracy through the use of flux-difference splitting and limiters. In addition, the algorithm chosen to meet the objective achieves second-order spatial accuracy away from points of extrema (e.g., shocks). A practical *bent* was taken throughout the study; optimiz-

28

ing the computational speed was given a priority, and the memory requirement was reduced whenever possible.

Some details are omitted here, and included in Appendix B. In particular, the eigenvectors obtained from a diagonalization of inviscid flux Jacobians are not included in this chapter, due to their length and complexity. The flux Jacobians come from the linearization of the nonlinear terms in (11). The construction of the grid and application of the boundary conditions are discussed after the algorithm is described.

3.3.2 General Algorithm Description. The Navier-Stokes equations (Reynolds-averaged for turbulent flows) are solved with an explicit, time-integration technique, incorporating an upwind, Roe-type, flux-difference-splitting (FDS) formulation based on the work of Harten [33] and Yee [104]. Because a finite-volume methodology is adopted, the integral form of (11) need not be recast into differential form. Equation (11) is repeated here for convenience.

$$\frac{d}{dt} \int_V U \, dV + \oint_S \hat{n} \cdot \vec{F} \, dS = 0. \tag{25}$$

This equation is a statement of the conservation laws for mass, momentum, and energy. In fact, use of a conservative form is necessary for shocks to represent physical waves when shock-capturing schemes are applied [1].

The fluid surrounding the body is partitioned into a structured, interconnecting set of cells, and the equations are applied to individual cells, incorporating the average flux over each face. For a fluid cell composed of 6 flat surfaces (Figure 10), this would take the following form using explicit time integration:

$$
\begin{aligned}
U^{n+1} = U^n \quad - \quad \frac{\Delta t}{V} \Big[& \left(\vec{S}^\xi \cdot \vec{F}^n \right)_1 - \left(\vec{S}^\xi \cdot \vec{F}^n \right)_2 \\
& + \left(\vec{S}^\eta \cdot \vec{F}^n \right)_3 - \left(\vec{S}^\eta \cdot \vec{F}^n \right)_4 \\
& + \left(\vec{S}^\zeta \cdot \vec{F}^n \right)_5 - \left(\vec{S}^\zeta \cdot \vec{F}^n \right)_6 \Big].
\end{aligned}
\tag{26}
$$

The superscript n represents an arbitrary time level, and Δt is the time step from n to $n + 1$. The geometric terms $\vec{S}^\xi_1$, $\vec{S}^\xi_2$, $\vec{S}^\eta_3$, $\vec{S}^\eta_4$, $\vec{S}^\zeta_5$, and $\vec{S}^\zeta_6$ represent the projections of the six faces of the cell into the three Cartesian directions. The volume of the cell is V. The method used to calculate the geometric quantities from the grid points is

29
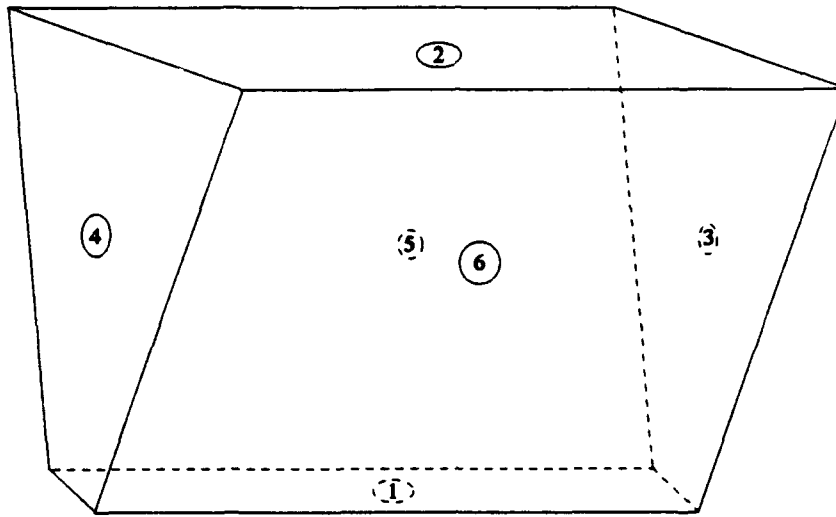
Figure 10. Typical fluid cell to which conservation laws are applied

adopted from Vinokur [91], and is outlined in Appendix B. For greater detail, the reader is referred to Vinokur's excellent treatment of the subject. Equation (26) yields information at the *center* of the cell, and the grid points are the vertices of the cell in Figure 10. The interconnecting cells are well ordered rather than random; this is usually referred to as a *structured grid*.

The orderliness of the cell arrangement allows a mathematical transformation from the physical (x, y, z) to a generalized (ξ, η, ζ) coordinate system. Although a finite-volume method makes the mathematical manipulations unnecessary, the concept is important for the implementation of the FDS scheme. We can visualize this transformation with a box in computational space. In this box, the grid spacing is denoted by $\Delta\xi$, $\Delta\eta$, and $\Delta\zeta$, such that $\xi = i\Delta\xi$, $\eta = j\Delta\eta$, and $\zeta = k\Delta\zeta$. The *node indices* i, j, and k identify the cell center of interest. Equation (26) can be rewritten using these node indices as

30

$$U_{ijk}^{n+1} = U_{ijk}^{n} - \frac{\Delta t}{V_{ijk}} \Big[\left(S_x^\xi E^n\right)_{i+\frac{1}{2}jk} - \left(S_x^\xi E^n\right)_{i-\frac{1}{2}jk}$$

$$+ \left(S_y^\xi F^n\right)_{i+\frac{1}{2}jk} - \left(S_y^\xi F^n\right)_{i-\frac{1}{2}jk} + \left(S_z^\xi G^n\right)_{i+\frac{1}{2}jk} - \left(S_z^\xi G^n\right)_{i-\frac{1}{2}jk}$$

$$+ (S_x^\eta E^n)_{ij+\frac{1}{2}k} - (S_x^\eta E^n)_{ij-\frac{1}{2}k} + \left(S_y^\eta F^n\right)_{ij+\frac{1}{2}k} - \left(S_y^\eta F^n\right)_{ij-\frac{1}{2}k} \qquad (27)$$

$$+ (S_z^\eta G^n)_{ij+\frac{1}{2}k} - (S_z^\eta G^n)_{ij-\frac{1}{2}k} + \left(S_x^\varsigma E^n\right)_{ijk+\frac{1}{2}} - \left(S_x^\varsigma E^n\right)_{ijk-\frac{1}{2}}$$

$$+ \left(S_y^\varsigma F^n\right)_{ijk+\frac{1}{2}} - \left(S_y^\varsigma F^n\right)_{ijk-\frac{1}{2}} + \left(S_z^\varsigma G^n\right)_{ijk+\frac{1}{2}} - \left(S_z^\varsigma G^n\right)_{ijk-\frac{1}{2}} \Big].$$

More importantly, a scheme is established which can easily be split into three one-dimensional operators. This will be discussed shortly.

First, consider the fluxes, E, F, and G, in (27). The explicit forms were given by (12)–(14). The convective terms are modified in an upwind manner, while the viscous terms remain unmodified. The modified fluxes are approximations to the average fluxes at each cell interface and, as such, are often called *numerical fluxes*. In addition, the modification is second-order preserving for those interfaces located away from extrema, like shocks. These numerical fluxes can be determined at cell interfaces in two ways, using either Monotonic-Upwind-Scalar-Conservation-Law (MUSCL) extrapolation or non-MUSCL extrapolation [104]. In the MUSCL approach, cell-centered values of primitive, conserved, or characteristic variables are extrapolated to the interfaces; numerical fluxes are then obtained from these quantities. The non-MUSCL approach, on the other hand, calculates the numerical fluxes at cell interfaces directly from cell-centered information. The current scheme uses the non-MUSCL technique. Non-MUSCL was chosen over MUSCL because it is more efficient and more straightforward. The flux in the ξ-coordinate direction at the $(i + \frac{1}{2}, j, k)$ interface, $\left(\vec{S}^\xi \cdot \vec{F}^n\right)_1$, is therefore approximated by

$$\hat{E}_{i+\frac{1}{2}jk} \equiv \frac{1}{2} \Big[\left(S_x^\xi\right)_{i+\frac{1}{2}jk}(E_{i+1jk} + E_{ijk}) + \left(S_y^\xi\right)_{i+\frac{1}{2}jk}(F_{i+1jk} + F_{ijk}) \qquad (28)$$

$$+ \left(S_z^\xi\right)_{i+\frac{1}{2}jk}(G_{i+1jk} + G_{ijk}) + \frac{1}{2}(V_{i+1jk} + V_{ijk})\hat{R}_{i+\frac{1}{2}jk}\hat{\Phi}_{i+\frac{1}{2}jk} \Big].$$

The other interfaces have numerical fluxes with similar construction. Equation (27) is then written as

$$U_{ijk}^{n+1} = U_{ijk}^{n} - \frac{\Delta t}{V_{ijk}} \Big[\hat{E}_{i+\frac{1}{2}jk}^n - \hat{E}_{i-\frac{1}{2}jk}^n + \hat{F}_{ij+\frac{1}{2}k}^n - \hat{F}_{ij-\frac{1}{2}k}^n + \hat{G}_{ijk+\frac{1}{2}}^n - \hat{G}_{ijk-\frac{1}{2}}^n \Big]. \quad (29)$$

31

The addition of the last term in (28) is a modification to Roe's first-order, FDS algorithm [71]. Roe's method was to approximate the nonlinear Riemann problem, and solve the approximate problem exactly. This is a simpler approach than Godunov's method [26], which advances the solution of a nonlinear system of conservation laws to the next time level by solving a set of Riemann problems. To approximate the Riemann problem, Roe's idea is to perform a local decoupling of the nonlinear system with a linear wave decomposition. He also requires that there exist an average state that is a nonlinear function of the states to the right and left [71]. More detail can be found in [71] or [104]. The main feature of the method that makes it valuable for nonlinear systems is that it returns the exact solution whenever the left and right states lie on opposite sides of a shock wave or contact discontinuity [104].

Second-order spatial accuracy is achieved by applying Roe's first-order algorithm to a modified inviscid flux [33]. The modified flux is cleverly chosen so that the scheme is second-order accurate in regions of smoothness and first-order at points of extrema (e.g., shocks). The modification of the flux is responsible for the appearance of the final term in (28), which will be left unspecified momentarily.

As stated above, the current scheme reduces to first-order at points of extrema. This behavior is common to all higher-order total-variation-diminishing (TVD) schemes, and is the main mechanism used to prevent spurious oscillations near a shock. Although the scheme *switches* to first-order in regions of rapid change, the global order of accuracy is not drastically degraded [104]. Thus, global accuracy is increased from that for a first-order upwind scheme, and the robust shock-capturing quality is preserved.

It is intended to characterize the scheme as a set of one-dimensional operators, and avoid the complexity of a truly multidimensional Riemann solver. The directions over which the operators act are the generalized coordinate directions. This implies a local-characteristic approach or generalization of Roe's approximate Riemann solver [104]. Since Roe requires the diagonalization of the inviscid flux Jacobians, this non-Cartesian method needs generalized inviscid flux Jacobians [104]. These are calculated as follows:

$$\hat{A} = \frac{\partial \hat{E}}{\partial \hat{U}} = \frac{S_x^\xi}{V}A + \frac{S_y^\xi}{V}B + \frac{S_z^\xi}{V}C, \qquad (30)$$

where

$$\hat{E} = S_x^\xi E + S_y^\xi F + S_z^\xi G,$$

$$\hat{U} = UV,$$

$$A = \frac{\partial E}{\partial u}, \qquad B = \frac{\partial F}{\partial u}, \quad \text{and} \; C = \frac{\partial G}{\partial u}.$$

Returning to the final term in (28), the matrix of right eigenvectors of $\hat{A}$, evaluated at the $(i + \frac{1}{2}, j, k)$ interface, is denoted by $\hat{R}_{i+\frac{1}{2}jk}$. The right and left eigenvectors appear through the diagonalization of $\hat{A}$. For Roe's scheme, $\hat{\Phi}$ is comprised of eigenvalues and characteristic variables, and simply acts as an upwinding term. Due to the work of Harten and Yee, $\hat{\Phi}$ also acts to limit the characteristic variables, thereby providing higher accuracy. This is done in the current study with the *minmod limiter*; details regarding the development and implementation of the limiter are contained in Appendix B. Explicit forms for $\hat{R}$ and $\hat{\Phi}$ are also set forth in Appendix B.

In this study, $\hat{\Phi}$ also provides an *entropy correction* when the magnitudes of the eigenvalues become small. The entropy correction prevents non-physical solutions from developing, as is well documented in the literature [32, 51, 96]. The form of the entropy-corrected eigenvalues, $\hat{\lambda}$, put forth by Harten [34] is

$$\hat{\lambda} = \begin{cases} \frac{\lambda^2 + \epsilon^2}{2\epsilon}, & \text{if } |\lambda| < \epsilon; \\ |\lambda|, & \text{if } |\lambda| \geq \epsilon. \end{cases} \tag{31}$$

where the proper value of ϵ can be very sensitive to the geometry and the flowfield structure. Three relations are tested in this study: a constant value, proposed by Harten [34]; a value proportional to the contravariant velocities, proposed by Yee [104], and a value proportional to the second derivative of the pressure, suggested by Palmer and Ventkatapathy [63]. Since the purpose for this correction is to avoid the computation of non-physical solutions, the functions are evaluated on this basis. In particular, for the current class of flows (external, supersonic, axisymmetric nose) avoiding aberrations near the singular line is the primary concern. Other factors considered are impact on convergence to steady-state and the side-effects of numerical dissipation. Entropy correction is not applied near the body surface to avoid adverse effects on the boundary layer. Lin [51] showed undesirable results when the function proposed by Yee was used in the boundary layer. Lin put forth a modification to

33

allow the function to be used globally. However, the author feels that the natural viscosity of the fluid prevents non-physical solutions near the body, without the addition of an entropy function.

By far, the most accurate and robust function, for the flows explored herein, is obtained when ϵ is proportional to the contravariant velocities:

$$\epsilon = c_1 \left(|U_c| + |V_c| + |W_c| + |C_c| \right), \tag{32}$$

where c_1 is varied from 0.2 to 1.0. The best results are calculated with $c_1 = 0.45$; results are judged best because non-physical solutions were avoided, convergence is not impeded, and shock smearing due to the added dissipation is minimized. A value of 0.45 is used for all three-dimensional calculations reported in this study. This differs from the value used for axisymmetric calculations (Appendix A).

Utilizing the Strang-type fractional-step [104] method ensures second-order accuracy (spatial for Navier-Stokes equations, spatial and temporal for the Euler equations):

$$\hat{U}_{ijk}^{n+2} = L_\eta^{h/2} L_\xi^h L_\zeta^h L_\eta^h L_\zeta^h L_\xi^h L_\eta^{h/2} \hat{U}_{ijk}^n, \tag{33}$$

where

$$\begin{aligned}
L_\eta^{h/2} \hat{U}_{ijk}^n &= \hat{U}_{ijk}^* = \hat{U}_{ijk}^n - \frac{\Delta t}{2} \left(\hat{F}_{ij+\frac{1}{2}k}^n - \hat{F}_{ij-\frac{1}{2}k}^n \right), \\
L_\xi^h \hat{U}_{ijk}^* &= \hat{U}_{ijk}^{**} = \hat{U}_{ijk}^* - \Delta t \left(\hat{E}_{i+\frac{1}{2}jk}^* - \hat{E}_{i-\frac{1}{2}jk}^* \right), \\
L_\zeta^h \hat{U}_{ijk}^{**} &= \hat{U}_{ijk}^{***} = \hat{U}_{ijk}^{**} - \Delta t \left(\hat{G}_{ijk+\frac{1}{2}}^{**} - \hat{G}_{ijk-\frac{1}{2}}^{**} \right).
\end{aligned} \tag{34}$$

Application of the entire sequence of operators advances the solution two time levels.

Driver [16] noted that second-order temporal accuracy is not preserved for the Navier-Stokes equations with Strang time splitting. Driver highlighted this fact for low Reynolds number, unsteady flows. For high Reynolds numbers, the actual accuracy achieved is much closer to second order. Figures 11a and 11b show the L_1-norm and L_∞-norm of computed errors for the current scheme and the second-order scheme of Driver (ATNSC2) applied to the linear, viscous, Burger's equation. The calculations are performed at a Courant number of 0.9 and $Re = 100,000$. For comparison, the second-order accurate line is plotted as the solid line and the first-order accurate line is plotted as the dashed line. Note that for both schemes the L_1-norm matches

34

the second-order curve extremely well, indicating that the numerical solution is indeed globally second-order accurate. Also, note the first-order (actually 1.5) behavior in the L_∞-norm due to the TVD property. This is indicated by the L_∞-norm falling between the first-order accurate line and second-order accurate line in Figures 11a and 11b. These same calculations, made for Courant number equal to 1.0, (Figures 12a and 12b) show that the stability behavior of the second-order scheme is superior. As the grid spacing is refined (Δx decreases), the current scheme shows larger errors in both norms. In contrast, the norms for ATNSC2 decrease. Since the explicit, second-order algorithm developed by Driver is very expensive computationally, the mild stability limitations of the current algorithm at high Reynolds numbers, and Courant numbers close to 1.0, is an acceptable tradeoff. The model problem does not have a region where viscous terms co-dominate, therefore stability limitations of the current algorithm, when applied to separated flows, remain an open question.

For steady-state calculations a much simpler approach is used. This fractional-step method is

$$\hat{U}_{ijk}^{n+1} = L_\eta^h L_\xi^h L_\zeta^h \hat{U}_{ijk}^n, \tag{35}$$

where again

$$L_\eta^h \hat{U}_{ijk}^n = \hat{U}_{ijk}^* = \hat{U}_{ijk}^n - \Delta t \left(\hat{F}_{ij+\frac{1}{2}k}^n - \hat{F}_{ij-\frac{1}{2}k}^n \right), \tag{36}$$

but now

$$L_\xi^h \hat{U}_{ijk}^* = \hat{U}_{ijk}^{**} = \hat{U}_{ijk}^* - \Delta t \left(\hat{E}_{i+\frac{1}{2}jk}^n - \hat{E}_{i-\frac{1}{2}jk}^n \right), \tag{37}$$

$$L_\zeta^h \hat{U}_{ijk}^{**} = \hat{U}_{ijk}^{***} = \hat{U}_{ijk}^{**} - \Delta t \left(\hat{G}_{ijk+\frac{1}{2}}^n - \hat{G}_{ijk-\frac{1}{2}}^n \right).$$

With non-MUSCL extrapolation, this is much more efficient, because the inviscid and viscous fluxes within the numerical flux need not be recalculated for each operator. Additionally there are only three operators per iteration, versus three and a half, as required by (33) before. A stability limitation is encountered when using local-time stepping with this technique. This limitation is overcome by evaluating the upwind terms for each operator with current information rather than time-level n information. More details are included in Appendix A.
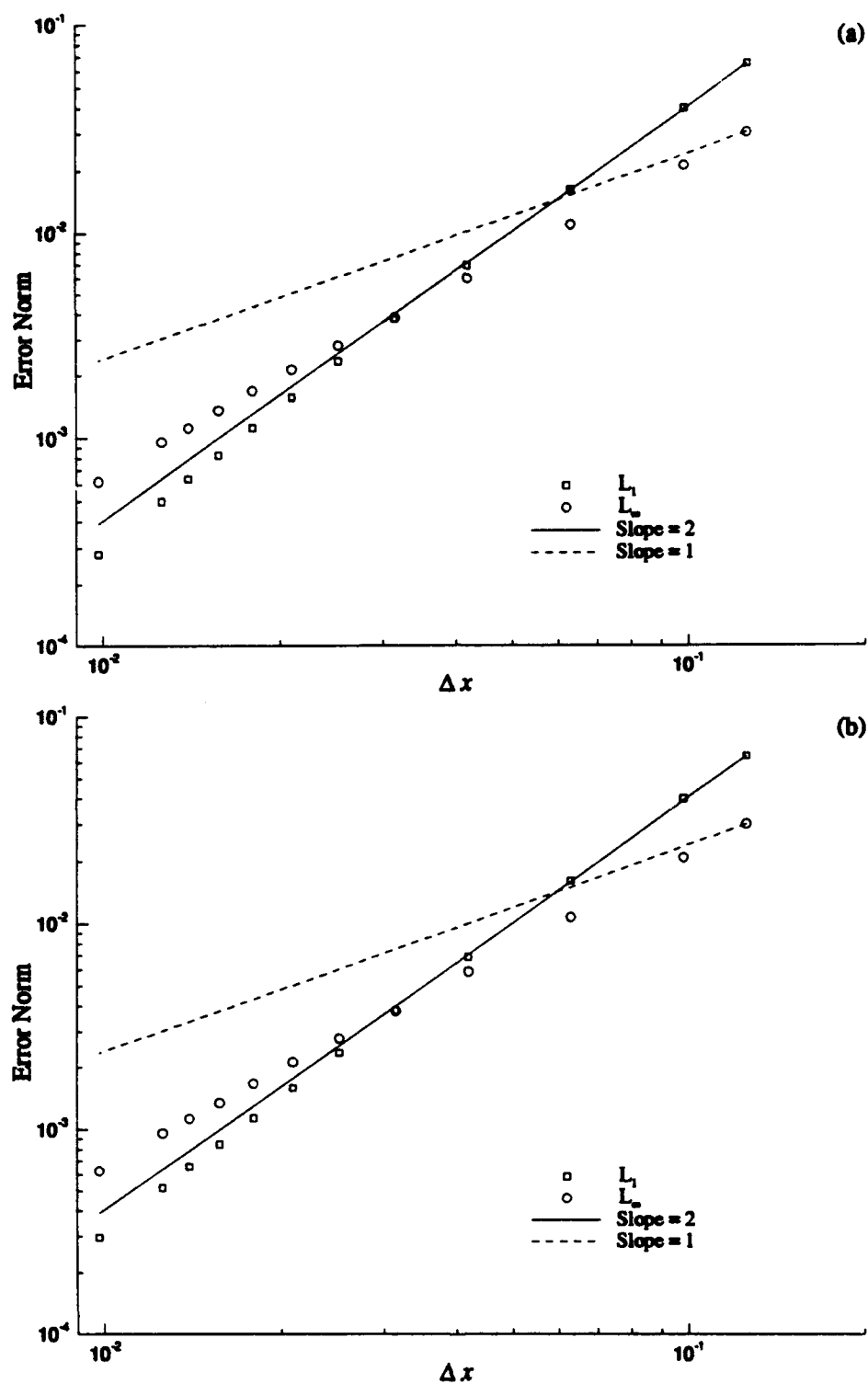
Figure 11.   Accuracy of scheme when applied to linear viscous Burgers equation
(Re=100,000; $CFL = 0.9$):   (a) current scheme, $O\left[\Delta t,\ \Delta x^2\right]$;   (b)
ATNSC2 scheme, $O\left[\Delta t^2,\ \Delta x^2\right]$

36
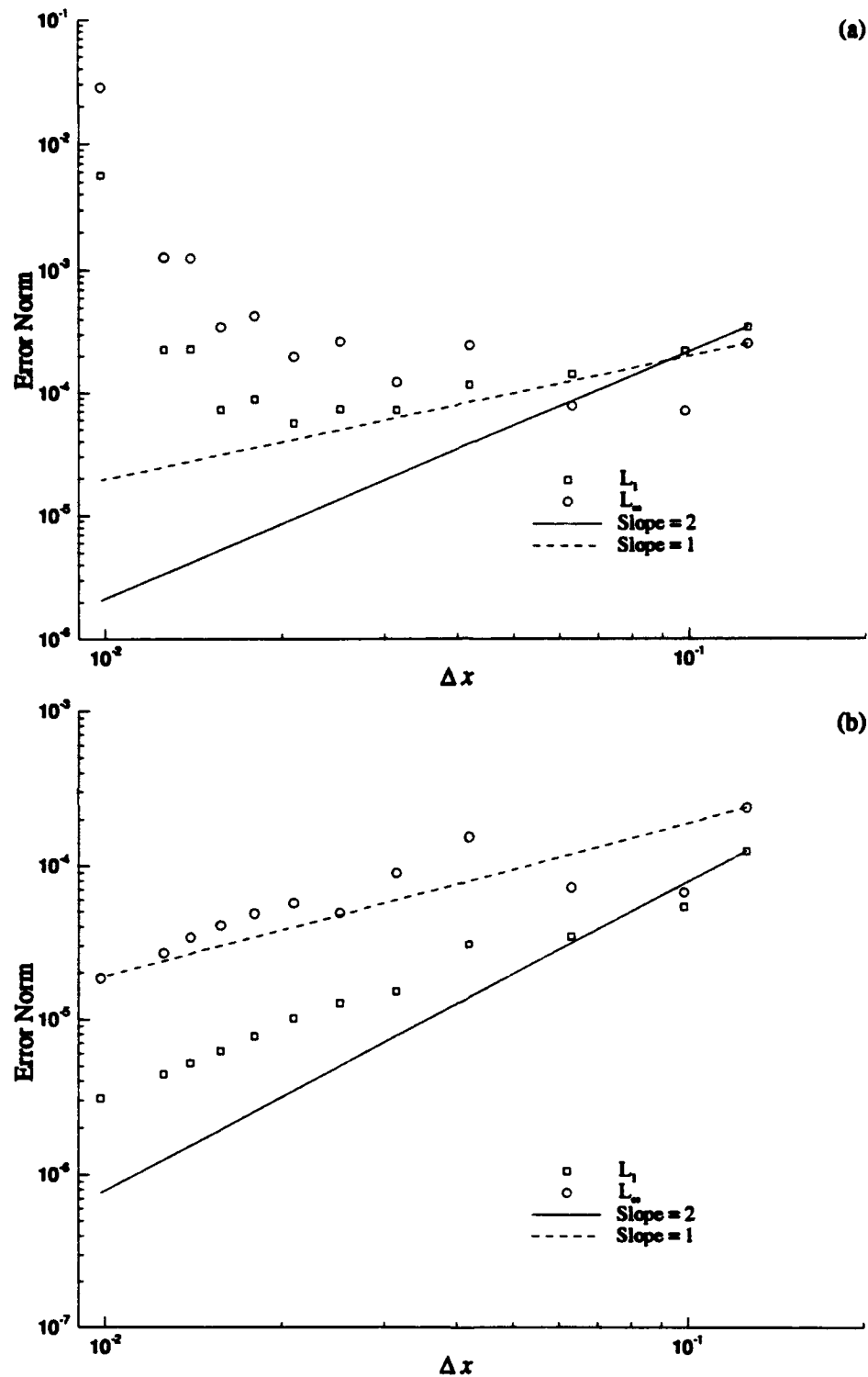
Figure 12. Accuracy of scheme when applied to linear viscous Burgers equation (Re=100,000; $CFL = 1.0$): (a) current scheme, $O[\Delta t,\ \Delta x^2]$; (b) ATNSC2 scheme, $O[\Delta t^2,\ \Delta x^2]$

3.4 Turbulence Modeling

The well known, and widely used, *zero-equation* Baldwin-Lomax turbulence model [5] is incorporated for the forebody boundary-layer simulations. The original model is described in Appendix A. Only important modifications are detailed in this section, specifically those for compressibility, pressure gradients, a two-wall domain, and the wake. No modifications are made to account for hypersonic flow, save those for compressibility. The limitations of this approach are not addressed as part of this research, and therefore remain unresolved.

Turbulence modeling is evaluated within the context of the assumptions made regarding secondary and tertiary effects (i.e., the boundary layer on the fin need not be accurately simulated). In addition, for the thin-fin investigation (Part I), fin cross-sectional shape is degenerate and boundary-layer separation is not anticipated.

All turbulent calculations have a point designated on the missile body to delineate the laminar and turbulent regions. For the sharp-nosetip model, this point is selected on the ogive nose at $\left(\frac{x}{D} = 1.25\right)$; for the blunt-nosetip model, this point is specified on the cylinder body at $\left(\frac{x}{D} = 6.75\right)$. A point closer to the tip is selected for the sharp nosetip because early boundary-layer transition was seen in experimental shadowgraphs of the HART missile. This is also consistent with turbulent calculations made on other pointed-ogive noses in this study (Appendix A). The effect of nosetip blunting to delay boundary-layer transition is documented in the literature, ([13], for example) and agrees with the computations performed in Appendix A on a blunted ogive nose.

3.4.1 Compressibility and Pressure-gradient Modifications. Two modifications to the original Baldwin-Lomax model proved important. The first changes the Van Driest damping factor to account for compressibility and pressure gradients [49, 28, 101]. The near wall region, denoted by A^+, is redefined as

$$A^+ = 26 \cdot N \cdot Z. \tag{38}$$

The nondimensional distance 26 is the incompressible value for a smooth, non-porous, flat plate [101], N is the pressure-gradient contribution, and Z is the compressibility

38

contribution:

$$N = \left[11.8\left(\frac{\rho_e}{\rho_w}\right)P^+ - 1\right]^{-\frac{1}{2}}; \quad Z = \left(\frac{\rho_w}{\rho}\right)^{\frac{1}{2}}\left(\frac{\mu}{\mu_w}\right); \quad P^+ = \left(\frac{\mu_e}{\rho_e^2}\right)\frac{(dp_e/dx)}{(\tau_w/\rho_w)^{\frac{3}{2}}}. \quad (39)$$

In (39), e refers to the value of a variable at the edge of the boundary layer, and w refers to the value of a variable at the wall. The second alteration improves the two coefficients in the outer region, C_{cp} and C_{kleb}. According to Granville, the following functional forms better match the law of the wake [27]:

$$C_{kleb} = \frac{2}{3} - \frac{0.01312}{0.1724 + \beta^*}, \quad C_{cp} = \frac{3 - 4C_{kleb}}{2C_{kleb}(2 - 3C_{kleb} + C_{kleb}^3)}, \quad \beta^* = \frac{y_{max}}{(\tau_w/\rho)^{\frac{1}{2}}}\frac{dU_e}{dx}. \quad (40)$$

3.4.2 Modification to the Length Scale in the Turbulence Model. The length scale for the turbulence model is locally modified to account for a two-wall domain near the fins. This modification has been implemented by other researchers [39, 73, 40] for wing/body junctions, and by McMaster and Shang [55] on a sweptback fin. The methodology of [55] is adopted without modification for this study. Since the grid is relatively coarse in the azimuthal direction (see Section 3.5), the boundary layers on the fins are not accurately simulated. The impact of this inadequacy is not clear. The grid limitations are discussed further in Section 3.5.1. The length scale, l, as reported by [55] for a dual-wall region is

$$l = \frac{2d_1 d_2}{d_1 + d_2 + \sqrt{d_1^2 + d_2^2}}, \quad (41)$$

where d_1 and d_2 are the normal distances from the two walls.

3.4.3 Empirical Model in Wake. A strictly empirical relation is used to compute turbulent viscosity in the wake because it is difficult to apply a conventional zero-equation turbulence model to a flat base with a large, nearly stagnant region. The difficulty is that the appropriate length scale is hard to define and not readily computable. The empirical technique was originally applied to subsonic flow by Magagnato [54]. The method is adapted and its validity tested for supersonic flow in

this investigation. Turbulent viscosity is determined from the local vorticity, ω, by

$$\mu_t = \hat{\mu}_t \left(\frac{|\omega|}{|\hat{\omega}|} \right)^{0.2}, \tag{42}$$

where $\hat{\mu}_t$ is the maximum viscosity in the boundary layer at the forebody/base junction computed from the Baldwin-Lomax model, and $\hat{\omega}$ is the vorticity at the same point. Magagnato smoothed the eddy-viscosity with an exponential damping factor. Smoothing is not believed desirable nor physical by the author, and thus, is not pursued in this study. The method has the advantage of speed and low memory requirement. Although highly empirical, the validity of this approach is shown through numerical examples in Appendix A.

3.5 Grid Structure

All grids are obtained using GRIDGEN [79], an elliptical grid generator developed for Wright Laboratory, Wright-Patterson AFB, Ohio. GRIDGEN has both two-dimensional and three-dimensional grid generating software. For this study, a single two-dimensional grid is constructed using GRIDGEN, and then rotated about the body centerline to produce a three-dimensional grid. In this way, each plane is normal to the missile body, and the fins coincide with distinct grid planes. This facilitates boundary-condition application because the body and fin boundary conditions are most easily enforced for a grid constructed with gridlines normal to surfaces. The domain size (outer boundary) is chosen to allow a bow shock wave at $M_\infty = 2$ to fit within the domain at the exit plane. The body shape (inner boundary) is generated analytically and input into GRIDGEN as a data file. The final two boundaries, singular line and outflow, are simple straight lines created within GRIDGEN.

The number of grid cells and the appropriate axial and radial spacing were determined from the validation experiments (see Appendices A and B). As a result of these tests, the grids for investigating the HART missile are constructed with grid cells clustered near the body and with a fixed minimum cell height. For the baseline grid, this spacing is $0.001D$. For refined turbulent calculations it is reduced to $0.000025D$ ($y^+ \approx 1$). The number of cells from the body to the outer domain varies from 81 for the baseline grid to 101 for refined calculations. Along the body, cells are clustered near the nosetip and fin/body junction. A total of 91 cells are

used in this direction, 61 from the nosetip to the base, and 31 in the wake. A non-rectangular domain composed of two regions results; one grid with 91 × 81 nodes and the other with 31 × 30 nodes.

The minimum spacing near the missile body can be relaxed for the turbulent calculations with some accuracy degradation. The value chosen above, $0.000025D$, is required to obtain grid independence. Larger spacing primarily affects only the velocity gradient very near the wall, and as such the prediction of skin friction. Because the present research is concerned with corroborating the experimentally determined drag, the small spacing is selected.

The baseline grid has cells clustered near fin surfaces with the angle between the fin and next plane of nodes, $\Delta\phi_{min}$, equal to $0.5°$ and 33 cells in the bisymmetric half-plane. The number of cells in the azimuthal direction and the angular spacing of these cells was determined from a refinement study discussed in Section 4.2. A total of 273,933 cells are used in the baseline grid (Figures 13 and 14).

In addition to the baseline grid, several other grids are used. A refined spacing for turbulent calculations is already mentioned. In addition, some grids are constructed to end at the missile body/base junction. These are used to assess baseflow effects. Finally, a refinement study for the azimuthal direction is made using equal angular spacing. The number of azimuthal cells is varied from 33 to 105. Without the base region, these extremes represent 163,053 and 518,805 cells, respectively.

Two issues are important regarding the grid near the nosetip: tip geometry and singular-line discretization. For the sharp-nosetip missile, the nose is very slightly rounded. This is more physical than an ideally sharp tip and enables the bow shock to be captured a small distance away from the surface. The modified nose is spherically rounded with $R_n/R_b = 0.05$ (Figure 15). Dolling and Gray [13] found that surface pressure (away from the tip) and boundary-layer development are virtually unaffected by this level of blunting. The second aspect of the grid near the nosetip deals with the cell structure closest to the singular line. Cells can be constructed such that their centers fall on the singular line, or such that the interfaces between cells lie on the singular line. The former is called a finite-difference (FD) grid, and the latter a finite-volume (FV) grid. Both grid structures are shown in Figure 16. Calculations with each grid type are made for several axisymmetric flows, and for an axisymmetric body at angle of attack. These are summarized in Appendix A and
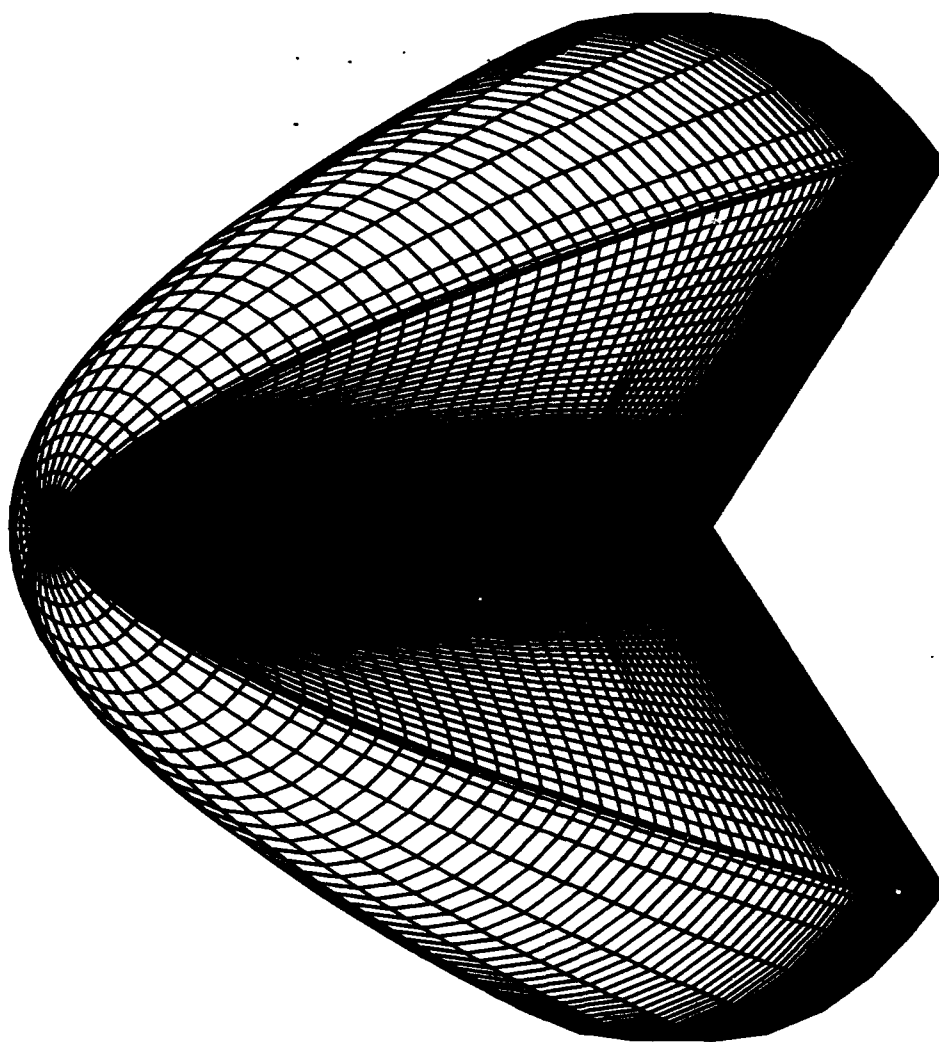
Figure 13.   Baseline grid cutaway view : $60 \times 81 \times 33$ around   forebody   and $31 \times 111 \times 33$ in the wake
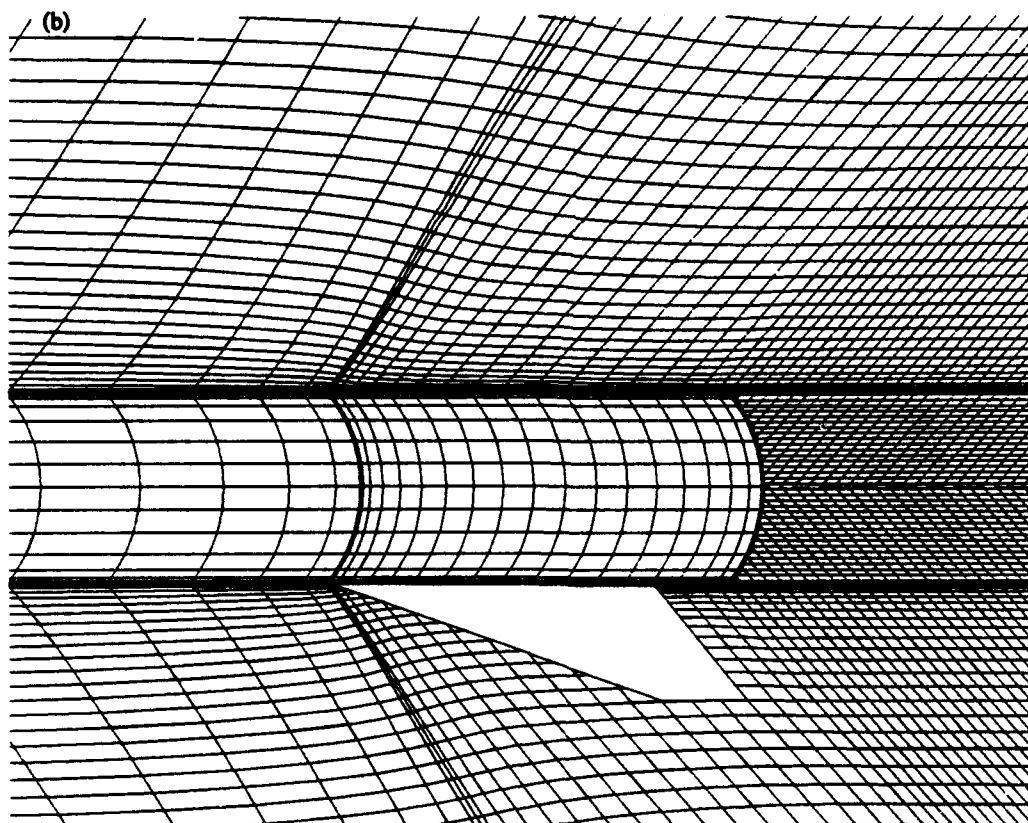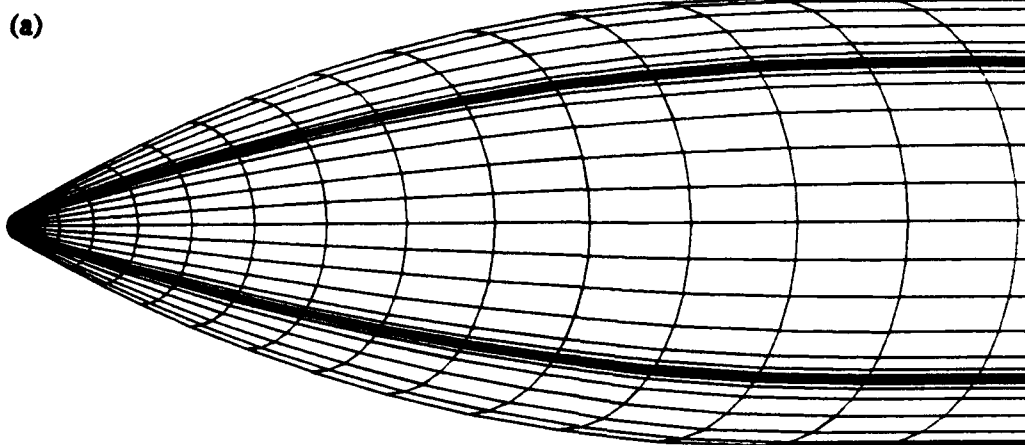
Figure 14. Baseline grid: (a) surface grid near nosetip, (c) aft-end view
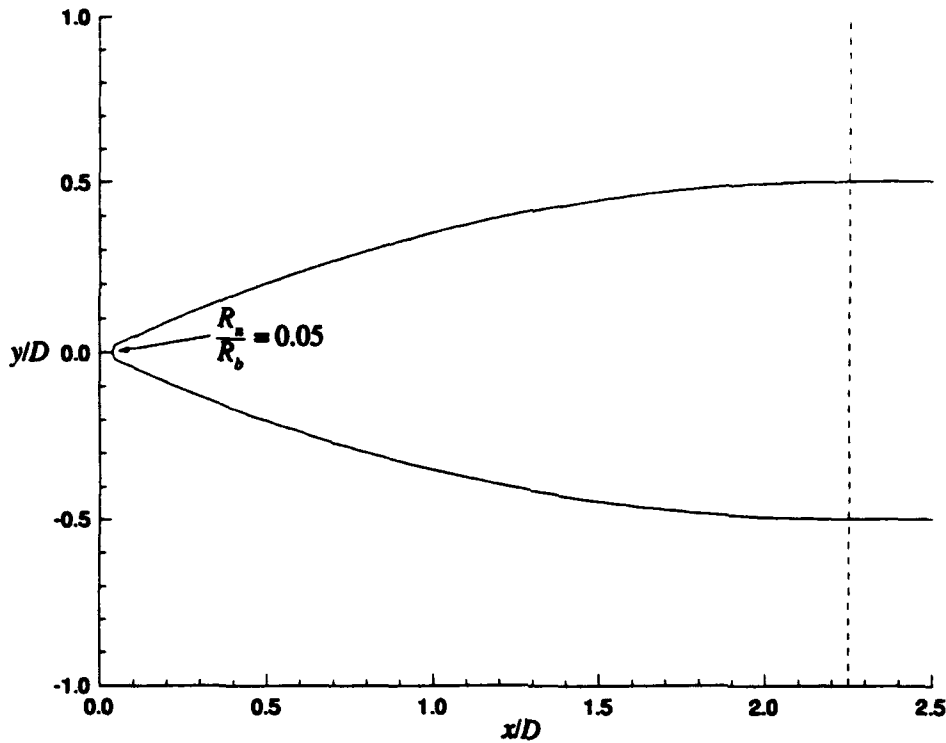
Figure 15. Modified nosetip showing very slight rounding of sharp nosetip

Appendix B. To maximize the accuracy near boundaries, a FV grid is used for all calculations in Part I.

With a FV grid, the cells adjacent to the singular line degenerate into wedge-like shapes, and prevent conserved quantities from fluxing into or out of portions of those cells. Although a FV method usually handle this without special treatment, the current method requires some changes because the terms which are added to the physical fluxes to produce the numerical fluxes (Section 3.3.2) do not go to zero at the singular line. This is overcome by setting the entire numerical flux to zero.

Although grid cells are clustered at the fin/body junction, grid lines do not conform to the fin leading-edge shape. For an infinitely thin fin, the junction is a singularity that is not easily resolved with a single block as a structured grid. The non-conformal nature of the grid represents an area of potential accuracy reduction because fluxes cannot be constructed such that they enforce the boundary conditions *exactly*. However, the fluxes are handled in a special manner near these points. For any interface that separates a cell upstream of a leading edge from one downstream

44

(a)

Singular Line
(Axisymmetry Line for $\alpha = 0^0$)

(b)

Singular Line
(Axisymmetry Line for $\alpha = 0^0$)
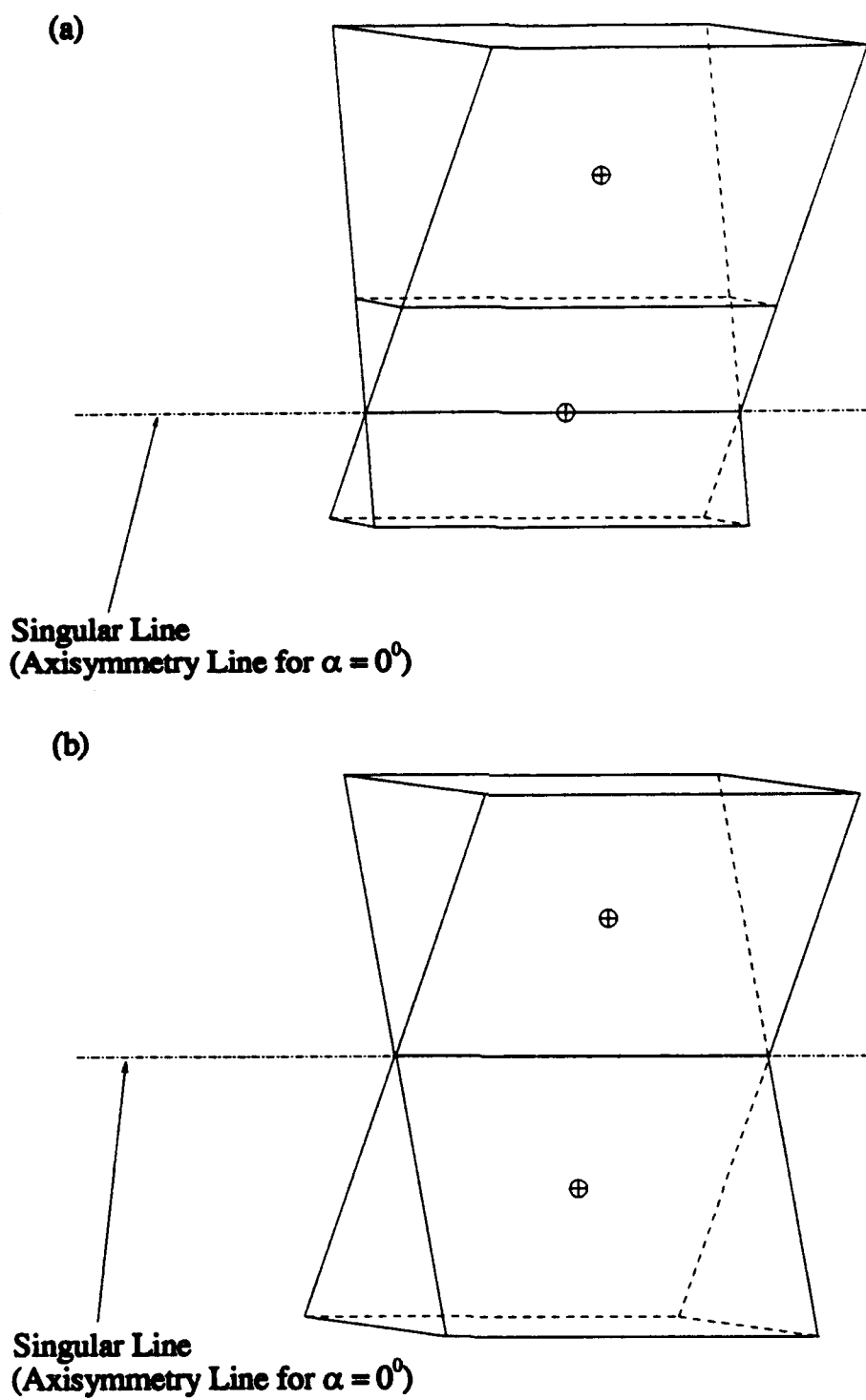
Figure 16. Grid structure near singular line: (a) finite-difference, (b) finite-volume

of a leading edge, the numerical flux is calculated from

$$
\hat{E}_{i+\frac{1}{2}jk} = \frac{1}{2} \left[\left(S_x^\xi \right)_{i+\frac{1}{2}jk} \left(\frac{1}{2} \left(E^l_{i+1jk} + E^u_{i+1jk} \right) + E_{ijk} \right) \right.
$$
$$
+ \left(S_y^\xi \right)_{i+\frac{1}{2}jk} \left(\frac{1}{2} \left(F^l_{i+1jk} + F^u_{i+1jk} \right) + F_{ijk} \right) \tag{43}
$$
$$
+ \left(S_z^\xi \right)_{i+\frac{1}{2}jk} \left(\frac{1}{2} \left(G^l_{i+1jk} + G^u_{i+1jk} \right) + G_{ijk} \right)
$$
$$
\left. + \frac{1}{2} \left(V_{i+1jk} + V_{ijk} \right) \hat{R}_{i+\frac{1}{2}jk} \hat{\Phi}_{i+\frac{1}{2}jk} \right],
$$

where u and l represent fluxes calculated on the upper side and lower side of the fin respectively. Also, $\hat{R}_{i+\frac{1}{2}jk}$ and $\hat{\Phi}_{i+\frac{1}{2}jk}$ are now functions of U_{ijk}, $\frac{1}{2} \left(U^l_{i+1jk} + U^u_{i+1jk} \right)$, and $\frac{1}{2} \left(U^l_{i+2jk} + U^u_{i+2jk} \right)$ instead of U_{ijk}, U_{i+1jk}, and U_{i+2jk}. The author believes practical, albiet not formal, accuracy is preserved. This is demonstrated for an axisymmetric compression ramp in Appendix B.

3.5.1 Grid Limitations. Again, it is emphasized that the azimuthal refinement is insufficient to predict accurately the boundary-layer properties on the fin surface. The grid is refined only normal to the missile body. Since the pressure is dominated by the shock structure, and the boundary layer of interest is the one on the body, this limitation is not deemed overly constraining by the author. This will be addressed in detail in the thick-fin analysis (Part II).

3.6 Boundary Conditions

The boundary conditions which were discussed briefly in Section 2.3 are now described in detail. For the no-slip condition used with viscous calculations, the velocities are set to zero:

$$
u = 0, \quad v = 0, \quad \text{and} \quad w = 0.
$$

The pressure-gradient and adiabatic-wall conditions are satisfied with second-order discrete representations of:

$$
\frac{\partial p}{\partial n} = 0, \quad \text{and} \quad \frac{\partial \rho}{\partial n} = 0.
$$

Three of the boundary conditions require further explanation. First, the extrapolation at the singular line is described. Next, the impermeability condition for a three-dimensional surface is discussed. Finally, the fin-surface conditions are shown.

3.6.1 Singular-line Conditions. When a body is not pitched ($\alpha = 0°$), the condition at the singular line is a symmetry condition. For the current FV grid, a cell center slightly displaced from the symmetry line is mirrored by one displaced exactly the same amount, but azimuthally located 180° apart (Figure 16). It is a simple matter to reflect v and w to achieve axisymmetry.

When a body is pitched, the condition is not so simple. Therefore, the following extrapolation is used whenever $\alpha \neq 0°$:

$$q_1 = q_2 + \left.\frac{\partial q}{\partial r}\right|_2 (-\Delta r) + \left.\frac{\partial^2 q}{\partial r^2}\right|_2 \left(\frac{(\Delta r)^2}{2}\right) + O\left[(\Delta r)^3\right]. \tag{44}$$

The subscript 2 denotes the first cell on the domain interior. The subscript 1 denotes its mirror (i.e., the boundary cell). The variable q represents any primitive variable. Using finite-difference expressions for the derivative terms in (44) yields

$$q_1 = 3q_2 - 3q_3 + q_4 + O\left[(\Delta r)^3\right]. \tag{45}$$

It is important to check the consistency of this extrapolation as $\alpha \to 0$. For axisymmetric flow, all primitive variables, except v and w, behave like [75]

$$q \sim c_1 + c_2 r^2 \quad (r \to 0), \tag{46}$$

where c_1 and c_2 are constants that depend on the flowfield. The remaining velocity components, v and w, behave as the radial velocity (except for a sign change) [75]:

$$q \sim c_3 r \quad (r \to 0), \tag{47}$$

where c_3 is also a constant that depends on the flowfield. By using (46)–(47) to determine q_2, q_3, and q_4, the behavior of q_1 as $r \to 0$ can be determined. Assuming that the grid is constructed with a nearly constant node spacing normal to the

symmetry line, then for v and w, as $r \to 0$,

$$q_2 \approx c_3 \frac{\Delta r}{2}, \qquad q_3 \approx c_3 \frac{3\Delta r}{2}, \qquad q_4 \approx c_3 \frac{5\Delta r}{2}, \qquad (48)$$

and from (45)

$$q_1 = -c_3 \frac{\Delta r}{2} = -q_2. \qquad (49)$$

The distance between the cell center at 2 and the symmetry line is given by $\Delta r/2$. In a similar manner, for ρ, u, and p, as $r \to 0$,

$$q_2 \approx c_1 + c_2 \left(\frac{\Delta r}{2}\right)^2, \qquad q_3 \approx c_1 + c_2 \left(\frac{3\Delta r}{2}\right)^2, \qquad q_4 \approx c_1 + c_2 \left(\frac{5\Delta r}{2}\right)^2, \qquad (50)$$

and again from (45)

$$q_1 = c_1 + c_2 \left(\frac{\Delta r}{2}\right)^2 = q_2. \qquad (51)$$

For a grid with constant spacing normal to the singular line, the proposed extrapolation is consistent with axisymmetric flow.

3.6.2 Impermeability Condition for a Three-dimensional Surface.

For viscous calculations, no slip is enforced on the missile surface, but for inviscid calculations, an impermeability condition is required. The impermeability of a three-dimensional surface depends on two angles, the local body inclination, θ, and the azimuth, ϕ, (Figure 17). A simple coordinate transformation using these two angles produces a relation between the Cartesian velocities and the normal, tangential, and swirl velocities (u_n, u_t, and u_s, respectively):

$$\begin{bmatrix} u_n \\ u_t \\ u_s \end{bmatrix} = [L] \begin{bmatrix} u \\ v \\ w \end{bmatrix} = \begin{bmatrix} \cos\theta & \cos\phi\sin\theta & \sin\phi\sin\theta \\ \sin\theta & -\cos\phi\cos\theta & -\sin\phi\cos\theta \\ 0 & -\sin\phi & \cos\phi \end{bmatrix} \begin{bmatrix} u \\ v \\ w \end{bmatrix}. \qquad (52)$$

Therefore,

$$\begin{bmatrix} u \\ v \\ w \end{bmatrix} = [L]^{-1} \begin{bmatrix} u_n \\ u_t \\ u_s \end{bmatrix}. \qquad (53)$$

48
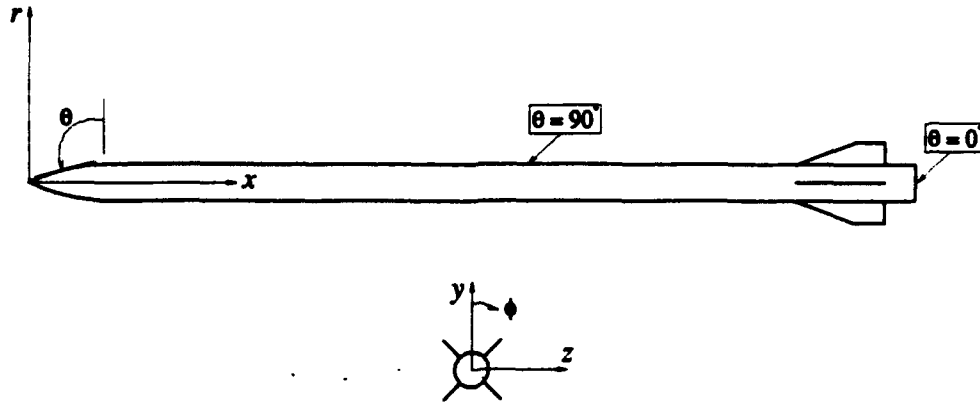
Figure 17. Body orientation showing references for body inclination angle, θ, and azimuthal angle, ϕ, where $y = r \cos \phi$ and $z = r \sin \phi$

For impermeability, the normal component of velocity is specified to vanish at the missile surface: $(u_n)_{j=1} = (-u_n)_{j=2}$. In addition, the tangential and swirl velocities are specified with the following: $(u_t)_{j=1} = (u_t)_{j=2}$, and $(u_s)_{j=1} = (u_s)_{j=2}$. Thus,

$$
\begin{bmatrix} u \\ v \\ w \end{bmatrix}_{j=1} = [L]^{-1} \begin{bmatrix} -u_n \\ u_t \\ u_s \end{bmatrix}_{j=2} = [L]^{-1} \begin{bmatrix} -1 & 0 & 0 \\ 0 & 1 & 0 \\ 0 & 0 & 1 \end{bmatrix} [L] \begin{bmatrix} u \\ v \\ w \end{bmatrix}_{j=2} . \tag{54}
$$

Finally,

$$
\begin{bmatrix} u \\ v \\ w \end{bmatrix}_{j=1} = \begin{bmatrix} -\beta_1 & -2\beta_3 \cos \phi & -2\beta_3 \sin \phi \\ -2\beta_3 \cos \phi & \beta_1 \cos^2 \phi + \sin^2 \phi & \beta_1 \beta_2 - \sin \phi \cos \theta \\ -2\beta_3 \sin \phi & \beta_1 \beta_2 - \sin \phi \cos \theta & \beta_1 \sin^2 \phi + \cos^2 \phi \end{bmatrix} \begin{bmatrix} u \\ v \\ w \end{bmatrix}_{j=2} , \tag{55}
$$

where

$$
\beta_1 = \cos^2 \theta - \sin^2 \theta, \qquad \beta_2 = \cos \phi \sin \phi, \qquad \text{and} \qquad \beta_3 = \cos \theta \sin \theta.
$$

Because the HART missile body is rotationally symmetric, and the grid is rotationally generated, very little memory is required to keep track of ϕ and θ. In fact, the angles are calculated as functions dependent on only one grid index: $\phi = \phi(k)$ and $\theta = \theta(i)$.

3.6.3 Fin Leading-edge, Trailing-edge, and Surface Conditions. Since the fins have no thickness, the same set of points in the grid that represent the upper surface of a fin must represent the lower surface. Additional variables are introduced to accomplish this. Using dual variables, the vanishing pressure-gradient and the adiabatic-wall conditions are enforced from above and below. For viscous calculations, no slip is also enforced on both sides of a fin. Again this is given by

$$u = 0, \quad v = 0, \quad \text{and} \quad w = 0.$$

As with the missile surface, fin surfaces in inviscid flow require an impermeability condition. The mechanics of this condition are different from Section 3.6.2. The main difference is the location where impermeability is enforced. For the body surface, it is between cells, but for the fin surfaces, it is at cell centers. This means that the swirl velocity is set to zero at a cell center. The Cartesian velocities are transformed into cylindrical velocities to facilitate the process:

$$
\begin{bmatrix} u_a \\ u_r \\ u_s \end{bmatrix} = [L] \begin{bmatrix} u \\ v \\ w \end{bmatrix} = \begin{bmatrix} 1 & 0 & 0 \\ 0 & \cos\phi & \sin\phi \\ 0 & -\sin\phi & \cos\phi \end{bmatrix} \begin{bmatrix} u \\ v \\ w \end{bmatrix}. \tag{56}
$$

For impermeability, $(u_s)_{k=kfin} = 0$. Also, on the top of each fin, $(u_a)_{k=kfin} = (u_a)_{k=kfin-1}$, and $(u_r)_{k=kfin} = (u_r)_{k=kfin-1}$. Similar expressions are used for the bottom of each fin. Thus,

$$
\begin{bmatrix} u \\ v \\ w \end{bmatrix}_{k=kfin} = \begin{bmatrix} 1 & 0 & 0 \\ 0 & \cos\phi_1 \cos\phi_2 & \cos\phi_1 \sin\phi_2 \\ 0 & \sin\phi_1 \cos\phi_2 & \sin\phi_1 \sin\phi_2 \end{bmatrix} \begin{bmatrix} u \\ v \\ w \end{bmatrix}_{k=kfin\pm1}, \tag{57}
$$

where ϕ_1 is the azimuthal angle of a point on the fin, and ϕ_2 is the azimuthal angle of a point above or below the fin, depending on which side of the fin u, v, and w are desired.

50

4. Results and Analysis from Thin-fin Tests

The results from this study are presented in terms of a grid-sensitivity analysis, a flow-structure analysis, a drag analysis, and a static-stability analysis. The experimental results and the EAGLE computational results [22, 93] serve as the primary basis for comparison. (Background for these results can be found in Section 1.1.)

4.1 Summary of Numerical Experiments

Over 80 numerical computations are performed using the thin-fin assumption. These include calculations to determine grid sensitivity, aerodynamic characteristics for the sharp-nosetip and blunt-nosetip models, and base-flow effects. The computations are summarized in the following paragraphs.

Table 1 lists the computations made to assess two sensitivity issues. Cases R1–R4 vary the angular spacing ($\Delta\phi$) near the fin to determine the sensitivity of the axial-force coefficient and the pitching-moment coefficient to the boundary condition that is used to extract pressure on the fin surfaces (vanishing pressure gradient, see Section 3.6). The spacing is varied from approximately 6° to 0.5°. In addition, the angle of attack is varied from 5° to 0.5° (Cases R4–R6) to determine the variation of C_{m_α} with α. All sensitivity calculations are conducted at $M_\infty = 3.5$.

Table 1. Summary of numerical experiments on the blunt-nosetip model used for grid sensitivity analysis

Case	M_∞	α	I × J × K	$\Delta\phi_{\min}$	$\Delta\phi_{\max}$	$\frac{\Delta r}{D}\vert_{\text{body}}$	Comments
R1	3.5	5.0	61 × 81 × 33	5.6250	5.6250	0.001	laminar
R2	3.5	5.0	61 × 81 × 65	2.8125	2.8125	0.001	laminar
R3	3.5	5.0	61 × 81 × 105	1.7308	1.7308	0.001	laminar
R4	3.5	5.0	61 × 81 × 33	0.5000	15.5000	0.001	laminar
R5	3.5	2.5	61 × 81 × 33	0.5000	15.5000	0.001	laminar
R6	3.5	0.5	61 × 81 × 33	0.5000	15.5000	0.001	laminar

The case history of calculations made for the sharp-nosetip model, without the base region, is tabulated in Table 2. The Mach number is varied from 2 to

51

6, and calculations are made at $\alpha = 0°$ and $\alpha = 5°$ for inviscid, laminar, and turbulent flowfield conditions. A limited number of computations are performed with refined spacing near the missile body (Cases S21, S22, S33, and S34). The spacing near the missile body for these cases is equivalent to $y^+ \approx 1$. Due to limited resources, computations with the refined grid are done for only two Mach numbers. Cases S11, S12, S16, and S17 were computed by Blake [8] as part of a Master's thesis involving parallel computing techniques. Blake used the present algorithm to make those computations. Also, two cases involve a larger fin, and are explained in Section 4.5.1.

For the sharp-nosetip model, calculations that include the base region are also made. These are used to assess the influence of the fins on base drag, and the effect of angle of attack on base drag. In addition, they are used to study the impact of the base region on pitching moment. Computations which include base effects are designated with an "SB" (Table 3). Again, Mach number is varied from 2 to 6 and calculations are made for $\alpha = 0°$ and $\alpha = 5°$. Only turbulent calculations are performed, and the grid spacing near the missile body is held fixed at $0.00005D$. One case involves a larger fin, and is explained in Section 4.5.1.

The aerodynamics of the blunt-nosetip model are also determined with a parametric Mach number study. The summary of cases for the blunt-nosetip configuration is provided in Table 4. Like the sharp-nosetip tests, Mach number is varied from 2 to 6. Also, as with the sharp-nosetip study, only two laminar and two turbulent tests are conducted with refined spacing near the missile body. For the blunt-nosetip, this spacing is $0.00005D$.

4.2 Grid Refinement and Sensitivity

Figure 18 shows the axial-force coefficient plotted against the angular spacing near the fins. The axial-force coefficient, C_a, is found to be very insensitive to the spacing near the fin. Over the range of spacing tested (6° to 0.5°), C_a varies only 1%. Also, the axial force does not depend on node clustering in the azimuthal direction. This is evidenced by the nearly identical results for unclustered and clustered spacing applied to the same number of azimuthal nodes (Cases R1 and R4, respectively).

The pitching-moment coefficient, C_{m_α}, shows a much greater sensitivity to angular spacing. Figure 19 demonstrates that C_{m_α} is influenced signific   ly by the

Table 2.   Summary of numerical experiments for sharp-nosetip model, without base region

	Case	M_∞	α	$I \times J \times K$	$\frac{\Delta r}{D}\big|_{body}$
Inviscid (coarse grid)	S1	2.0	0	61 × 81 × 33	0.001
	S2	3.0	0	61 × 81 × 33	0.001
	S3	3.5	0	61 × 81 × 33	0.001
	S4	4.5	0	61 × 81 × 33	0.001
	S5	6.0	0	61 × 81 × 33	0.001
	S6	2.0	5	61 × 81 × 33	0.001
	S7	3.0	5	61 × 81 × 33	0.001
	S8	3.5	5	61 × 81 × 33	0.001
	S9	4.5	5	61 × 81 × 33	0.001
	S10	6.0	5	61 × 81 × 33	0.001
Laminar (coarse grid)	S11	2.0	0	61 × 81 × 33	0.001
	S12	3.0	0	61 × 81 × 33	0.001
	S13	3.5	0	61 × 81 × 33	0.001
	S14	4.5	0	61 × 81 × 33	0.001
	S15	6.0	0	61 × 81 × 33	0.001
	S16	2.0	5	61 × 81 × 33	0.001
	S17	3.0	5	61 × 81 × 33	0.001
	S18	3.5	5	61 × 81 × 33	0.001
	S19	4.5	5	61 × 81 × 33	0.001
	S20	6.0	5	61 × 81 × 33	0.001
Laminar (fine grid)	S21	2.0	0	61 × 101 × 33	0.000025
	S22	3.5	0	61 × 101 × 33	0.000025
Turbulent (coarse grid)	S23	2.0	0	61 × 81 × 33	0.001
	S24	3.0	0	× 81 × 33	0.001
	S25	3.5	0	81 × 33	0.001
	S26	4.5	0	61 × 81 × 33	0.001
	S27	6.0	0	61 × 81 × 33	0.001
	S28	2.0	5	61 × 81 × 33	0.001
	S29	3.0	5	61 × 81 × 33	0.001
	S30	3.5	5	61 × 81 × 33	0.001
	S31	4.5	5	61 × 81 × 33	0.001
	S32	6.0	5	61 × 81 × 33	0.001
Turbulent (fine grid)	S33	2.0	0	61 × 101 × 33	0.000025
	S34	3.5	0	61 × 101 × 33	0.000025
Large fin	S35	3.5	5	61 × 81 × 33	0.001
	S36	4.5	5	61 × 81 × 33	0.001
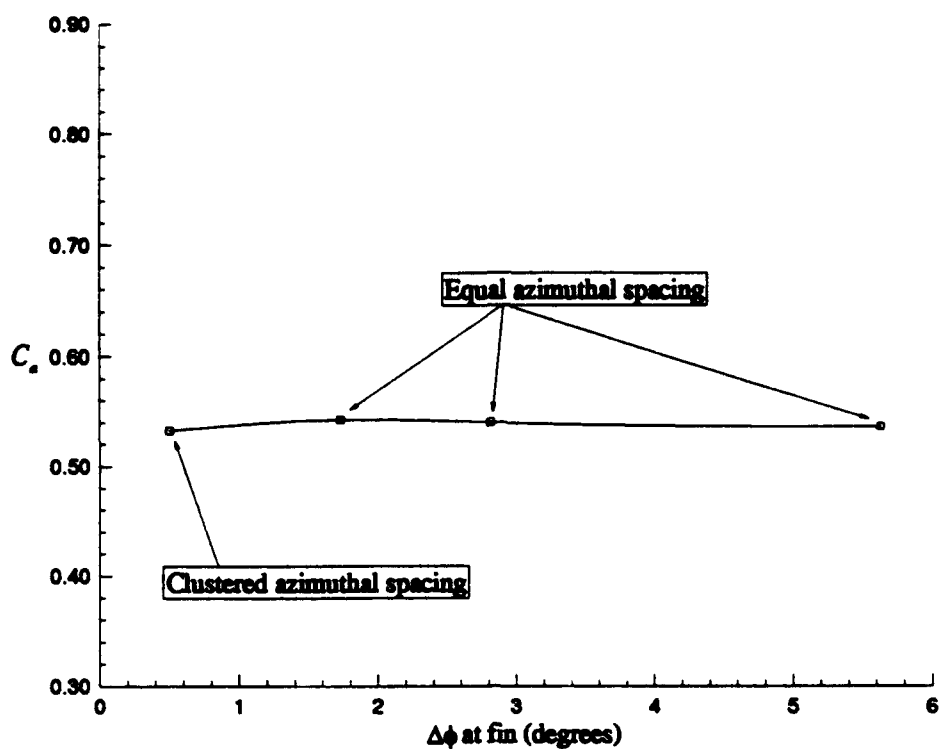
Figure 18. Sensitivity of axial-force coefficient, C_a, to angular spacing, $\Delta\phi$, near the fin
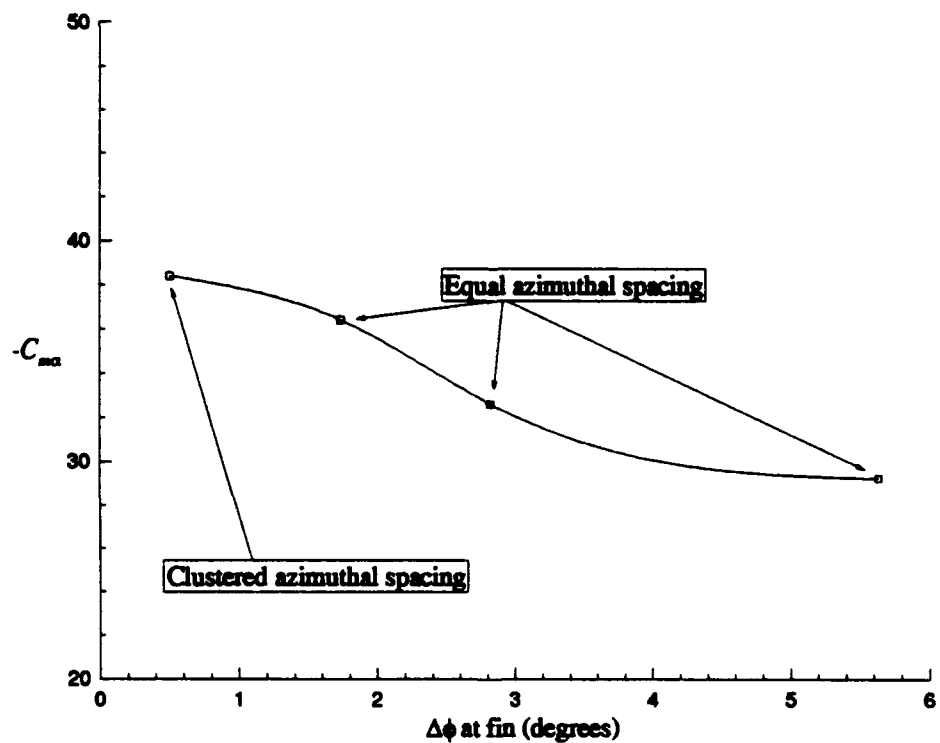
Figure 19. Sensitivity of pitching-moment coefficient, C_{m_α}, to angular spacing, $\Delta\phi$, near the fin

54

Table 3. Summary of numerical experiments for sharp-nosetip model, with base region

	Case	M_∞	α	I × J × K (Forebody)	I × J × K (Wake)	$\frac{\Delta r}{D}\big|_{body}$	$\frac{\Delta x}{D}\big|_{base}$
	SB1	2.0	0	60 × 81 × 33	31 × 111 × 33	0.00005	0.07
	SB2	3.5	0	60 × 81 × 33	31 × 111 × 33	0.00005	0.07
	SB3	4.5	0	60 × 81 × 33	31 × 111 × 33	0.00005	0.07
Turbulent	SB4	6.0	0	60 × 81 × 33	31 × 111 × 33	0.00005	0.07
	SB5	2.0	5	60 × 81 × 33	31 × 111 × 33	0.00005	0.07
	SB6	3.5	5	60 × 81 × 33	31 × 111 × 33	0.00005	0.07
	SB7	4.5	5	60 × 81 × 33	31 × 111 × 33	0.00005	0.07
	SB8	6.0	5	60 × 81 × 33	31 × 111 × 33	0.00005	0.07
Large fin	SB9	2.0	5	60 × 81 × 33	31 × 111 × 33	0.00005	0.07

angular spacing near the fins. As $\Delta\phi$ decreases from (6° to 0.5°), C_{m_α} decreases (more negative) about 30%. In addition, C_{m_α} appears to be approaching an asymptotic value near 0.5°. Due to resource limitations, grids with uniform angular spacing less than 1.7° (Case R3) were not attempted. Also, other boundary conditions to obtain pressure were not attempted. However, Riner [69] found that EAGLE computations made with the pressure-gradient boundary condition and characteristic-variable boundary conditions differed dramatically. For a grid with constant angular spacing and $\Delta\phi = 10°$, he found that the pressure-gradient boundary condition underpredicted C_{m_α} by a nearly constant amount over a Mach number range from 1.2 to 8.0. The difference in C_{m_α} found by Riner is nearly equivalent in magnitude to the difference in C_{m_α} from the present computations between the coarsest and finest spacing used. Thus, the use of node clustering near fins overcomes the deficiency of the pressure-gradient boundary condition, and nodes are clustered near the fins throughout the rest of this study.

The rate at which the pitching moment vanishes as $\alpha \to 0$ is shown in Figure 20. As the angle of attack increases, the pitching-moment coefficient changes only slightly. The three values of C_{m_α} plotted in Figure 20 differ by about 1%. Unfortunately, resource limitations prevent this analysis from being repeated at other Mach numbers. However, the results at $M_\infty = 3.5$ agree with inviscid linear theory given by (9), which indicates that C_{m_α} is independent of α.

In free-flight testing, the HART missile occasionally achieved angles of attack in excess of 5 degrees, and only over a portion of some trajectories. Therefore,

Table 4. Summary of numerical experiments for blunt-nosetip model, without base region

	Case	M_∞	α	I × J × K	$\frac{\Delta r}{D}\big|_{body}$
	B1	2.0	0	61 × 81 × 33	0.001
	B2	2.95	0	61 × 81 × 33	0.001
	B3	3.5	0	61 × 81 × 33	0.001
	B4	4.0	0	61 × 81 × 33	0.001
	B5	4.5	0	61 × 81 × 33	0.001
	B6	5.0	0	61 × 81 × 33	0.001
Inviscid	B7	6.0	0	61 × 81 × 33	0.001
(coarse grid)	B8	2.0	5	61 × 81 × 33	0.001
	B9	2.95	5	61 × 81 × 33	0.001
	B10	3.5	5	61 × 81 × 33	0.001
	B11	4.0	5	61 × 81 × 33	0.001
	B12	4.5	5	61 × 81 × 33	0.001
	B13	5.0	5	61 × 81 × 33	0.001
	B14	6.0	5	61 × 81 × 33	0.001
	B15	2.0	5	61 × 81 × 33	0.001
	B16	2.95	5	61 × 81 × 33	0.001
Laminar	B17	3.5	5	61 × 81 × 33	0.001
(coarse grid)	B18	4.0	5	61 × 81 × 33	0.001
	B19	4.5	5	61 × 81 × 33	0.001
	B20	5.0	5	61 × 81 × 33	0.001
	B21	6.0	5	61 × 81 × 33	0.001
Laminar	B22	2.95	0	61 × 81 × 33	0.00005
(fine grid)	B23	3.5	0	61 × 81 × 33	0.00005
	B24	2.0	5	61 × 81 × 33	0.001
	B25	2.95	5	61 × 81 × 33	0.001
Turbulent	B26	3.5	5	61 × 81 × 33	0.001
(coarse grid)	B27	4.0	5	61 × 81 × 33	0.001
	B28	5.0	5	61 × 81 × 33	0.001
	B29	6.0	5	61 × 81 × 33	0.001
Turbulent	B30	2.95	0	61 × 81 × 33	0.00005
(fine grid)	B31	3.5	0	61 × 81 × 33	0.00005
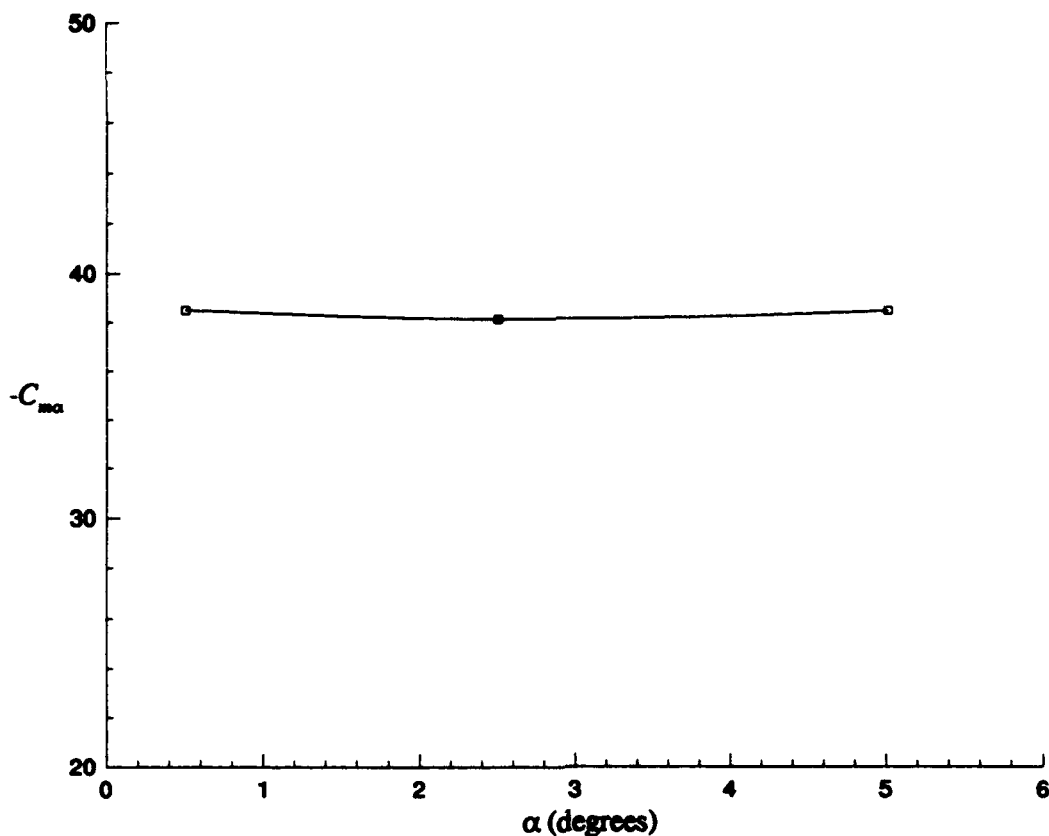
Figure 20. Sensitivity of pitching-moment coefficient, C_{m_α}, to angle of attack.

$\alpha = 5°$ is representative of the experiments and is selected in the current study for all remaining computations performed with a nonzero angle of attack.

4.3 Flowfield Near Fin

The flowfield near the fins is examined through analysis of the shock-wave shape and strength of the shock/boundary-layer interaction. The angles of the shock waves created by the fins are compared to the theoretical and experimental angles discussed in Section 2.1.1. The interaction of the shocks with the boundary layer growing on the missile body is assessed with surface pressure line plots and contour plots.

4.3.1 Shock-wave Shape. In Figure 21, the shock wave created by a thin-swept fin at angle of attack is compared directly to the shock wave from a wedge-shaped delta wing. The wedge angle is equivalent to the angle of attack of the thin fin. For the delta wings, small wedge angles and highly swept leading edges produce shocks that emanate from the leading edge at angles very close to the Mach angle. The Mach angle based on the local Mach number is indicated with a dashed line in

Figure 21 for reference. Figure 21 shows pressure contours on the missile body for $M_\infty = 2$ and $\alpha = 5°$ (Case B8). The pressure contours show a shock below each fin and an expansion above each fin. The shock-wave angle is well predicted using the thin-fin assumption.

Figures 22 and 23 show the pressure on the upper and lower surfaces of the two fins (one on the expansion side of the missile and one on the compression side of the missile) for $M_\infty = 2$ and $\alpha = 5°$. Rapid expansions to the upper surfaces are visible at the leading edges of both fins. Note the clustering of contour lines near the leading edges in Figures 22a and 23a. Likewise, attached shocks are seen on the lower surface leading edges, as evidenced by the clustered contour lines in Figures 22b and 23b. Although the pressure contours show weak compressions on the upper fin surfaces and weak expansions on the lower fin surfaces, the pressure is relatively constant on each surface. In addition, the compression on the lower surface and the expansion on the upper surface are distinctly separated in the inviscid flow.
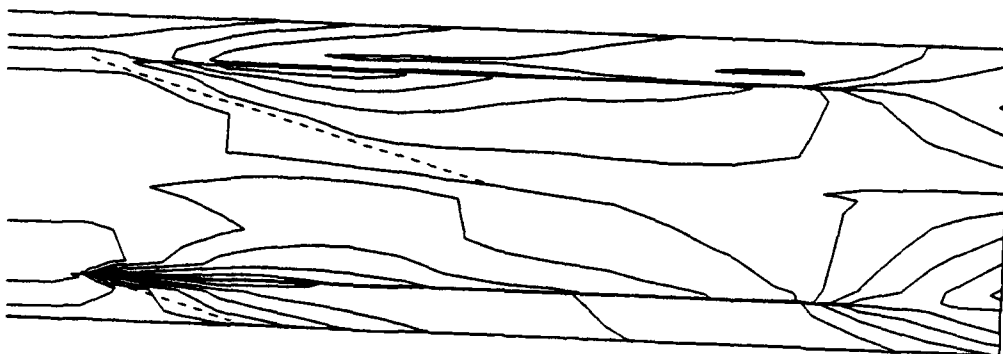
Figure 21. Pressure contours on the missile near the fin/body junction (Case B8)

4.3.2 Shock/Boundary-layer Interaction. The boundary-layer does not separate in any of the laminar or turbulent computations, and indicates that the shock/boundary-layer interaction is weak. To further assess the weakness of the interaction, the surface pressure is examined. In Figure 24, pressure is plotted along the missile body upstream of the fin/body junction for $M_\infty = 2$, $\alpha = 5°$, laminar flow (Case S16), and turbulent flow (Case S28). The pressure ahead of each fin
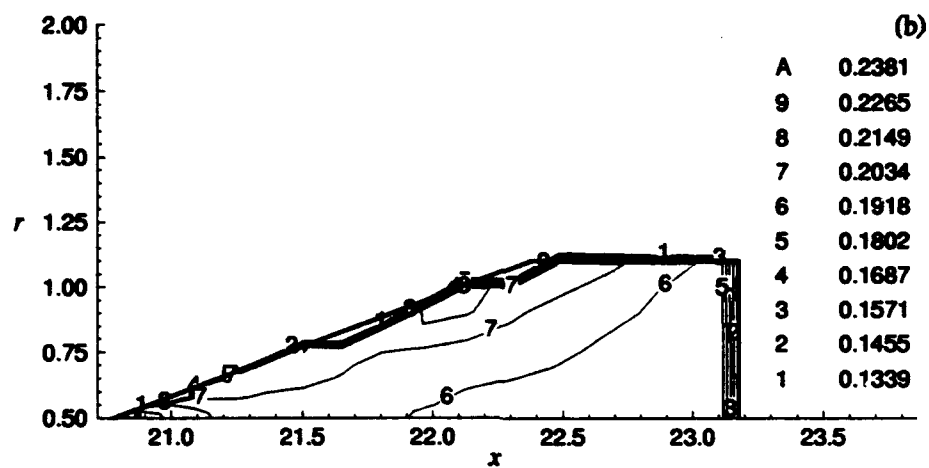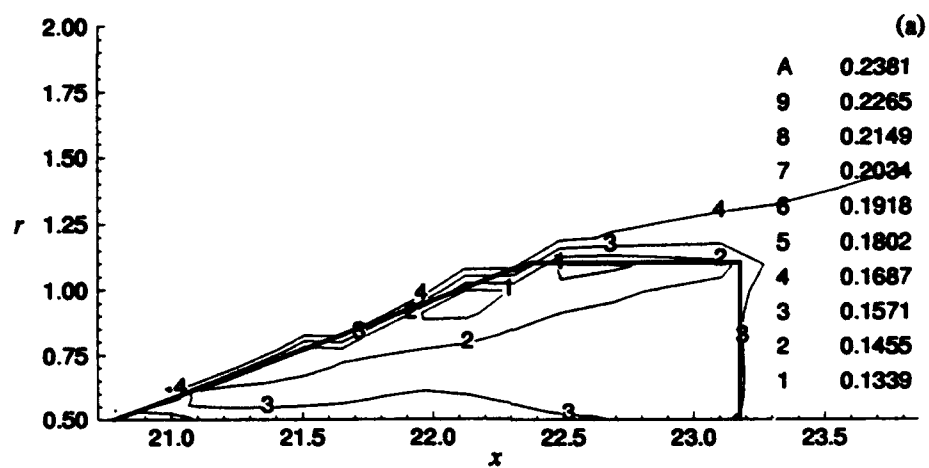
Figure 22.   Pressure contours for the fin on expansion side of the missile (Case B8):
(a) upper surface, (b) lower surface
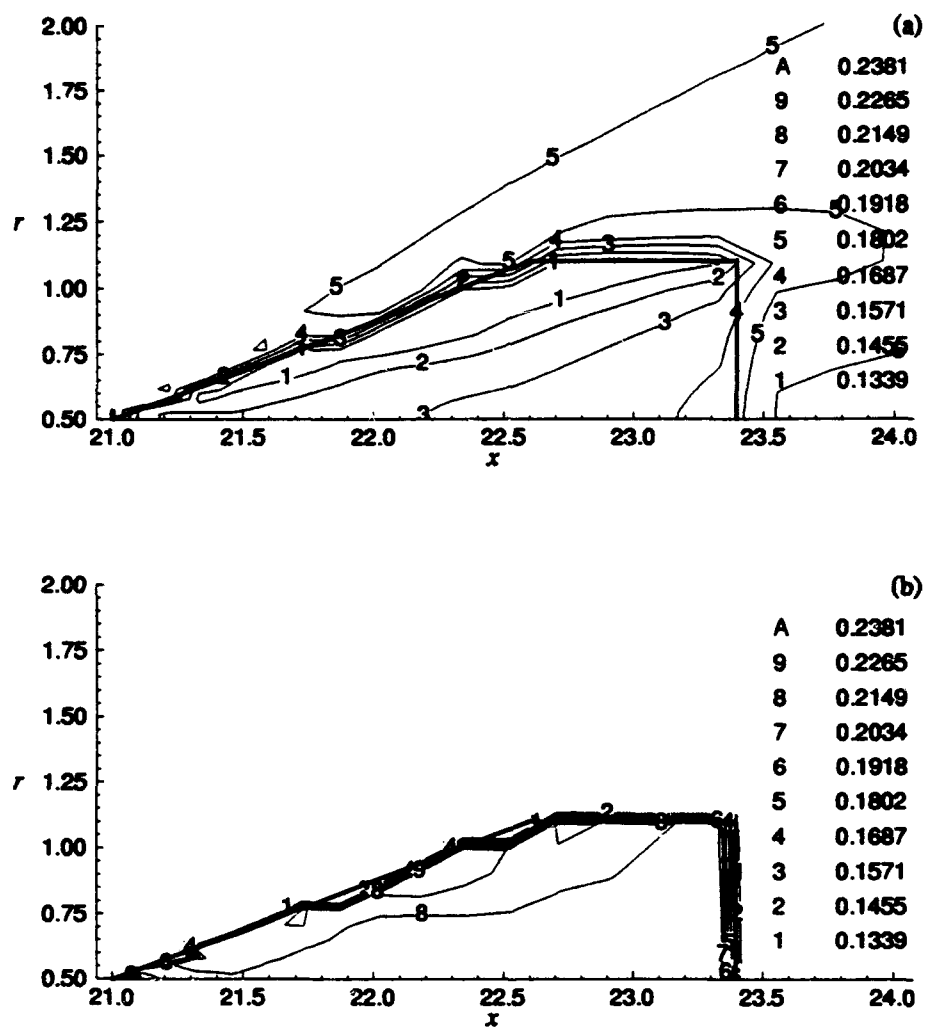
Figure 23. Pressure contours for the fin on the compression side of the missile (Case B8): (a) upper surface, (b) lower surface

is plotted separately, and the location of the fin leading edge is indicated for reference. The pressure is only slightly disturbed ahead of the leading edges, and is nearly the same for laminar and turbulent conditions. Moreover, the plateau associated with separation [2] is not visible. Again, this is due to the weakness of the shock/boundary-layer interaction. Eliminating the fin's cross section may have prevented separation, but other researchers have shown that highly-swept fins exhibit no boundary-layer separation [64, 99, 55].

4.4 Drag Analysis

To facilitate a detailed analysis of missile drag, the drag coefficient is broken down into components, and the components are analyzed individually and then collectively. The drag breakdown was discussed in Section 2.4.1. The empirical components used with previous EAGLE computations are graphically compared to quantities directly calculated in this study. Additionally, the influence of the fins on the base drag and the effect of angle of attack on the base drag are discussed with plots showing the variation of base drag with Mach number. Finally, the drag obtained from free-flight testing is compared to the current computation of total drag. Comparisons with free-flight data are also made with C_d versus M_∞ plots.

The base drag in the current study is computed in two ways. First, it is directly obtained from calculations on the complete HART missile configuration. The base drag is also computed for axisymmetric bases, in axisymmetric flow ($\alpha = 0°$), using axisymmetric equations. These simpler computations allow much finer grid resolution, and are described in Appendix A. Total drag is computed using the base drag from Appendix A because of the greater level of validation.

All drag values computed in this study at $\alpha = 0°$ are summarized in Table 5 for the sharp-nosetip model and Table 6 for the blunt-nosetip model. These tables contain the wave-drag, base-drag, and friction-drag components for the missile body and the fins tabulated separately. In addition, the data are delineated by the flow-field condition (inviscid, laminar, or turbulent) and grid coarseness. The following sections discuss and analyze each component more fully.

The wave-drag coefficient and pitching-moment coefficient from EAGLE computations on the sharp-nosetip model with clipped-delta fins are summarized in Table 7. The coefficients are tabulated for Mach numbers ranging from 2 to 8. Included

61
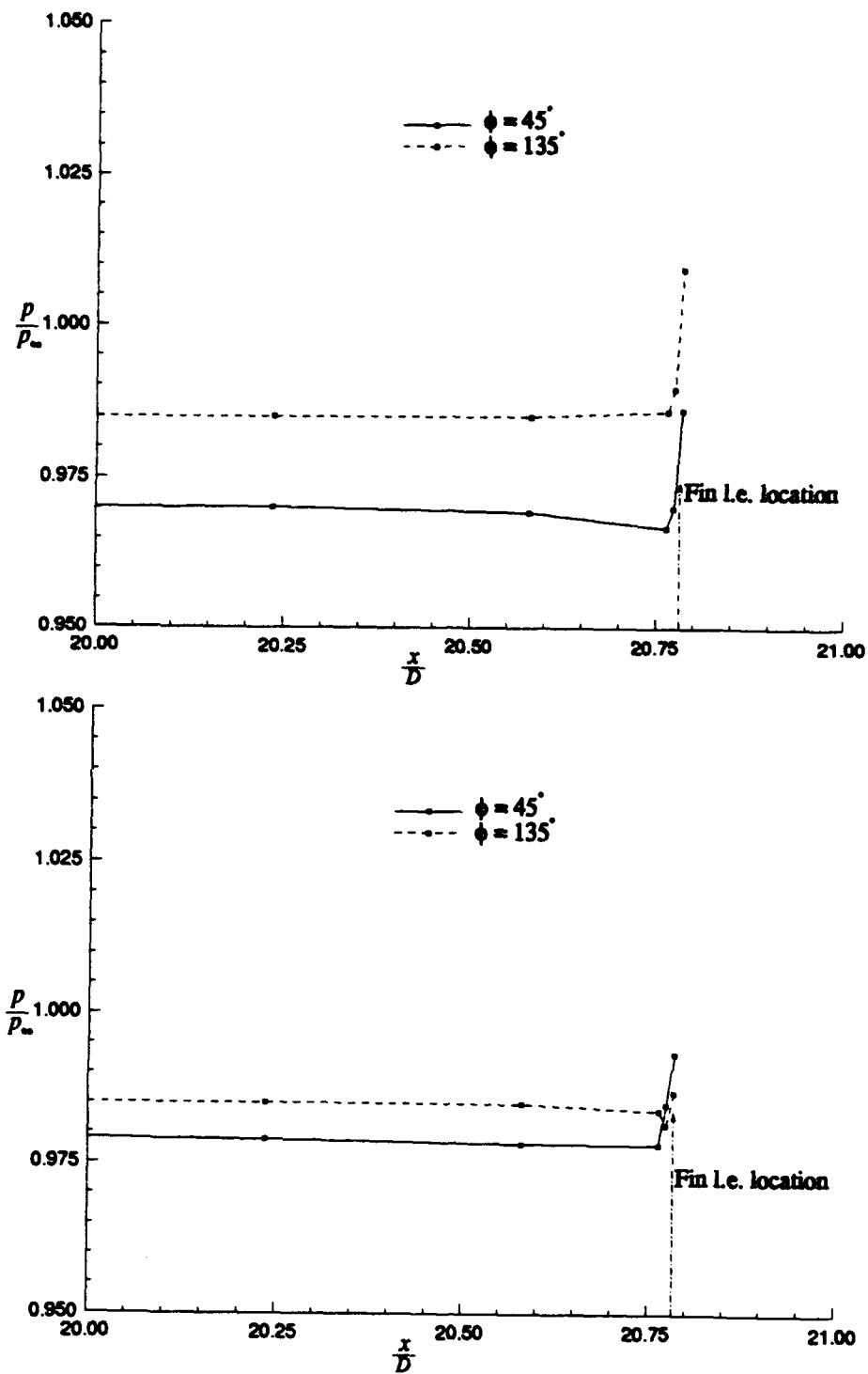
Figure 24. Pressure along the missile body upstream of the fin/body junction: (a) laminar flow (Case S16), (b)turbulent flow (Case S28)

Table 5. Computed drag components for sharp-nosetip model ($\alpha = 0°$)

	Case	C_{d_w} (body)	C_{d_v} (body)	C_{d_b} (body)	$C_{d_w}+C_{d_b}$ (fins)	C_{d_v} (fins)	C_d (total)
Inviscid (coarse grid)	S1	0.160	-	0.145*	0.047	-	0.352
	S2	0.145	-	0.098*	0.048	-	0.291
	S3	0.140	-	0.079*	0.049	-	0.268
	S4	0.135	-	0.045*	0.050	-	0.230
	S5	0.129	-	0.024*	0.051	-	0.204
Laminar (coarse grid)	S11	0.160	0.074	0.145*	0.045	0.010	0.434
	S12	0.145	0.057	0.098*	0.046	0.009	0.357
	S13	0.140	0.054	0.079*	0.047	0.008	0.328
	S14	0.135	0.046	0.045*	0.048	0.007	0.281
	S15	0.129	0.034	0.024*	0.049	0.006	0.242
Laminar (fine grid)	S21	0.160	0.073	0.145*	0.045	0.010	0.433
	S22	0.140	0.053	0.079*	0.047	0.008	0.327
Turbulent (coarse grid)	S23	0.162	0.238	0.145*	0.042	0.012	0.599
	S24	0.147	0.168	0.098*	0.043	0.010	0.468
	S25	0.142	0.135	0.079*	0.043	0.008	0.407
	S26	0.137	0.093	0.045*	0.044	0.007	0.326
	S27	0.131	0.059	0.024*	0.045	0.006	0.265
Turbulent (fine grid)	S33	0.162	0.257	0.145*	0.042	0.013	0.619
	S34	0.142	0.165	0.079*	0.043	0.009	0.438
Turbulent (with base)	SB1	0.162	0.244	0.151	0.042	0.012	0.611
	SB2	0.142	0.147	0.078	0.042	0.007	0.416
	SB3	0.137	0.103	0.044	0.043	0.007	0.334
	SB4	0.131	0.060	0.021	0.044	0.006	0.262

* - Base drag taken from Appendix A.

in Table 7 are the empirical values for viscous drag (turbulent) and base drag used to *correct* the inviscid EAGLE results. These corrections were detailed in Section 1.1.2, and are given by (1) and (2). The following sections compare this data to the present results.

4.4.1 Forebody Wave Drag. The forebody pressure, or wave drag, is dominated by the nosetip geometry, and shows very little sensitivity to viscous effects. This is seen in Table 5 or Table 6 with M_∞ fixed, where the wave drag is nearly identical for inviscid, laminar, and turbulent calculations.

The wave drag from the turbulent calculations on the sharp-nosetip model (Cases S23–S27 and S33–S34) is plotted versus Mach number with the EAGLE results in Figure 25. Also included is the value predicted by slender-body theory [4]

63

Table 6. Computed drag components for blunt-nosetip model ($\alpha = 0°$)

	Case	C_{d_w} (body)	C_{d_p} (body)	C_{d_b} (body)	$C_{d_w}+C_{d_b}$ (fins)	C_{d_v} (fins)	C_d (total)
Inviscid (coarse grid)	B1	0.416	-	0.145*	0.023	-	0.584
	B2	0.457	-	0.100*	0.023	-	0.580
	B3	0.465	-	0.079*	0.024	-	0.568
	B4	0.471		0.063*	0.024	-	0.558
	B5	0.475	-	0.045*	0.024	-	0.544
	B6	0.477	-	0.039*	0.025	-	0.541
	B7	0.479	-	0.024*	0.025	-	0.528
Laminar (fine grid)	B22	0.457	0.078	0.100*	0.021	0.015	0.671
	B23	0.465	0.043	0.079*	0.022	0.010	0.619
Turbulent (fine grid)	B30	0.457	0.129	0.100*	0.018	0.016	0.720
	B31	0.465	0.086	0.079*	0.019	0.010	0.659
Laminar (with base) (Axi-Eqns)**	$M_\infty = 2$	0.415	0.049	0.110	-	-	0.574
	$M_\infty = 3$	0.453	0.035	0.063	-	-	0.552
	$M_\infty = 4$	0.475	0.028	0.036	-	-	0.539
	$M_\infty = 5$	0.484	0.024	0.024	-	-	0.529
	$M_\infty = 6$	0.490	0.019	0.015	-	-	0.523
	$M_\infty = 7$	0.492	0.015	0.011	-	-	0.519

* - Base drag taken from Appendix A.

** - Calculated from axisymmetric equations for blunt-nosetip model without fins.

Table 7. Drag and pitching-moment coefficients from EAGLE results for sharp-nosetip model with clipped-delta fins

M_∞	C_{d_w}	$C_{d_v}^*$	$C_{d_b}^{**}$	C_d	C_{m_α}
2.0	0.159	0.330	0.172	0.661	-62.41
3.0	0.145	0.310	0.108	0.563	-39.99
4.0	0.136	0.296	0.073	0.505	-22.92
4.5	0.133	0.291	0.060	0.484	-15.21
5.0	0.130	0.286	0.051	0.467	-11.88
6.0	0.126	0.278	0.037	0.441	-5.30
7.0	0.123	0.272	0.028	0.423	0.09
8.0	0.121	0.266	0.022	0.409	2.83

* - Empirical, also corrected to account for Reynolds number error.

** - Empirical.

and the area-rule theory [15] for $M_\infty = 2$ (see Section 2.2.1). As expected from theory, the variation with Mach number is modest. For the present computations, C_{d_w} decreases from 0.162 at $M_\infty = 2$ to 0.131 at $M_\infty = 6$. For the EAGLE computations, C_{d_w} decreases from 0.159 at $M_\infty = 2$ to 0.126 at $M_\infty = 6$. The wave drag from the current coarse grid and fine grid computations is identical. The agreement between all the results, except slender-body theory, is considered excellent.

The wave drag from the blunt-nosetip model is plotted versus Mach number in Figure 26. Here the wave drag increases with Mach number. The variation with Mach number is again small, however.

4.4.2 Forebody Friction Drag. Accurate prediction of friction drag depends primarily on adequate grid resolution normal to the missile body surface. Because the velocity gradients near the wall are less severe for laminar flow than for turbulent flow, the laminar friction drag is calculated equally well with the coarse grid (Cases S11–S15) and the fine grid (Cases S21–S22). An accurate prediction of the turbulent friction drag required more refined grid spacing near the missile body. At $M_\infty = 2$, the turbulent friction drag from the coarse-grid test (Case S23) is 0.238, and turbulent friction drag from the fine-grid test (Case S33) is 0.257. Likewise, at $M_\infty = 3.5$, the turbulent friction drag increased with grid refinement from 0.135 to 0.165.

The effects of compressibility on friction drag cannot be understated. Turbulent skin friction on a flat plate varies considerably with supersonic Mach numbers [101]. One method to compute friction drag is to utilize the concept of a flat plate of equivalent size. By this method, the wetted area of the HART missile is calculated and used with an empirical relation for friction drag on a flat plate to compute friction drag for the missile. This was done for previous EAGLE results (Table 7), using an incompressible formula, (2). A similar procedure is employed here with a compressibility correction to (2). Figure 27 compares the turbulent viscous drag (Cases S23–S27), the EAGLE results, and both equivalent flat-plate formulas. For $M_\infty = 1.5$ to $M_\infty = 8$ compressibility results in a very large decrease in C_{d_v} as M_∞ increases. The trend in C_{d_v} with increasing Mach number from the compressible flat-plate formula agrees well with the current computations. The relatively flat profile of the relation used to correct the inviscid EAGLE results is a direct consequence of neglecting compressibility effects. This is also seen seen in Figure 3 for the baseline HART model.
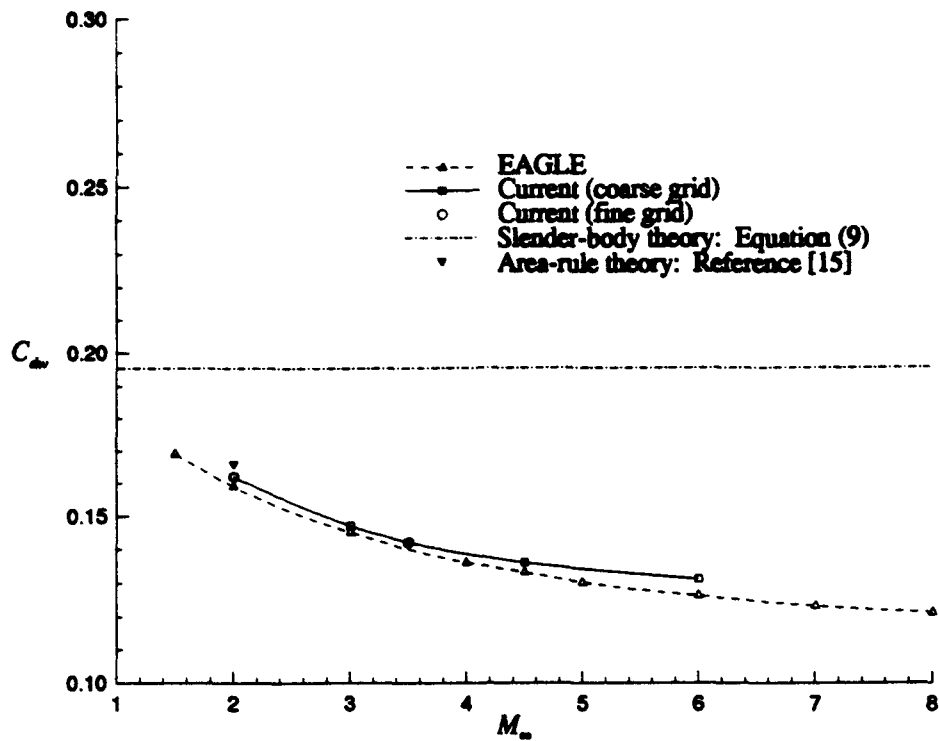
Figure 25. Wave-drag coefficient, C_{d_w}, for sharp-nosetip model ($\alpha = 0°$)
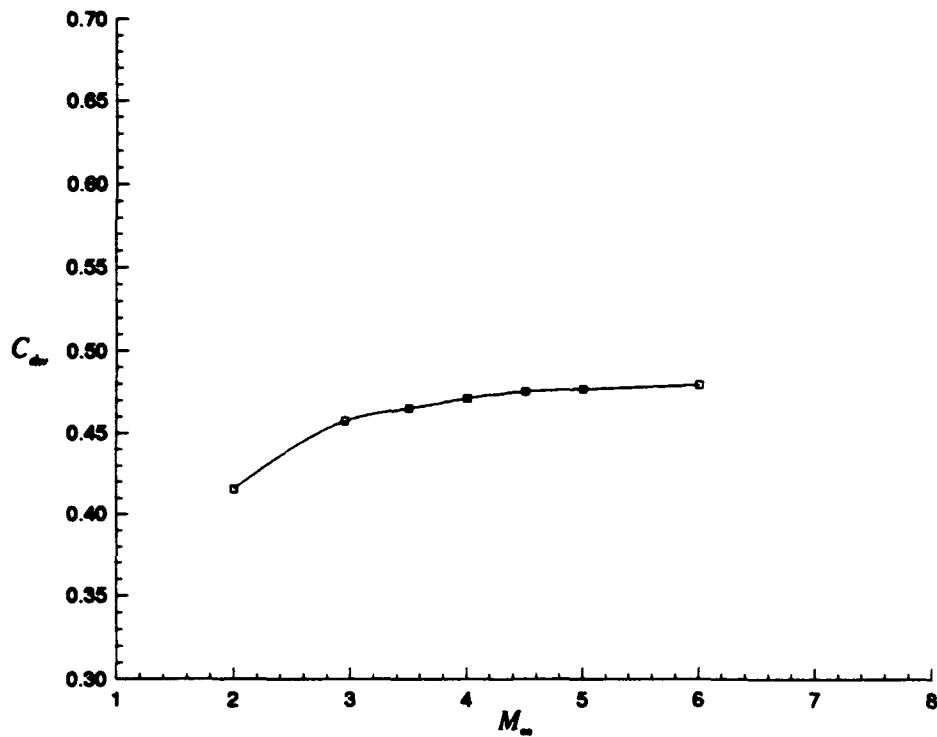
Figure 26. Wave-drag coefficient, C_{d_w}, for blunt-nosetip model ($\alpha = 0°$)

66

4.4.3 Base Drag. The empirical correction used with the EAGLE results, (1), is compared to the values computed with the current axisymmetric equations in Figure 28. The correlation is good for Mach number from 1.5 to 7. The empirical formula consistently predicts a higher value of base drag for all Mach numbers. Since the small difference between (1) and the current results can be eliminated by modifying the empirical constant appearing in (1), this demonstrates the accuracy that can be achieved with the empirical formula.

Base drag should increase with increasing angle of attack [76], and is confirmed with the current method. Figure 29 shows base drag from computations at $\alpha = 0°$ compared to base drag from $\alpha = 5°$. Very similar results are obtained for the two angles of attack. The base drag for $\alpha = 5°$ increases slightly.

4.4.4 Effect of Fins on Base Drag. The influence of the fins on base drag has been documented by Love [53]. Love showed that both the proximity of the fins to the base and the thickness of the fins can alter base pressure. He also showed that the interference effect decreases significantly with increasing Mach number, and Reynolds numbers effects are small for turbulent condition... Base drag taken from calculations made on the complete configuration agree with the trends cited by Love. Figure 30 shows the base drag from the complete configuration (Cases SB1–SB4) compared to the base drag from calculations without fins (Appendix A). The base drag from the complete configuration calculations is generally lower than the axisymmetric calculations. The curves cross around $M_\infty = 3$ due to the effects of the fins. At the lowest Mach number tested, the drag from the complete configuration with fins is greater.

4.4.5 Uncertainty Due to Boundary-layer Transition. Because the error associated with fitting the theoretical trajectories to the experimental trajectories was not documented, this author initiated a reevaluation of the free-flight data in order to quantify the error in the trajectory match for each test and obtain more reliable data. The reevaluation was done through an existing contract between Wright Laboratory and Arrow Tech Associates, and is documented in a contractor test report [37]. Several data points were eliminated based on a poor fit to the flight trajectory. The reason why it was more difficult to correlate trajectories for the clipped-delta-fin was not ascertained. The original and reevaluated drag data are plotted in Figure 31, and provided in Table 8. The error for the reevaluated trajectories is summarized in
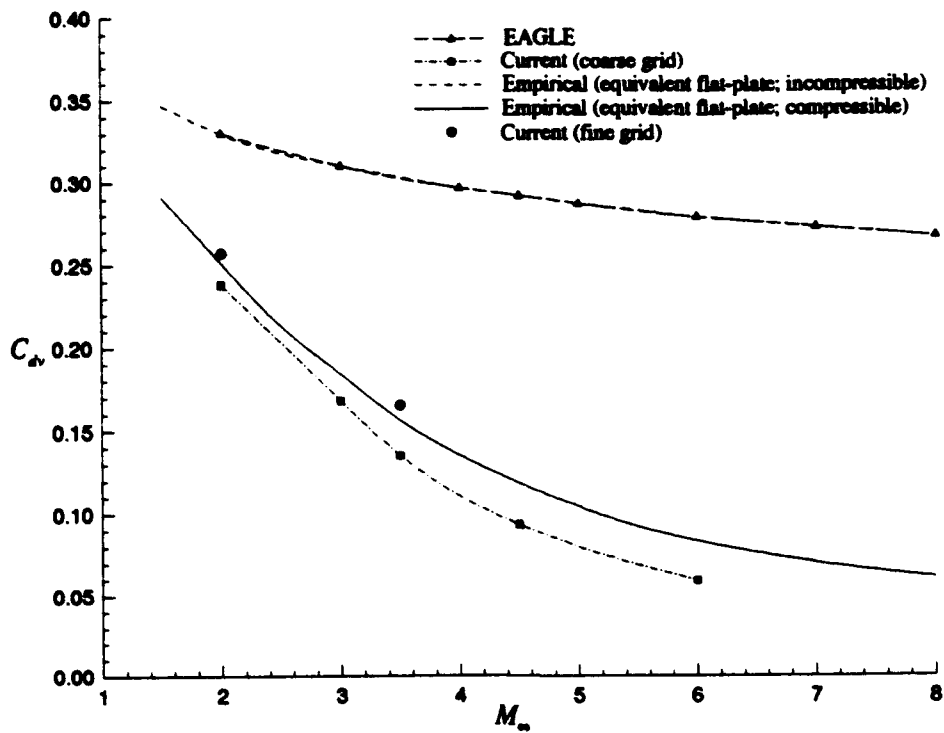
Figure 27. Viscous-drag coefficient, C_{d_v}, for the sharp-nosetip model in turbulent flow ($\alpha = 0°$)
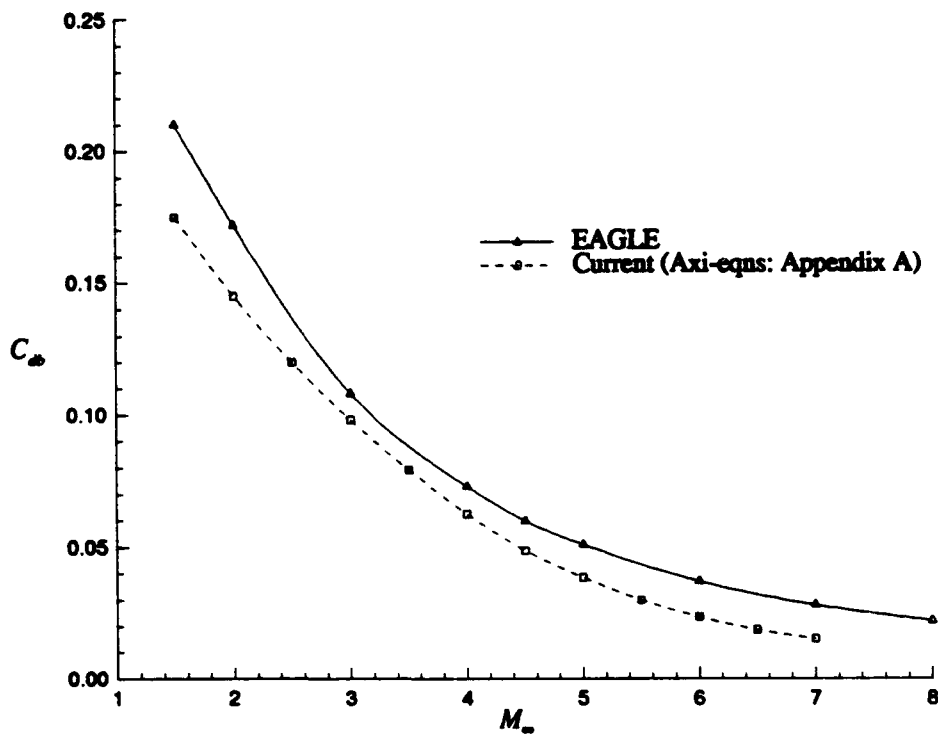
Figure 28. Base-drag coefficient, C_{d_b}, for the HART missile ($\alpha = 0°$)

68
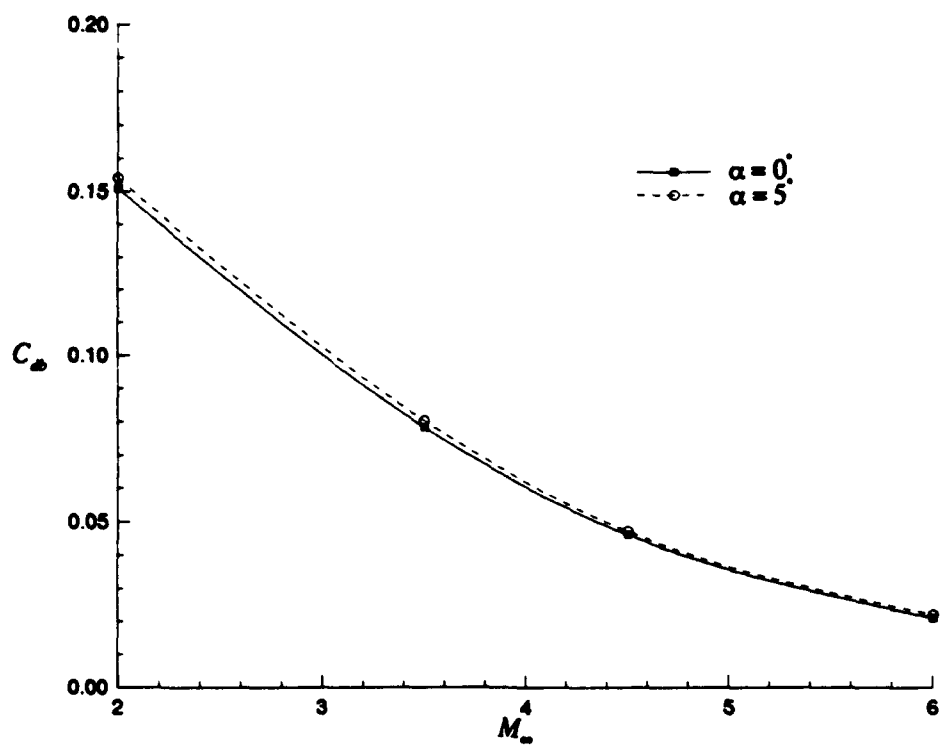
Figure 29. Base-drag coefficient, C_{d_b}, showing effect of angle of attack
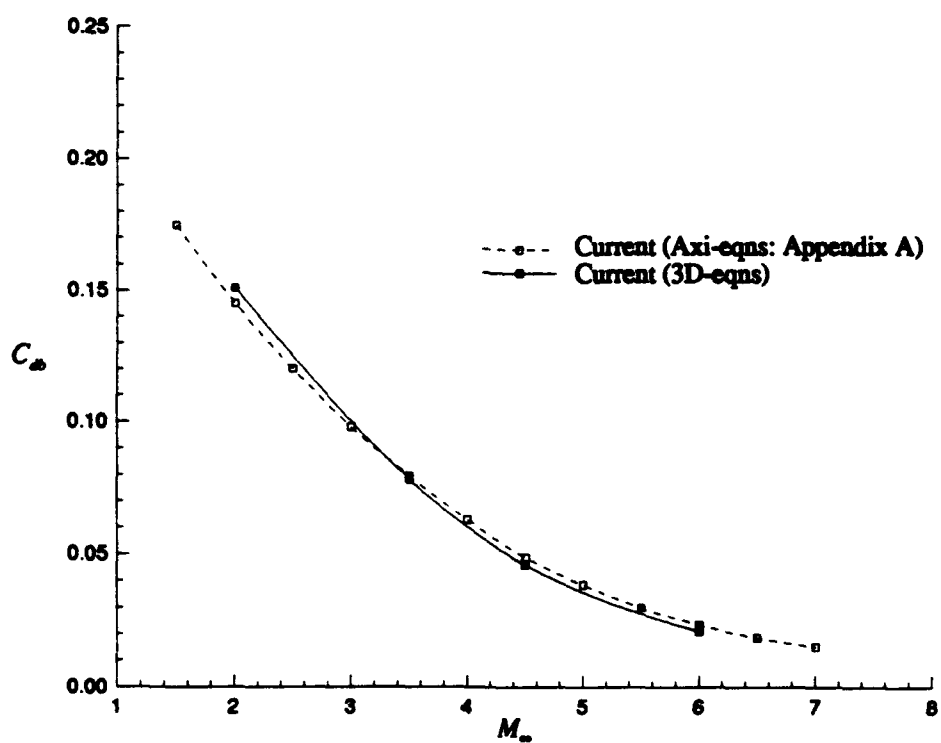
Figure 30. Base-drag coefficient, C_{d_b}, showing fin interference effects ($\alpha = 0°$)

Table 9. By eliminating those data with a poor trajectory fit, the scatter is decreased considerably.

It is, however, still possible that the variation with Mach number is influenced by boundary-layer transition. Several factors related to the nature of free-flight testing are important. First, natural transition has a Mach number and Reynolds number dependence [101]. Also, the high-entropy layer of a blunt nosetip can delay transition [79]. Second, turbulent bursts, which are observed experimentally through shadowgraphs, can affect transition [42]. Finally, induced transition may occur due to a lack of model fidelity. The experimental missile body is a two-piece construction, and weak shocks can be seen emanating from the location where the two pieces are joined [93]. This edge may disturb the boundary layer into a turbulent state prematurely.

4.4.6 Total Drag. Total drag from laminar and turbulent calculations at $\alpha = 0°$ for the sharp-nosetip model and for $M_\infty = 2 - 6$ (Cases S11–S15 and S23–S27, respectively) are compared to the reevaluated experimental data in Figure 32a. Both coarse-grid and fine-grid results are shown. The laminar drag severely underpredicts the experimental drag due to the much lower friction drag. In addition, the laminar drag trend with Mach number does not agree well with the experimental trend. The turbulent drag predicts the trend with Mach number much better, but the computations using the coarse grid still underpredict the drag significantly. The computations with the fine grid (Cases S33–S34) accurately resolve the boundary layer on the missile body, giving much better results.

The drag from the fine-grid turbulent computations in Figure 32a is still lower than the experimental drag because of the coarseness of the grid in the azimuthal direction. Due to inadequate resolution near the fin surfaces, the boundary layers on the fins are not well resolved. Subsequently, fin friction drag is underpredicted, especially for the turbulent cases. Based on the excellent agreement obtained between computations of forebody friction drag and an equivalent flat plate (compressible), the turbulent fin friction drag used to obtain the total drag in Figure 32b is determined using (2) with a compressibility correction obtained graphically from White [101]. This approach yields friction drag that agrees well with the flat-plate theory of van Driest (van Driest II) [101]. When the coarse grid results are corrected using this equivalent flat plate method, excellent correlation is obtained between the

Table 8. Experimental drag and pitching-moment coefficients for sharp-nosetip model with clipped-delta fins ($\alpha = 0°$)

Free-flight No. (yymmdd##)	M_∞	C_d (original)	C_{m_α}	M_∞	C_d (reevaluated)	C_{m_α}
90012359	2.805	0.574	-42.24	2.811	0.577	-45.267
90011957	2.914	0.554	-42.87	2.916	0.553	-50.465
89090794	3.174	0.535	-	*	-	-
89090896	3.188	0.525	-28.88	3.190	0.524	-28.717
89090895	3.363	0.512	-27.51	3.363	0.508	-27.557
89053149	3.499	0.444	-25.93	3.501	0.444	-26.758
90011654	3.541	0.482	-	*	-	-
89060150	3.572	0.473	-23.51	3.556	0.461	-19.943
89103134	3.603	0.518	-22.67	*	-	-
90020564	3.621	0.452	-	3.633	0.461	-21.881
89060758	3.677	0.460	-24.93	3.678	0.446	-25.913
90020263	3.725	0.445	-27.45	*	-	-
90011856	3.801	0.462	-	*	-	-
89103032	3.823	0.490	-25.06	*	-	-
90041706	4.119	0.419	-28.42	4.123	0.410	-29.650
90041203	4.138	0.416	-27.82	4.143	0.415	-28.484
90041304	4.193	0.418	-29.25	4.194	0.416	-29.816
90041605	4.239	0.418	-30.09	4.240	0.415	-28.563

* - Poor fit between theoretical trajectory and experimental trajectory.

Table 9. Error between theoretical trajectory and experimental trajectory (from reevaluation of free-flight data)

Free-flight No. (yymmdd##)	Longitudinal error (m)	Lateral or Swerve error (m)	Pitch or Yaw error (deg)	Roll error (deg)
90012359	0.0014	0.0028	0.230	10.810
90011957	0.0017	0.0012	0.128	6.865
89090896	0.0023	0.0012	0.206	12.220
89090895	0.0023	0.0018	0.190	6.982
89053149	0.0023	0.0022	0.132	9.264
89060150*	0.0022	0.0057	0.443*	7.308
90020564*	0.0018	0.0051	0.588*	10.200
89060758	0.0023	0.0007	0.199	10.710
90041706	0.0017	0.0025	0.255	24.370
90041203	0.0017	0.0019	0.127	5.598
90041304	0.0016	0.0010	0.151	9.863
90041605	0.0021	0.0021	0.306	16.670

* - Not use in this study due to larger pitch error.

experimental data and the present turbulent results, as seen in Figure 32b. Nearly identical results are obtained from the fine-grid calculations when only the fin friction drag is corrected using the flat-plate method.

Drag on the blunt-nosetip model for $M_\infty = 2 - 6$ and $\alpha = 0°$ is compared to experimental data (Table 10) in Figure 33. Laminar and turbulent calculations are made for only two Mach numbers, so extensive comparison is not possible. However, it is apparent that the computations predict higher drag; both laminar and turbulent predictions exceed the free-flight data. It is important to note that the blunt-nosetip experimental data was not reevaluated, so accuracy for those free-flight tests is uncertain.

4.5 Static-stability Analysis

Next, the static stability is assessed for the clipped-delta-fin HART missile. There are two goals to this phase of the analysis. First, corroborate and/or identify the cause of the restabilization trend observed in free-flight testing. This trend is shown in Figure 34, where experimentally determined $C_{m\alpha}$ is plotted versus M_∞. Figure 34 shows the pitching-moment coefficient obtained from the original experimental data for the sharp-nosetip configuration (Table 8), the original experimental data for the blunt-nosetip configuration (Table 10), and recent experimental data for a grooved version of the sharp-nosetip model (Table 11), [37]. A second-order polynomial is fit through the combined data. The static stability apparently increases ($C_{m\alpha}$ becomes more negative) from Mach 3.5 to Mach 4.5. The second goal of the analysis in this section is to determine the stability characteristics above Mach 4.5. Recall that for the baseline model, the ZEUS and EAGLE computations differed markedly above Mach 4.5 (Figure 4). The data used in Figure 4 is summarized in Table 12.

The pitching-moment coefficient from the reevaluation of the free-flight data confirmed the change in stability trend. As discussed in Section 4.4.3, a reevaluation of the raw experimental data was initiated by the author because the error for individual free-flight tests is not available. The pitching-moment coefficient from the reevaluated data is shown in Figure 35 versus Mach number. The second-order polynomial curve fit that was used in Figure 34 is included for comparison. The agreement between the curve fit and the reevaluated data suggests that the restabilization trend is confirmed with the reevaluation.

72
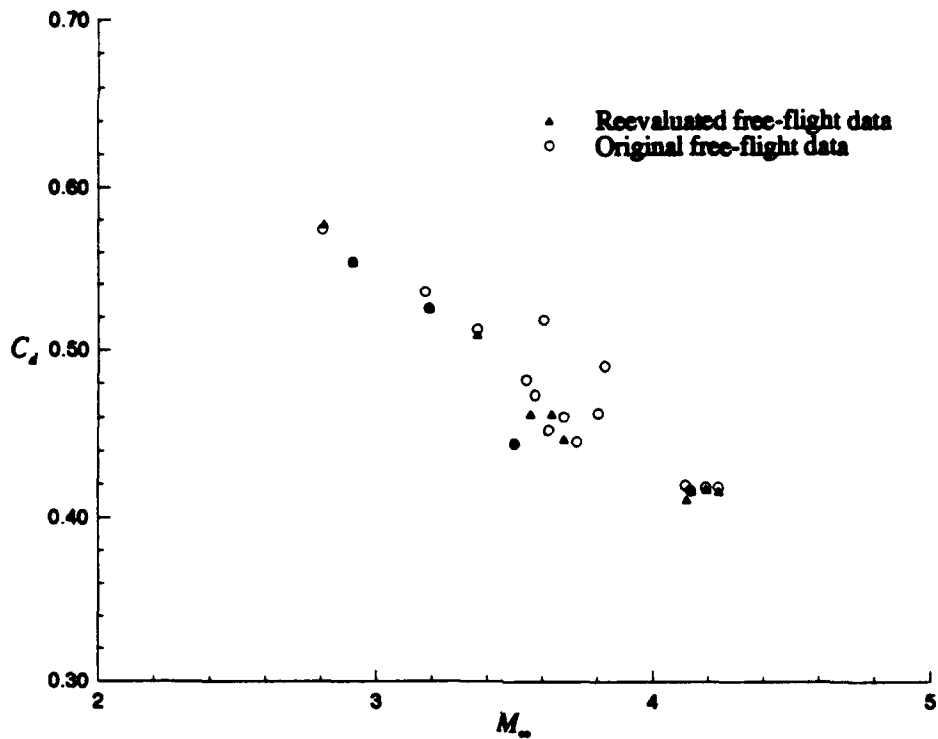
Figure 31. Total-drag coefficient, C_d, extracted from free-flight tests of the sharp-nosetip, clipped-delta-fin, HART missile

Table 10. Experimental drag and pitching-moment coefficients for blunt-nosetip model with clipped-delta fins

Free-flight No. (yymmdd##)	M_∞	C_d	C_{m_α}
91041741	1.653	0.708	-72.38
91041740	1.667	0.756	-71.71
91041742	1.669	0.731	-71.64
91041843	3.070	0.640	-42.67
91041944	3.125	0.593	-36.86
91050248	4.336	0.514	-27.01
91050147	4.369	0.531	-27.72
91050249	4.393	0.544	-31.22
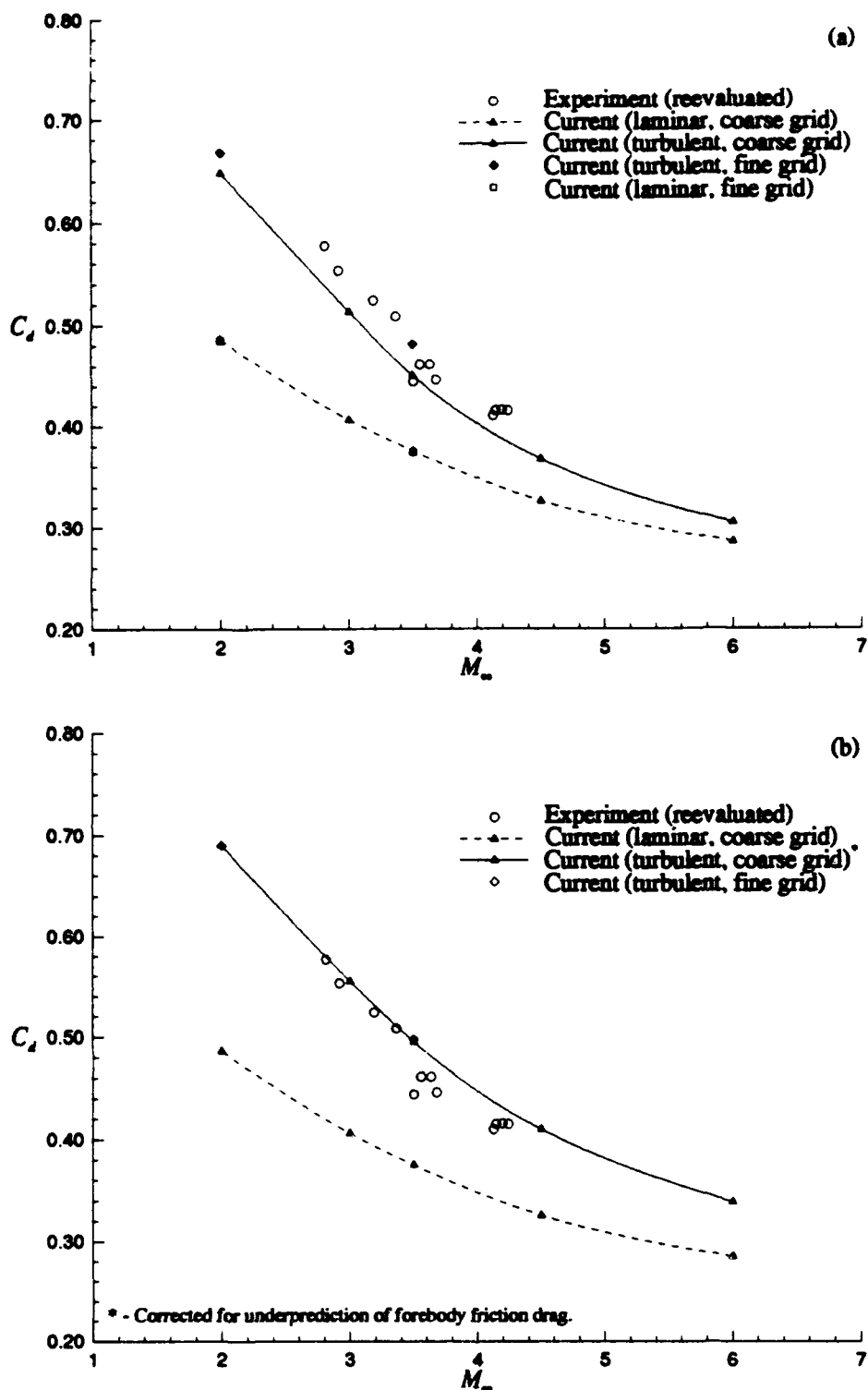
Figure 32. Comparison of the total-drag coefficient, C_d, between computation and experiment for the sharp-nosetip, clipped-delta-fin, HART missile ($\alpha = 0°$): (a) fin friction drag not accounted for, (b) flat-plate model of fin friction drag

74
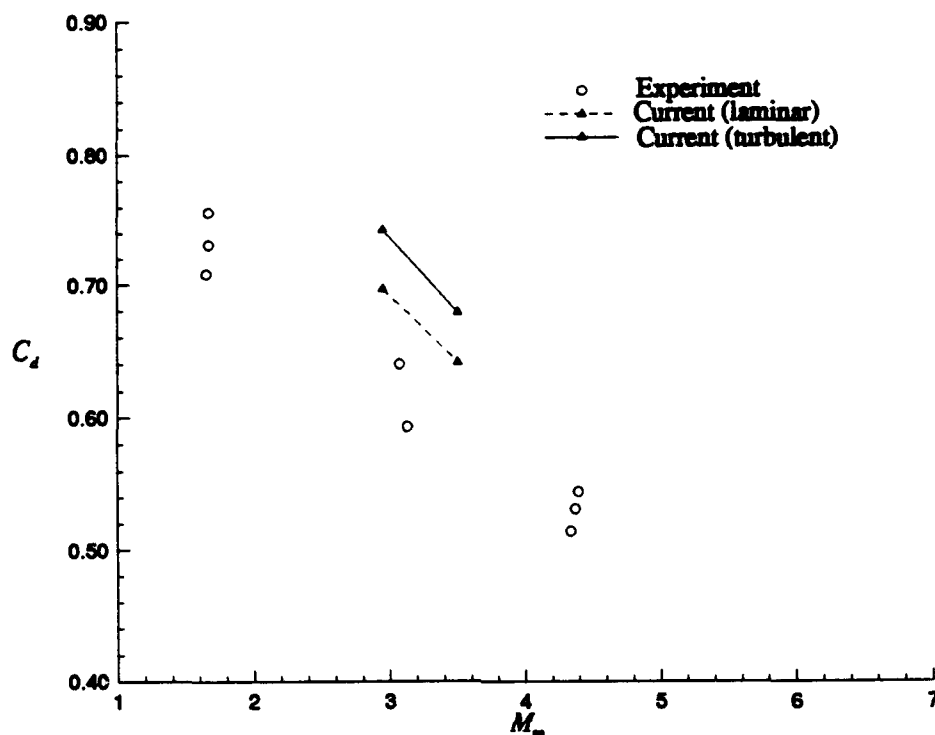
Figure 33. Comparison of the total-drag coefficient, C_d, between computation and experiment for the blunt-nosetip, clipped-delta-fin, HART missile ($\alpha = 0°$)

Table 11. Pitching-moment coefficient, C_{m_α}, from free-flight tests of the grooved, sharp-nosetip model with clipped-delta fins

Free-flight No. (yymm##)	M_∞	C_{m_α}
930710	2.958	-33.567
930707	3.260	-26.513
930708	3.357	-27.794
930705	3.767	-24.226
930709	3.777	-24.178
930706	3.838	-21.910

Table 12. Pitching-moment coefficient, C_{m_α}, from ZEUS and EAGLE results for sharp-nosetip model with delta fins

M_∞	ZEUS	EAGLE
1.2	-	-100.05
1.5	-	-89.26
2.5	-	-59.37
3.0	-43.0	-47.02
3.5	-32.0	-
4.0	-23.0	-25.41
4.5	-17.0	-17.37
5.0	-14.0	-12.06
6.0	-12.7	-4.69
7.0	-12.0	0.02
8.0	-	2.42
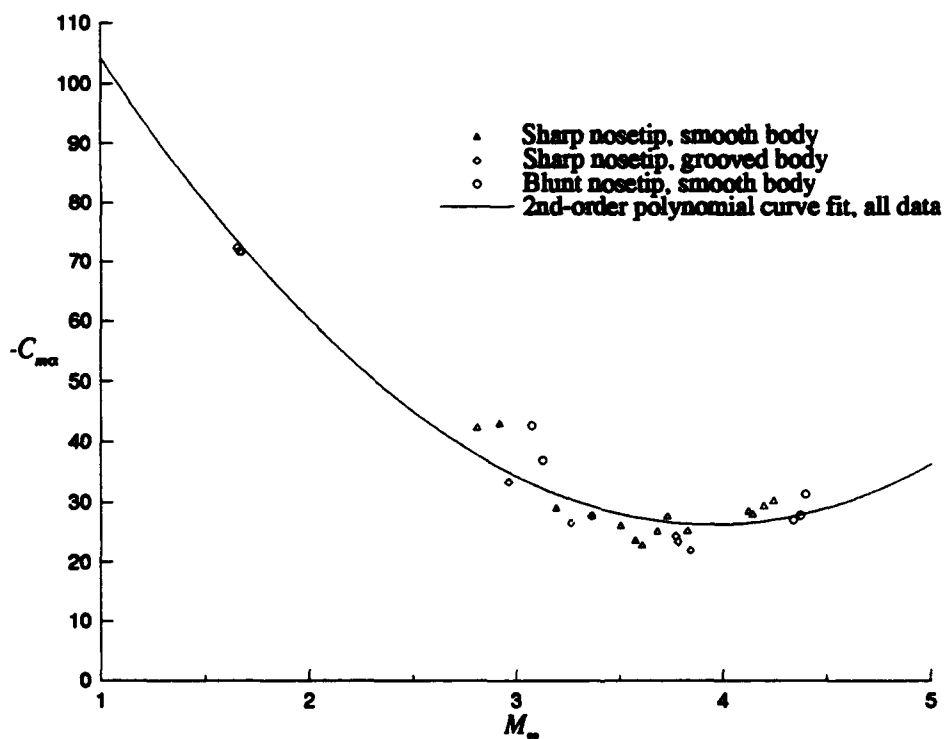
Figure 34. Pitching-moment coefficient, C_{m_α}, for HART missile showing restabilization trend at higher Mach numbers

4.5.1 Experimental Model Uncertainty. Based on shadowgraph photography from the free-flight tests, the author proposes that model inconsistencies might be the cause of the apparent restabilization. Several shadowgraphs appear to show different size fins on identical missile bodies [93]. The documented size is depicted in Figure 36. This size provides a surface area equal to the delta fin on the baseline model [93]. Also, this is the fin size used in the post-processing of the time, position, and orientation data to extract the aerodynamic coefficients [37].

Free-flight tests in the ARF (see Section 1.1.1 for a description) are destructive, therefore, obtaining verification of model anomalies is difficult. Three key pieces of documentation are available, however. These are the model construction log, the test range log, and still photographs of the models taken prior to launch. The photographs are digitized for inclusion in this thesis (Figure 37 and Figure 38). Figure 37 shows a model with a clipped-delta fin that agrees with the documented fin size and fin location. Conversely, Figure 38 shows that models were constructed with larger fins. It is impossible to associate specific models with specific data points.

During the 1989-1990 time frame, 45 individual free-flight tests were performed (sharp-nosetip model), including the clipped-delta-fin models discussed throughout this document, and several inverted-delta-fin models. The construction of the models for these tests was not done at one time. The construction log from the Eglin AFB model shop indicates that 30 models were fabricated in May 1988 and 15 models were fabricated in February 1990. The pitching-moment coefficient for all 45 tests is summarized by Figure 39. Due to model failure, and poor trajectory fits, only 28 data points are shown.

The purpose of Figure 39 is to propose a relation between when a model was constructed and at what Mach number it was fired. In Figure 39, a line is used to distinguish the highest Mach number tests. The records regarding the date and Mach number for individual tests show that 15 models were fired between 29 March 1990 and 17 April 1990. More importantly, these 15 models correspond to the 15 highest Mach numbers (due to model failures Figure 39 shows only 12 data points above Mach 3.88). While it is not possible to associate specific models with specific tests, the construction and test logs indicate that the 15 models for the tests above Mach 3.88 were fabricated later than the models for the 30 other tests.

The author suggests that the higher Mach number tests were flown with models that had larger fins. To further confirm this possibility, three numerical experiments
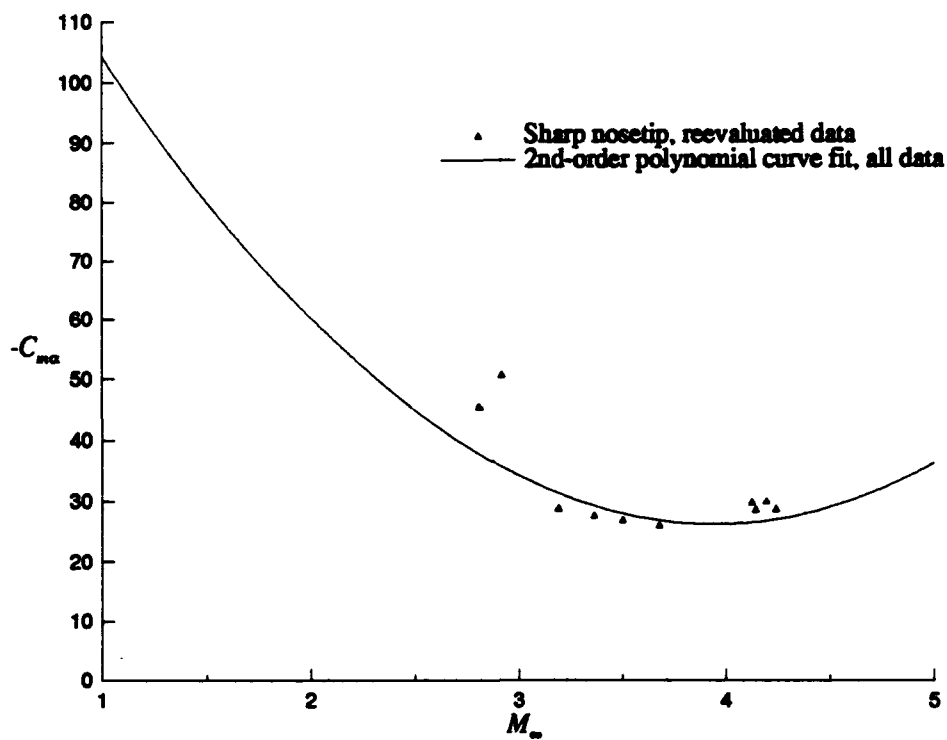
Figure 35. Pitching-moment coefficient, C_{m_α}, for HART missile from reevaluated free-flight data
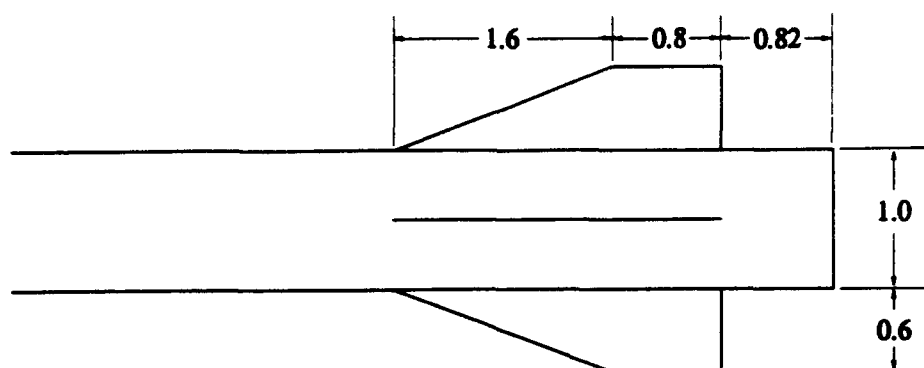
Figure 36. Documented fin size and position of clipped-delta fin (normalized by the body diameter)

are conducted with a larger fin. The size and position of this *large fin* are determined solely from the photograph shown in Figure 38: the larger fin's root cord is $3.2D$, the tip cord is $1.6D$, and the distance from the missile base is unchanged. Large-fin computations are made for $M_\infty = 2$, $M_\infty = 3.5$, and $M_\infty = 4.5$. These are designated Cases SB9, S35, and S36, respectively. The pitching-moment coefficient from computations with the original fin size (Cases S28–S32) are compared to Cases SB9, S35, and S36 in Figure 40; the results for the original fin size will be discussed at length in Sections 4.5.2-4.5.4. Spline curves are fit through the computed data in Figure 40. The small-fin data correlates best with the free-flight data below Mach 3.9 and the large-fin data correlates best with the data above Mach 3.9. Although it is not possible to link the photograph of the larger fin to specific tests, the information available suggests that the restabilization trend is the result of a model discrepancy and not aerodynamics.

The stability analysis is now continued to determine the stability characteristics at Mach numbers exceeding 4.5. Throughout the remaining analysis of static stability for the HART missile, experimental data for any sharp-nosetip test that exceeded $M_\infty = 3.9$ is treated as unreliable. The models for the blunt-nosetip tests were constructed in February 1991, and the fins for those models are believed to be correct. Therefore, all data from blunt-nosetip experiments are used for comparison.

Results from all thin-fin calculations are summarized in Tables 13-16. In Table 13, C_{m_α} is tabulated for the sharp-nosetip computations for $M_\infty = 2$ to $M_\infty = 6$ under inviscid, laminar, and turbulent conditions. Similarly, in Table 14, C_{m_α} is tabulated for the blunt-nosetip computations for $M_\infty = 2$ to $M_\infty = 6$ under inviscid, laminar, and turbulent conditions. The normal-force coefficient and the center of

79
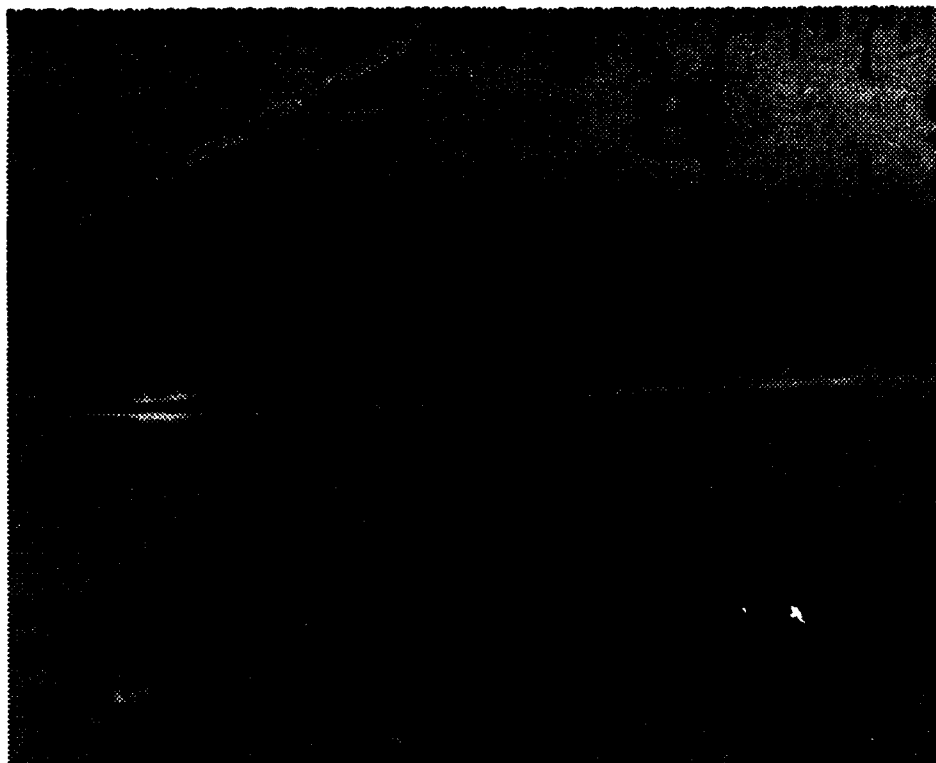
Figure 37.   A model that was constructed in agreement with the documented fin size and position

Figure 38. A model that was constructed with a larger fin

80
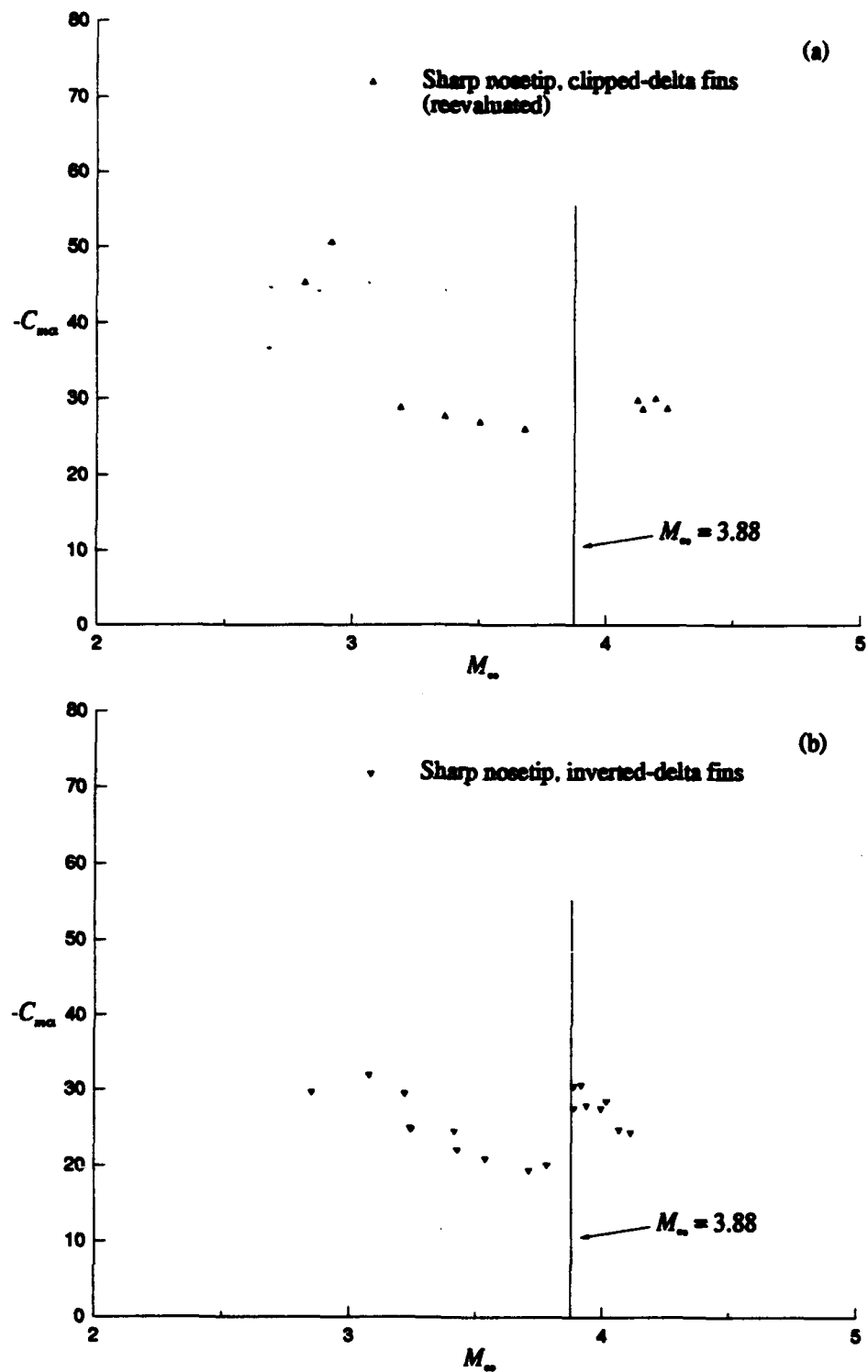
Figure 39. Experimental pitching-moment coefficient, C_{m_α}: (a) clipped-delta-fin models, (b) inverted-delta-fin models

81

pressure are tabulated in Tables 15 and 16 for the sharp-nosetip and blunt-nosetip computations, respectively. The data in these tables are also for $M_\infty = 2$ to $M_\infty = 6$. Before boundary-layer effects (laminar and turbulent) are discussed, the primary pitching characteristics are determined from the inviscid data in Tables 15 and 16.

4.5.2 Inviscid Results. The inviscid pitching-moment results are primarily compared with EAGLE results and the theory provided by (9) and (10). Comparisons are also made to the experimental data to confirm the trends of C_{m_α} with M_∞ at lower Mach numbers. The coefficients in (10) are recalculated for a center of gravity located at 43.5% of length to establish consistency with the experimental clipped-delta-fin model. The locations of the centroid for the fins and the center of gravity for the clipped-delta-fin model differ slightly from the baseline model, and are discussed in Section 4.5.6. Equation (9) is shown with the EAGLE results, the experimental data, and the current inviscid results (Cases S1–S10) in Figure 41a for the sharp-nosetip model. The experimental data in Figure 41b are from the blunt-nosetip tests and the reevaluated sharp-nosetip tests. Sharp-nosetip experimental data above Mach 3.9 is not shown in either figure based on the possible experimental model variations noted in Section 4.5.1.

Several levels of agreement exist in Figures 41a and b. First, each set of data indicate the decreasing trend in static stability with increasing Mach number, predicted by inviscid, linear theory. Second, the qualitative relation between C_{m_α} and M_∞ that is exhibited by the experimental data (for $M_\infty < 3.9$) is equally well predicted by the current computations and previous EAGLE solver computations. Third, below $M_\infty = 4$, the magnitude of C_{m_α} from Cases S1–S10 agrees reasonably well with the EAGLE results.

The interesting disagreements in Figures 41a and b exist above Mach 4. In contrast to the EAGLE results, the current results show a much gentler decrease in the stability margin as Mach number increases beyond 4. The author believes the difference is related to the azimuthal clustering of nodes in the present study versus coarse unclustered nodes in the EAGLE study. Although free-flight data is apparently unreliable for $M_\infty > 3.88$, it also appears to exhibit a more modest decline in C_{m_α}. The difference between the values predicted by the EAGLE solver and those predicted by the current solver are very important. Neutral stability is

82
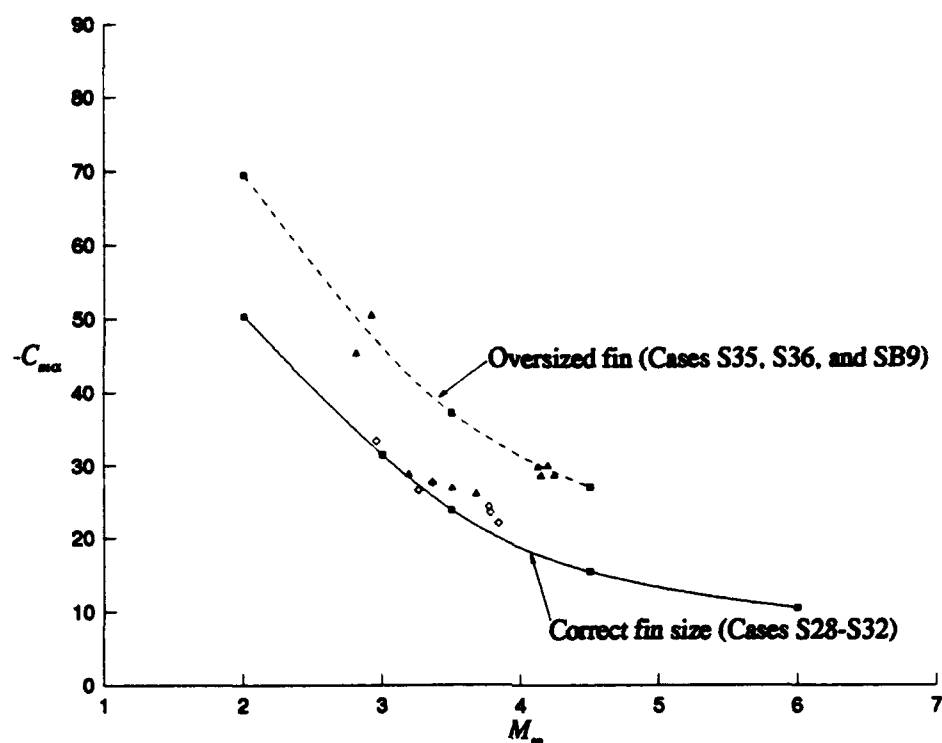
Figure 40. Pitching-moment coefficients from the correct fin and the larger fin

Table 13. Pitching-moment coefficient, C_{m_α}, from current computations for sharp-nosetip model with clipped-delta fins (Cases S1–S34)

M_∞	Inviscid	Laminar	Turbulent
2.0	-58.53	-57.36	-50.37
3.0	-34.79	-33.60	-31.46
3.5	-27.64	-27.93	-23.73
4.5	-17.26	-19.20	-15.34
6.0	-11.50	-14.72	-10.44

Table 14. Pitching-moment coefficient, C_{m_α}, from current computations for blunt-nosetip model with clipped-delta fins (Cases B1–B31)

M_∞	Inviscid	Laminar	Turbulent
2.0	-66.00	-64.89	-58.64
2.95	-43.32	-42.73	-38.63
3.5	-35.00	-34.59	-30.79
4.0	-29.69	-30.83	-27.06
4.5	-27.14	-28.34	-24.51
5.0	-24.89	-26.03	-22.17
6.0	-21.46	-23.96	-20.54

83

Table 15. Normal-force coefficient, C_{n_α}, and center of pressure, x_{cp}, from current computations for sharp-nosetip model with clipped-delta fins

M_∞	Laminar C_{n_α}	Laminar x_{cp}/L	Turbulent C_{n_α}	Turbulent x_{cp}/L
2.0	12.89	0.621	11.92	0.611
3.0	10.88	0.564	10.15	0.564
3.5	10.23	0.549	9.56	0.538
4.5	9.50	0.519	8.81	0.508
6.0	8.84	0.504	8.09	0.489

Table 16. Normal-force coefficient, C_{n_α}, and center of pressure, x_{cp}, from current computations for blunt-nosetip model with clipped-delta fins

M_∞	Laminar C_{n_α}	Laminar x_{cp}/L	Turbulent C_{n_α}	Turbulent x_{cp}/L
2.0	13.08	0.642	12.50	0.631
3.5	9.83	0.582	9.05	0.577
5.0	8.03	0.570	7.62	0.556
6.0	7.48	0.569	7.01	0.557
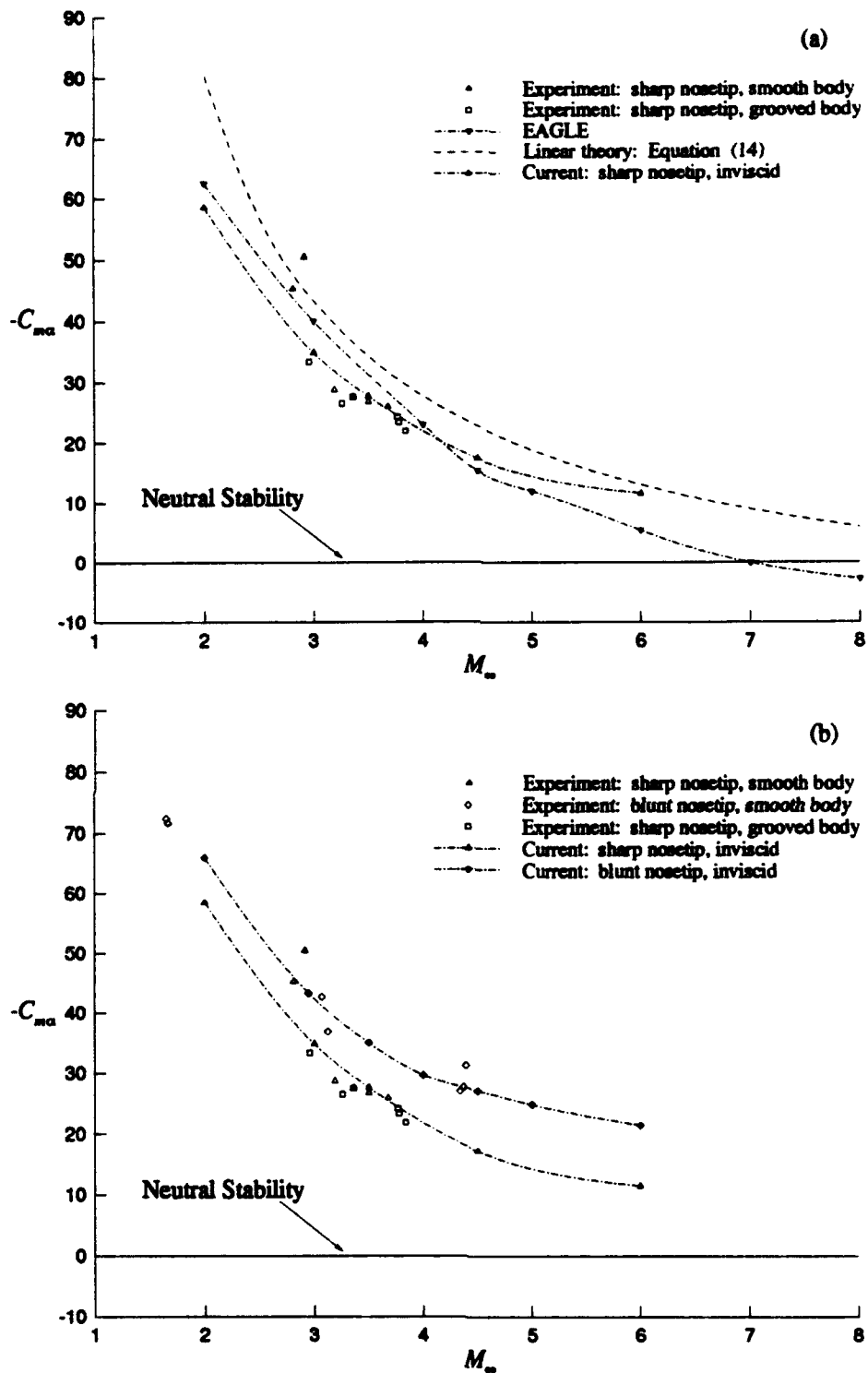
Figure 41. Pitching-moment coefficient, C_{m_α}, for clipped-delta-fin model: inviscid results: (a) sharp-nosetip computations versus theory, experiment, and EAGLE results, (b) sharp-nosetip and blunt-nosetip computations versus experiment
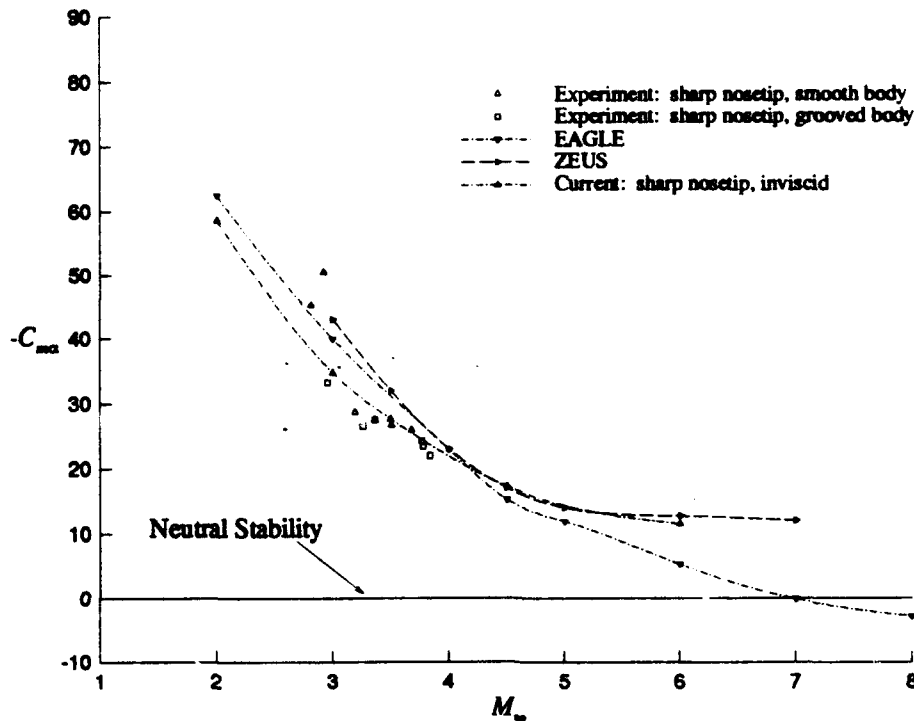
Figure 42. Comparison of pitching-moment coefficient, C_{m_α}, from three inviscid solvers

reached at $M_\infty = 7$ with EAGLE, but beyond $M_\infty = 7$ with extrapolation of the current sharp-nosetip results, and beyond that with the blunt-nosetip results.

The blunt-nosetip results differ from the sharp-nosetip results, at higher Mach numbers, due to a shift in the center of pressure on the missile body. This is directly related to the nosetip geometries, and persists for the laminar and turbulent calculations, as shown in Sections 4.5.3-4.5.4. In Figure 41b, at $M_\infty = 2$, C_{m_α} for the blunt-nosetip model is 13 % more negative than the sharp-nosetip model. At $M_\infty = 6$, C_{m_α} for the blunt model is twice that for the sharp model.

In Figure 42, the C_{m_α}-M_∞ trends for all inviscid computations (prior and present) on the sharp-nosetip model are compared. The experimental data are included for reference. The ZEUS results from the baseline delta-fin configuration are included to provide useful qualitative information at higher Mach numbers. All three sets of computational data predict similar trends in C_{m_α} with M_∞ below Mach 4. Above Mach 4, the present computations depict a trend with Mach number that is between the EAGLE trend and the ZEUS trend. Again, the difference is believed to be related to azimuthal clustering near the fin surfaces.

86

The cross-plane velocity components are shown in Figure 43 for inviscid flow at $M_\infty = 2$ and $\alpha = 5°$ (Case S6). Streamlines created from the cross-plane velocities are also shown in Figure 43. The shape of the streamline which begins on the windside of the missile near the symmetry plane ($y = -1.25$, $z = 0$), shows that the cross flow is not significantly displaced from the missile surface (expect for the region above the leeside fin). In addition, the velocity vectors show that the crossflow is small, and the expansion and compression on each fin are distinctly separated.

4.5.3 Laminar Results. The effects of viscosity are initially assessed for laminar boundary-layer conditions. Most experiments indicated that the boundary layer had become turbulent upstream of the fins, but the impact of turbulence is best determined after laminar results are documented. Again, the sharp-nosetip and blunt-nosetip pitching-moment coefficients from the present study are plotted versus Mach number with the experimental data (Figure 44). The inviscid results that were previously discussed are included for reference. Interestingly, the laminar and inviscid results agree at low Mach numbers, and begin to diverge at about $M_\infty = 3.5$. At the higher Mach numbers, the boundary layer appears to improve C_{m_α} (i.e., C_{m_α} is more negative). The impact of the boundary layer is approximately the same for the sharp and blunt models.

The agreement at low Mach number is also evidenced by the fins' surface pressures. In Figure 45, the pressure contours are shown on the fin surfaces for laminar flow, $\alpha = 5°$, and $M_\infty = 2$. The pressure contours in Figure 45 are very similar to those for inviscid flow (Figures 22 and 23).

The pressure contours in the cross plane (y–z plane) for $\alpha = 5°$, $M_\infty = 2$ to $M_\infty = 6$, and laminar flow (Cases S16–S20) are compared to those for inviscid flow (Cases S6–S10) in Figures 46-55, These cross-plane contour plots are for $\frac{z}{D} = 21.8$. This is a point near the middle of the fins.

As M_∞ increases, the pressure gradient near the fin surfaces increases. This is evidenced by the *piling up* of pressure contours on the bottom of the leeward fin. It also shows that a refined grid is needed in this area (clustering near fin surfaces is employed in all computations in this study).

The cross-plane pressure contours in Figures 46-55, also indicate that the laminar flow structure is similar to the inviscid structure below Mach 3.5. At higher Mach numbers, however, the boundary layer has influenced the pressure distribution

Figure 43. Cross-plane velocity components, Case S6 ($M_\infty = 2$, $\alpha = 5°$)
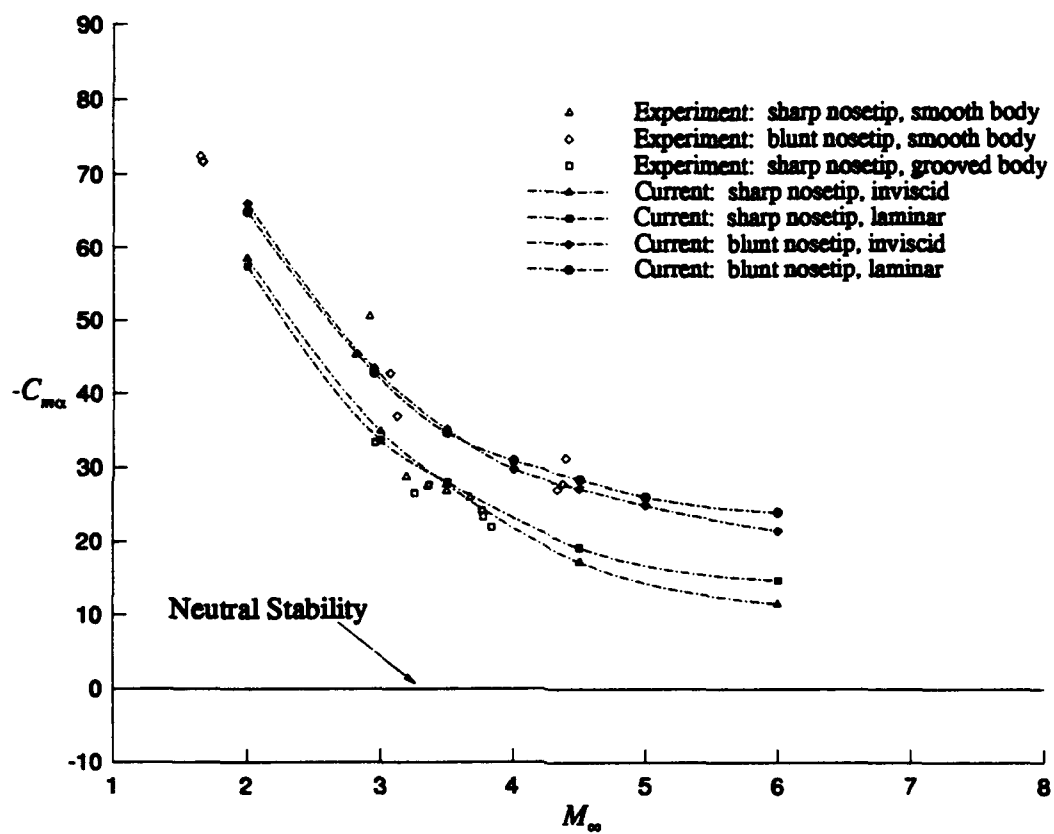
Figure 44. Pitching-moment coefficient, C_{m_α}, for clipped-delta-fin model: laminar results

89
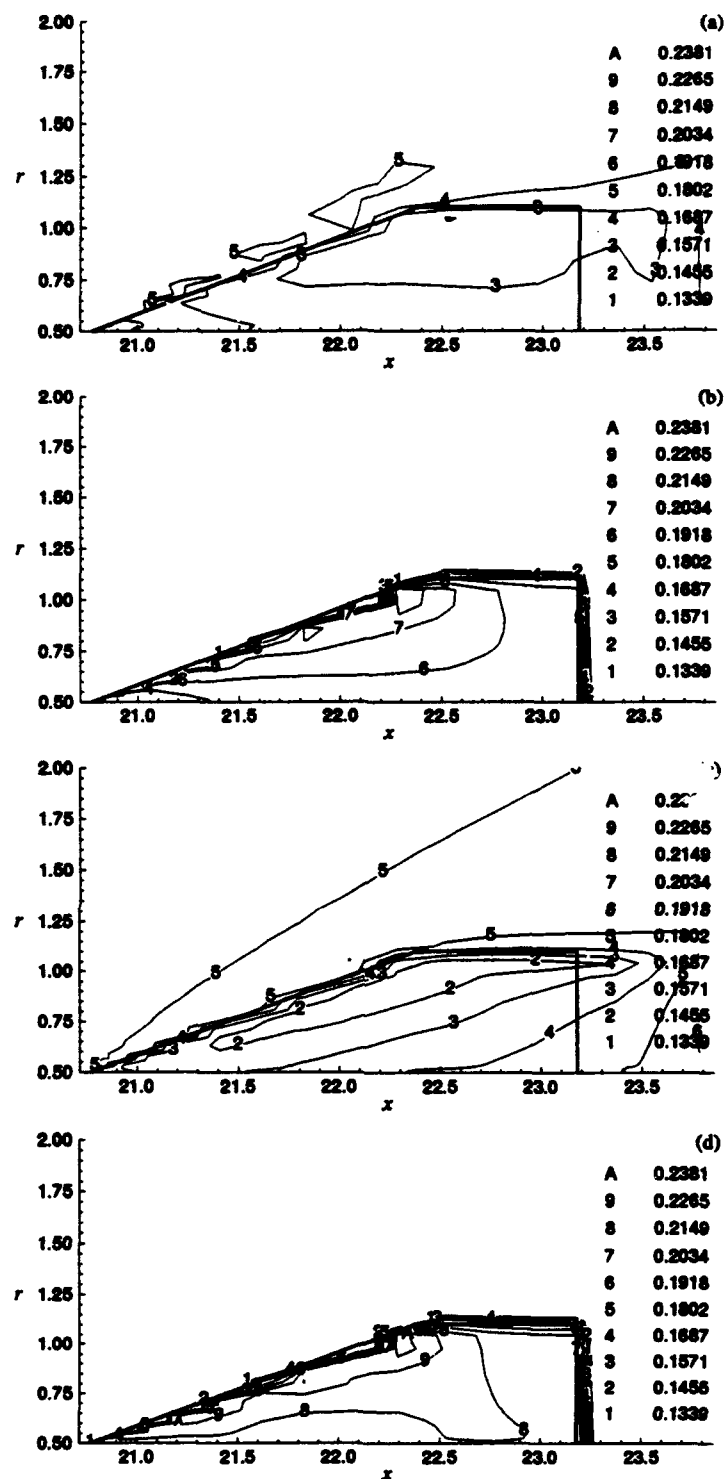
Figure 45. Pressure contours on the fin surfaces for Case S16 ($M_\infty = 2$, $\alpha = 5°$): (a) upper surface of the fin on the expansion side of the missile, (b) lower surface of the fin on the expansion side of the missile, (c) upper surface of the fin on the compression side of the missile, (d) lower surface of the fin on the compression side of the missile

90
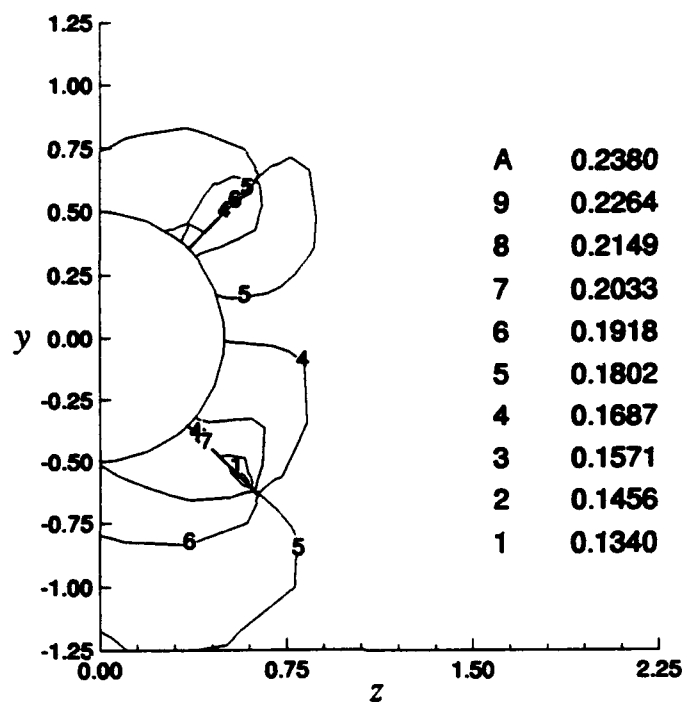
Figure 46. Pressure contours, Case S6 ($M_\infty = 2$, $\alpha = 5°$, inviscid)
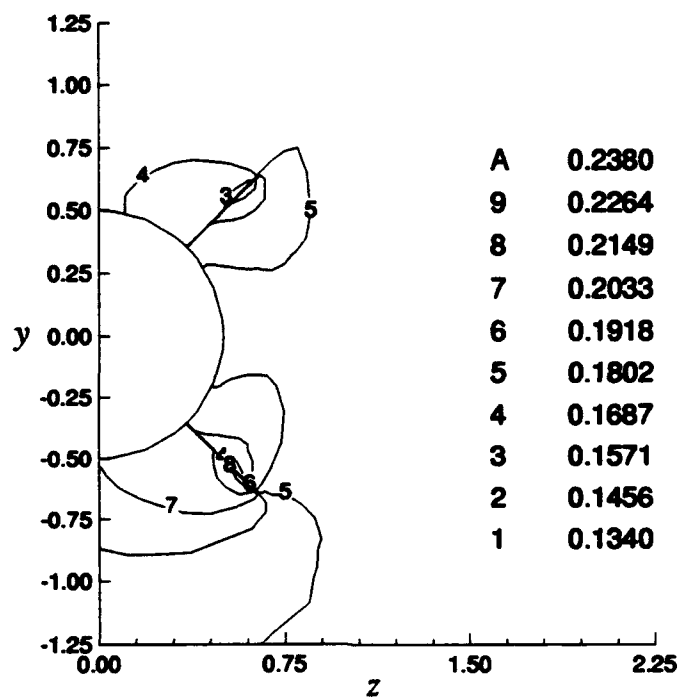
Figure 47. Pressure contours, Case S16 ($M_\infty = 2$, $\alpha = 5°$, laminar)

91
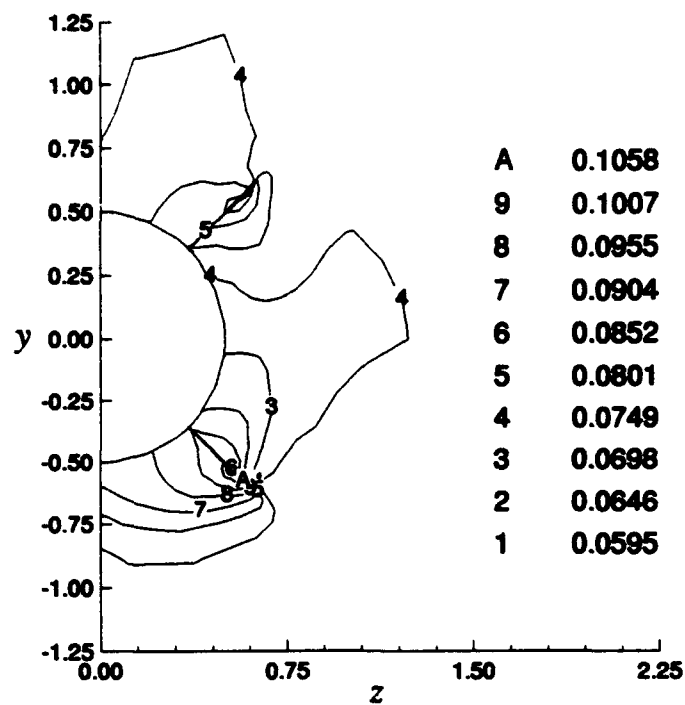
Figure 48. Pressure contours, Case S29 ($M_\infty = 3$, $\alpha = 5°$, inviscid)
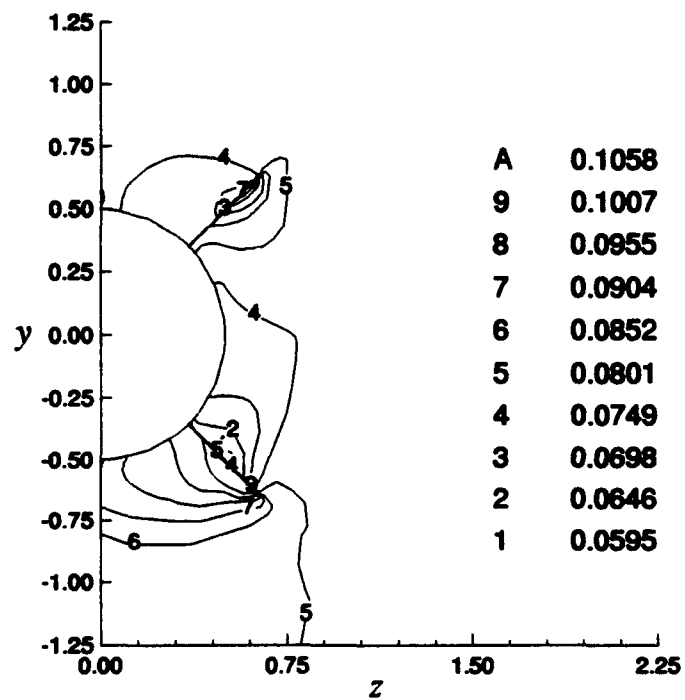
Figure 49. Pressure contours, Case S17 ($M_\infty = 3$, $\alpha = 5°$, laminar)

92
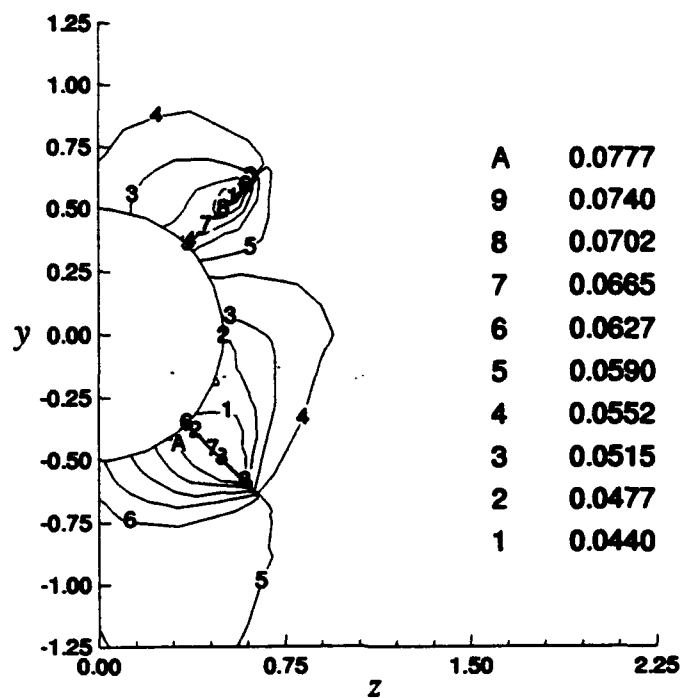
Figure 50. Pressure contours, Case S30 ($M_\infty = 3.5$, $\alpha = 5°$, inviscid)
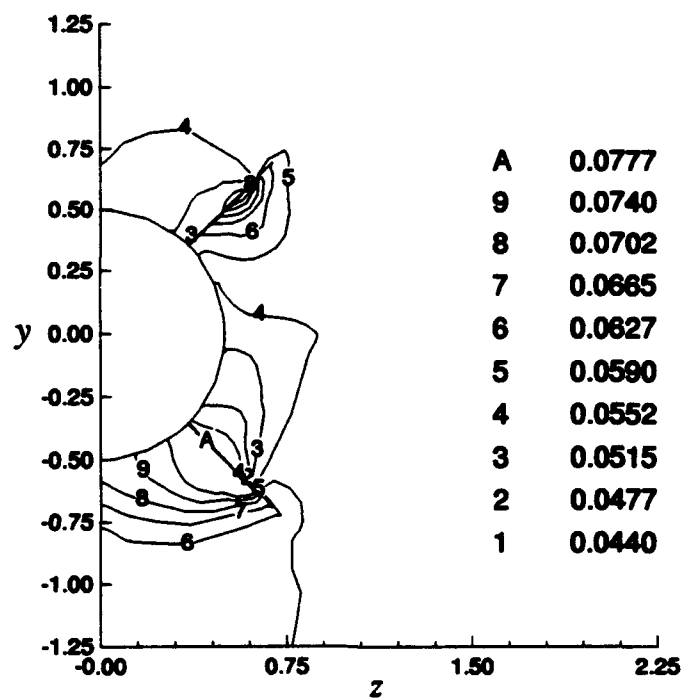
Figure 51. Pressure contours, Case S18 ($M_\infty = 3.5$, $\alpha = 5°$, laminar)

93

Figure 52. Pressure contours, Case S31 ($M_\infty = 4.5$, $\alpha = 5°$, inviscid)

A	0.0470
9	0.0447
8	0.0424
7	0.0402
6	0.0379
5	0.0356
4	0.0333
3	0.0311
2	0.0288
1	0.0265

Figure 53. Pressure contours, Case S19 ($M_\infty = 4.5$, $\alpha = 5°$, laminar)

A	0.0470
9	0.0447
8	0.0424
7	0.0402
6	0.0379
5	0.0356
4	0.0333
3	0.0311
2	0.0288
1	0.0265
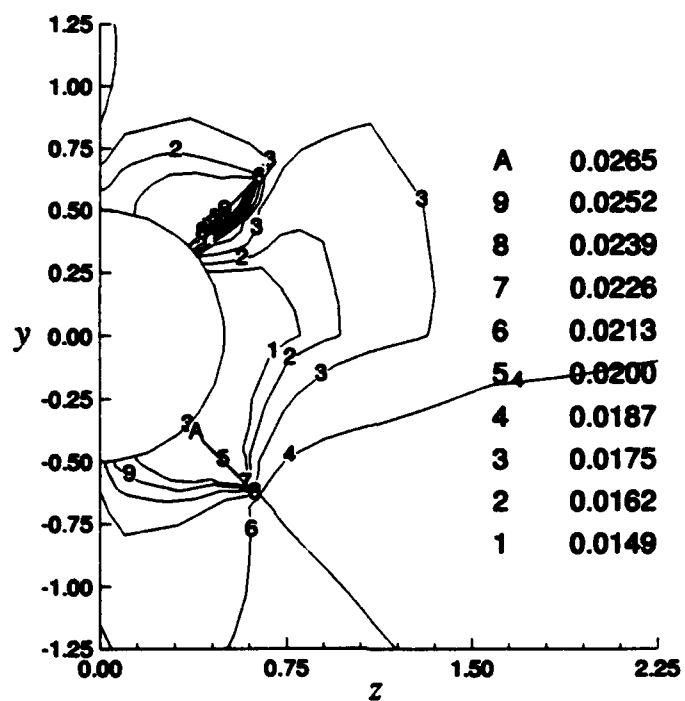
Figure 54. Pressure contours, Case S10 ($M_\infty = 6$, $\alpha = 5°$, inviscid)
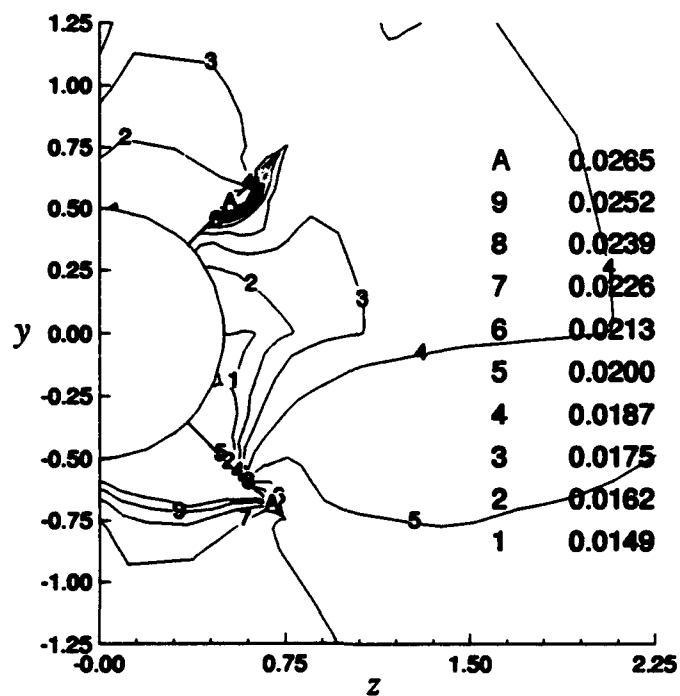
Figure 55. Pressure contours, Case S20 ($M_\infty = 6$, $\alpha = 5°$, laminar)

slightly. The higher pressure values on the compression sides of the fins for $M_\infty = 6$ can be seen in Figure 55 versus Figure 54. Thus, the pitching-moment coefficient decreases less with increased Mach number owing to the presence of viscosity.

Figure 56 shows the cross-plane velocity components for laminar flow at $M_\infty = 2$ and $\alpha = 5°$ (Case S16). The cross-plane velocity components show that crossflow is small for laminar flow also. Streamlines are again created from the cross-plane velocities, and shown in Figure 56. These streamlines are slightly more displaced than those for inviscid flow.

4.5.4 Turbulent Results. The influence of turbulence is now addressed. The sharp-nosetip and blunt-nosetip turbulent results are plotted with the laminar results in Figures 57a and 57b, respectively. The position of the transition point does not seem to have a large impact on C_{m_α}, since sharp-nosetip results (Figure 57a) and blunt-nosetip results (Figure 57b) show similar decreases in C_{m_α} from the laminar results. Recall that the sharp-nosetip models and the blunt-nosetip models have different transition points (Section 3.4). Also, the same modest trend with Mach number is seen for both nosetips at higher Mach number. The pitching-moment coefficient for turbulent flow increases measurably over that for laminar flow. The lower static stability (C_{m_α} less negative) for the turbulent computations is due to the compression *bleeding* around the leading edge of the windside fin, and affecting the pressure on the expansion side of the fin.

The cause of this phenomenon is seen in the streamlines of the cross-plane velocity components (Figure 58). The streamlines are significantly displaced from the missile body between the windside fin and the symmetry plane. This indicates that the turbulence plays a significant role in the region where the cross flow is blocked.

The *bleeding* effect for turbulent flow is also seen in the cross-plane pressure contours. The cross-plane pressure contours for turbulent flow, $\alpha = 5°$, and $M_\infty = 2$ (Cases S28) are compared to those from laminar flow in Figures 59 and 60. The bleeding of higher pressure air around the fin leading edges is visible in the turbulent case.

Figure 61 compares the turbulent pitching-moment results for both nosetips. The experimental values are added for comparison. Agreement between the computed and experimental values of C_{m_α} is within about 10%. The blunt-nosetip re-
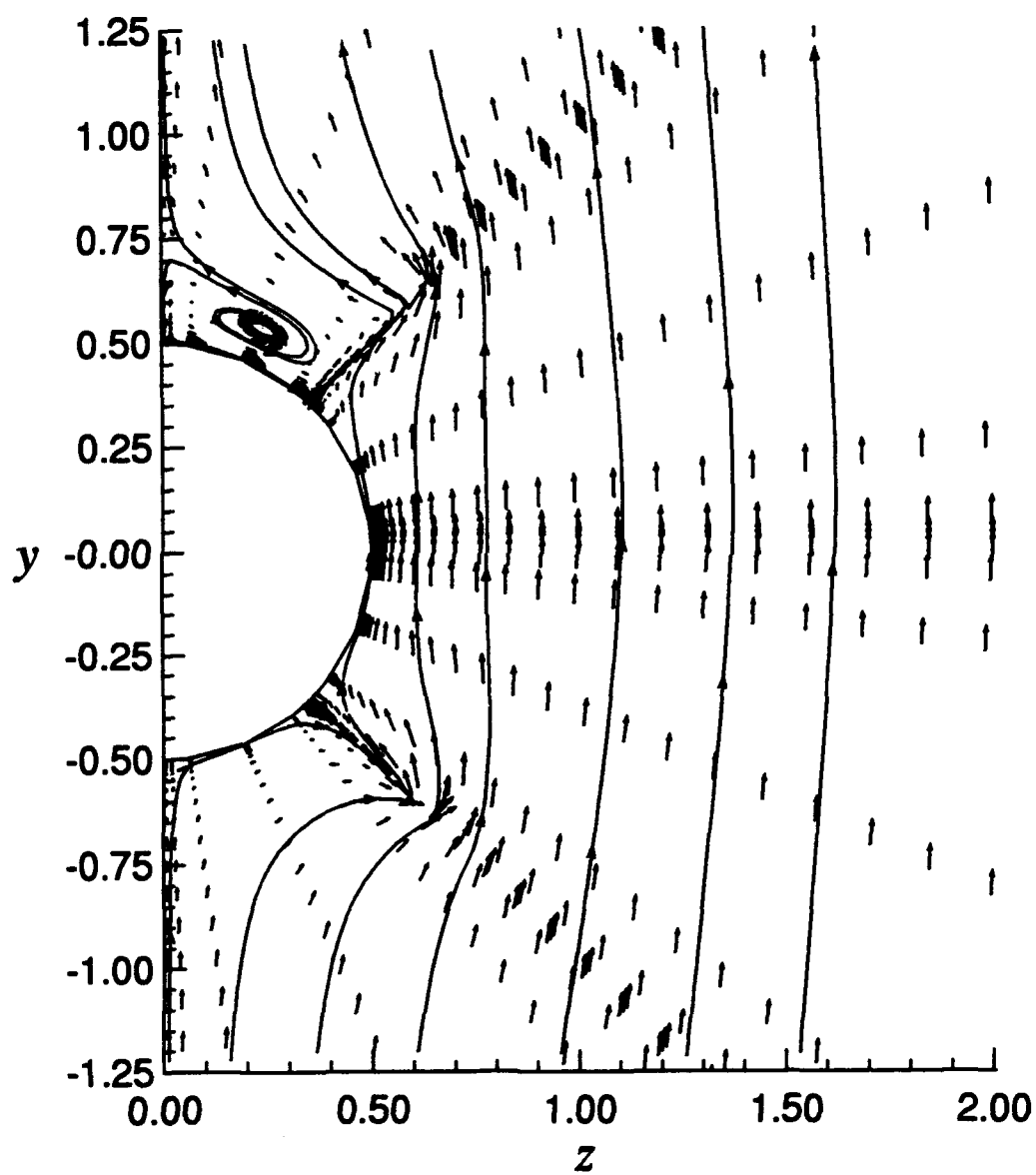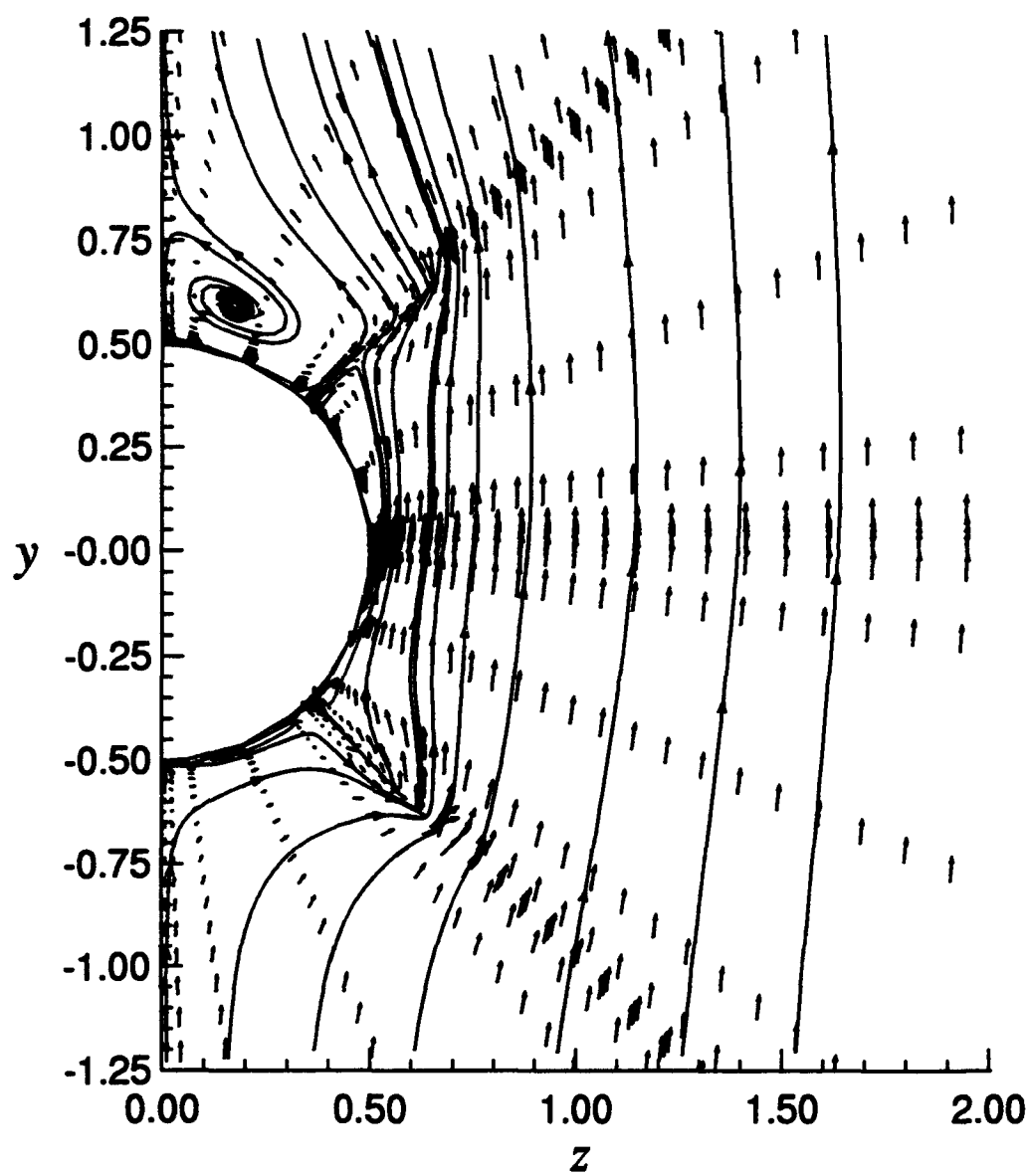
Figure 56. Cross-plane velocity components, Case S16 ($M_\infty = 2$, $\alpha = 5°$)
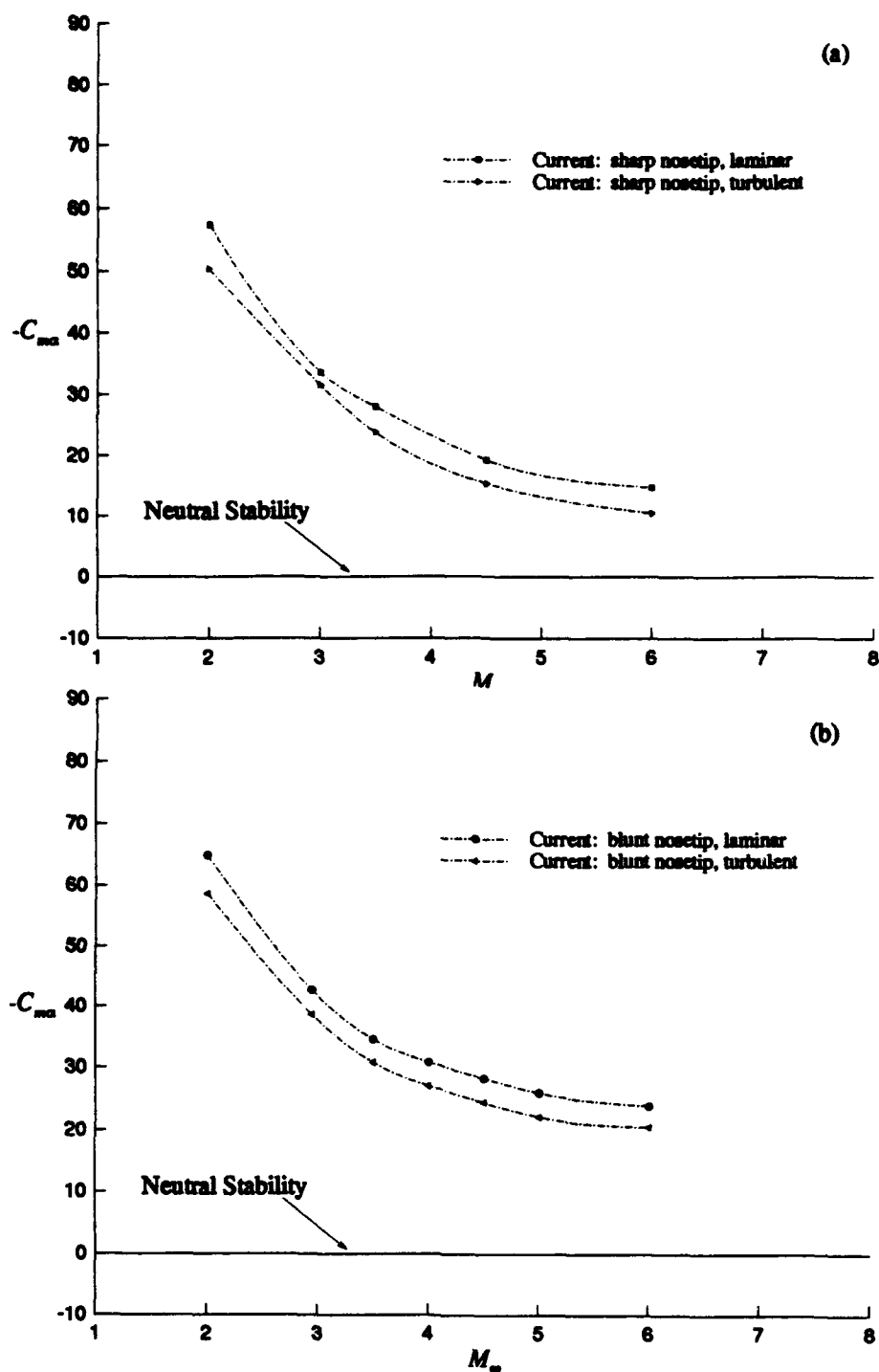
Figure 57. Pitching-moment coefficient, C_{m_α}, for clipped-delta-fin model, turbulent
results versus laminar results: (a) sharp nosetip, (b) blunt nosetip
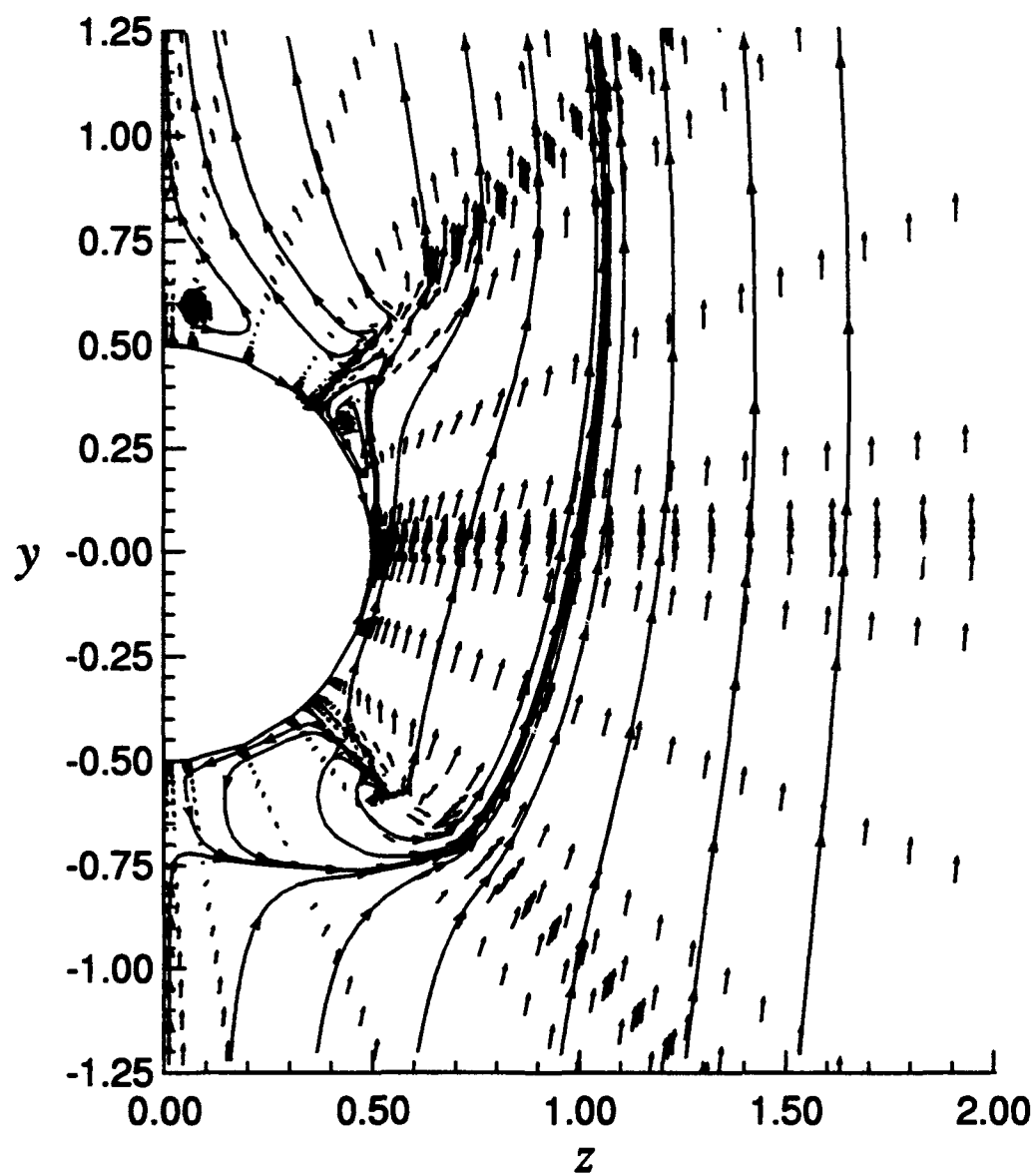
Figure 58. Cross-plane velocity components, Case S28 ($M_\infty = 2$, $\alpha = 5°$)
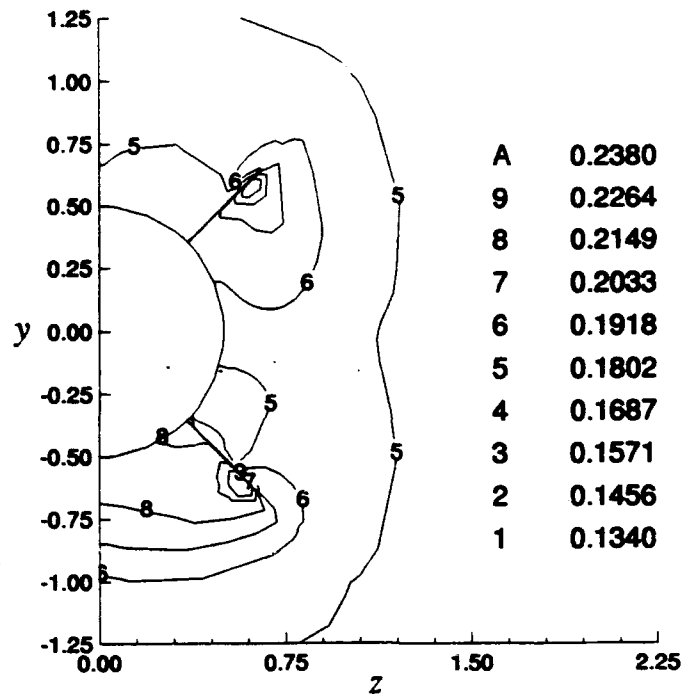
Figure 59. Pressure contours, Case S28 ($M_\infty = 2$, $\alpha = 5°$, turbulent)
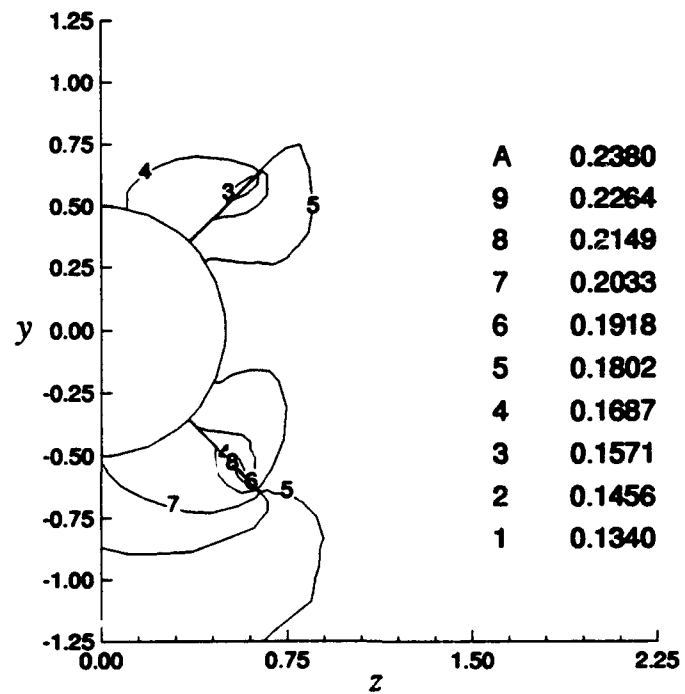
Figure 60. Pressure contours, Case S16 ($M_\infty = 2$, $\alpha = 5°$, laminar)

100

sults provide further clarification to the suspected restabilization phenomenon. The present computations indicate that the stability of the blunted model is superior; the blunt-data curve has more negative C_{m_α} values than the sharp-data curve. A more favorable pressure distribution on the missile body causes a small shift in the center of pressure, and thus better stability. The correlation of the blunt-nosetip experimental pitching-moment coefficients with the erroneous sharp-nosetip pitching-moment coefficients was purely coincidental.

4.5.5 Influence of Base Flow. The effects of the base flow on pitching moment are examined next. Four computations are performed to assess the impact of the base region on the pitching-moment coefficient. These computations are made for $\alpha = 5°$ and $M_\infty = 2$ to $M_\infty = 6$ (Cases SB5–SB8). Throughout the range of Mach numbers tested, the base flow did not appreciably affect the pitching-moment coefficient (Table 13). The variation of pressure across the missile base is mild (Figure 62), thus producing almost no contribution to the pitching moment.

4.5.6 Comparison Between the Clipped-delta-fin Configuration and the Baseline Configuration. First, differences between the two configurations are discussed. The aerodynamic coefficients (drag and pitching moment) are then contrasted to determine the impact of changing the planform of the fins.

4.5.6.1 Change in Center-of-gravity and Fin Position. In order to compare the results for the clipped-delta-fin model to the baseline model, which has delta fins, similarities and differences in the models must be taken into account. Both models had identical tangent-ogive noses with smooth cylindrical bodies, and equivalent fin surface areas. Two differences that do exist, however, are the center-of-gravity locations and the fin-leading-edge locations. The delta-fin model has a center of gravity at 43% of length, while the clipped-delta-fin model has a center of gravity at 43.5% of length. Although this may not seem very dramatic, it does affect the pitching-moment coefficient measurably. In addition to a slightly different center of gravity, the locations of the fin leading edges differed. Figure 63 shows both fins and their positions on the missile body. The different leading-edge locations will also affect the pitching-moment coefficient.

4.5.6.2 Aerodynamic Comparison. Given the differences stated above, characteristics for the clipped-delta-fin model are contrasted with the traits of the
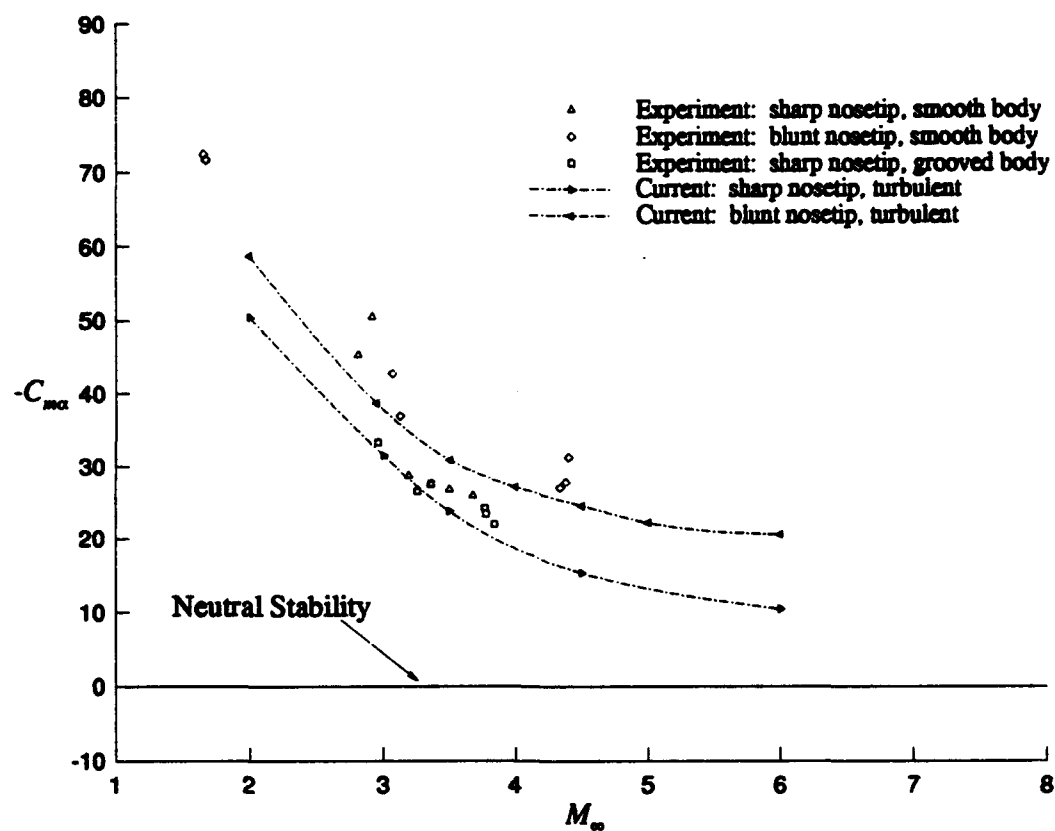
Figure 61. Pitching-moment coefficient, C_{m_α}, for clipped-delta-fin model: turbulent results versus experiment

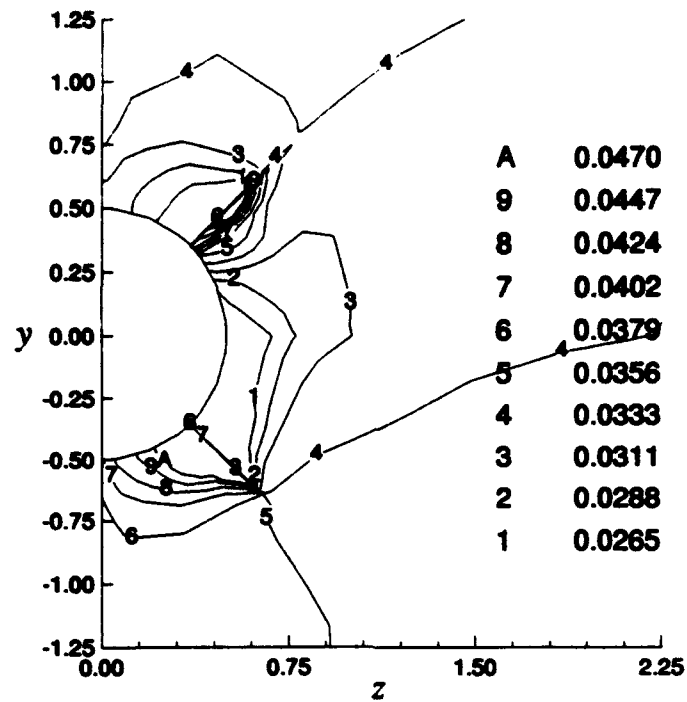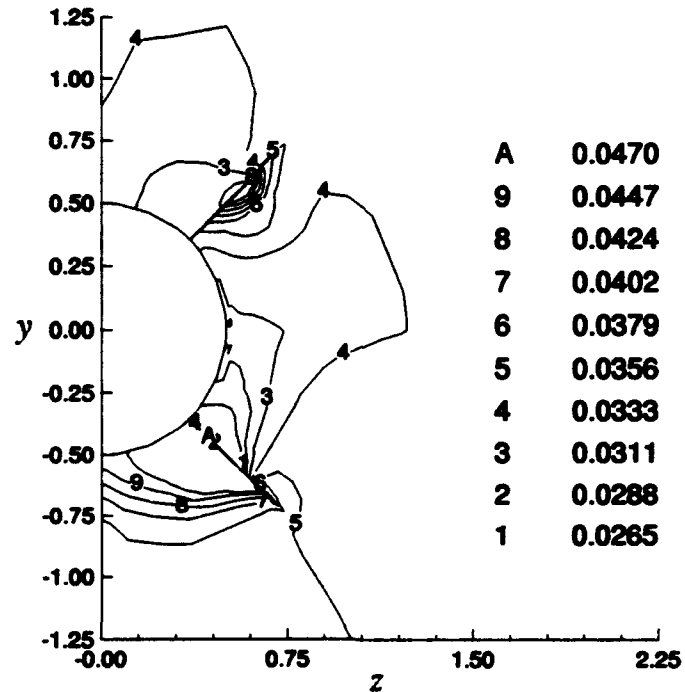| A	0.0300
9	0.0286
8	0.0271
7	0.0257
6	0.0242
5	0.0228
4	0.0213
3	0.0199
2	0.0184
1	0.0170
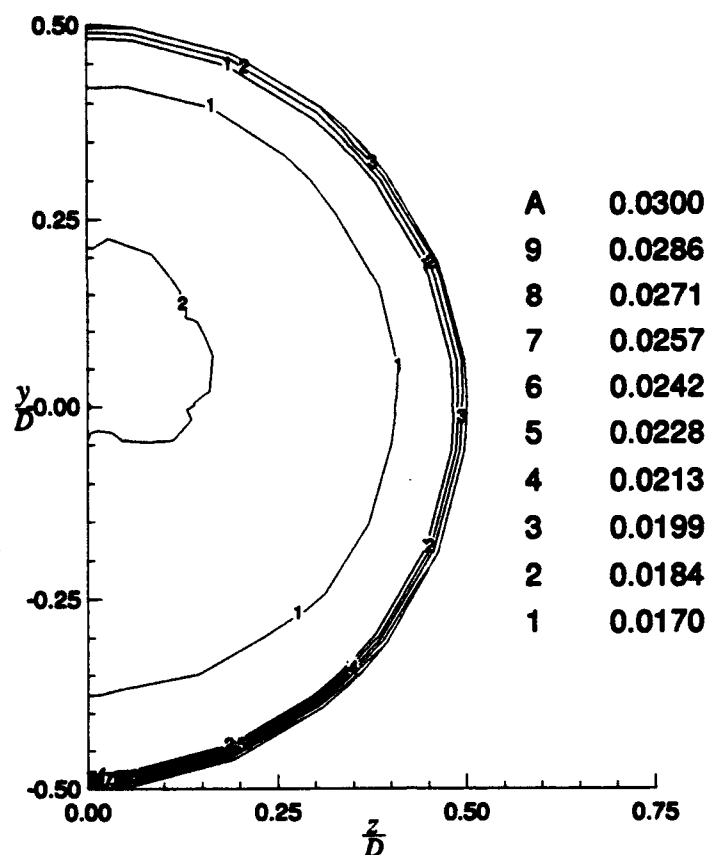
Figure 62. Pressure contours on the missile base, Case SB7 ($M_\infty = 6$, $\alpha = 5°$)

baseline, delta-fin model. The effect on drag is minor. Figure 64 combines the drag data from delta-fin free-flight analysis, and the drag data from the clipped-delta-fin free-flight analysis, and compares it to the current turbulent results. The wave drag on the fins of the delta-fin model should be slightly greater than the wave drag on the fins of the clipped-delta-fin model. This difference is impossible to detect within the scatter of the data. Thus, the experimental data is in agreement, despite the small discrepancies in the models.

The static-stability characteristics differ much more. The pitching-moment coefficients from both models are shown in Figure 65. The delta-fin model demonstrates better (more negative) stability due to the more forward center of gravity and the more rearward fin position. The difference is smaller at higher Mach numbers. In addition, the slope of the C_{m_α}–M_∞ curve for the clipped-delta-fin configuration is slightly less steep than the curve for the delta-fin configuration. The direct comparison indicates that the clipped-delta-fin has slightly inferior stability characteristics at lower Mach numbers, but potentially superior characteristics at higher Mach num-

103

Figure 63. Positions of the clipped-delta fin and the delta fin relative to the base

bers. This is supported by the present viscous calculation which extend to $M_\infty = 6$. The author attributes the difference to greater portions of the fin area being submerged in the boundary layer. As stated in Section 4.5.3, for the present calculations, at higher Mach numbers, the boundary layer affects the pressure distribution in a manner which increases fin effectiveness.
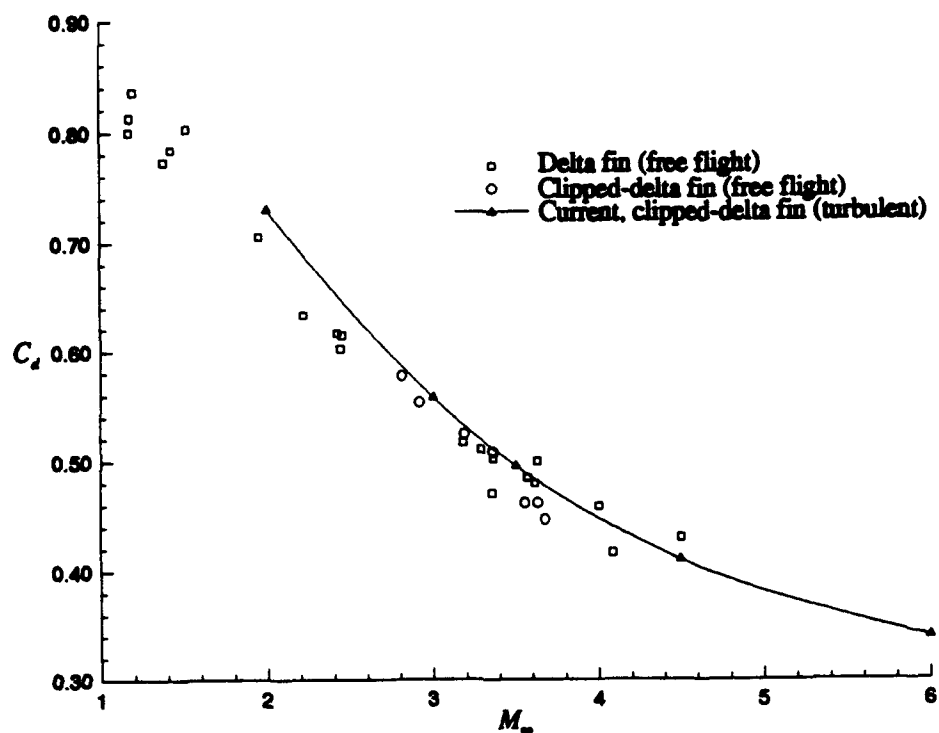
Figure 64.   Drag coefficient, C_d, comparison between delta-fin missile and clipped-delta-fin missile
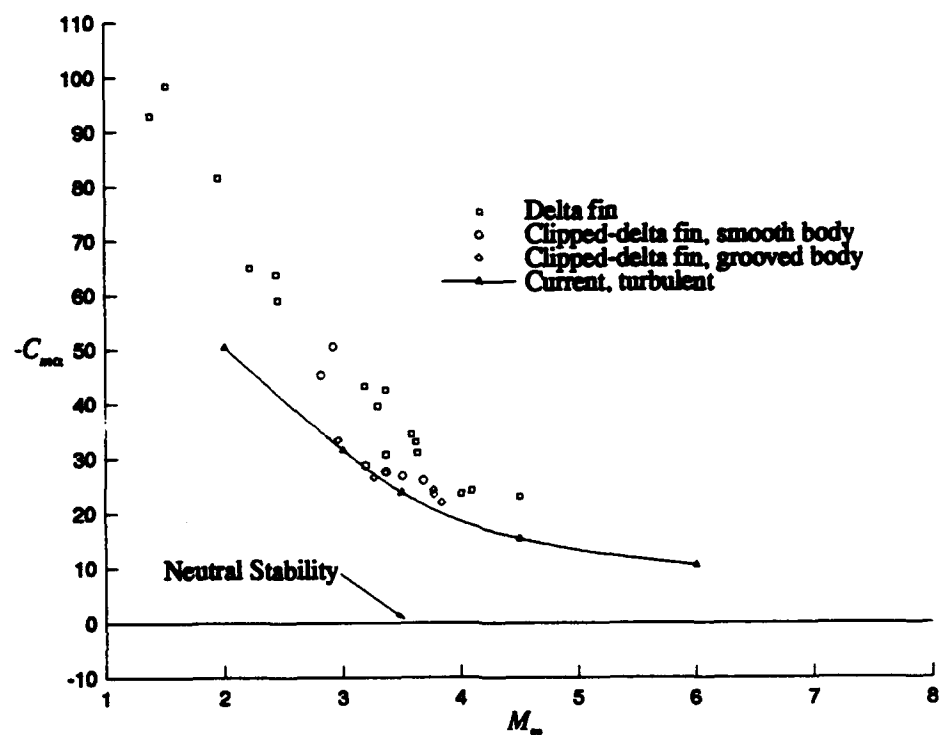
Figure 65.   Pitching-moment coefficient, C_{m_α}, comparison between delta-fin missile and clipped-delta-fin missile

105

5. Summary and Conclusions from Thin-fin Investigation

An efficient and accurate computational tool has been constructed to predict the aerodynamics for fin-stabilized missiles in supersonic flow. An *infinitely thin-fin* assumption is used to decrease the grid requirements, and the method can be used on sharp-nosetip or blunt-nosetip configurations, with or without a base region. Inviscid, laminar, or turbulent conditions can be simulated. The accuracy to which shock waves, boundary-layer properties and base-flow effects are calculated is documented over a broad range of Reynolds numbers and Mach numbers. Using the present developed technique, the flow about the complete Hypersonic Applied Research Technology (HART) missile configuration is simulated.

In general, all forces on the body and normal forces on the fins are accurately modeled with the present method. Due to the degenerate cross sections of the fins, forces on fin edges cannot be directly calculated, so semi-empirical corrections are proposed for fin wave drag and fin base drag. These overcome the deficiency in drag prediction from the thin-fin assumption, as demonstrated by the fine-grid calculations on the sharp-nosetip model. By using an empirical correction for the viscous drag on the fins (required due to the coarseness of the grid in the azimuthal direction), an accurate upper limit on drag is established. This limit corresponds to turbulent conditions over most of the body $\left(\frac{x}{D} > 1.25\right)$.

Both drag and pitching moment are dominated by compressibility effects. For the former, the base drag and turbulent viscous drag decrease substantially with increasing Mach number. For the latter, fin effectiveness is seen to decrease with increasing Mach number.

Also, the presence of turbulence is found to be significant. The expansion and compression associated with the upper and lower surfaces of the inclined fins produce less net lift for the present turbulent computations than the present inviscid or laminar computations. The discrepancy between the present prediction of C_{m_α} and the experimental prediction of C_{m_α} around $M_\infty = 2.9$ cannot be explained by the author. Most experimentally determined pitching-moment coefficients fall between the present laminar and turbulent calculations (Figure 66).

The base flow is found not to affect the pitching characteristics significantly. For the small angle of attack used in this study, $\alpha = 5°$, the flow structure between

106
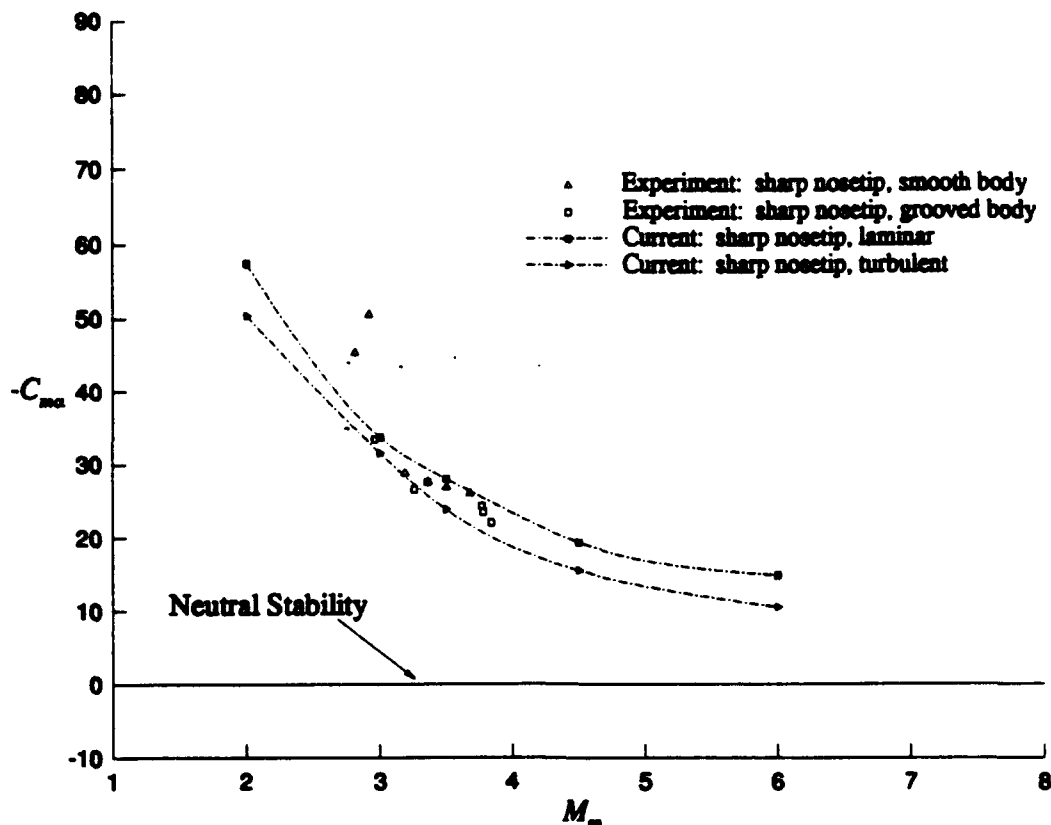
Figure 66. Pitching-moment coefficient, C_{m_α}, for sharp-nosetip HART missile with clipped-delta fins ($\alpha = 0°$).

the fins and the base does not change significantly from the structure for simulations made without a wake. In addition, the variation of pressure across the base does not contribute measurably to the pitching moment.

The aerodynamic characteristics of the HART missile, at Mach numbers beyond the experimental testing capabilities, are predicted. The current predictions indicate that C_{m_α} decreases with increasing Mach number much less than the previous EAGLE computations. The differences in C_{m_α} between the current inviscid results and EAGLE results above $M_\infty = 4$ are not fully explained. The clustering of nodes near the fin surfaces may explain the difference, and should be explored further for future EAGLE computations. The current results agree more closely with the trends predicted by ZEUS. Extrapolating the current results beyond $M_\infty = 6$ suggests that the clipped-delta-fin configuration is stable past $M_\infty = 7$.

The larger than expected drag scatter, that is seen experimentally for the sharp-nosetip configuration, is explained. A reevaluation of the experimental data

107

reveals that much of the scatter is due to poor fits between theoretical and experimental trajectories. Boundary-layer effects are the presumed cause for the remaining scatter. The reevaluated drag data falls between the current laminar and turbulent calculations, and very close to the latter. This suggests that for most flights boundary-layer transition does occur on the ogive nose, as modeled, and for a few flights the boundary layer was laminar over a larger portion of the forebody.

The poor correlation between previous computational predictions of drag (EAGLE with corrections) and experimental drag is also explained. The poor agreement is caused by the empirical corrections not the EAGLE results. The empirical relation used for turbulent viscous drag does not take into account compressibility and the large Mach number dependence exhibited by turbulent skin friction. In addition, fin pressure drag is neglected. In this study, it is determined that the wave drag and base drag on the fins are not negligible. The same causes (neglecting compressibility effects and fin pressure drag) are traced to the mediocre agreement between corrected EAGLE results and experimental results for the baseline HART missile (delta-fin configuration).

An explanation for the restabilization trend with increasing Mach number has been offered. This trend is seen only in the experimental data, and is believed to be the result of model discrepancies. Documentation is provided to show that a larger fin was used in some of the free-flight tests. In addition, a reevaluation of the data, using the correct smaller fin size, confirmed the apparent change in the static-stability trend with increasing Mach number. Finally, computations were performed with a larger fin, and these calculations agree with the suspect experimental data.

The effects of nosetip blunting are demonstrated. As expected, drag is much higher for a blunt nosetip. Fin effectiveness decreases due to compressibility by an amount approximately equal to that for the sharp-nosetip model, but the contribution to pitching moment from the missile body is demonstrated to depend on nosetip shape. The pressure distribution on the blunt-nosetip missile body affects the center of pressure significantly, and results in better static-stability characteristics, particular as M_∞ increases.

A direct comparison of the drag and pitching moment between the clipped-delta-fin configuration and the baseline, delta-fin configuration reveals two important points. First, the effect on drag in minor. Although the wave drag on the fins of the delta-fin model should be slightly greater than the wave drag on the fins

of the clipped-delta-fin model, the difference is within the scatter of data. Second, the static-stability characteristics differ markedly. The slope of the C_{m_α}-M_∞ curve for the clipped-delta-fin model is slightly less steep than the curve for the delta-fin model, and indicates that the clipped-delta-fin configuration has slightly inferior stability characteristics at lower Mach numbers,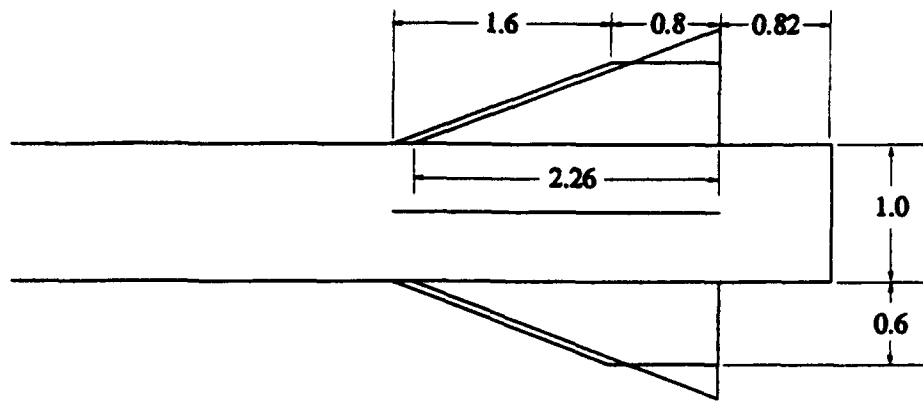 put potentially superior characteristics at higher Mach numbers. This is supported by the current viscous calculations which extend to $M_\infty = 6$. The author attributes the effect to greater portions of the fins being submerged in the boundary layer. For the present computations, at higher Mach numbers, the boundary layer affects the pressure distribution in a manner which increases fin effectiveness. This remains an unresolved issue, and viscous calculations for the delta-fin configuration are warranted to further discern the cause(s) of the differences.

The grid requirements are found to be demanding to simulate flow for a complete missile configuration. It is demonstrated that accurate calculation of turbulent skin friction necessitates a very small node size near the missile surface. In terms of the nondimensional, boundary-layer length scale, y^+, a spacing of $y^+ \approx 1$ is needed with at least 40 points (cells) in the boundary layer. Simulating the flow in the base or wake region adds considerably to the computational requirements. It is important to emphasize that these requirements are needed to achieve grid independence for skin friction. The requirements are less to predict other boundary-layer properties and surface pressure with reasonable accuracy.

Two simplifications are found to greatly reduce the grid requirements in general. First, it is not necessary to simulate the base flow in order to predict C_d or C_{m_α}. This is because the effects of the base region on pitching moment are small, and the accuracy of the empirical base drag relation is reasonable. Eliminating the wake region decreases the overall number of grid points required. In addition, the pitching characteristics of the HART missile are accurately predicted with the thin-fin assumption. The deficiency in the pressure-gradient boundary condition is overcome by clustering nodes near fin surfaces, and the drag on the fins is calculated using the degenerate cross sections with semi-empirical corrections. Therefore, a reasonably small number of nodes are required in the azimuthal direction (33 for the bisymmetric half plane in this study).

Part II: Investigation Using Thick Fin

6. Methodology for Thick-fin Investigation

Many aspects of the fins influence the stability characteristics of a fin-stabilized missile. Obviously, the size, shape, location, and orientation of a fin will dominate its pitching capability, by virtue of the fin's impermeable nature. This was seen in Part I with a series of inviscid computations. Other factors will affect pitching moment and static stability in a second-order manner. In general, these include viscous effects, the amount of fin area submerged in the missile boundary layer, and the cross-sectional shape of a fin. The precise values of properties within the boundary layer on the fin will impact the pitching moment at a tertiary level. The secondary viscous effects were examined in Part I by neglecting the impact of cross-sectional shape and thickness. The accuracy of this assumption, and thereby the effect of thickness and cross section, is addressed in this part of the research.

First, the flow structure near a blunt-swept-fin/body junction is reviewed with the emphasis on highly swept fins. A boundary for incipient separation at the fin-leading-edge/body junction was suggested by Stollery [80], and is also discussed. Finally, the numerical implementation of the thick fin is presented.

6.1 Increased Modeling Complexity

The intent of this part of the research is to determine whether the thickness and cross-sectional shape of the fins influence the pitching moment of the HART missile significantly. As stated above, the author has categorized the effect as secondary. It is possible that the shock waves created by the highly swept fins do not induce boundary-layer separation. In this case, the effect of fin thickness may be tertiary, and would depend on the average thickness of the fin in causing flow blockage, not on the actual cross-sectional shape. The results from the infinitely thin fin assumption in Part I agree very well with the experimental data. This suggests that the impact of the fin's thickness and cross section may in fact be small. Unfortunately, to the best of the author's knowledge, nobody has investigated turbulent, supersonic flow past a swept, flat-faced fin. Therefore, no quantitative information is readily available in the literature.

111

6.2 Flow Structure Near a Blunt-Swept-Fin/Body Junction

The flow structure which should be predicted for this fin geometry is not entirely clear. In general, a fin/body junction results in the formation of a corner vortex, which influences the flow near the body and around the fin, near its root. Also, for a blunt fin, it is possible (definite for an unswept fin) that the shock created by the fin separates the boundary layer on the missile body. This results in flow reversal, and the development of a horseshoe vortex structure [80]. The higher pressure in the interaction region, and the lower pressure associated with the vortical flow region may in turn modify the static-stability characteristics of the missile.

The interaction weakens dramatically, however, as the fin sweep angle increases. Several researchers have questioned whether separation occurs for severely swept, cylindrically-blunted fins at high Mach numbers [64, 99, 55]. Again, there is a general lack of data for flat-faced fins. To gauge the benefit of sweep in reducing the level and extent of the disturbed pressure field, the pressure distributions generated by a blunt, swept fin at incidence are taken from [41] for $\Lambda = 30°$ and $\Lambda = 75°$ and $M_\infty = 2.95$ (Figure 67). The current turbulent thin fin results ($\Lambda = 70°$) are also shown in Figure 67 for Case S29 ($M_\infty = 2.95$ and $\alpha = 5°$). The pressure is measured along the junction line and nondimensionalized by the pressure 5 fin thicknesses, t, upstream of the fin-leading-edge/body junction, $\hat{p}$. Because the fin from [41] is spherically blunted, some data does not correspond to the fin/body junction, but is from a line projected upstream from the junction.

Both the pressure ahead of the fin/body junction and the pressure immediately downstream are affected significantly by sweep. As discussed in Chapter 4, the boundary layer does not separate in the current computations with the thin-fin assumption. This could be due to the severe sweep angle, as suggested by the data from [41]. To further clarify the thin-fin results, calculations are made for two Mach numbers and a thick fin.

6.3 Suggested Boundary for Incipient Separation at Fin Leading Edge

The strength of the interaction at the fin/body junction relies on the sweep angle of the fin. This was discussed in Secion 2.4.2. However, it may be possible to identify more precisely the sweep angle required to prevent separation. Stollery [80] suggests that there is a direct relationship between the Mach number and sweep
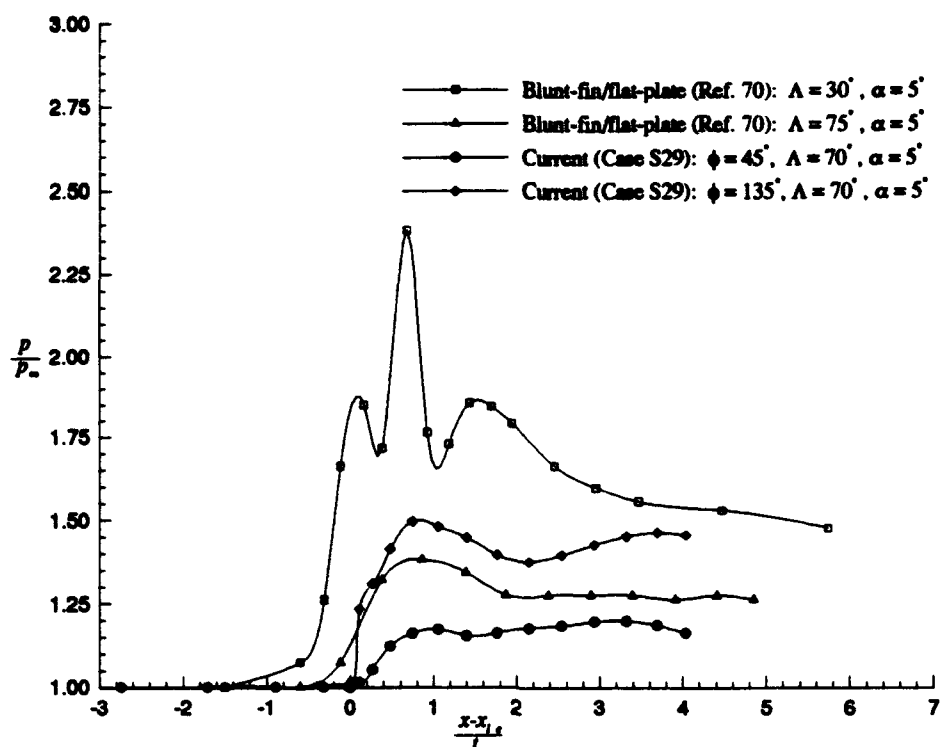
Figure 67.   Surface pressure from a swept-blunt-fin/flat-plate interaction and the
current thin-fin/missile-body interaction.

angle such that a boundary for incipient separation exists. Within a $\Lambda - M_\infty$ region
defined by this boundary, separation is possible; everywhere else, it is not.

The boundary is established by two conditions required for an attached shock
at the nose. The first condition is the maximum sweep angle that ensures the leading
edges are supersonic, in the sense that the normal component of the Mach number
is greater than one ($M_N > 1$). The second condition is the minimum sweep angle
required for an attached oblique shock to a wedge. The region bounded by these
two conditions is shown in Figure 68. In Figure 69, a line is added to show where
incipient separation occurs in supersonic flow over a compression corner [80]. Kubota
and Stollery [48] have shown that separation occurs more readily for a glancing
interaction (fin/body) than for a two-dimensional interaction. Therefore, the line
representing separation over a compression corner helps to further define the region
where the shock is attached at the leading edge. The region above this line is where
an attached boundary layer is likely, and below the line it is only possible. Also, in
Figure 69, the two Mach numbers examined in Part II of this study are indicated.

113
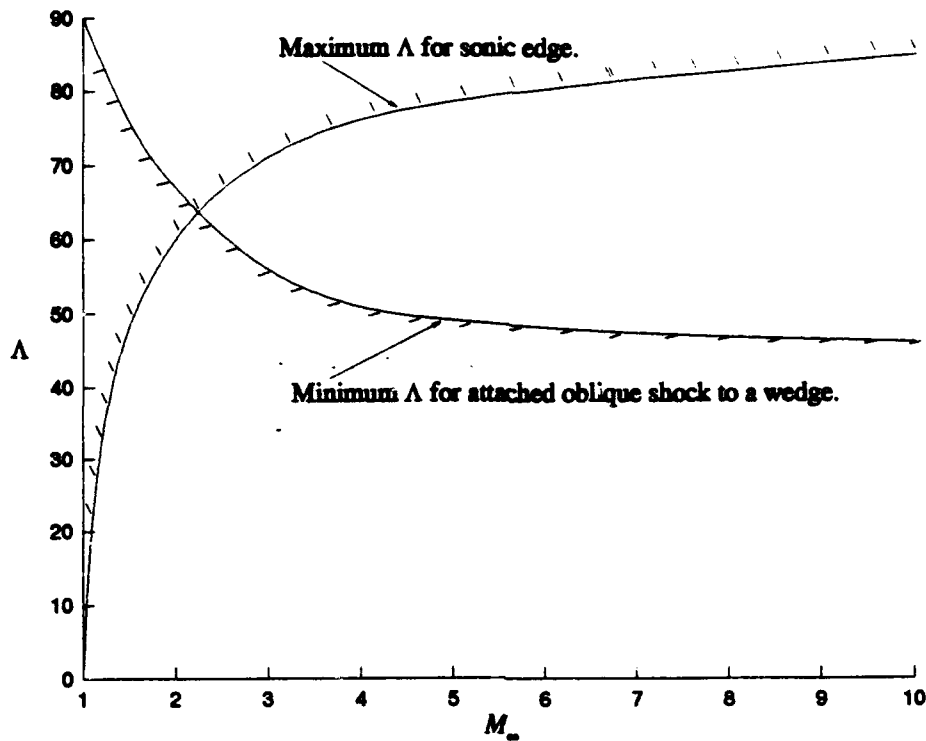
Figure 68. Boundary for an attached shock at the leading edge of a blunt fin.

The point $M_\infty = 2$ and $\Lambda = 70°$ lies outside the "attached" region, and the point $M_\infty = 6$ and $\Lambda = 70°$ lies well within the region.

6.4 Numerical Implementation

Due to increased computational demand, necessitated by grid refinement near the fin leading edge, the entire configuration is not reexamined. Instead, a much smaller region is defined around the fins and aft part of the missile. The thick fin is modeled using an H-grid [86] to minimize algorithm and boundary condition changes. The structure of the grid and modifications to the boundary conditions are discussed in the next two sections.

6.4.1 Grid Structure. The domain size is reduced to add more cells in the finned region. The inflow boundary is placed ten fin thicknesses upstream of the fin-leading-edge/missile-body junction, allowing for potential disturbances ahead of the junction. The shape of the inflow boundary is taken from grid points used in Part I. In addition, the outer boundary is placed only three body diameters from the missile surface. Both of these boundaries require different boundary conditions than used in Part I. The new boundary conditions are described in Section 6.4.2.

114
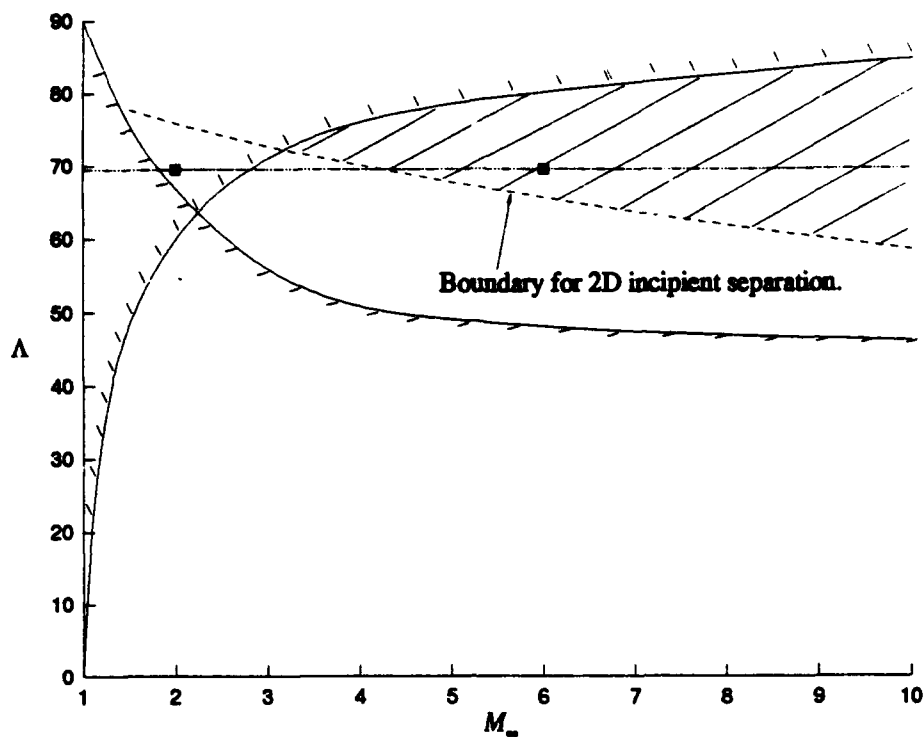
Figure 69. Boundary for incipient separation at the leading edge of a blunt fin.

Unlike Part I, the grid used in Part II is constructed such that the grid lines conform to the leading edges of the fins. Additionally, the cells are distributed azimuthally so that the grid conforms to the upper and lower surfaces of the fins. Because the fins now have thickness, some cells are arranged with the curvilinear grid lines not normal to the missile surface. The deviation from a normal distribution is small. To achieve a grid which is aligned with the fin leading edges, the cells are skewed substantially. The author assumes that the current finite-volume methodology of handling grid-cell geometric terms will minimize the error associated with skewing, as proposed by [91].

A total of 121 cells are distributed in the azimuthal half plane, some of which are located on the interior of the fin. Those points are essentially ignored during the computation. The node spacing at the fin-leading-edge/missile-body junction is $0.001D$, and the spacing along the fin upper and lower surface is $0.00085D$. Spacing at the body surface is the same as for the fine grid computations in Part I $(0.000025D)$. Like Part I, the boundary conditions for the fin surfaces are enforced on the interior of the domain, and the flow solver is restrained from obtaining information across or through a fin.

115

6.4.2 Modification of Boundary Conditions. The solutions from the computations in Part I are used for the inflow boundary. Linear interpolation is then employed to determine boundary data between points available from the solutions of Part I. Because the shape of the inflow boundary is chosen to correspond to grid points from the grid used in Part I, the author believes that linear interpolation will provide an adequate inflow solution.

The initial far-field boundary condition is also an interpolation of the solutions from Part I. From then after, two point extrapolation is used. This extrapolation is given by:

$$q_{i,jmax,k} = 2q_{i,jmax-1,k} - q_{i,jmax-2,k},$$
(58)

where q is any conserved variable. All other boundary conditions remain unchanged and are described in Section 3.6.

7. Results and Conclusions from Thick-fin Investigation

In Part II, the effect of fin thickness on HART missile aerodynamics is addressed, and the accuracy of the thin-fin assumption (Part I) assessed. The primary intent of this part of the research is to determine whether the pitching moment of the HART missile is significantly influenced by the thickness and cross-sectional shape of the fins. Secondarily, the drag contribution from the fins is computed and compared to the semi-empirical relations used in Part I. Due to increased memory requirements, thick-fin effects are determined for only two Mach numbers ($M_\infty = 2$ and $M_\infty = 6$) and two angles of attack ($\alpha = 0°$ and $\alpha = 5°$). All cases are for clipped-delta fins and turbulent conditions.

The effects of fin thickness are assessed by examining changes in the flow structure near the fins and the drag and pitching-moment coefficients of the missile. First, the inviscid structure is examined by measuring the surface pressure on the missile body and both fins. Next, the structure near the fin/body junction is explored through the use of streamlines and surface pressure plots. The strength of the shock/boundary-layer interaction for the thick-fin geometry is gauged by comparing this data in the fin/body junction region with similar thin-fin data. Finally, the structure near the missile body and along the fin leading edges is shown with contour and velocity vector plots. Again this data are compared to the results from the thin-fin investigation. The impact of any differences found is evaluated by reexamining the drag and pitching-moment contributions from the fins.

7.1 Flow Structure Changes Near Fin

The flow expands and compresses several times around each fin. The nondimensional surface pressure along the centerline of the fins is used in this section to show the effects of the shocks and expansions that take place near each fin. The surface pressure is measured along the missile body, the fin leading edge, and the fin trailing edge in a plane that intersects each fin's centerline. Figure 70 shows the surface pressure plotted against the axial coordinate for $M_\infty = 6$ and $\alpha = 5°$. The shock wave created by the fin leading edge results in a rapid pressure rise at approximately $x/D = 20.78$. The pressure is then relatively constant along the fin's leading edge for the windside fin ($\phi = 135°$), and rises gradually for the leeside fin

117

($\phi = 45°$). A sudden expansion at the clipped portion of the fin is evidenced by the fall in pressure at $x/D = 22.38$. The flow continues to expand along the top of the fin, then rapidly expands again at the base of the fin ($x/D = 23.18$). Finally, the flow recompresses downstream of the fin.

The boundary layer near the fin/body junction is not significantly affected by fin thickness. Through examination of the velocity field near the fin/body junction, it is observed that the boundary layer remains attached for the thick-fin geometry, as was the case for all thin-fin computations. Figure 71 shows the streamlines in the vicinity of the windside-fin ($\phi = 135°$)/body junction for $M_\infty = 2$ and $\alpha = 5°$. The streamlines are constructed from the axial and radial velocity components (u and $v \cos \phi + w \sin \phi$), which are extracted from the three-dimensional solution in the plane that intersects the centerline of the windside fin. The streamlines depict an attached boundary layer. An attached boundary layer is also found at the leeside fin ($\phi = 45°$, not shown).

Although the boundary layer does not separate, the shock/boundary-layer interaction influences the pressure upstream of the fin/body junction. Figure 72 is a plot of the surface pressure along the curve of intersection joining the fin and missile body for the thick-fin calculation at $M_\infty = 2$ and $\alpha = 5°$. Results are presented for both the windside and leeside fins. The pressure is nondimensionalized by the pressure 5 fin thicknesses upstream of the fin leading edge, $\tilde{p}$. The upstream influence through the boundary layer leads to a gradual pressure rise ahead of the fin/body junction ($x - x_{le} = 0$) for the thick-fin geometry.

The upstream influence of the thick fin is also evident in data obtained experimentally for a blunt-fin/flat-plate geometry [41]. This blunt-fin/flat-plate data is included in Figure 73 with the present thick-fin results. The data from [41] are for $M_\infty = 2.95$ and two sweep angles (30° and 70°). Exact agreement between the present results and those from [41] are not expected because of differences in Mach number, fin cross-sectional shape, and body curvature. Specifically, the fin in [41] is cylindrically blunted and the current fin is flat-faced. Also, a flat plate in [41] replaces the curved missile body used in the present computations. The author attributes the small differences in magnitude to these geometric differences. A sharp drop in pressure is seen in the current data around $x - x_{le} = 0$, and is attributed to the more abrupt expansion around the leading edge of the flat-faced fin. Clearly, however, the

118
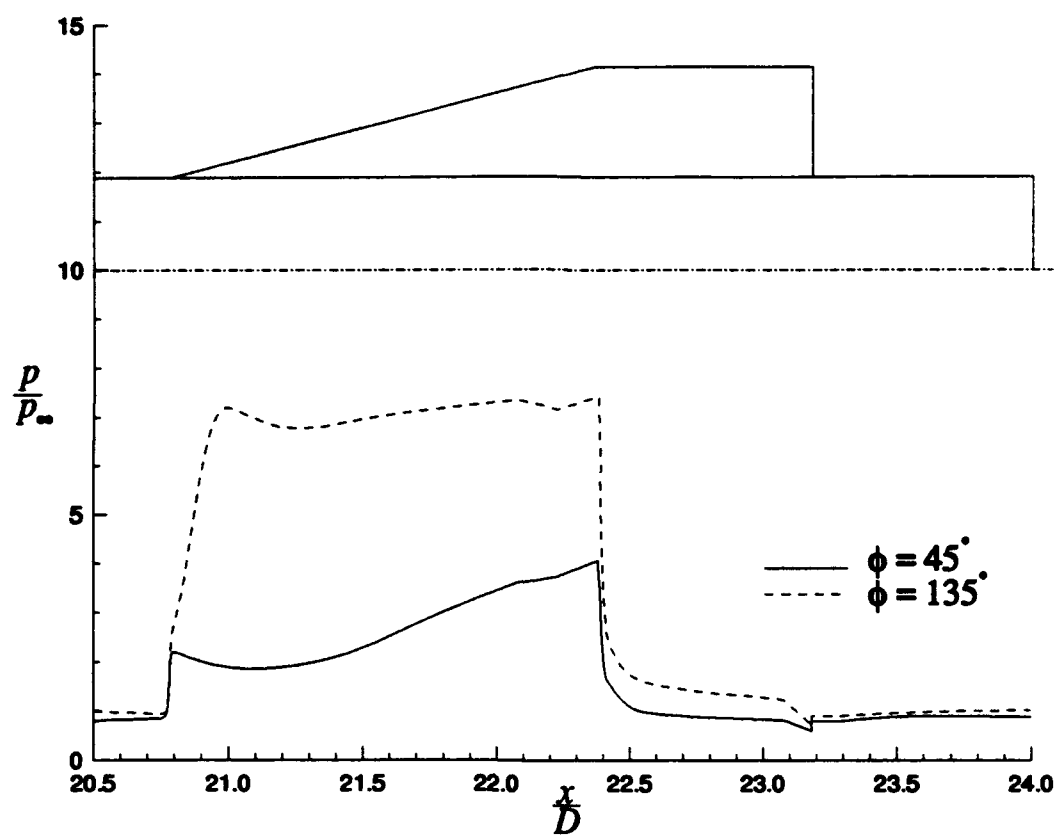
Figure 70. Surface pressure coplanar with fin centerlines ($M_\infty = 6$ and $\alpha = 5°$)

119
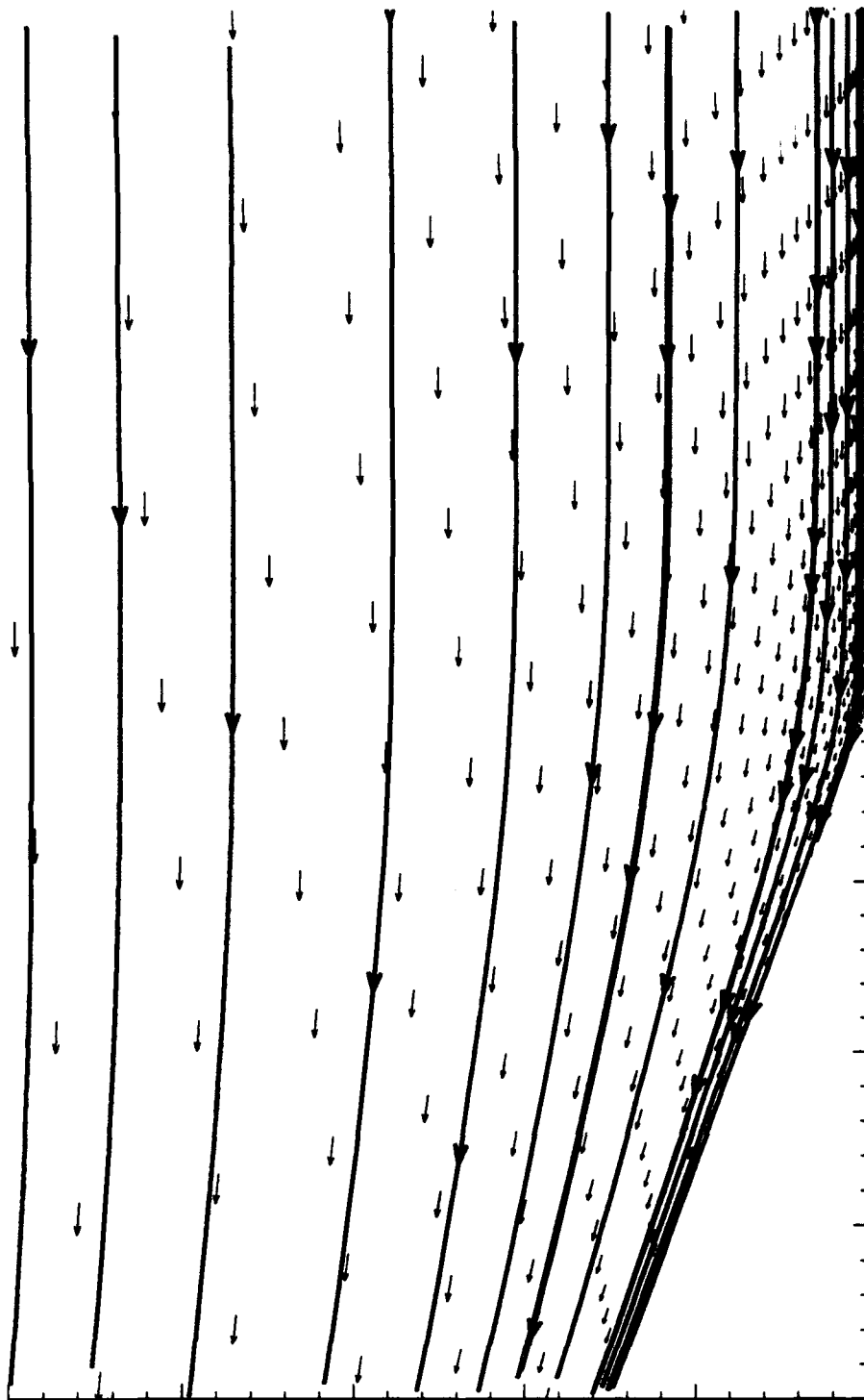
Figure 71. Streamlines in the plane of the windside fin ($M_\infty = 2$ and $\alpha = 5°$)

upstream extent of the pressure disturbance for the thick-fin calculations agrees well with the similarly swept fin from [41].

7.2 Analysis of Fin Drag

The fin drag from the thick-fin computations ($\alpha = 0°$ only) is summarized in Table 17. The pressure drag (wave drag plus base drag) and viscous drag is tabulated to allow direct comparison to the semi-empirical data used in Part I. Also included in Table 17 is the total drag obtained by adding the thin-fin results upstream of the thick-fin domain to the thick-fin results.

The pressure-drag calculations from the thick-fin tests are in reasonable agreement with the semi-empirical data used in Chapter 4. In fact, the wave and base drag due to the fins is nearly identical at $M_\infty = 2$. The thin-fin result is 0.042 and the thick-fin result is 0.041. The agreement between the computed pressure drag on the thick fins and the semi-empirical drag on the thin fins suggests that the semi-empirical relations give adequate estimates for the drag.

The turbulent viscous drag differs by a slightly larger amount because the leading edge and trailing edge contributions are included in the thick-fin calculations, and an empirical correction for these edges was not added to the thin-fin results. At $M_\infty = 6$, the viscous drag coefficient is 0.006 and 0.011 for the thin fins and thick fins, respectively. However, the agreement is much closer when only the contribution from the upper and lower surfaces is examined. Again the coefficient for the thin fins is 0.006, but now the coefficient for the thick fins is 0.007. This is not surprising, since the azimuthal distribution near the fin is similar for thin-fin and thick-fin computations.

Table 17. Drag components from thick-fin computations ($\alpha = 0°$)

M_∞	$C_{d_w} + C_{d_b}$ (thin fins)	C_{d_v} (thin fins)	C_d (total)	$C_{d_w} + C_{d_b}$ (thick fins)	C_{d_v} (thick fins)	C_d (total)
2.0	0.042*	0.013*	0.619*	0.041	0.019	0.632
6.0	0.045*	0.006*	0.265*	0.026	0.011	0.262

* See Table 5.
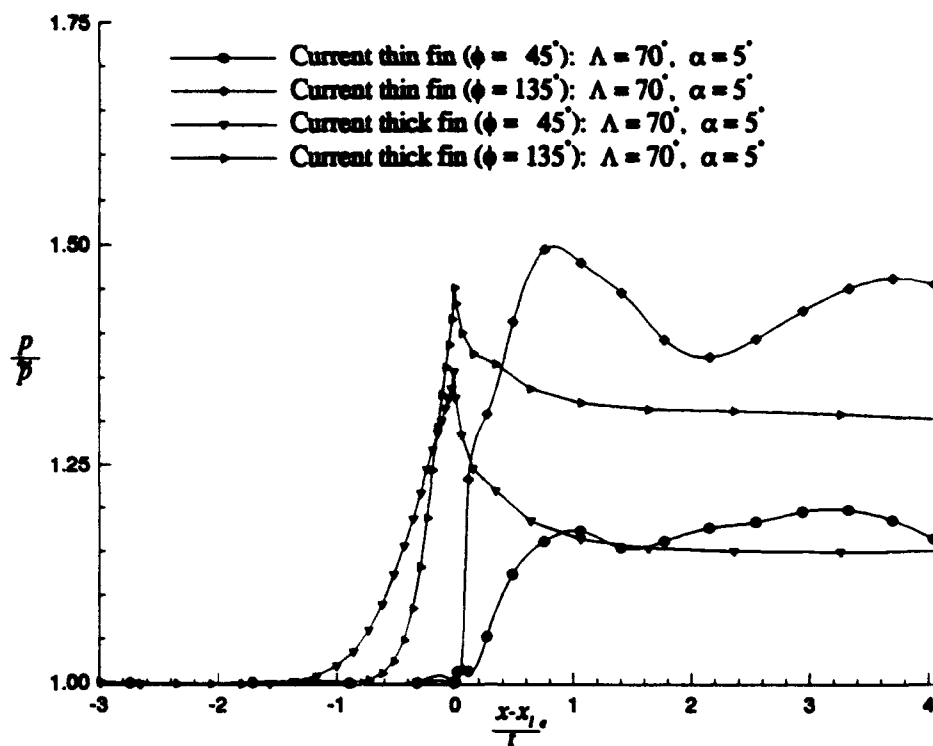
Figure 72. Pressure near fin/body junction: thin-fin versus thick-fin computation $(M_\infty = 2$ and $\alpha = 5°)$
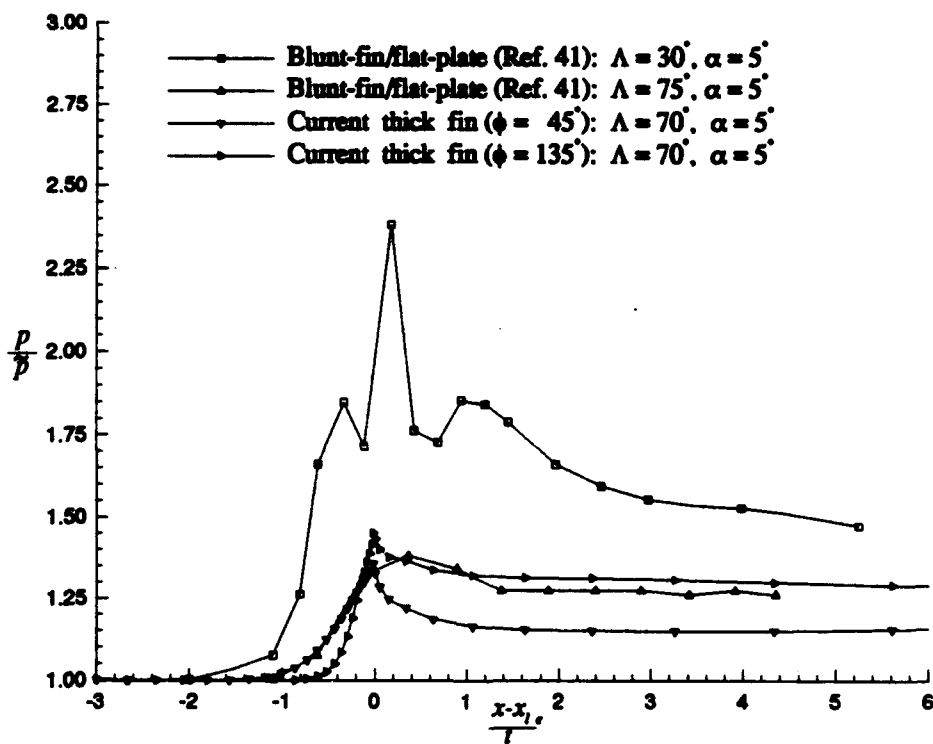
Figure 73. Pressure near fin/body junction: experiment versus thick- fin computation

122

7.3 Impact of Fin Interaction on Static Stability

As with the turbulent, thin-fin tests in Chapter 4, bleeding of the pressure took place around the leading edges of the thick fins. Figure 74 is a contour plot showing the pressure in the cross plane (y-z plane) for $M_\infty = 2$ and $\alpha = 5°$. The cross-plane plot is for $x/D = 21.8$. This is the same location used for the contour plot of pressure near the thin-fin (Figure 58), and is a point near the middle of the fins. Figure 58 is duplicated in Figure 75 for convenience. Comparing Figures 74 and 75 shows the bleeding of high-pressure to the leeward side of each fin in both cases. Although the influence extends further away from the fins in the thick-fin case, the differences in the pressure along the fin surfaces are relatively small.

Like the thin-fin configuration, the bleeding around the thick fins is caused by the turbulent transport of momentum in a region of blocked flow. For the windside fin, the flow is blocked by the fin surface and the symmetry plane. For the leeside fin, the flow is blocked by the fin surface and the expanding flow near the body. Figures 76(a) and (b) show the cross-plane velocity components at $M_\infty = 2$ and $\alpha = 5°$, for the thick-fin and thin-fin computations, respectively. The velocity vectors are also included in Figure 76. Complex flow structures are clearly evident below each fin. The similarity in the thick-fin cross-plane streamlines with those for the thin-fin case suggests that the structure of the flow is dominated by the blockage phenomenon.

Two relatively small effects of fin thickness are discernible in Figure 76. First, the extent of the structure below the windside fin is greater for the thick fin than the thin fin. Also, the structure below the leeside fin is more fully developed in the thick-fin case.

The impact of fin thickness on C_{m_α} is also relatively small. Figure 77 is a plot showing the variation of C_{m_α} with M_∞ for the sharp-nosetip missile. The experimental data are represented as open symbols, and the thin-fin results from Chapter 4 are connected by a cubic spline curve. The two data points from the thick-fin tests are obtained using the thin-fin data upstream of the thick-fin domain. The level of correlation between C_{m_α} from the thick fins and C_{m_α} from the thin fins, supports the categorization of thickness as a secondary effect on pitching moment. The value of C_{m_α} changed 4.9% at $M_\infty = 2$ and 31.9% at $M_\infty = 6$. Therefore, although a secondary effect, thickness has a growing contribution to C_{m_α} with increasing Mach number.
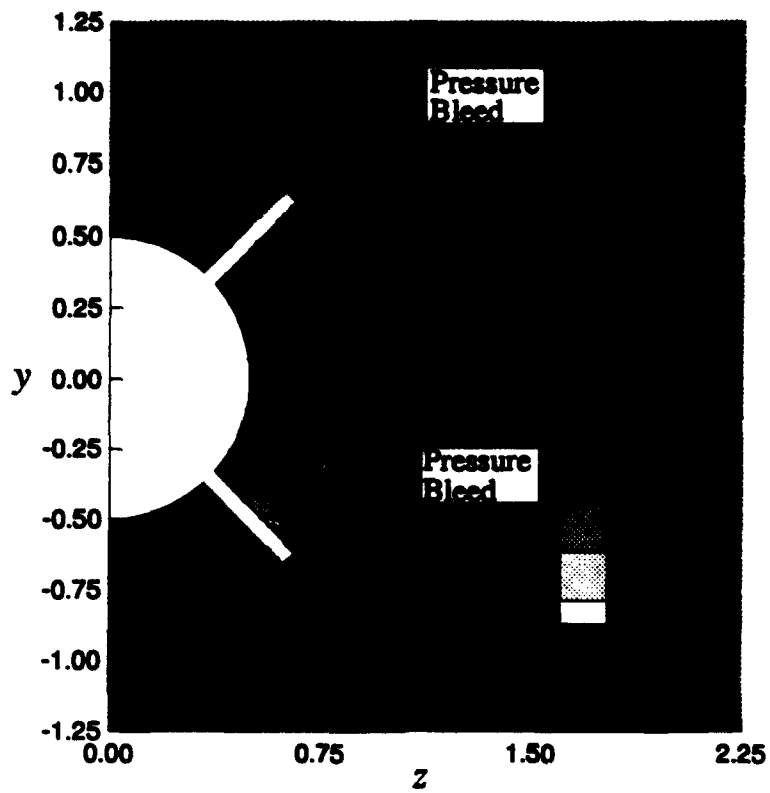
Figure 74. Pressure contours for thick-fin model ($M_\infty = 2$ and $\alpha = 5°$)
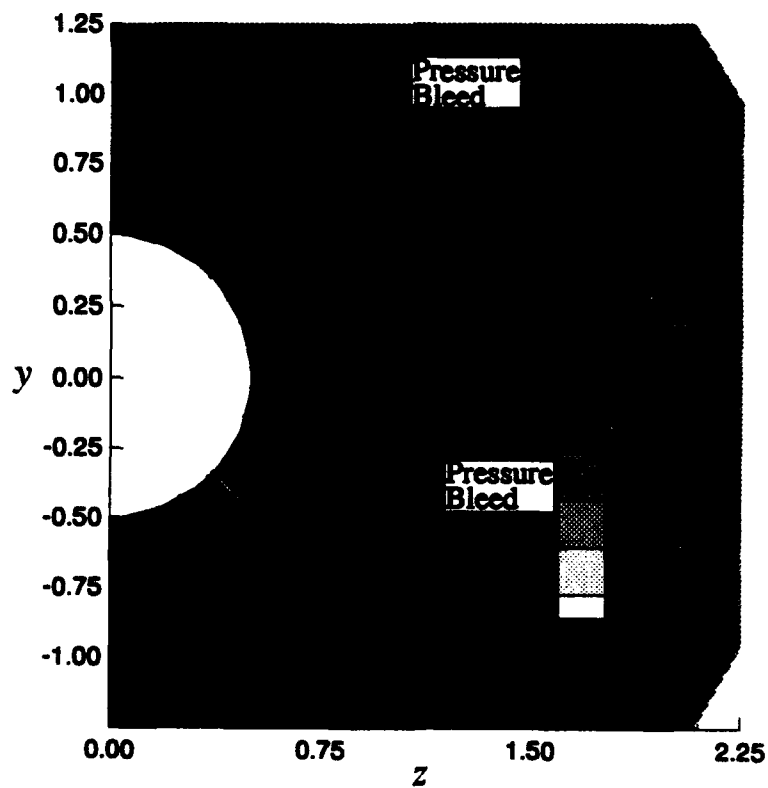
Figure 75. Pressure contours for thin-fin model, Case S28 ($M_\infty = 2$ and $\alpha = 5°$)

124
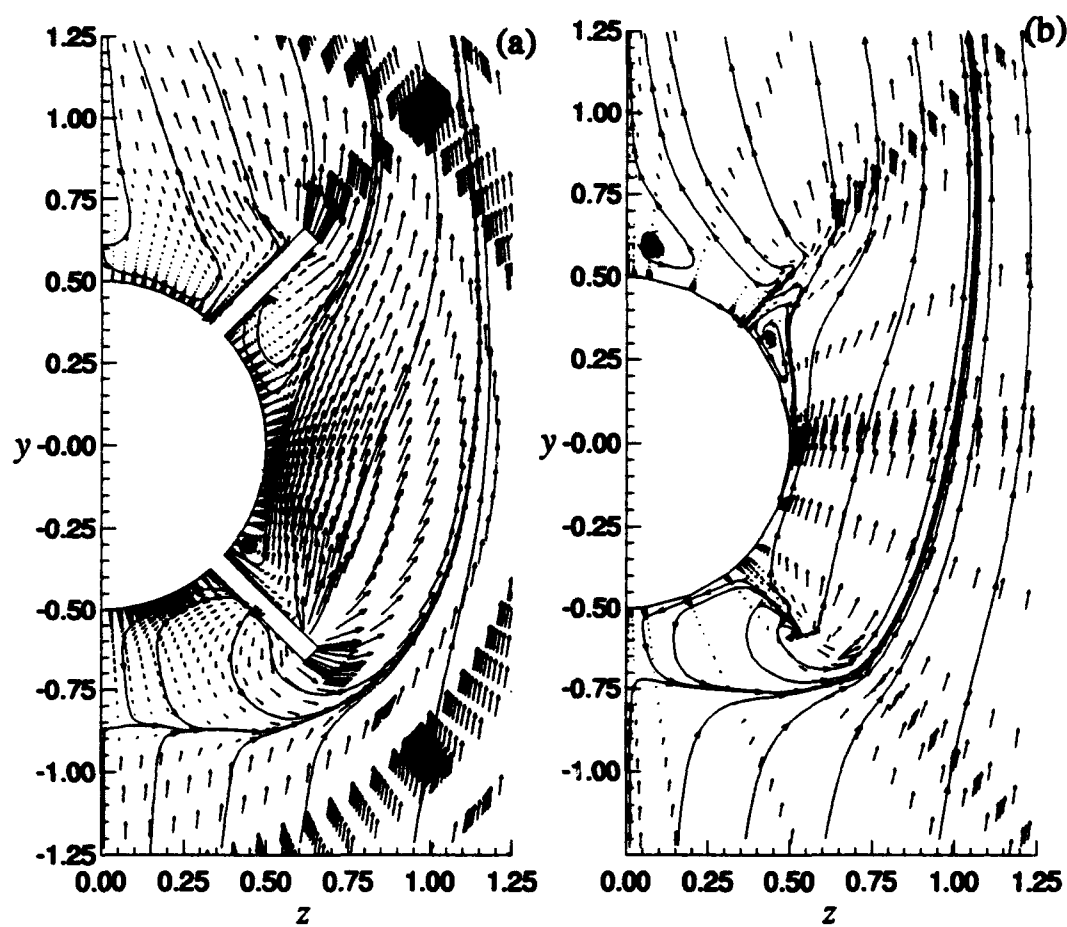
Figure 76. Cross-plane velocity components ($M_\infty = 2$ and $\alpha = 5°$), (a) thick fins, (b) thin fins (Case S28)

125
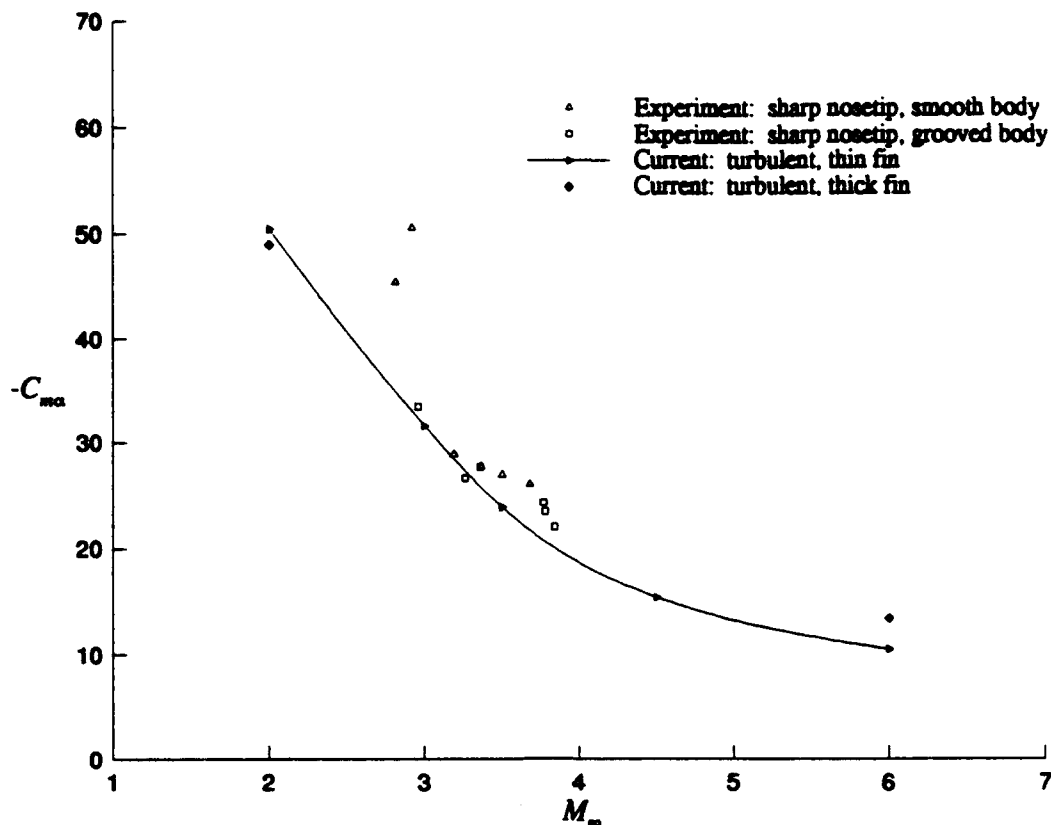
Figure 77. Pitching-moment coefficient, C_{m_α}, for sharp-nosetip, clipped-delta-fin model: thick-fin results versus thin-fin results

Several factors contribute to the differences in the thin-fin and thick-fin pitching moment. First, the thick fin occupies some of the body surface that was used to calculate C_{m_α} in the thin-fin tests. Second, the flat-faced fin design allows an additional contribution to the pitching moment from the fin leading edges in the thick-fin tests. At $M_\infty = 2$, these two competing factors nearly offset each other, and the change in C_{m_α} is small. In contrast, at $M_\infty = 6$, the leading edges provide a much larger component and the impact of fin thickness on C_{m_α} is larger.

Interestingly, the pitching moment created by the upper and lower surfaces of the fins is found not to depend on fin thickness. The contribution from these surfaces differed less than 2% between the thin-fin and thick-fin computations.

7.4 Summary and Conclusions of Thick-Fin Analysis

Due to the highly swept configuration of the fins, the shock/boundary-layer interaction at the fin/body junction is very weak. The clearest indication of the weakness is that separation does not occur at either Mach number tested. In ad-

126

dition, the disturbance in pressure is limited to one fin thickness upstream of the junction. The level of disturbance found in this investigation is similar to that found by other investigators on simpler geometries [64, 99, 55].

Although the fins are highly swept, the pressure drag is still significant because the fin edges are square. The contribution to the total drag is 6% at $M_\infty = 2$ and 10% at $M_\infty = 6$. Changing the leading edge shape through rounding or sharpening will undoubtedly reduce this drag component considerably.

The structure of the flow near the fins is affected by the turbulent transport of momentum in regions of blocked flow. As with the thin-fin tests, this blockage phenomenon causes bleeding of pressure around the fin leading edges. The strength and extent of the flow structures that develop in the blocked regions appear to be enhanced by fin thickness. The author speculates that this is caused by further constraint of the flow geometrically dictated by the physical thickness of the fins.

As stated in Section 7.3, the level of correlation in C_{m_α} between the thick-fin and thin-fin configurations supports the categorization of thickness as a secondary effect on pitching moment. The change in pitching-moment coefficient for the thick-fin tests is caused by lift on the leading edges.

It may be possible to empirically model the pitching contribution from the fin leading edges. This could be accomplished in much the same way that the pressure drag from the leading edges is determined. An empirical approach to modeling thickness effects is attractive because of the dramatic reduction in memory requirements for the calculation of the entire missile flowfield.

Appendix A. *Algorithm Validation Using Axisymmetric Equations*

The intent of the validation experiments is to determine the algorithm's accuracy and sensitivity, and then establish the grid requirements for HART missile research. Therefore, one objective of the current study is to build a computational methodology that is sufficiently general to compute accurately a wide variety of flow structures. At the same time, this method must be both frugal in its computer utilization and accurate in predicting the aerodynamics of long projectiles. These requirements must be met so that the approach can be effectively used to study the stability of long, slender, fin-stabilized missiles.

The Navier-Stokes equations are solved with an explicit, time-integration technique, incorporating an upwind, Roe-type, flux-difference splitting (FDS) scheme [71]. To establish a baseline, an initial assessment of the algorithm is made assuming axisymmetric flow. This provides an appropriate reference point for future investigations using the full, three-dimensional equations (Chapter 3). The cylindrical form of the Navier-Stokes equations is described in Section A.1.

The current research investigates the robustness and accuracy of the basic algorithm for the flight conditions of interest. Specifically, tests are run for Mach numbers ranging from 1.5 to 8, and Reynolds numbers from $1 \times 10^6/m$ to $2 \times 10^8/m$. Calculations are made on axisymmetric bodies with fineness ratios between 9 and 23. In Addison, several different nose-tip shapes (Figure 78), with varying degrees of bluntness, are investigated. Both laminar and turbulent conditions are simulated on the forebody and base. Since the ongoing goal of the research is to predict the aerodynamics of both finned and unfinned bodies, the ability of the algorithm to calculate a complete configuration is paramount. To demonstrate this ability, laminar flow is computed on a highly blunted, tangent ogive-cylinder model with a flat base. The fineness ratio is 23, and Mach number is varied from 2 to 7; total drag is compared to experimental tests of this shape (with fins) [93]. Laminar flow is also computed on a hemisphere-cylinder, $L/D = 14$, at Mach 7.78 and compared to experiments [47]. These comparisons provide a refined level of flow interrogation to verify the algorithm's accuracy. Then, turbulent flow is computed on pointed, flat, and spherically tipped tangent ogive shells, $L/D = 9$, at Mach 2.95. These results are compared to both experiment [13] and independent computational results [29].

128

Highly Blunted Tangent Ogive-Cylinder
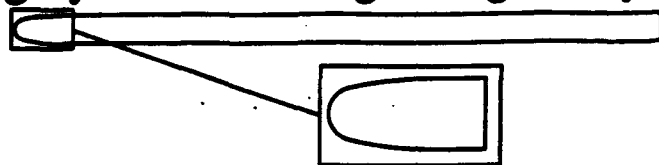
Hemisphere-Cylinder
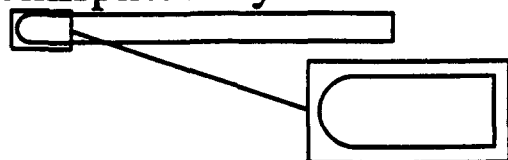
Pointed Tangent Ogive-Cylinder
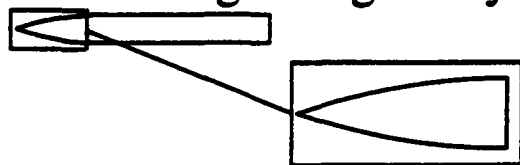
Spherically Blunted Tangent Ogive-Cylinder

Flat Tip Tangent Ogive-Cylinder
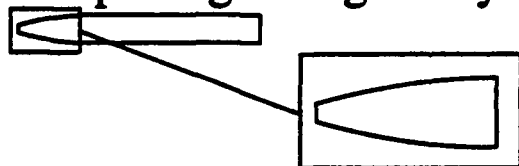
Figure 78. Experimental/computational models and nose-tip shapes

129

These tests determine the algorithm's ability to predict accurately the influences of upstream effects on boundary-layer development. Finally, turbulent flow is computed for a flat base region and Mach numbers between 1.5 and 7.0. These results are compared to experimental data reported in [10, 11, 31, 38, 53, 66]. The base-flow tests are performed to demonstrate the validity and accuracy of the wake-region turbulence model, described later.

Accuracy and sensitivity issues are summarized in Tables 18 and 19. Details are highlighted in the sections that follow. Numerical accuracy is judged from comparisons with theoretical solutions for stagnation pressure and velocities in a turbulent boundary layer. Additionally, the effect of the entropy correction parameter on surface pressure is assessed for both the nose and wake regions.

A.1 Axisymmetric Equations

The geometric singularity associated with axisymmetry poses significant difficulty when employing either two-dimensional or three-dimensional grids. Recent work reported in [63] proposed two methods of handling this singularity for three-dimensional grids. Both of these methods are explored here, in the context of axisymmetric flow. Some differences are found on both the forebody and base. These are highlighted in subsequent discussions.

A.1.1 Reformulation of Finite-difference Equations.

The first procedure reformulates the governing equations, transferring the curvilinear terms to source-like vectors, $\bar{H}$ and $\bar{W}$. For the cylindrical form of the Navier-Stokes equations, which incorporate the axisymmetric assumption, transformation would yield

$$\frac{\partial \bar{U}}{\partial t} + \frac{\partial \bar{E}}{\partial \xi} + \frac{\partial \bar{F}}{\partial \eta} + \bar{H} = \frac{\partial \bar{R}}{\partial \xi} + \frac{\partial \bar{S}}{\partial \eta} + \bar{W}, \tag{59}$$

where

$$\bar{U} = J^{-1}U, \tag{60}$$

$$\bar{E} = J^{-1}(\xi_x E + \xi_r F), \tag{61}$$

$$\bar{F} = J^{-1}(\eta_x E + \eta_r F), \tag{62}$$

$$\bar{H} = \frac{1}{rJ}\left[\rho v, \ \rho uv, \ \rho v^2, \ (e+p)v\right]^T, \tag{63}$$

130

Table 18. Summary of sensitivity evaluations

Parameter Varied	Min-Max Values	Quantity Observed	Change in Quantity	Tested Configuration	Notes
Number of Nodes Along Body	61-121	C_d	4%	HC	Laminar
Number of Nodes Normal to Body	61-181	Pressure One Body Diam. From Surface	0.1%	HC	Laminar
Spacing at Sing. Line, $\Delta s/D$	0.005-0.04	Tip Stagnation Pressure	2%	HC	Laminar
Wall Spacing $\Delta y/D$	0.0001-0.001	Tip Stagnation Pressure	0.1%	HC	Laminar
Wall Spacing $y^+\vert_{wall}$	0.6-24.0	$\partial u/\partial y\vert_{wall}$	15%	PTOC & BTOC	Turbulent
Entropy Func. Coefficient, c_1	0.002-0.85	Base Stagnation Pressure	28%	CFB	Turbulent
Entropy Func. Coefficient, c_1	0.002-0.85	Integrated Base Pressure	4%	CFB	Turbulent

Table 19. Summary of comparison between computation and theory or experiment

Basis of Comparison	Comparison With	Configuration	Case Description	Difference in Result	Notes
Tip Stagnation Pressure	Inviscid, Perf. Gas Theory	HC	Case 5 (see Table 20)	0.5%	Laminar
Streamwise Velocities	Law of Wall/ Law of Wake [101]	PTOC & BTOC	$y^+ \approx 1$ (see Table 19)	0.2%	Turbulent
Surface Pressure	Experiment [12]	PTOC & BTOC	121 Nodes Along Body and $y^+ \approx 1$	4% (max) 1% (avg)	Turbulent
Integrated Base Pressure	Experiment [10, 11, 31, 38, 53, 66]	CFB	31 Nodes Along Base and $c_1 = .85$	10% (max) 1% (avg)	Turbulent

131

and E and F are the convective flux vectors in *Cartesian* coordinates. The other vectors $\bar{R}$, $\bar{S}$, and $\bar{W}$ are the generalized viscous flux vectors and the viscous source term, respectively. The explicit forms of E, F and the viscous flux vectors can be found in [1]; $\bar{J}^{-1}$ is computed from the following expression:

$$\bar{J}^{-1} = x_\xi r_\eta - x_\eta r_\xi. \tag{64}$$

Since $\bar{H}$ and $\bar{W}$ are not evaluated on the singular (symmetry) line, they are never singular.

Unlike the approach taken in [63], which was finite-difference, the current technique implements the discretization of (59) with the finite-volume methodology. Although the transformed equation deviates from its integral formulation *roots*, local physical conservation is addressed when applying (59) to a cell in physical space by calculating the flux terms and geometric terms at the *faces* of the cell. The grid points themselves represent the vertices of the cells. This is important at computational boundaries, where the boundary conditions are handled in a manner consistent with a cell interface representing a boundary. The geometric terms (metrics and Jacobian) associated with (60)–(63) are calculated at cell *centers* from finite-difference expressions, and averaged to obtain values at cell interfaces. This approach is considered a hybrid finite-difference/finite-volume approach by the author.

A.1.2 Governing Equations for Finite-volume Method. For the second procedure, a pure, three-dimensional, finite-volume representation of the geometric terms is utilized. Again (59) applies, but now

$$\bar{U} = (r\bar{J}^{-1})U, \tag{65}$$

$$\bar{E} = (r\bar{J}^{-1}\xi_x)E + (r\bar{J}^{-1}\xi_r)F, \tag{66}$$

$$\bar{F} = (r\bar{J}^{-1}\eta_x)E + (r\bar{J}^{-1}\eta_r)F, \tag{67}$$

$$\bar{H} = \bar{J}^{-1} \, [0, \; 0, \; -p, \; 0]^T. \tag{68}$$

As before E and F are the inviscid Cartesian flux vectors, but $\bar{H}$ differs. Expressions for the geometric terms appearing in (65)–(68) are calculated at cell interfaces from grid cell vertices (grid points). These evaluations are straightforward for two-dimensional grids, and the reader is referred to [91] for an excellent treatment of the subject (expressions for three-dimensional grids are given in Appendix B).

132

A.1.3 Discretization of the Navier-Stokes Equations. For both procedures, the viscous terms are centrally differenced, while the convective terms are upwind differenced. Discretization of (59) is as follows:

$$\bar{U}_{i,j}^{n+1} = \bar{U}_{i,j}^{n} - \Delta t \left[\left(\hat{\bar{E}}_{i+\frac{1}{2},j}^{n} - \hat{\bar{E}}_{i-\frac{1}{2},j}^{n} \right) + \left(\hat{\bar{F}}_{i+\frac{1}{2},j}^{n} - \hat{\bar{F}}_{i-\frac{1}{2},j}^{n} \right) \right. \tag{69}$$
$$\left. - \left(\bar{R}_{i+\frac{1}{2},j}^{n} - \bar{R}_{i-\frac{1}{2},j}^{n} \right) - \left(\bar{S}_{i+\frac{1}{2},j}^{n} - \bar{S}_{i-\frac{1}{2},j}^{n} \right) + \bar{H}_{i,j}^{n} - \bar{W}_{i,j}^{n} \right].$$

The exact form of $\hat{\bar{E}}$ and $\hat{\bar{F}}$ are provided below. The convective fluxes are typically determined at cell interfaces in two ways, using either MUSCL or non-MUSCL extrapolation. The current scheme uses the non-MUSCL technique; this is discussed in Section 3.1.

The explicit, second-order formulation employed for this study is based on the work of Yee and Harten [104, 33]. The formulation is a modification of Roe's first-order algorithm, and has been referred to in the literature as a modified-flux scheme. This scheme achieves second-order accuracy by applying Roe's first-order, flux-difference-splitting algorithm to a modified inviscid flux. The flux is chosen so that the scheme is second-order accurate in regions of smoothness and first-order at points of extrema (e.g., shocks). When using finite-volume expressions for the geometric terms, the convective flux in the ξ-coordinate direction at the $(i + \frac{1}{2}, j)$ interface is approximated by

$$\hat{\bar{E}}_{i+\frac{1}{2},j} = \frac{1}{2} \left[(r\bar{J}^{-1}\xi_x)_{i+\frac{1}{2},j} (E_{i+1,j} + E_{i,j}) \right. \tag{70}$$
$$\left. + (r\bar{J}^{-1}\xi_r)_{i+\frac{1}{2},j} (F_{i+1,j} + F_{i,j}) + (r\bar{J}^{-1})_{i+\frac{1}{2},j} R_{i+\frac{1}{2},j} \Phi_{i+\frac{1}{2},j} \right].$$

A similar expression is obtained for the hybrid finite-difference/finite-volume approach; only the terms involving metrics differ. The vector Φ acts to limit the characteristic variables, thereby providing higher accuracy. The elements of the vector $\Phi_{i+\frac{1}{2},j}$, denoted by $\phi^l_{i+\frac{1}{2},j}$, are

$$\phi^l_{i+\frac{1}{2},j} = \sigma(a^l_{i+\frac{1}{2},j})(g^l_{i+1,j} + g^l_{i,j}) - \Psi(a^l_{i+\frac{1}{2},j} + \gamma^l_{i+\frac{1}{2},j})\alpha^l_{i+\frac{1}{2},j}, \tag{71}$$

133

where $a^l_{i+\frac{1}{2}j}$ is the characteristic speed evaluated at some average of $U_{i+1,j}$ and $U_{i,j}$ (here with Roe's average [71]). The function, σ, is given by

$$\sigma(z) = \frac{1}{2}(\Psi(z) - \lambda z^2),$$

where Ψ is an entropy correction to $|z|$. It is the same as (31) in Chapter 3. The characteristic speed is modified by γ which is defined by

$$\gamma^l_{i+\frac{1}{2}j} = \begin{cases} \sigma(a^l_{i+\frac{1}{2}j})\frac{(g^l_{i+1j}-g^l_{ij})}{\alpha^l_{i+\frac{1}{2}j}}, & \text{if } \alpha^l_{i+\frac{1}{2}j} \neq 0; \\ 0, & \text{if } \alpha^l_{i+\frac{1}{2}j} = 0. \end{cases} \tag{72}$$

The characteristic variables, $\alpha_{i+\frac{1}{2}j}$, are given by

$$\alpha_{i+\frac{1}{2}j} = R^{-1}_{i+\frac{1}{2}j}(U_{i+1j} - U_{ij}). \tag{73}$$

Finally, the current study uses the *minmod* function, for the limiter function, g^l_{ij}, as follows:

$$g^l_{i+1j} = \text{minmod}(\alpha^l_{i+\frac{1}{2}j}, \alpha^l_{i+\frac{3}{2}j}), \tag{74}$$

or

$$g^l_{i+1j} = \text{sgn}(\alpha^l_{i+\frac{1}{2}j})\left[\max\left(0, \min\left[|\alpha^l_{i+\frac{1}{2}j}|, \text{sgn}(\alpha^l_{i+\frac{1}{2}j})\alpha^l_{i+\frac{3}{2}j}\right]\right)\right]. \tag{75}$$

A.1.4 Boundary Conditions. Due to the supersonic condition at both the inflow and outflow, the boundary conditions are very straightforward. At the inflow, freestream conditions are applied, and at the outflow, two-point extrapolation is used. For the body surfaces, no-slip is applied, zero normal pressure gradient is used, and either constant wall temperature or an adiabatic wall is used. Finally, centerline symmetry is enforced using ghost cells for the finite-volume grid, and second-order expressions for the finite-difference grid.

A.1.5 Stability Analysis for Source Term. Since a source term appears in the governing equations, a scheme developed for a homogeneous system may not be stable. Therefore, a simplified stability analysis was done to anticipate any stability restrictions. Consider a scalar, one-dimensional, nonlinear, inhomogeneous equation of the form

$$\frac{\partial u}{\partial t} + \frac{\partial e}{\partial x} = s. \tag{76}$$

Linearizing the equation yields

$$\frac{\partial u}{\partial t} + A\frac{\partial u}{\partial x} = Bu. \tag{77}$$

Implementing the current algorithm gives:

$$u_i^{n+1} = u_i^n - \frac{A\Delta t}{\Delta x}\left(\frac{u_{i+1}^n - u_{i-1}^n}{2}\right) + \Delta t B u_i^n \tag{78}$$

$$+ \underbrace{\frac{|A|\Delta t}{\Delta x}\left(\frac{u_{i+1}^n - 2u_i^n + u_{i-1}^n}{2}\right)}_{\text{first-order term}} + \underbrace{\frac{|A|\Delta t}{\Delta x}\left(1 - \frac{|A|\Delta t}{\Delta x}\right)\left(\frac{-u_{i+2}^n + 2u_i^n - u_{i-2}^n}{2}\right)}_{\text{second-order term}}.$$

The above form of the equation applies away from discontinuities. Near a discontinuity the second-order term is zero. For the limiter evaluations, it is assumed that a local extrema did not exist. Therefore, without additional loss of generality: $u_{i+2} \geq u_{i+1} \geq u_i \geq u_{i-1} \geq u_{i-2}$. Furthermore, it is assumed that the algorithm does not modify the wave speed (e.g., no entropy correction function). Since the purpose for this stability analysis is to investigate limitations due to the source term, these assumptions should not hinder the analysis.

Using a Fourier stability analysis [1] produces the following relationships for the amplification factor, G:

$$2\text{nd} - \text{order} \quad G = 1 - \nu(i\sin\beta) + |\nu|\left(\frac{\Delta x B}{|A|}\right) + |\nu|(\cos\beta - 1) + |\nu|(1 - |\nu|)\left(\frac{1 - \cos 2\beta}{2}\right)$$

$$1\text{st} - \text{order} \quad G = 1 - \nu(i\sin\beta) + |\nu|\left(\frac{\Delta x B}{|A|}\right) + |\nu|(\cos\beta - 1)$$

where, $\nu = \frac{A\Delta t}{\Delta x}$ and $|G| \leq 1$ for stability.

Enforcing $|G| \leq 1$ produces the following:

$$\text{2nd - order} \quad |\nu|^3 - \left(2\frac{\Delta x B}{|A|}\right)|\nu|^2 + \left[\left(\frac{\Delta x B}{|A|}\right)^2 - 1\right]|\nu| + 2\frac{\Delta x B}{|A|} \leq 0$$

$$\text{1st - order} \quad |\nu| \leq \frac{1 - \frac{\Delta x B}{|A|}}{1 - \frac{\Delta x B}{|A|} + \frac{1}{2}\left(\frac{\Delta x B}{|A|}\right)^2}$$

Note that for $B = 0$, both reduce to $|\nu| \leq 1$, which is the familiar Courant-Friedrichs-Levy (CFL) condition [1]. Clearly, as B gets very large, the stability may be adversely impacted. Referring to (59)–(63), as $r \to 0$, B may get large relative to A for this study, due to the $1/r$ dependence of $\bar{H}$. The actual effect of the source term in the second-order formulation is plotted in Figure 79. This shows that the source term should have negligible impact as the grid is refined.

A.1.6   Turbulence Modeling.   The well known and widely used zero-equation Baldwin-Lomax turbulence model [5] is incorporated for the forebody boundary-layer simulations. The boundary layer is divided into inner and outer regions. In the inner region, the eddy viscosity, μ_i, is given by the Prandtl-van Driest formula

$$\mu_i = \rho(\kappa y D_v)^2 |\omega|, \tag{79}$$

where ω is the vorticity, y is the normal distance from the surface, κ is the von Karman constant (0.4), and D_v is the van Driest damping factor, which is given by

$$D_v = 1 - \exp\left[-\frac{y^+}{A^+}\right]. \tag{80}$$

The superscript "+" in (80) denotes a nondimensional variable; the value of A^+ is 26 for a smooth, nonporous, flat-plate in incompressible flow [101]. The nondimensional

distance, y^+, is

$$y^+ = \sqrt{\frac{y^2 \rho_w |\omega_w|}{\mu_w}}. \tag{81}$$

The subscript "w" denotes conditions at the wall or surface.

In the outer region of the boundary layer, the eddy viscosity is defined by

$$\mu_o = \rho C_{claus} C_{cp} l_{max} F_{max} F_c, \tag{82}$$

where $F_{max} = \max(l|\omega|D_v)$, and l_{max} is the value of l corresponding to F_{max}. The function F_{max} is maximized over the l values at each station. The Clauser constant, C_{claus}, is 0.0168, and the value for the C_{cp} is modified from the incompressible value (explained below). The Clebanoff intermitancy factor, F_c, is given by

$$F_c = \left[1 + 5.5(C_{cleb} l / l_{max})^6\right]^{-1}. \tag{83}$$

The constant, C_{cleb}, is also modified from the incompressible value and is explained below. The turbulence model switches from the inner to the outer formulation at the first (closest to surface) value of l for which $\mu_i > \mu_o$.

Two modifications prove important. The first changes the van Driest damping factor to account for compressibility and pressure gradients [49, 28, 101]. The near-wall region, denoted by A^+, is redefined as

$$A^+ = 26 \cdot N \cdot Z. \tag{84}$$

Again, the non-dimensional distance 26 is the incompressible value for a smooth, non-porous, flat plate [101], N is the pressure gradient contribution, and Z is the compressibility contribution. Both N and Z are defined in Section 3.4 by (39). The second alteration improves the two coefficients in the outer region, C_{cp} and C_{kleb}. These modifications are also outlined in Section 3.4.

137

For a flat base with a large, nearly stagnant region, it is difficult to apply a conventional zero-equation turbulence model. So, a strictly empirical relation is used to compute turbulent viscosity in the wake. This technique was originally applied to subsonic flow in [54]. The method is adapted, and its validity tested, for supersonic flow in this investigation. Turbulent viscosity is determined from (42) in Section 3.2. The method has the advantage of speed and low memory requirement. Although highly empirical, the validity of this approach is shown through numerical examples.

A.1.7 Computer Resources All grids are obtained using GRIDGEN [80], an elliptical grid generator developed for Wright Laboratory, Wright-Patterson Air Force Base, OH. Both finite-volume grid types (cell interface along singular line), and finite-difference grid types (cell center along singular line) are employed. Surface clustering is employed in the generation of all grids. A typical grid, 61 × 61, for the hemisphere-cylinder is shown in Figure 80.

A.2 Integration of the Navier-Stokes Equations for a Laminar Forebody

Numerical simulations are performed for several geometries and flow conditions to assess the general applicability of the methodology developed.

A.2.1 Spherical Nosetip.

A.2.1.1 Adiabatic Wall Results. Freestream conditions representative of flight at an altitude of $30km$ are used. The freestream velocity is varied through the Mach number, and the nose radius is varied through the Reynolds number. Figures 81a and 81b are the pressure and density contours for $M_\infty = 5$ and $R_n = 1m$. The solution fidelity is quite good, and representative of the second-order accuracy. The accurate calculation of stagnation quantities behind the shock, and the precise prediction of the expansion around the sphere are illustrative of the accuracy. A first-order TVD scheme does not predict the stagnation quantities as well, nor does
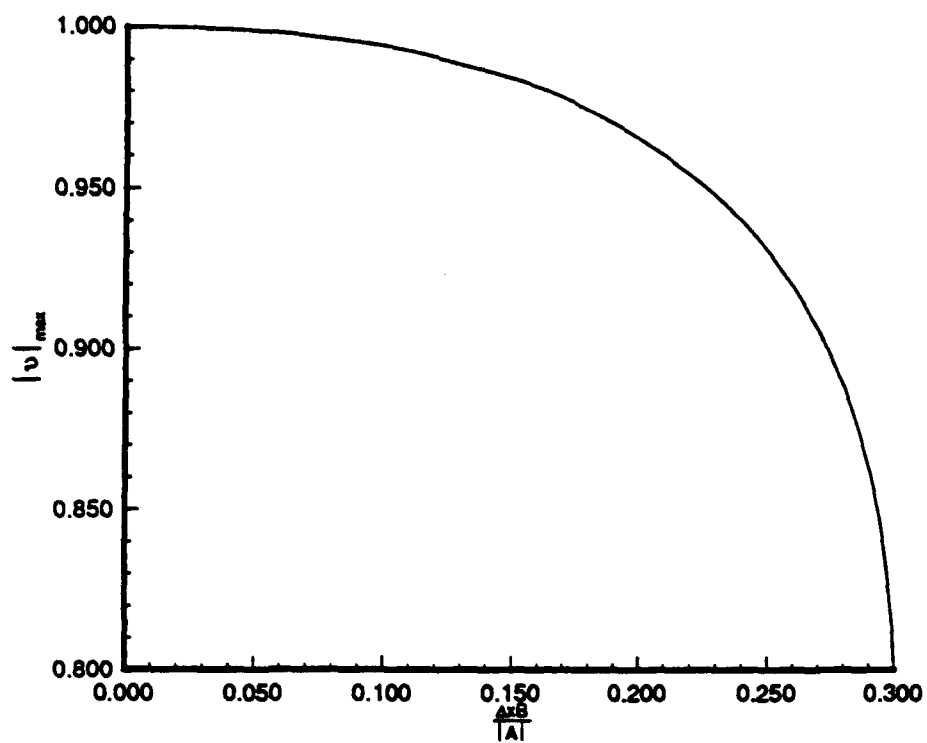
Figure 79. Effect of source term on stability
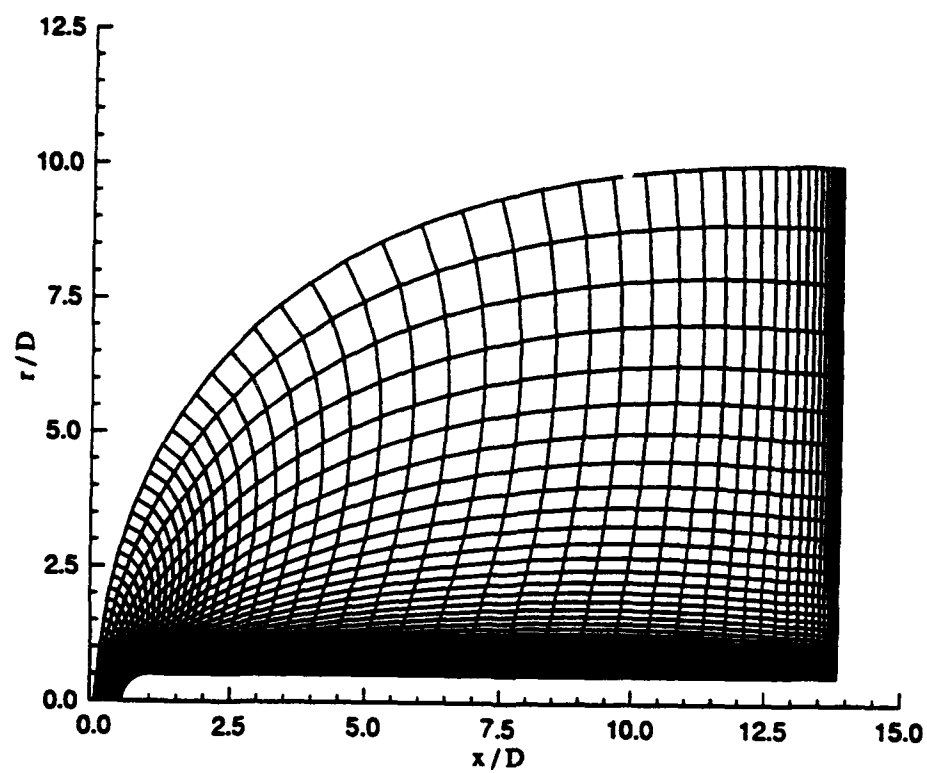
Figure 80. 61 × 61 grid for hemisphere-cylinder

it predict the expansion as precisely [57].

Of primary concern is the surface pressure. Figure 82 is a plot of the nondimensional surface pressure around the body. The stagnation pressure is within 0.5 percent of the value predicted from the normal-shock relations. Also the pressure around the body agrees well with the experimental data of Oliver [62].

For $Pr = 1$, the adiabatic-wall temperature is the stagnation temperature ($T_{aw} = T_0$). This is an excellent test for the adiabatic-wall condition. When Pr was set to 1, the computed temperature was constant to within $1K$ and very close to the stagnation temperature predicted by the normal-shock relations (within $10°$).

A.2.1.2 Cold Wall Results. Freestream conditions representative of flight at an altitude of $30km$ are maintained. A surface temperature of $300°K$ and a nose radius of .66cm are selected to make direct comparisons with experimental data [72]. At these conditions and $M_\infty = 10$, the Reynolds number based on nose radius is $Re_{R_n} = 24,400$.

Again the solution fidelity is very good. Figure 83 is a density contour plot showing the large density gradients across the boundary layer. Note the smooth expansion in the inviscid region, and the growth of the boundary layer around the body. Since surface pressure is perhaps the most important computed quantity, this is examined in detail. No appreciable change in the surface pressure from the adiabatic tests is noted; the same level of agreement with the experimental data of Oliver is achieved using the cold-wall boundary condition.

Heat transfer is much less important for the current study than surface pressure or skin friction, but provides some further measure of overall accuracy. The stagnation point heating is within 15 percent of the experimental value of Rose [72]. Since no chemistry effects are included in the numerical calculations, this level of agreement is good. Away from the shoulder, the heat transfer distribution can be well modeled with a $\cos^{\frac{3}{2}} \theta$ profile [2]. Figure 84 shows the heat transfer distribution
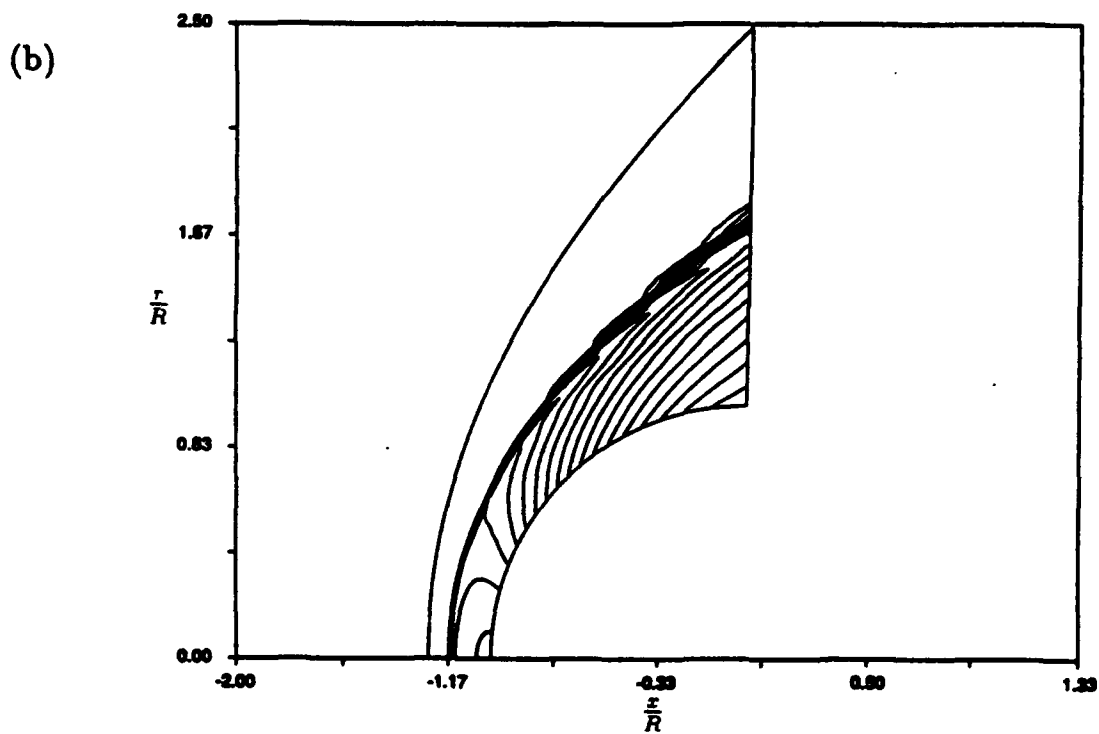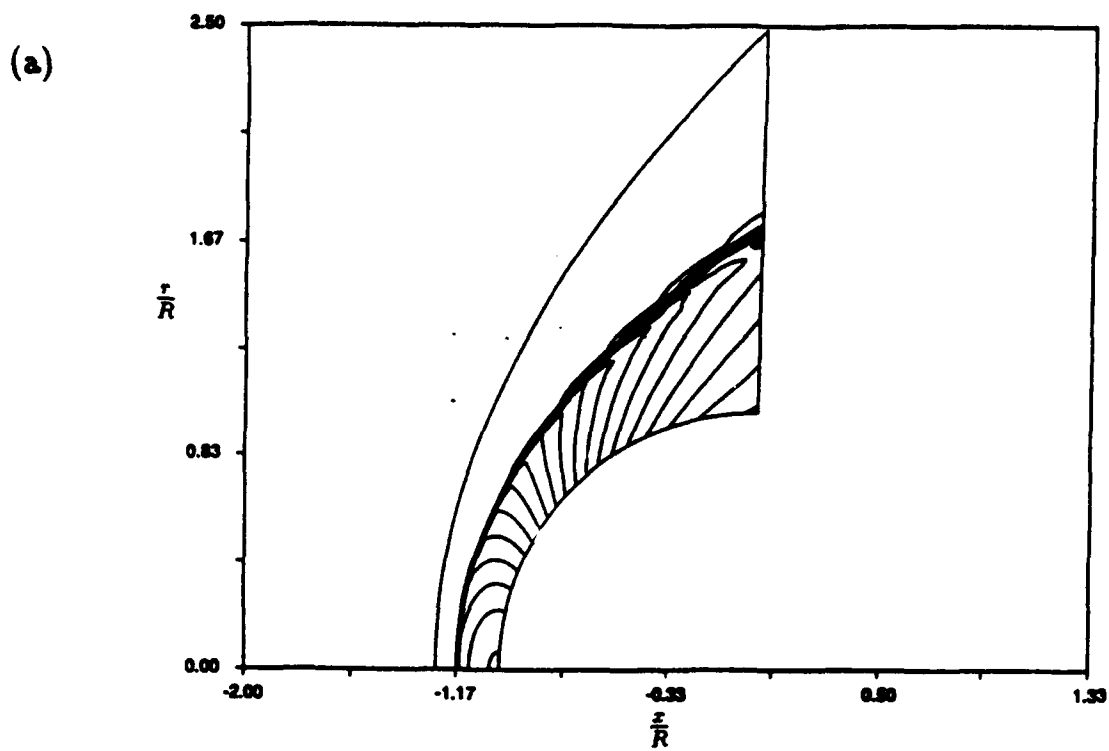
Figure 81.   Nondimensional pressure and density contours ($M_\infty = 5$, $R_n = 1m$, altitude $= 30km$, adiabatic wall) (a) pressure , (b) density
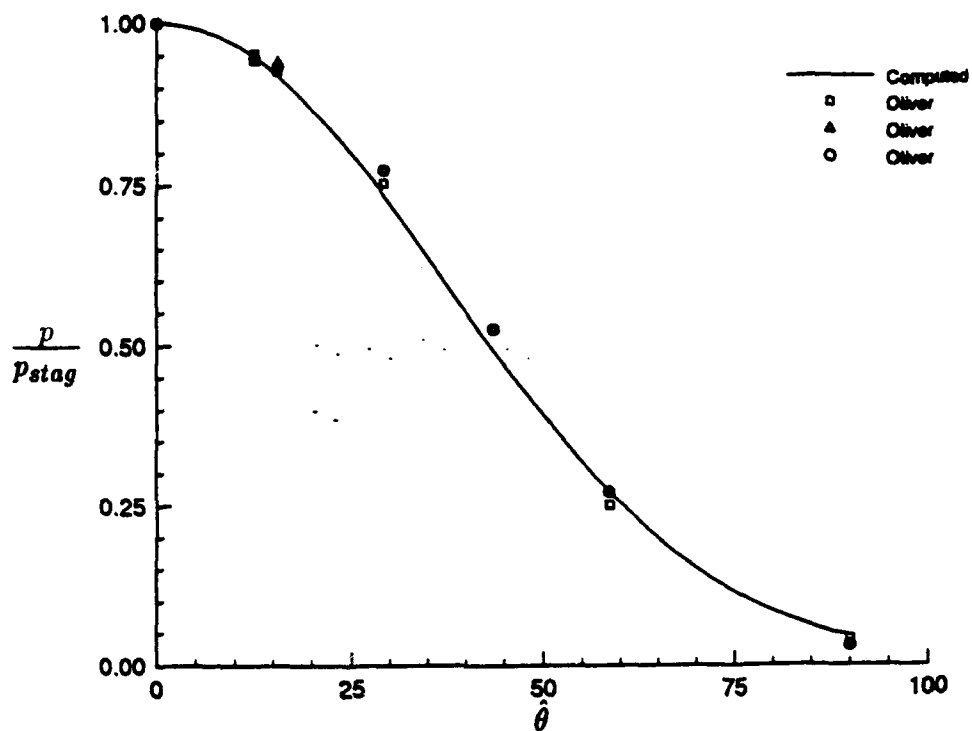
Figure 82. Surface pressure versus angular position: $M_\infty = 5.8$ ($\hat{\theta} = \pi - \theta$ where θ is the body inclination angle given by Figure 16)
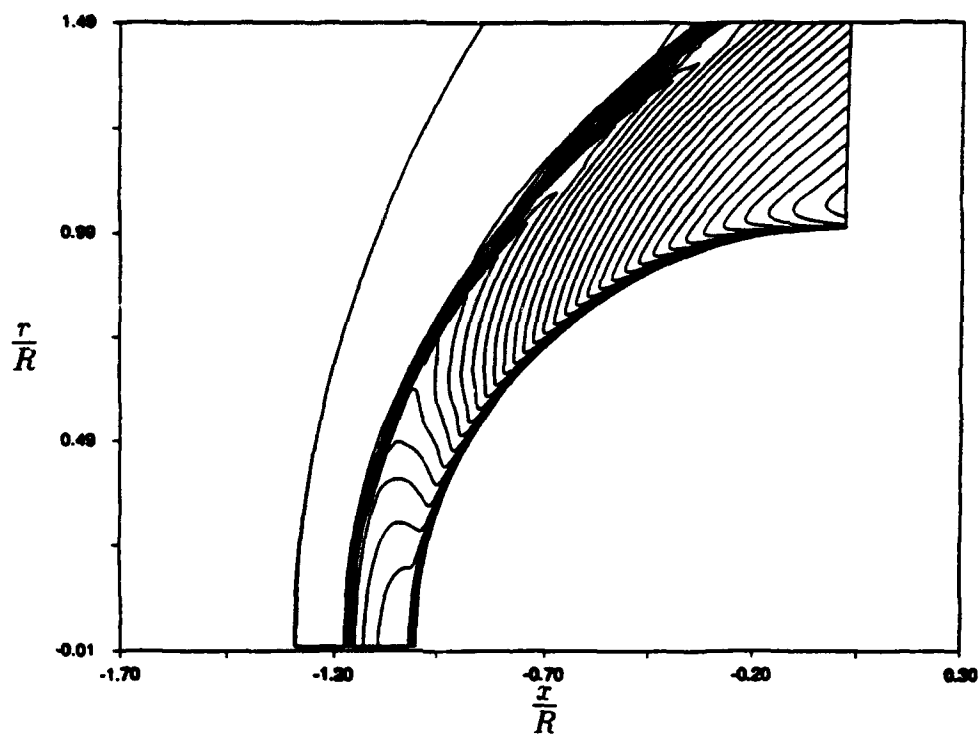
Figure 83. Density contours: $M_\infty = 5$, $R_n = 0.66cm$, altitude $= 30km$, and cold wall

142

nondimensionalized by the stagnation point heating. Note the excellent agreement with the $\cos^{\frac{3}{2}} \theta$ rule.

A.2.1.3 Skin Friction and Heat Transfer Coefficients.

Local skin friction and heat transfer coefficients (C_{f_e} and C_{H_e}) are usually based on local information at the boundary-layer edge. The following relations are used to compute C_{f_e} and C_{H_e}:

$$C_{f_e} = \frac{\tau_w}{\frac{1}{2}\rho_e u_e^2}, \quad and \quad C_{H_e} = \frac{q_w}{\rho_e u_e (h_{aw} - h_w)}, \tag{85}$$

or

$$C_{f_e} = \left(\frac{1}{Re}\right) \frac{\mu_w^* \frac{\partial u^*}{\partial n^*}\big|_w}{\frac{1}{2}\rho_e^* u_e^{*2}}, \tag{86}$$

$$C_{H_e} = \left(\frac{1}{Re\,Pr}\right) \frac{\mu_w^* \frac{\partial T^*}{\partial n^*}\big|_w}{\rho_e^* u_e^* \left[\left(1 + \frac{\gamma-1}{2}M_\infty^2\right) - T_w^* - \left(1 - \sqrt{Pr}\right)(\gamma - 1)M_\infty^2 \frac{u_e^{*2}}{2}\right]}. \tag{87}$$

These relations are only slightly modified when computing C_{f_∞} and C_{H_∞}.

$$C_{f_\infty} = \left(\frac{1}{Re}\right) \mu_w^* \frac{\partial u^*}{\partial n^*}\bigg|_w, \tag{88}$$

$$C_{H_\infty} = \left(\frac{1}{Re\,Pr}\right) \frac{\mu_w^* \frac{\partial T^*}{\partial n^*}\big|_w}{\left[\left(1 + \frac{\gamma-1}{2}M_\infty^2\right) - T_w^* - \left(1 - \sqrt{Pr}\right)(\gamma - 1)M_\infty^2 \frac{u_e^{*2}}{2}\right]}. \tag{89}$$

A reliable set of experimental data for skin friction could not be obtained by the author. However, the order of magnitude agrees with other computational results on similar geometries [2]. Perhaps equally important is the *trend* in skin friction. On a log-log scale, the skin friction should exhibit a linear proportionality with distance around the body, approaching zero at the stagnation point [2]. The heat transfer coefficient should be nearly constant over a fairly large portion of the nose region. Both of these trends can be seen in Figure 85.
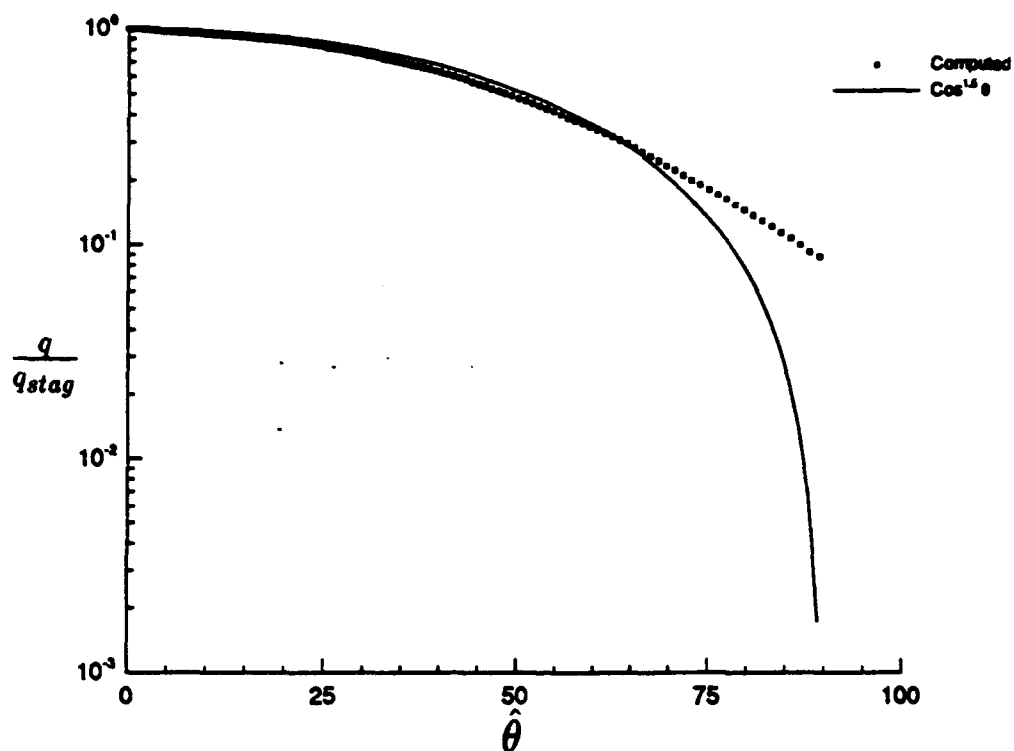
Figure 84. Heat transfer distribution, computed versus theoretical: $M_\infty = 7$, $R_n = 5cm$, altitude $= 30km$, and cold wall
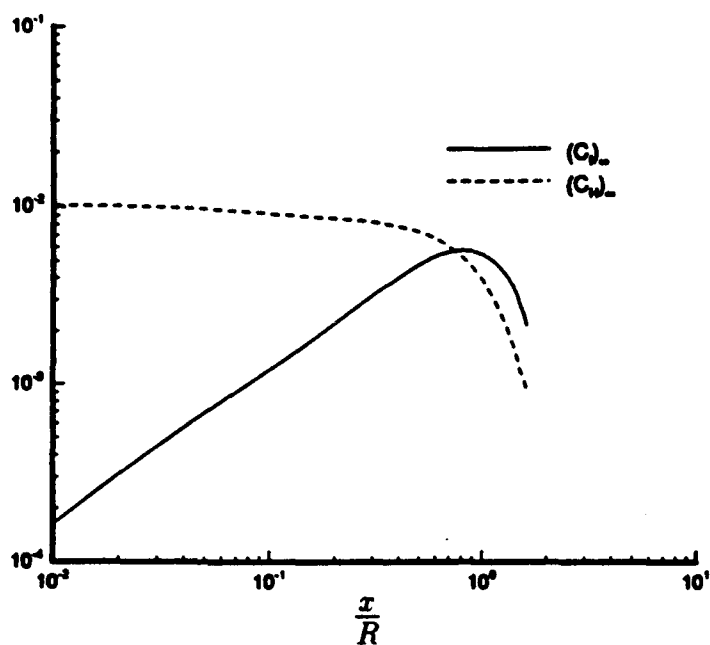
Figure 85. Computed skin friction and heat transfer coefficients: $M_\infty = 7$, $R_n = 5cm$, altitude $= 30km$, $\text{Re}_D = 259,000$, and cold wall

144

A.2.1.4 Effect of Nose Radius on Stagnation Heating. The behavior of
a computational model when various parameters (e.g., M and Re) are changed is
a good indication of its accuracy. In other words, the computational procedure
may give remarkably good results at one set of conditions, but unexpectedly poor
results at some other conditions. Since a well known trend in stagnation point
heating exists $\left(q_w \propto \frac{1}{\sqrt{R_n}}\right)$, the nose radius is systematically varied to test accuracy
in this somewhat broader sense. Calculations are done with three grids of successive
refinement. The three grids are 61×61, 91×91, and 121×121, with spacing near the
surface equal to $0.01D$, $0.001D$, and $0.0001D$, respectively. The results are shown in
Figure 86. The variation in stagnation heating clearly follows the $\frac{1}{\sqrt{R_n}}$ theory. Note
that a finer grid is required to model accurately the thinner boundary layers, that
develop at higher Reynolds numbers.

A.2.2 Hemisphere-Cylinder (HC). The experimental data for flow over a
hemisphere-cylinder [47], provides a more complete basis for evaluating the accu-
racy of computed solutions both near the body and away from the body. Again,
laminar flow is assumed in all simulations for this configuration.

The experiment was conducted in the continuous flow, closed return, hy-
personic, wind tunnel located at the California Institute of Technology. Com-
puted solutions are compared to experimental estimates of shock location, sur-
face pressure, and impact pressure. For the experiment, the reservoir pressure was
$2.17 \times 10^6 N/m^2 \pm 0.01\%$, the supply temperature was $645°K \pm 0.4\%$, and the Mach
number was $7.7 \pm 1\%$. At Mach 7.78, the freestream test conditions correspond to
$Re = 9.2 \times 10^6/m$. The experimental model was 19.1 mm in diameter (Figure 78).
Measured surface pressure and impact pressure are accurate to within 2%; shock
slope and position are accurate to within 3% [47].

Except where noted, all solutions are obtained using $T_w = 700°K$, local time
stepping, and the cylindrical transformation, (59)–(63). Table 20 summarizes the

145
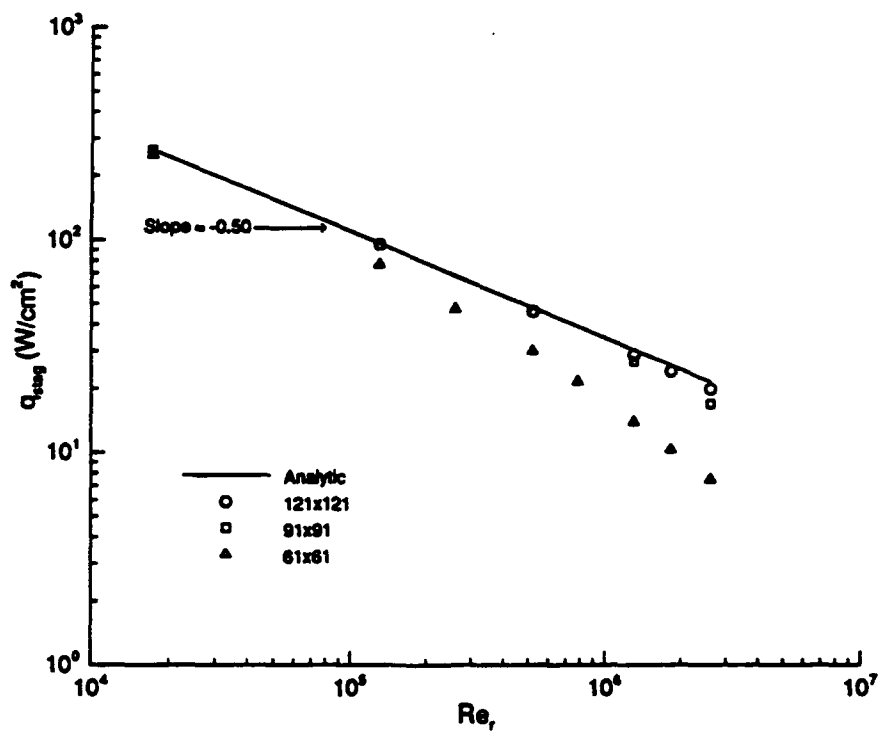
Figure 86.   Effect of nose radius on computed stagnation heating: $M_\infty = 7$, $R_n = 5cm$, altitude $= 30km$, and cold wall

146

case history of numerical experiments. The distance along the body is s, and θ is the angular spacing near the symmetry line. The grid type [finite-volume (FV) or finite-difference (FD)] has an undesirably large influence on the solution character near the stagnation point. Again, a FV grid has cell interfaces on the symmetry line, while a FD grid has cell centers on the symmetry line. As seen in Figure 87, the FV grid produces a local aberration in the pressure, manifested as an over-prediction in stagnation pressure. It is important to note that this error is not the same as distortions in the stagnation region reported in the literature as "carbuncles" [63, 43]. This phenomenon does not appear to begin at the shock, and is not accompanied by recirculating flow as with the carbuncle. The entropy function appears to prevent effectively the carbuncle anomaly. Since similar calculations, using MUSCL extrapolation to achieve higher accuracy [43], do not demonstrate this error, the author believes non-MUSCL extrapolation accentuates the geometric singularity when using a FV grid. According to Palmer and Ventkatapathy [63], the "key to effectively treating the singularity line boundary lies not in boundary conditions themselves, but rather in the proper determination of the metric and flux terms on the singular line." This observation is underscored by the results of this work. A different form of extrapolation (non-MUSCL versus MUSCL) is used in the current scheme, as well as cylindrical versus Cartesian equations. None the less, either technique works well when using a FD grid (Figure 88). For the remainder of tests on this geometry, and the rest of the validation study, a FD grid is employed.

Since the entropy correction function is not used in the boundary layer on the nose and forebody computations, its magnitude primarily affects the solution away from the body. As previously stated, the entropy correction function is made large enough to prevent non-physical solutions; increases beyond that point affect stagnation pressure less than 0.2%.

The grid-refinement experiments (Cases 1-6) are evaluated by examining the stagnation pressure as a function of the node spacing at the surface, $\Delta\left(y/D\right)_{\min}$,
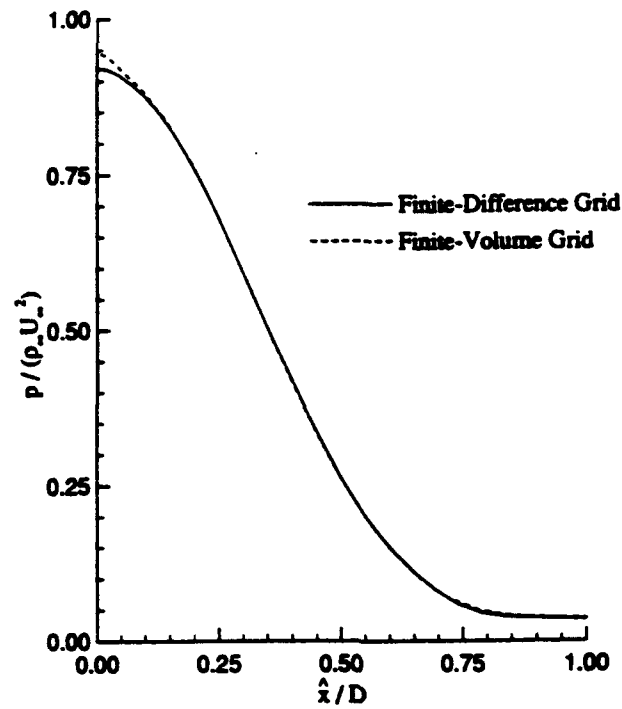
Figure 87. Aberration in surface pressure near the stagnation point ($\alpha = 0°$)
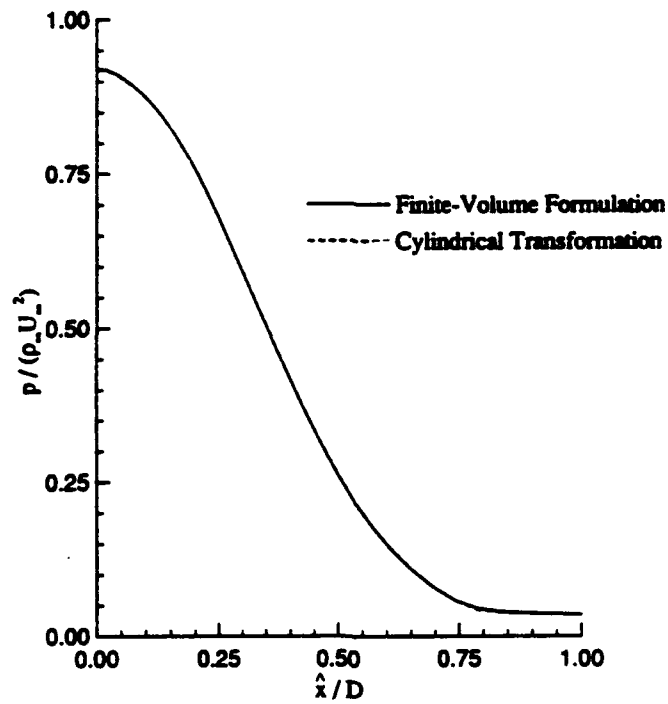
Figure 88. Comparison of surface pressure for modified solution procedures

148

and the node spacing at the singular line, $\Delta\theta_{\min}$. The computed stagnation pressure is compared to the value predicted from inviscid, perfect gas theory. The computed stagnation pressure accuracy depends primarily on the grid spacing, along the body, near the symmetry line; the error decreases as this spacing decreases. The effect due to spacing at the singular line is shown in Figure 89. The computed pressure (nondimensional) appears to approach asymptotically the theoretical value of 0.925. The values differ by about 2% for the coarsest grid and less than 0.5% for $\Delta\theta_{min} \approx 0.57°$ (see Table 19). In contrast, stagnation pressure error is virtually unaffected by grid refinement normal to the body, and varied $<$ .1% for the range of spacing tested, $.0001 \leq \Delta(y/D)_{\min} \leq .001$ (see Table 18). Although not compared to an exact solution, surface pressure away from the stagnation point exhibits identical sensitivity to grid refinement. A comparison with experiment is shown in Figure 90 for Cases 1 and 7. Agreement within experimental accuracy is achieved. The computed pressure contours illustrate that shock location and shape are also accurately predicted (Figure 91). A notable exception is the slight over prediction in standoff distance, which the author attributes to the perfect gas assumption. Finally, impact pressure profiles examined at a station downstream of the nose, $\hat{x}/D = 3$ are given in Figure 92 for Cases 1, 3, 7, and 10. There are two important results from the comparisons of the impact pressure profiles. First. as with surface pressure, grid refinement does not appreciably alter the solutio   the body. Second, although undocumented by the experiment, an adiabatic-wall condition matches the experimental data best. Again, agreement within the experimental accuracy is achieved.

A.2.3 Highly Blunted Tangent Ogive-Cylinder (HBTOC). This is the longest model used ($L/D = 23$), and is particularly blunt in comparison to other tangent ogive models tested. Its length, highly blunted nose, and flat base make it a demanding choice for full-configuration analysis. To increase the demand on the algorithm, the solution is impulsively started from freestream initial conditions. These conditions are set to match those of the ballistic gun range testing facility at Eglin AFB.

Table 20. Summary of numerical experiments for hemisphere-cylinder

Case	Grid Size	$\Delta(s/D)_{min}$	$\Delta\theta_{min}$	Comments
1	61 × 61	0.0390	4.49	$\Delta y/D = .001$, Finite-Difference (FD) Grid
2	91 × 61	0.0150	1.72	"
3	121 × 121	0.0100	1.15	"
4	121 × 121	0.0075	0.86	"
5	121 × 121	0.0050	0.57	"
6	121 × 181	0.0100	1.15	"
7	121 × 181	0.0100	1.15	$\Delta y/D = .0001$, FD Grid
8	121 × 181	0.0100	1.15	Global Time Step (GTS), FD Grid
9	121 × 181	0.0100	1.15	FV Metrics, GTS, FD Grid
10	121 × 181	0.0100	1.15	Adiabatic Wall, GTS, FD Grid
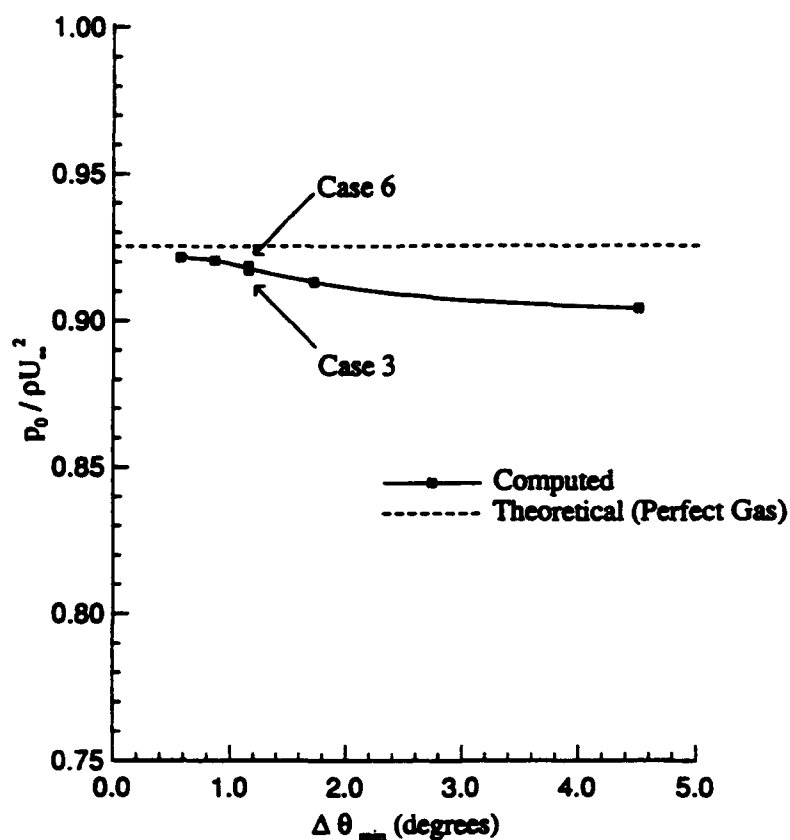
Figure 89. Sensitivity of stagnation pressure to refinement of node spacing near the axisymmetry line

150
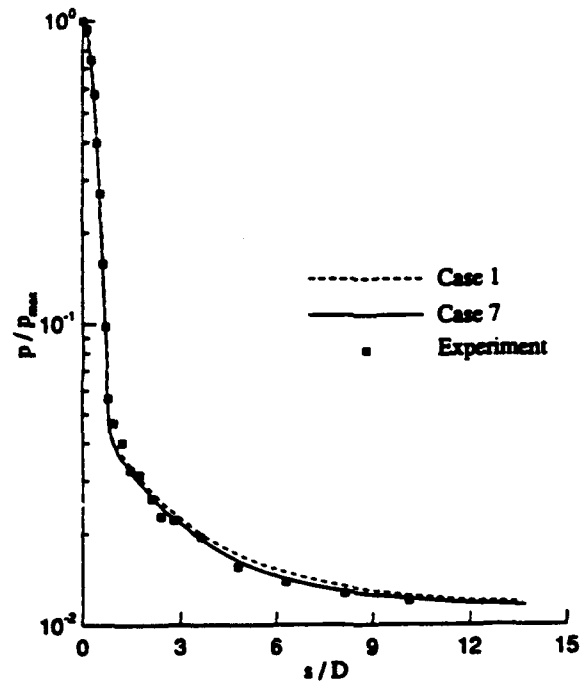
Figure 90. Surface pressure, Case 1 and Case 7
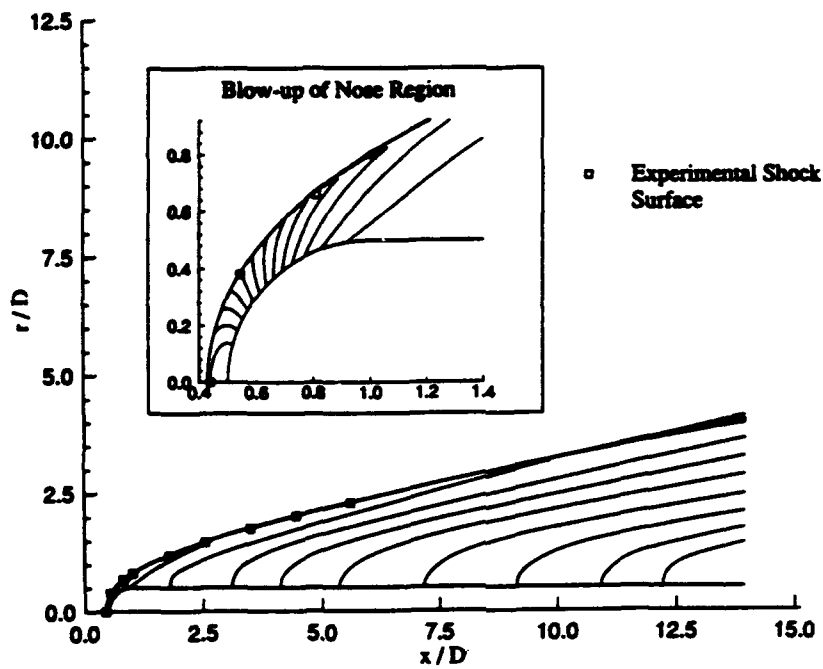
Figure 91. Pressure contours, Case 7

151
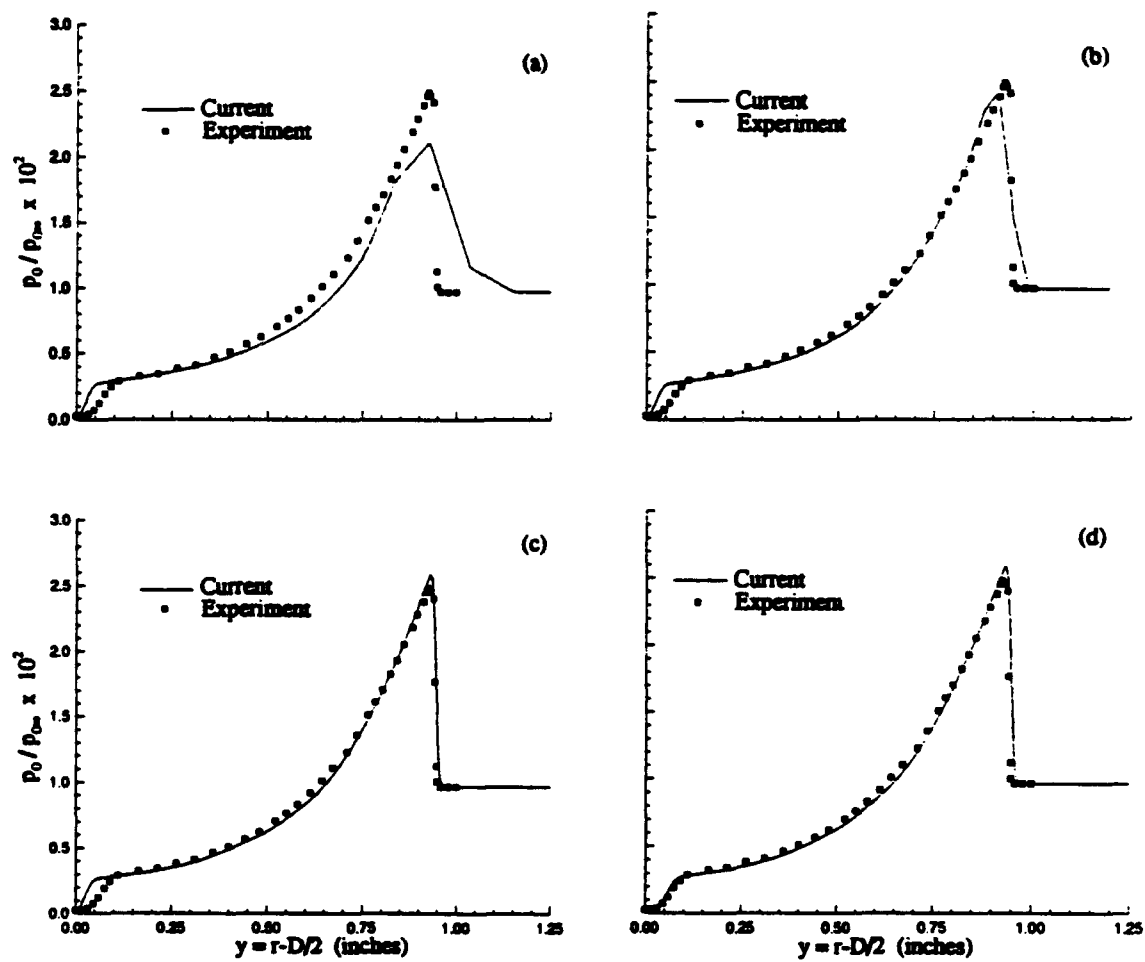
Figure 92.   Impact pressure ($\hat{x}/D = 3$): (a) Case 1, (b) Case 3, (c) Case 7, (d) Case 10

A description of the system is given in [93]. This is essentially an open atmosphere system, so standard sea-level conditions are chosen. To provide an unambiguous baseline for subsequent turbulent calculations, strictly laminar flow is simulated on this configuration.

The computed solution for $M_\infty = 3$ and $Re = 6.99 \times 10^7/m$ is presented in terms of pressure contours and surface pressure in Figures 93(a) and 93(b) respectively. The effects of the highly blunted nose are evidenced by the relatively long recovery of surface pressure to the freestream value.

A.3 Computations for a Pointed and Blunted Tangent Ogive-Cylinder (PTOC and BTOC) in Turbulent Flow

The turbulent boundary layer on a projectile or missile is affected by the nose geometry for several reasons. First, the transition to turbulent flow is affected by the higher entropy, lower Mach number fluid near the stagnation point of blunt noses. Second, the vorticity associated with shock curvature interacts with the boundary layer downstream of the nosetip. Third, for the case of a flat nosetip, the flow separates. Therefore, a series of nose shapes are investigated to evaluate the accuracy of the current algorithm to calculate a developing boundary layer, under differing upstream conditions. Experiments are used for comparison [12].

The experiments were carried out in the Princeton University 20×20 cm, supersonic, high Reynolds number, blow-down tunnel [12]. The reservoir pressure was 6.8×10^5 $N/m^2 \pm 1\%$ and the supply temperature was $265°K \pm 5\%$. At Mach 2.95 these correspond to $Re = 6.3 \times 10^7/m$. The experimental models were 4.95 cm in diameter and are shown in Figure 78. To distinguish between the nose shapes, the experimental terminology is adopted; tip 'P' refers to the pointed model, tip 'F3' refers to the flat nose model, and tip 'R3' refers to the spherically blunted model.

During the Princeton experiments, the wall temperature remained within 3% of the adiabatic value. Boundary-layer transition occurred at $s/D \sim 0.9 - 1.5$ for
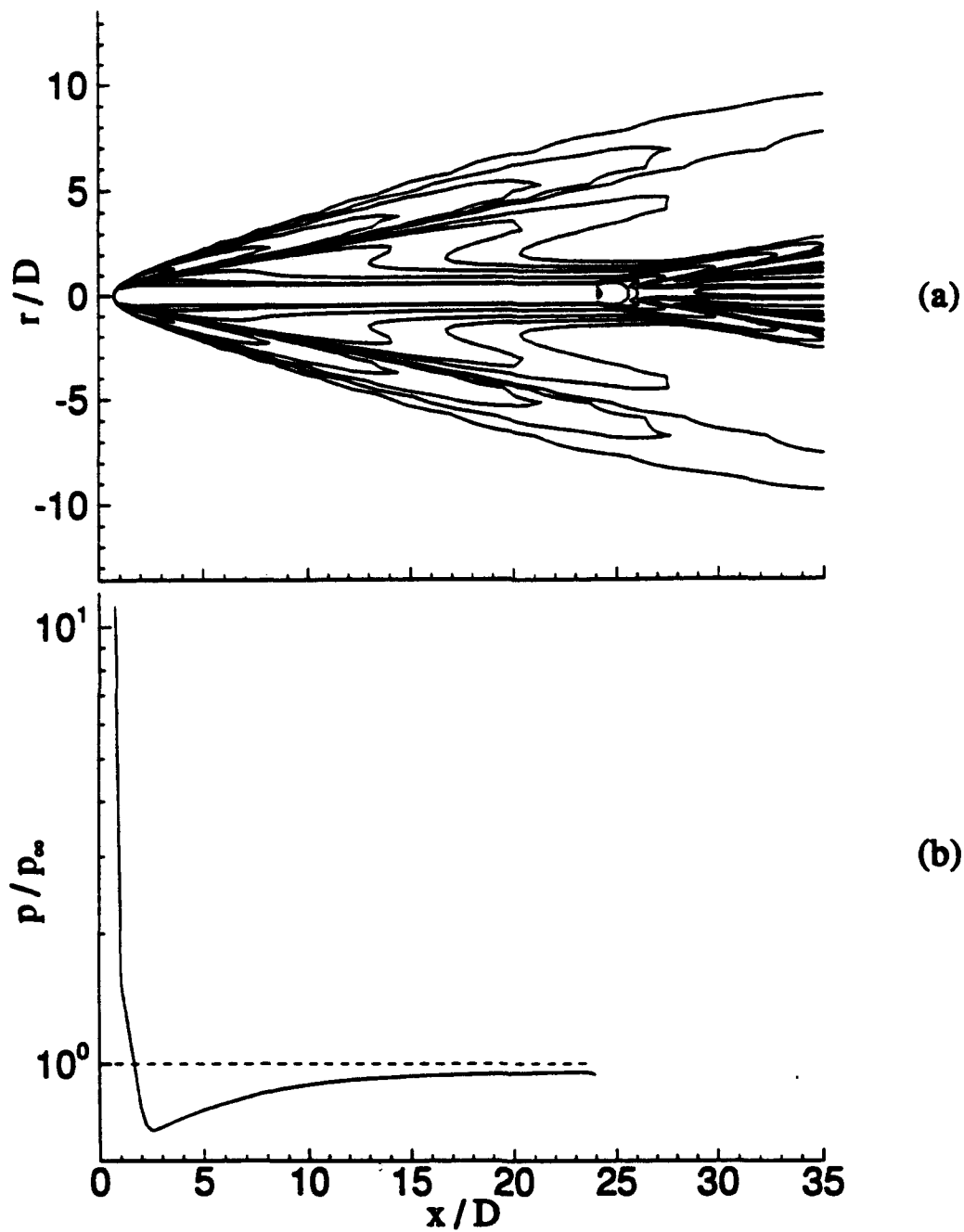
Figure 93. Solution for highly-blunted, tangent-ogive/cylinder ($M_\infty = 3.0$, $\alpha = 0°$, 5612 grid points): (a) pressure contours, (b) surface pressure

154

tip P, at $s/D \sim 0.7 - 1.1$ for tip F3, and at $s/D \sim 1.5 - 2.5$ for tip R3, where s is the distance along the surface from the stagnation point. The accuracy in the surface pressure measurements was $\pm 1.0\%$. However, variations in the data due to changing stagnation conditions over the duration of the experiments showed a stagnation pressure variance of about $\pm 3\%$.

Boundary-layer transition is not simulated. Rather, a point of transition to a fully turbulent boundary layer is specified. Downstream of this point, the turbulence model is used. These "transition" points are $s/D = 0.8$, $s/D = 1.0$, and $s/D = 1.7$ for tips F3, P, and R3 respectively. The performance of the algorithm is not adversely affected by the abrupt change in effective viscosity (a small variance is detectable in the pressure at the surface).

It is well known that Roe-type approximate Riemann solvers, which include information about all waves, can calculate accurately boundary layers with relatively coarse meshes [90]. Therefore, the grid-refinement analysis concentrated on the appropriate spacing nearest the body. For turbulent flow computations, the velocity gradients at the surface vary significantly with grid spacing normal to the surface. However, there are no further variations for grid refinement equivalent to $l^+_{\text{wall}} < 1$; see Table 18 (l^+ is the distance from the body surface nondimensionalized using shear velocity as given in [5]). For $l^+_{\text{wall}} \approx 1$, the time-averaged velocities in the turbulent boundary layer are compared to the law of the wall/law of the wake. Velocity error throughout the boundary layer is $\pm 0.2\%$ (see Table 19). This is an appropriate comparison, since the Baldwin-Lomax turbulence model was developed to produce law of the wall/law of the wake profiles.

Surface pressures are computed to within experimental accuracy; a comparison is shown in Figure 94 for tips P, R3, and F3. Also shown is the computations of [30] for tip R3. Figure 95 shows the comparison for the first six pressure taps on the nose of tips R3 and F3. The current calculation shows expansion on tip F3 slightly sooner than the experimental data. The pressure rise due to the recompression shock

is accurately predicted, however.

Since boundary-layer development is sensitive to a pressure gradient, the modifications to the turbulence model described earlier prove important in this region. Figure 96 shows computed velocity profiles for tip R3 using the original Baldwin-Lomax turbulence model and the modified model. The computations of [30] are also included for comparison. In [30], the original Baldwin-Lomax model and a transition model (polynomial function) were used; transition was initiated at $s/D \approx .5$, and fully turbulent conditions were achieved at $s/D \approx 1.5$. Results from [30] agree qualitatively with the current results using the original Baldwin-Lomax model. The author attributes differences between the current calculations using the original model and those of [30] to differences in transition modeling. Significant improvement with the modified Baldwin-Lomax model is visible.

The boundary layer thickens quickly downstream of the transition point. This is discernible from the vorticity contours (Figure 97a). The vorticity associated with the bow-shock interacts with the rapidly thickening boundary layer near the ogive-cylinder shoulder. The vorticity contours clearly depict that the shock layer and boundary layer merge. The arrow in Figure 97b shows the approximate point above the surface where this merger can be seen for $x/D = 3.26$. The small depression in the velocity profile is further evidence of the interaction.

Computed profiles from the modified model are also shown for tips P and F3 in Figures 98 and 99, respectively. Excellent agreement with experiment is again obtained, with the exception of the final station on tip P. The author has no explanation for this isolated discrepancy.

Separation on the flat nose tip, $F3$, is visible in the streamlines produced from the current calculations (Figure 100). The extent of the separation region is approximately 1 caliber. Although separation was not clearly visible in the experimental data, this result agrees both qualitatively and quantitatively with the calculations of [30].

156
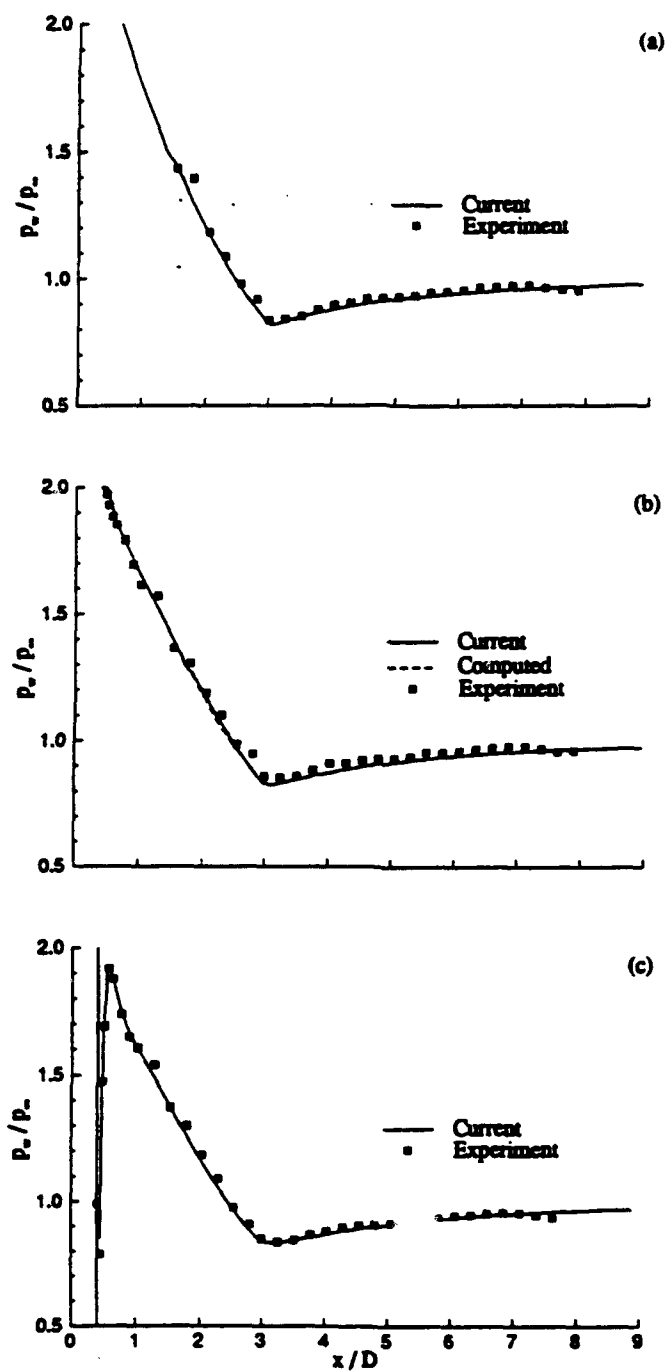
Figure 94. Surface pressure for tangent-ogive/cylinder ($M_\infty = 2.95$, $\alpha = 0°$): (a) tip P, (b) tip R3, (c) tip F3

157
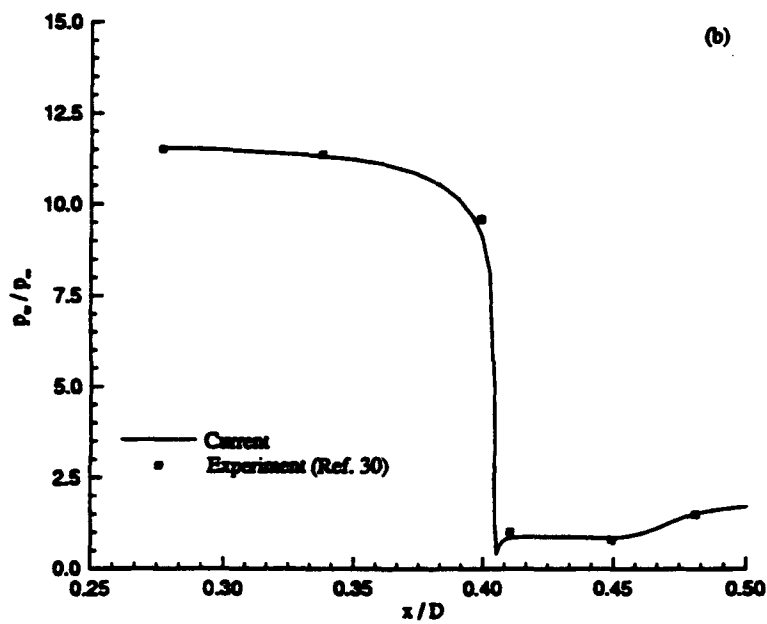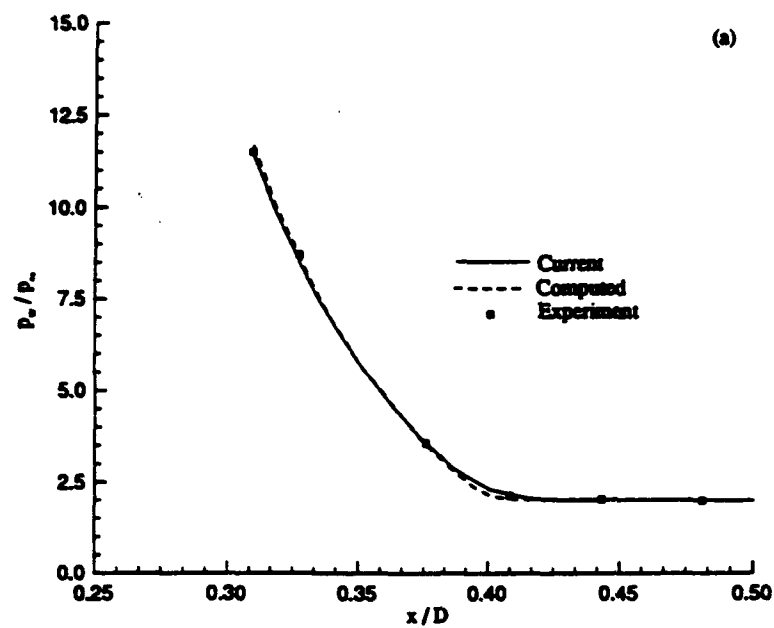
Figure 95. Surface pressure in nose region of a tangent-ogive/cylinder ($M_\infty =$ 2.95, $\alpha = 0°$): (a) tip R3, (b) tip F3

158
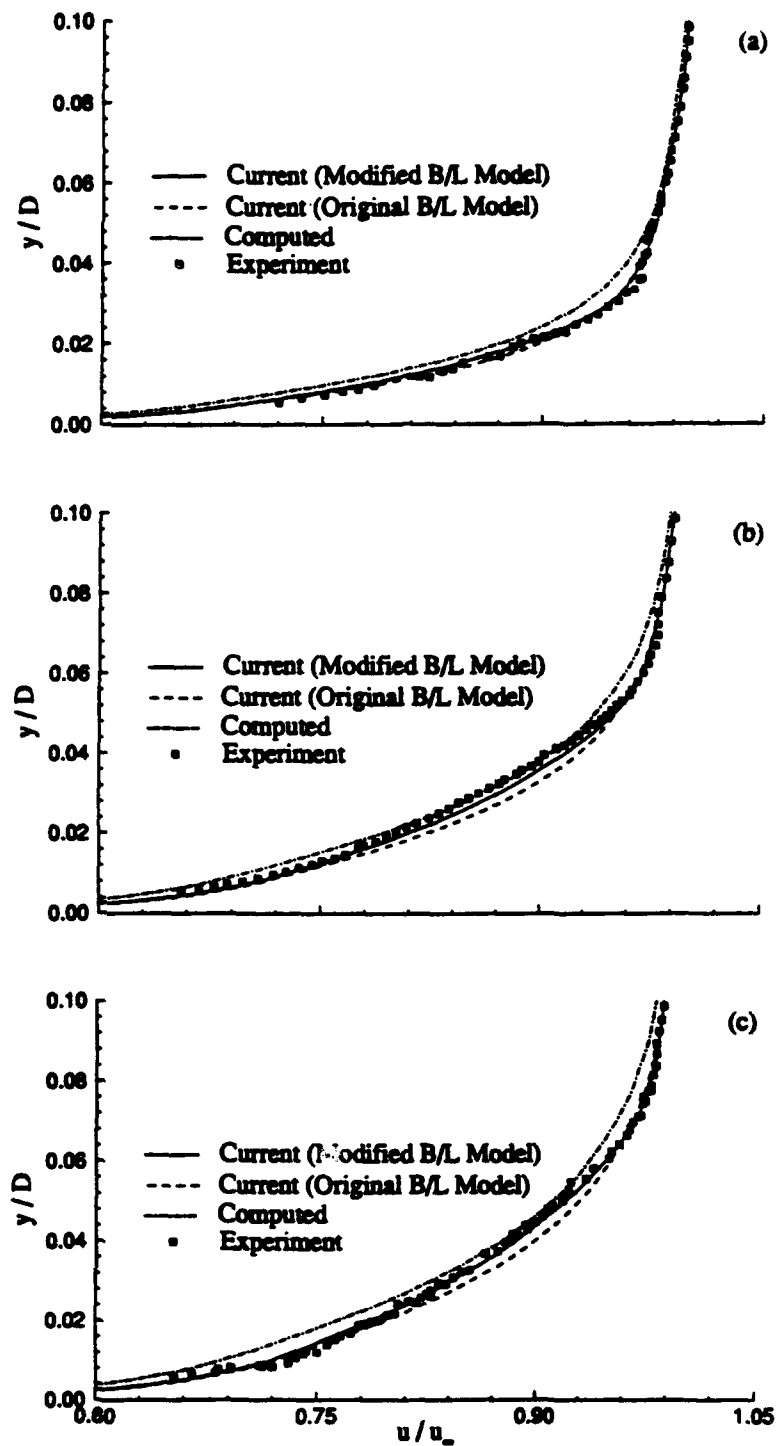
Figure 96. Velocity profiles for tangent-ogive/cylinder ($M_\infty = 2.95$, $\alpha = 0°$, tip R3): (a) $x/D = 3.26$, (b) $x/D = 5.05$, (c) $x/D = 6.33$

159
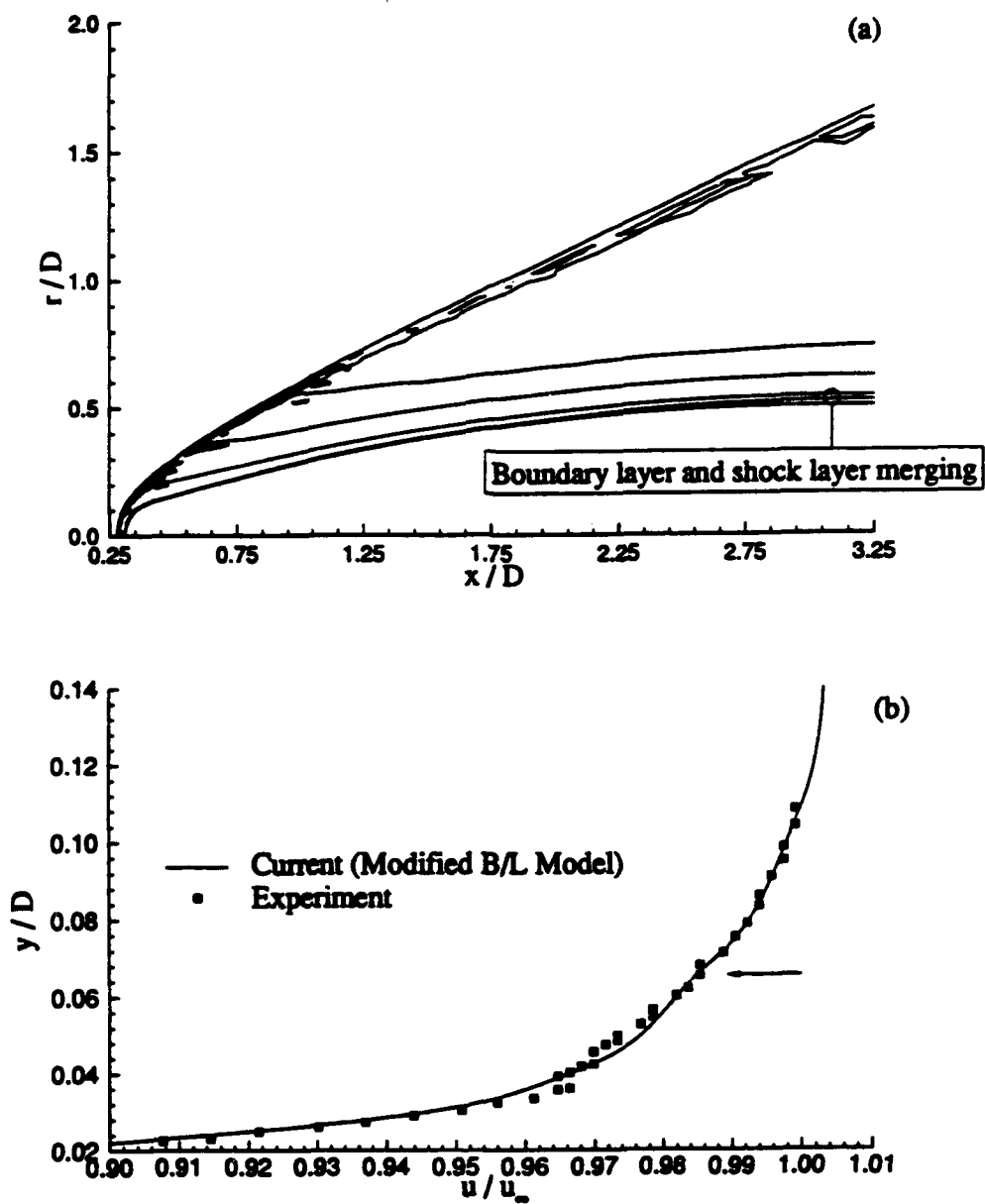
Figure 97.   Vorticity interaction on a tangent-ogive/cylinder ($M_\infty = 2.95$, $\alpha = 0°$, tip R3): (a) vorticity contours, (b) velocity profile at $x/D = 3.26$
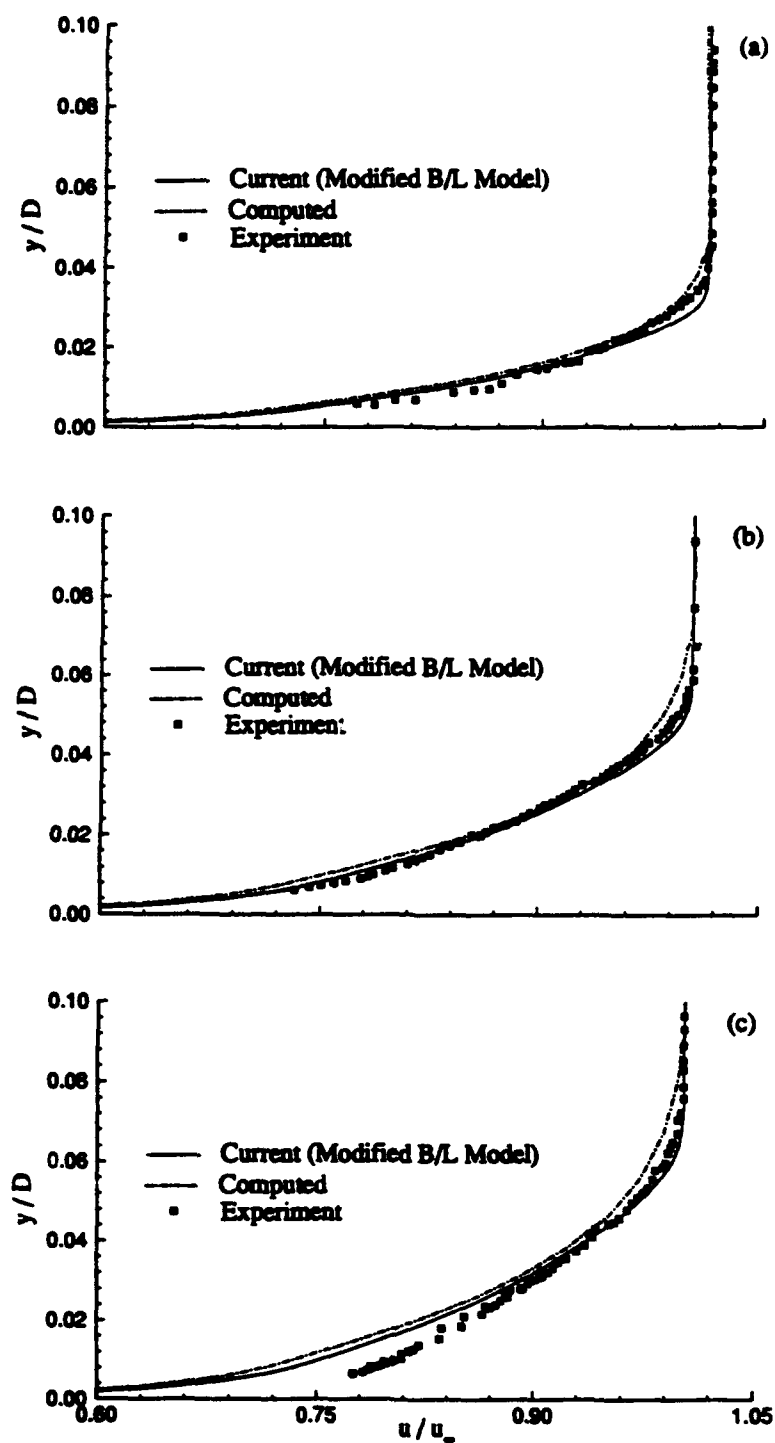
Figure 98. Velocity profiles for tangent-ogive/cylinder ($M_\infty = 2.95$, $\alpha = 0°$, tip P): (a) $x/D = 3.26$, (b) $x/D = 5.05$, (c) $x/D = 6.33$

161
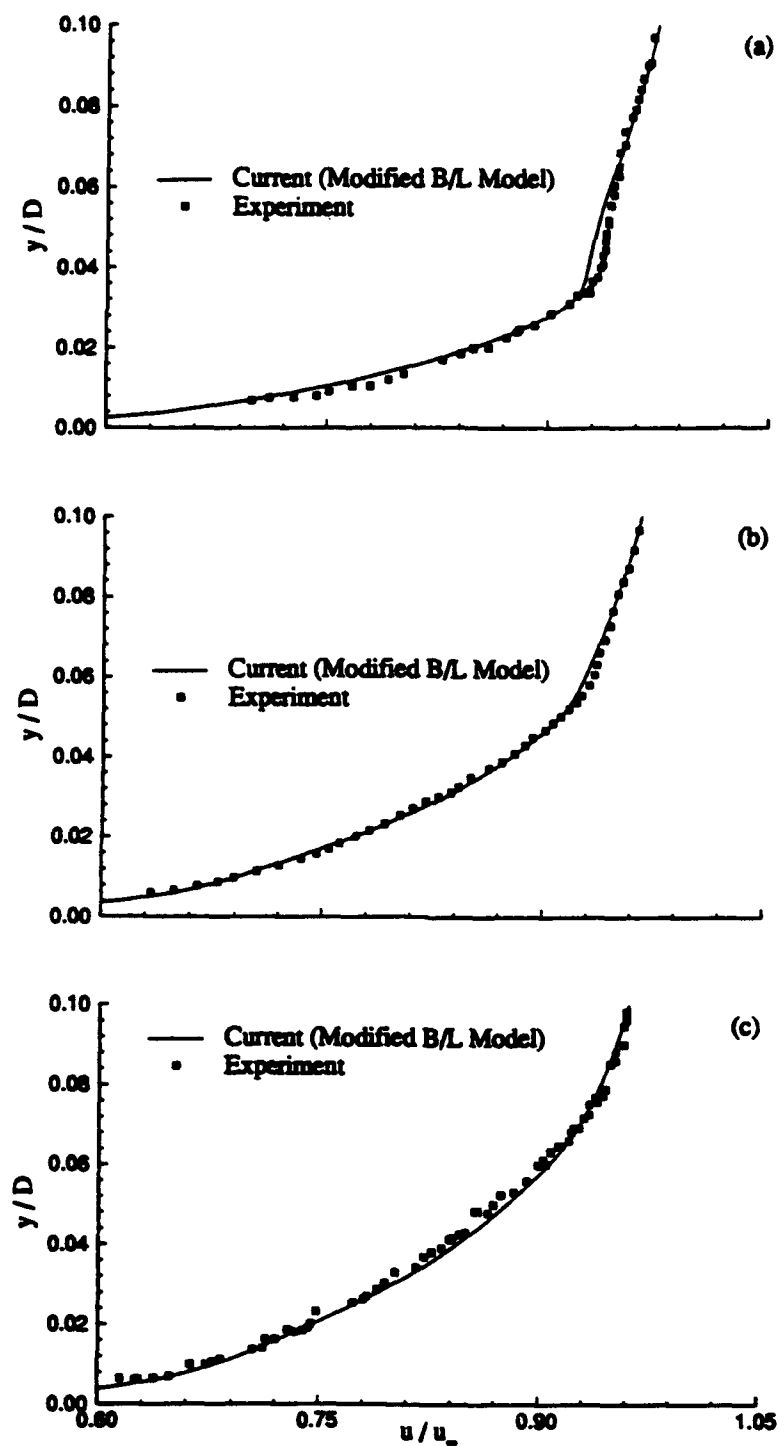
Figure 99.   Velocity profiles for tangent-ogive/cylinder   ($M_\infty = 2.95$, $\alpha = 0°$, tip
F3): (a) $x/D = 3.26$, (b) $x/D = 5.05$, (c) $x/D = 6.33$

162
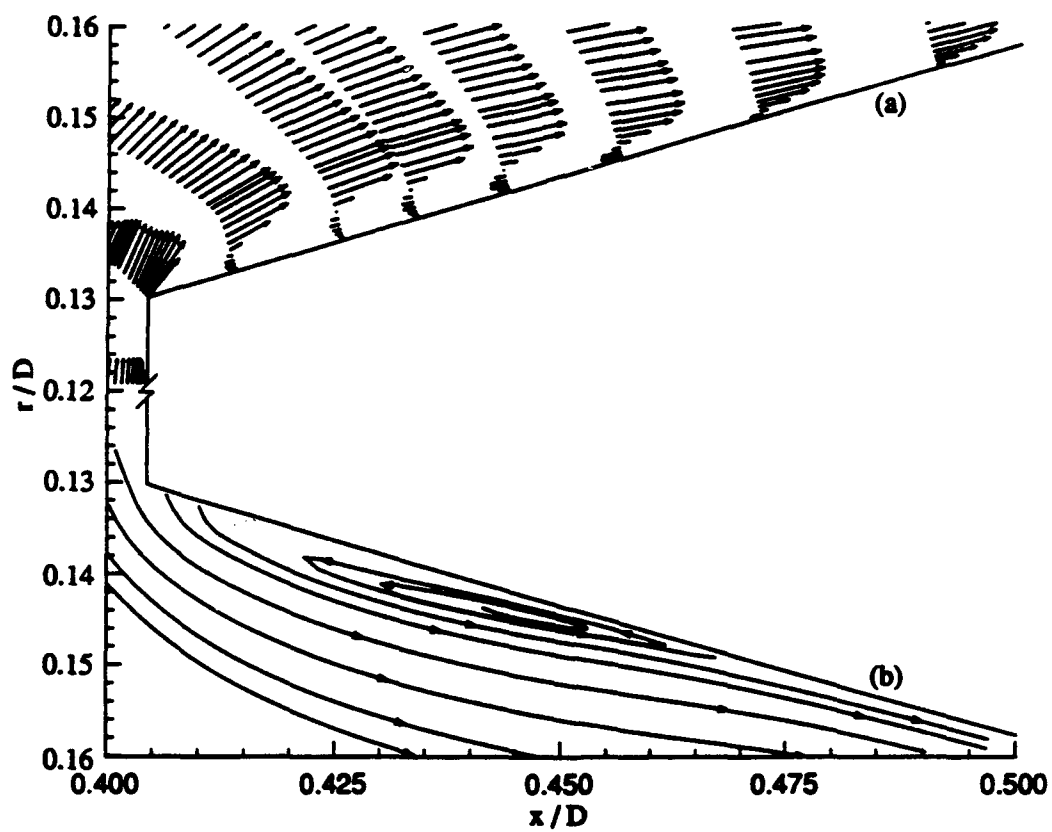
Figure 100. Separation on flat nose tip (tip F3): (a) velocity vectors, (b) streamlines

A.4 Calculations for a Cylinder-Flat Base (CFB) Configuration Using an Empirical Turbulence Model

To establish the validity of the wake-region turbulence model, the analysis is done with the base flow isolated from the forebody. The computational model has a small cylindrical section ($\approx .05D$) prior to the flat base allowing upstream influence of the corner expansion within the boundary layer. The boundary-layer solution, specified at the inflow boundary of the computational domain, is taken from theory [101]. Upstream of the corner, the modified Baldwin-Lomax model is used. Downstream of the corner, (42) is implemented. Over the range of Mach numbers, the Reynolds number is held fixed at $Re_D = 5 \times 10^5$.

The compiled experimental measurements [31, 10, 53, 66, 38, 11] are all for pointed, cylindrical, unfinned bodies with $L/D \approx 10$, and turbulent flow at the body/base corner. The exception is [38] which had fins and $6.5 \leq L/D \leq 30$. For all bodies, $Re_L = 2$ to 9×10^6.

The computed solution at the rearward stagnation point exhibits behavior similar to the forward stagnation point; local aberration in pressure results in an overprediction at the stagnation point. Although some improvement results from using a FD grid type, the pressure still varies across the base an order of magnitude above experimental measurements. By increasing the coefficient in the entropy correction function to 0.85, much better behavior is seen (Figure 101). The effect of changing the entropy function on the total or integrated base pressure coefficient is small (about 4%). Therefore, all base flow numerical experiments were conducted with $\epsilon = 0.85$. It is very important to keep in mind that entropy corrections manifest themselves as additional artificial dissipation in the algorithm. In addition, a universal function does not yet exist, and they remain very geometry dependent. Due to the empiricism of the turbulence model, a more rigorous approach is not attempted.

The integrated pressure coefficient compares very well with the experimental data (Figure 102). In spite of its empiricism, the wake turbulence model accurately

simulates the macroscopic nature of the flow.

A.5 Convergence Acceleration Techniques for Steady-State Computations

Local time stepping is used to accelerate the solution to steady-state. The convergence criterion is the reduction of the correction norm, $||\Delta^n U||_2$, by 5 orders of magnitude from the initial conditions. The correction norm is defined by

$$||\Delta^n U||_2 = \sqrt{\sum_i \sum_j \sum_{l=1}^4 \left[\left(U_{i,j}^l\right)^{n+1} - \left(U_{i,j}^l\right)^n \right]^2}, \tag{90}$$

where n represents an arbitrary time level, and the subscript l denotes one of the four conserved variables. For a turbulent solution, 5 microseconds of CPU time are required per time step, per node point, on a CRAY Y-MP8. Also, approximately 110 words of memory are required per node point, or 2.4 megawords for the finest grids used (22,000 points).

Two techniques dramatically accelerate convergence to steady state. First, the Reynolds number is artificially set to 1×10^{10} at $t = 0$. After the shock wave moves away from the body (outside the boundary layer), the Reynolds number is reset to the correct value. Second, during the transient flow development, a lower limit on density and pressure is used to prevent negative values on the base. Typically, $\rho_{min} = 0.01 \ \rho_\infty$ and $p_{min} = 0.01 \ p_\infty$ are enforced. This additional restriction on the base is continuously enforced, but actually only necessary for the first few hundred iterations from an impulsive start.

The convergence history shows the robustness of the present method (Figure 103). Total computing time, using the convergence criterion related above, is about 9 minutes on a CRAY Y-MP8.

165
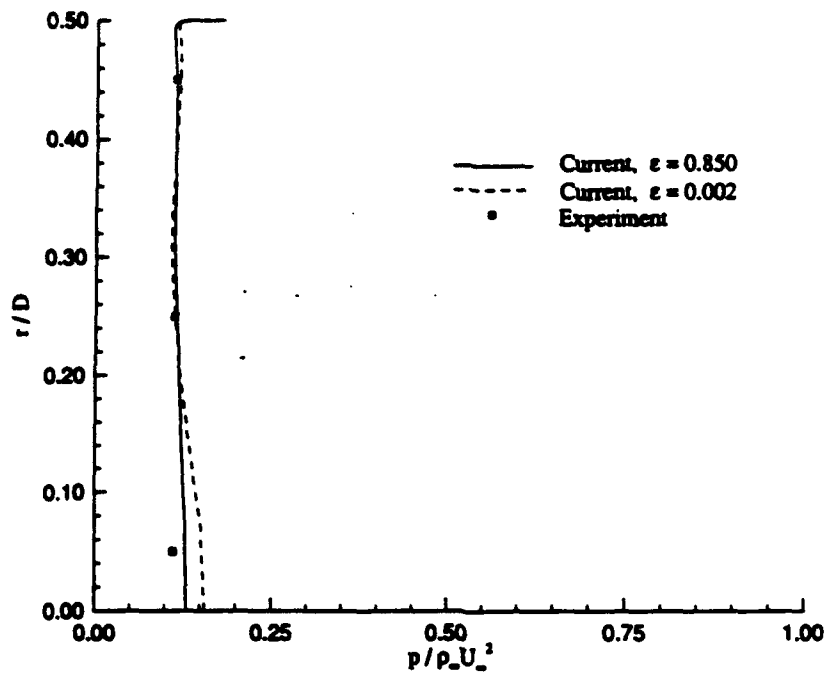
Figure 101. Influence of entropy correction parameter on computed base pressure $(M_\infty = 2.0, \; \alpha = 0°)$
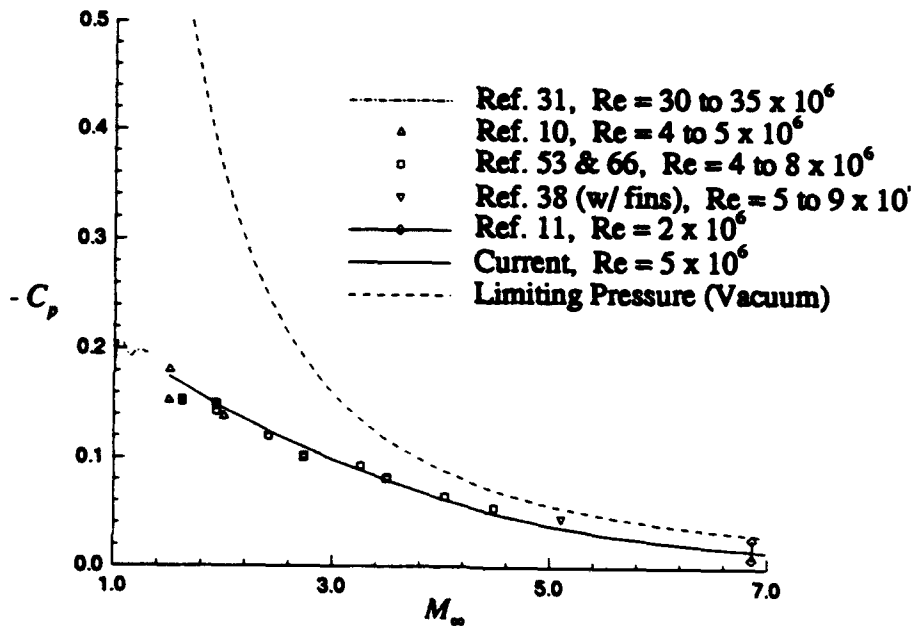
Figure 102. Computed versus experimental base pressure coefficient

10^1
10^0
10^{-1}
10^{-2}
10^{-3}
10^{-4}
10^{-5}
10^{-6}
10^{-7}
10^{-8}
10^{-9}
10^{-10}
10^{-11}
10^{-12}

$L_2(\Delta Q)$

0   2000   4000   6000   8000   10000
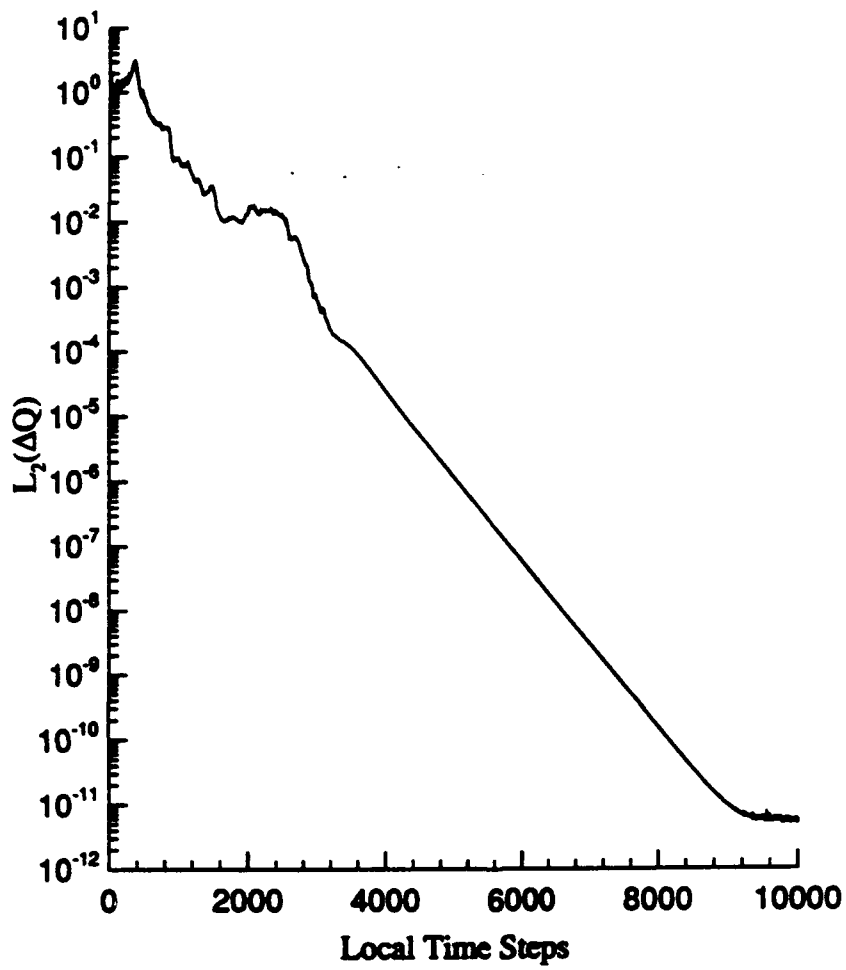
Local Time Steps

Figure 103.   Convergence history for forebody/base combination with local time stepping

167

A.6 Conclusions from Axisymmetric Validation

The current algorithm represents an efficient implementation of finite-volume methodology, both in terms of computational rate and memory requirement. The general applicability of the method is validated through the accurate calculation of a wide variety of axisymmetric flow structures: detached bow shocks, recompression shocks (both in the wake and at a separated region near the nosetip), corner-point expansions, base-flow separations and associated recirculations, and turbulent boundary layers. Results are in close agreement with published experimental estimates (within experimental accuracy). The complicated turbulent boundary-layer development is accurately calculated for various nose-tip shapes with a modified Baldwin-Lomax turbulence model. The algorithm's robustness is enhanced by artificially increasing the Reynolds number and controlling the boundary conditions on the base during the initially transient flow development. The effectiveness of this approach is demonstrated by the algorithm's efficiency throughout the range of conditions tested, including the case of a complicated boundary layer/shock interaction associated with the separation near the corner of the flat nosetip.

The results bolster the primary purpose of this investigation: the de p-ment and validation of an efficient, accurate, and flexible numerical scheme for the simulation of high-speed, viscous flows. The axisymmetric algorithm is the foundation for the construction of the three-dimensional algorithm described in Chapter 3. While completing the validation, some notable complexities arose that required the development of important modifications of previously published techniques. These improvements are reflected in the analyses of three-dimensional flows in Part I and Part II.

Modifications are primarily made to the treatment of singular lines, the wake turbulence model and the entropy correction function of Yee. An aberration is encountered near stagnation points that is different from the previously documented carbuncle phenomenon. When using non-MUSCL extrapolation to obtain fluxes,

THIS PAGE IS MISSING IN ORIGINAL DOCUMENT

- 169 -

Appendix B. *Validation of Three-dimensional Equations*

The axisymmetric form of the algorithm is capable of determining the many aspects of the general behavior of the current method. In particular, the effects of dissipation and the influence of grid refinement along the body and normal to the body are addressed in Appendix A for several forebody configurations in both laminar and turbulent flow. The extension of the algorithm for three-dimensional flow requires that further validation be performed. First, the differences in the algorithm which arise out of the extension to a higher dimension are outlined. Then, a comparison with previous results is made for the ogive/cylinder body analyzed in Appendix A. Next, a nonconformal grid structure is applied to a combination axisymmetric compression ramp and axisymmetric expansion ramp. These computations are performed to determine the accuracy of the method developed to compute the flow near a surface (Section 3.3). Finally, the three-dimensional algorithm is applied to an ogive/cylinder forebody at a small angle of attack. These computations serve two purposes: assessing the ability of the present method to capture the azimuthal variation in the flow, and determining the sensitivity to azimuthal refinement.

B.1 *Modifications to Algorithm for Three-dimensional Equations*

The governing equations for a three-dimensional flow are described in Chapter 2. There are three differences between the axisymmetric form and the three-dimensional form of the governing equations that require the algorithm to be modified. First, there is no source term associated with the three-dimensional form of the equations. This represents a small simplification to the algorithm. Second, an additional momentum equation is added to the set of conservation equations. The added equation necessitates a rederivation of the generalized inviscid flux Jacobians and the associated eigenvectors. This is addressed below in Section B.1.1. Finally,

the geometric terms that correspond to projections of cell faces into the Cartesian directions become more complicated. They are discussed in Section B.1.2.

B.1.1 *Generalized Jacobian and eigenvector.* The generalized inviscid flux Jacobian for the ξ-direction is now given by [25]

$$
\begin{bmatrix}
0 & \xi_x & \xi_y & \xi_z & 0 \\
\tilde{\gamma}\xi_x - U_c u & (1-\beta)\xi_x u + U_c & -\beta\xi_x v + \xi_y u & -\beta\xi_x w + \xi_z u & \beta\xi_x \\
\tilde{\gamma}\xi_x - U_c v & -\beta\xi_y u + \xi_x v & (1-\beta)\xi_y v + U_c & -\beta\xi_y w + \xi_z v & \beta\xi_y \\
\tilde{\gamma}\xi_x - U_c w & -\beta\xi_z u + \xi_x w & -\beta\xi_z v + \xi_y w & (1-\beta)\xi_z w + U_c & \beta\xi_z \\
\tilde{\gamma}U_c - U_c H & -\beta u U_c + H\xi_x & -\beta v U_c + H\xi_y & -\beta w U_c + H\xi_z & \gamma U_c
\end{bmatrix} , \quad (91)
$$

where γ is the ratio of specific heats, $\beta = \gamma - 1$, and

$$
\tilde{\gamma} = \frac{1}{2}(\gamma - 1)(u^2 + v^2 + w^2).
$$

Also, H is the total enthalpy and U_c is the contravariant velocity given by

$$
U_c = \xi_x u + \xi_y v + \xi_z w.
$$

The generalized inviscid flux Jacobians for the other two directions have similar construction and are obtained by replacing ξ with η or ζ, and replacing U_c with V_c or W_c. The terms ξ_x, ξ_y, and ξ_z are computed from the projected cell-face surface areas from:

$$
\xi_x = \frac{S_x^\xi}{\hat{V}}, \qquad \xi_y = \frac{S_y^\xi}{\hat{V}}, \qquad \text{and} \qquad \xi_z = \frac{S_z^\xi}{\hat{V}}, \qquad (92)
$$

where $\hat{V}$ is some average cell volume at the interface that S^ξ is evaluated (S^ξ is defined in Section B.1.2).

171

The associated right eigenvectors are [25]

$$
\begin{bmatrix}
\tilde{k}_x & \tilde{k}_y & \tilde{k}_z & 1 & 1 \\
\tilde{k}_x u & \tilde{k}_y u - \tilde{k}_z \rho & \tilde{k}_z u + \tilde{k}_y \rho & u + \tilde{k}_x c & u - \tilde{k}_x c \\
\tilde{k}_x v + \tilde{k}_z \rho & \tilde{k}_y v & \tilde{k}_z v - \tilde{k}_x \rho & v + \tilde{k}_y c & v - \tilde{k}_y c \\
\tilde{k}_x w - \tilde{k}_y \rho & \tilde{k}_y w + \tilde{k}_x \rho & \tilde{k}_z w & w + \tilde{k}_z c & w - \tilde{k}_z c \\
s\tilde{k}_x + (\tilde{k}_z v - \tilde{k}_y w)\rho & s\tilde{k}_y + (\tilde{k}_x w - \tilde{k}_z u)\rho & s\tilde{k}_z + (\tilde{k}_y u - \tilde{k}_x v)\rho & H + \tilde{U}_c c & H - \tilde{U}_c c
\end{bmatrix},
$$

where

$$
s = \frac{1}{2}q^2 = \frac{1}{2}(\vec{u} \cdot \vec{u}).
$$

The density, ρ, is averaged using the following [25]: $\rho = \sqrt{\rho_R \rho_L}$. The subscripts R and L denote a value to the right and left of an interface, respectively. The terms $\tilde{k}_x$, $\tilde{k}_y$, and $\tilde{k}_z$ are defined by

$$
\tilde{k}_x = \frac{S_x^\xi}{\sqrt{\left(S_x^\xi\right)^2 \left(S_y^\xi\right)^2 \left(S_z^\xi\right)^2}}, \tag{93}
$$

$$
\tilde{k}_y = \frac{S_y^\xi}{\sqrt{\left(S_x^\xi\right)^2 \left(S_y^\xi\right)^2 \left(S_z^\xi\right)^2}}, \tag{94}
$$

$$
\tilde{k}_z = \frac{S_z^\xi}{\sqrt{\left(S_x^\xi\right)^2 \left(S_y^\xi\right)^2 \left(S_z^\xi\right)^2}}. \tag{95}
$$

The normalized contravariant velocity, $\tilde{U}_c$, is given by

$$
\tilde{U}_c = \tilde{k}_x u + \tilde{k}_y v + \tilde{k}_z w.
$$

B.1.2 Geometric Terms of a Three-dimensional Fluid Cell. The geometric terms for a finite-volume methodology are obtained by using the two diagonals for each face on a cell. For the typical cell (Figure 104), the terms are defined by [91]

$$
\vec{S}_{4378} = \vec{S}^\xi = (\vec{r}_4 - \vec{r}_7) \times (\vec{r}_8 - \vec{r}_3), \tag{96}
$$
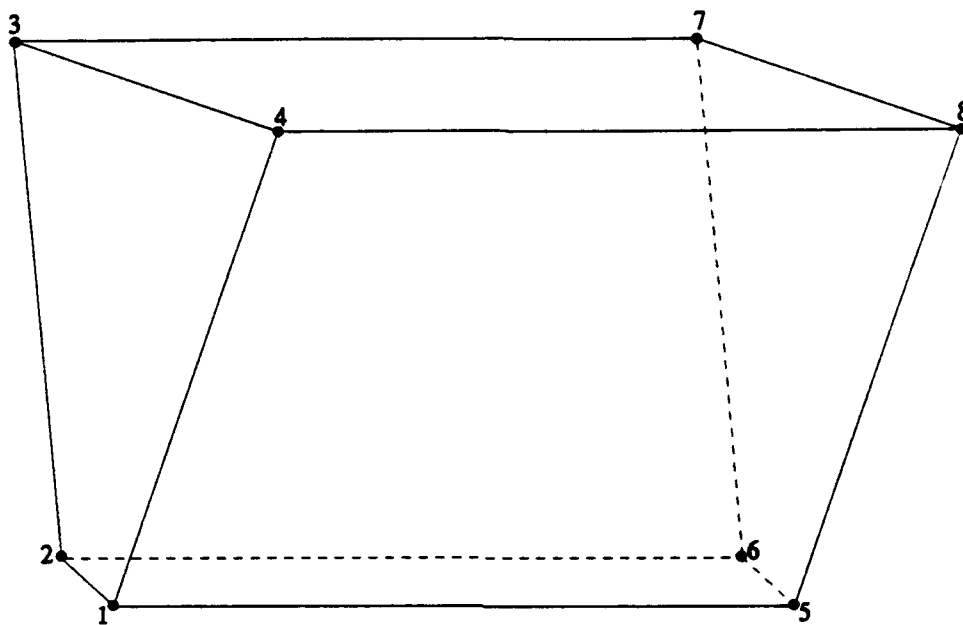
Figure 104. Typical six-sided fluid cell from a structured grid

$$\vec{S}_{1234} = \vec{S}^\eta = (\vec{r}_1 - \vec{r}_3) \times (\vec{r}_4 - \vec{r}_2), \tag{97}$$

$$\vec{S}_{4158} = \vec{S}^\zeta = (\vec{r}_4 - \vec{r}_5) \times (\vec{r}_8 - \vec{r}_1). \tag{98}$$

B.2 Application to Axisymmetric Baseline

Validation of the three-dimensional algorithm is begun using the results from Appendix A. Specifically, the axisymmetric results from the supersonic, turbulent flow over a spherically blunted tangent-ogive/cylinder are used for comparison. The pressure and boundary-layer velocity profiles are directly compared to assess any differences. The computation is performed in only half the azimuthal plane by enforcing a symmetry condition (Section 3.4). A two-dimensional grid is constructed

173

with spacing normal to the body identical to that used for the axisymmetric calculation, $(0.000025D)$. This grid is rotated about the body centerline to produce a three-dimensional grid with dimensions $61 \times 201 \times 33$ for the half plane. This is the same procedure used to obtain grids for the analysis of the HART missile in Part I and Part II.

The pressure comparison shows that the three-dimensional algorithm predicts essentially the same surface pressure as the axisymmetric algorithm (Figures 105 and 106). Only very small differences in the pressure are discernible. The velocity profiles show that the growth of the boundary layer is also the same as the axisymmetric computations (Figures 107a-107c). The small difference in the boundary layer from the three-dimensional calculations is due primarily to different levels of convergence. The axisymmetric solution is converged such that the residual error is several orders of magnitude less than the convergence criteria outlined in Appendix A (Section A.5). The level of "non-axisymmetry" in the three-dimensional computations is seen to decrease as the solution converges.

The agreement in pressure and boundary-layer development indicate that axisymmetric flow is accurately calculated with the three-dimensional algorithm.

B.3 Nonconformal Grid Applied to Axisymmetric Compression Ramp

The grid used in the analysis of the HART missile does not conform to the fin leading edges (Section 3.3). To validate the method developed to handle the nonconformal grid structure, turbulent flow is computed for a combination axisymmetric compression ramp and axisymmetric expansion ramp downstream of an axisymmetric ogive/cylinder forebody ($M_\infty = 2.95$). Both a conformal grid and a nonconformal grid are built and used with the three-dimensional algorithm. The two grids are shown in Figures 108 and 109. Again, two-dimensional grids are built (61×81) and rotated about the body centerline to produce the three-dimensional grids. Also, the computation is performed in only half the azimuthal plane by enforcing a symmetry

174
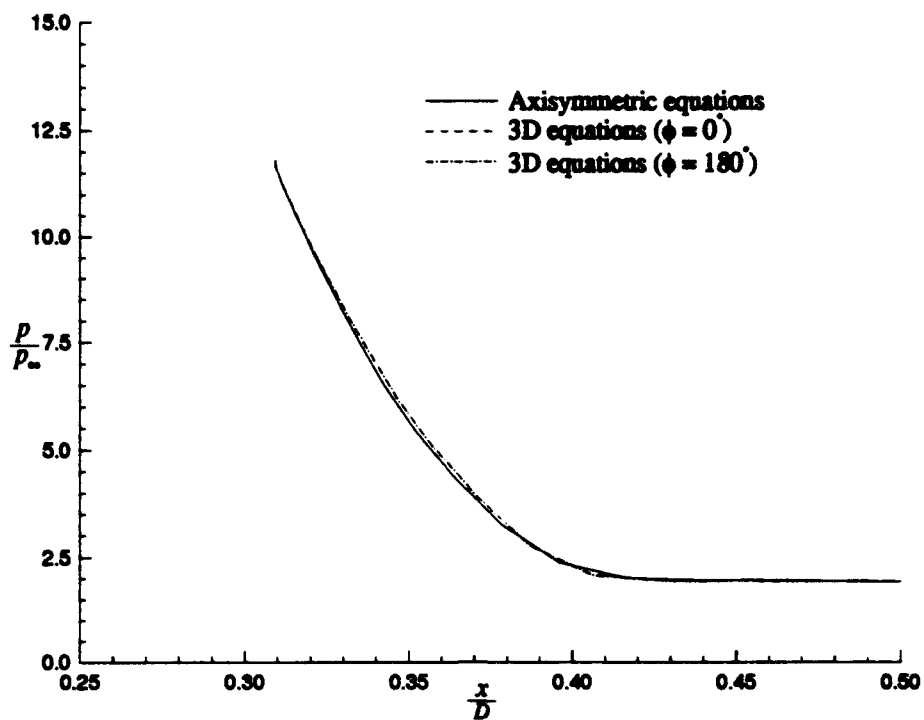
Figure 105. Surface pressure near the nosetip of a tangent-ogive/cylinder in turbulent flow: $M_\infty = 2.95$ and $\alpha = 0°$
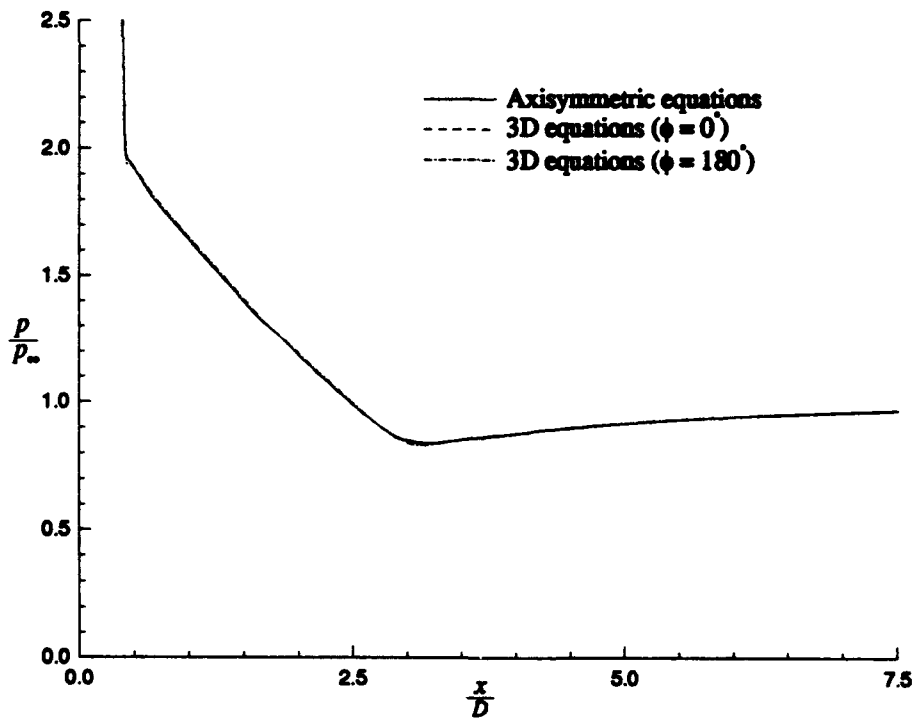
Figure 106. Surface pressure away from the nosetip of a tangent-ogive/cylinder in turbulent flow: $M_\infty = 2.95$ and $\alpha = 0°$

175
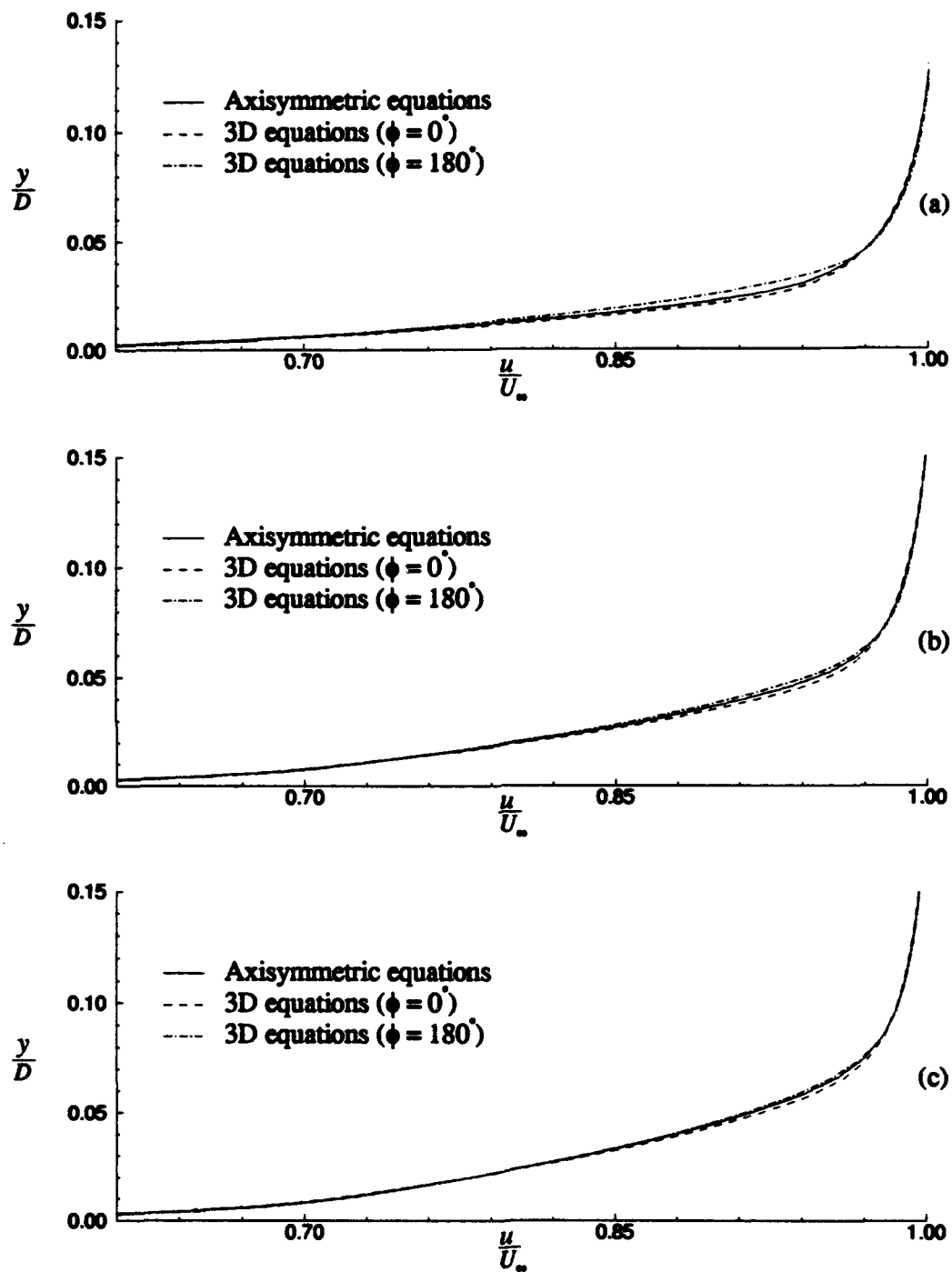
Figure 107. Velocity profiles for a tangent-ogive/cylinder in turbulent flow with $M_\infty = 2.95$ and $\alpha = 0^\circ$: (a) $\frac{x}{D} = 3.26$, (b) $\frac{x}{D} = 5.05$, (c) $\frac{x}{D} = 6.33$

condition (Section 3.4). For the half plane, both the conformal and nonconformal grids have dimensions $61 \times 81 \times 33$. The nonconformal grid is intentionally coarsened to test the limitations of the methodology. The conformal grid is also used with the axisymmetric form of the algorithm to provide additional data for comparison.

Separation occurs prior to the compression ramp for all three computations. Figure 110 shows that the extent of the disturbance upstream of the compression ramp is slightly underpredicted by the nonconformal method. The pressure in the separated region and at the expansion ramp are equally well predicted by each method. Given the coarseness of the nonconformal grid, the level of agreement between the conformal results and the nonconformal results is believed to be acceptable by the author.

B.4 Calculations for an Ogive-Cylinder Forebody at Angle of Attack (Turbulent Flow)

Next, the accuracy to which the surface pressure and the turbulent boundary layer are calculated, for a forebody at some nonzero angle of attack, is determined. The tangent-ogive/cylinder body used in Appendix A and Section B.2 of this appendix is pitched $2.9°$. This angle is selected to compare with experiment. Again the surface pressure and boundary layer are compared to values determined experimentally [13]. The grid in this part of the validation is the same as that described in Section B.2. Results using this grid will be referred to as "fine-grid" results. Grids with slightly coarser spacing near the surface are also implemented to conduct an azimuthal refinement study. Results from these grids will be referred to as "coarse-grid" results. The refinement study is made to determine the sensitivity of the current method to azimuthal spacing. The number of nodes in the azimuthal direction is varied from 17 to 65, corresponding to angular spacings of $11.25°$ and $2.8125°$, respectively.

For the fine grid, the computed pressure on the leeside ($\phi = 0°$) and windside

177
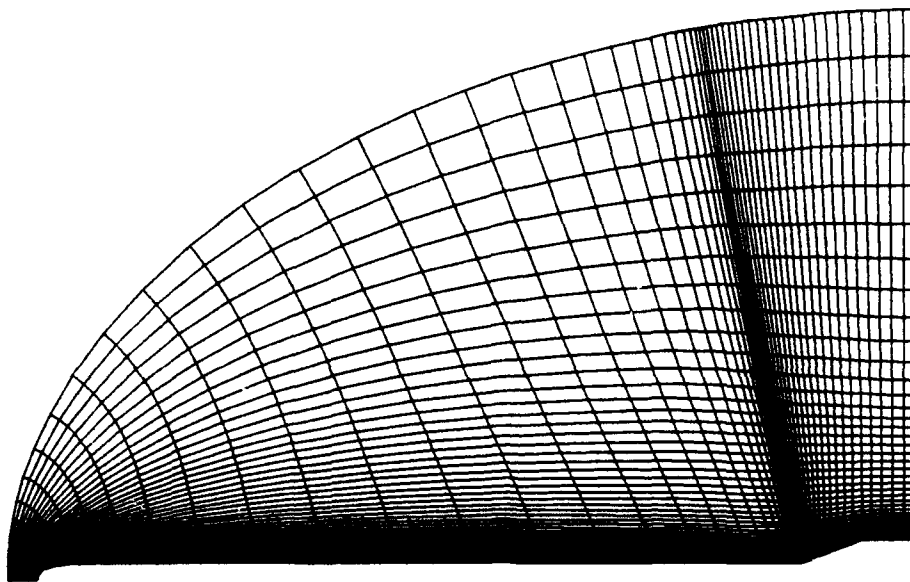
Figure 108. Conformal grid for axisymmetric compression ramp
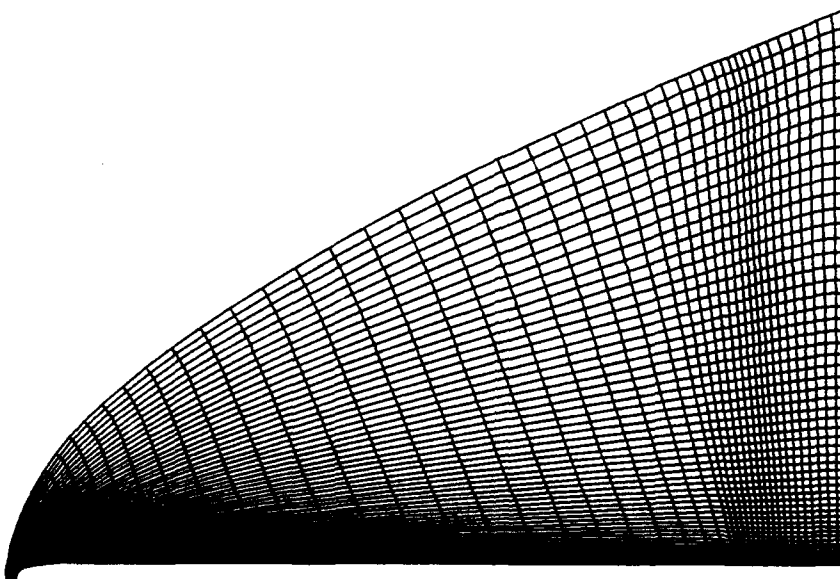
Figure 109. Nonconformal grid for axisymmetric compression ramp

178
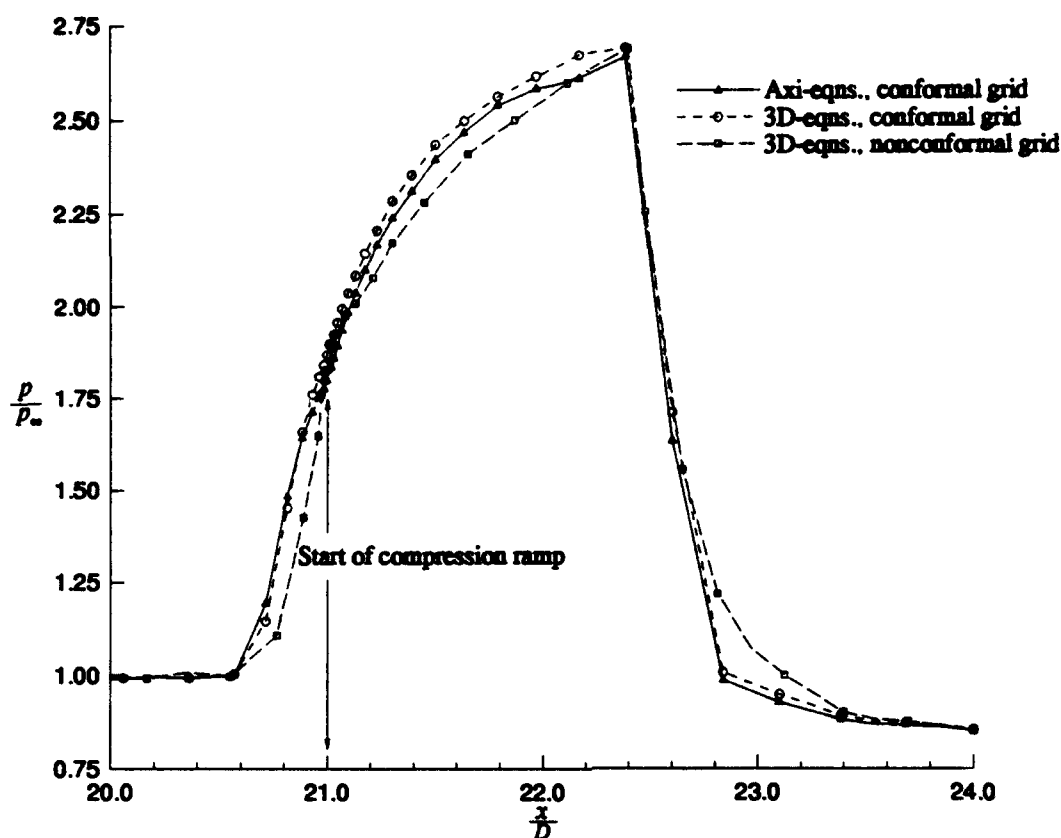
Figure 110. Surface pressure from computations for an axisymmetric compression
ramp: $M_\infty = 2.95$

($\phi = 180°$) of the ogive/cylinder body is compared to the experimental pressure
in Figures 111 and 112. Agreement within the reported experimental accuracy is
achieved. Also, for the fine grid, the velocity profiles on the leeside and windside are
compared to the experimentally determined profiles (Figures 113 and 114). Agree-
ment within about 10% is seen. For the computations, the point used to separate
laminar and turbulent regions, is the same as the point designated in Appendix A
and Section B.2 ($\frac{s}{D} = 1.7$). The point which separates the laminar region from
the turbulent region is not varied around the body because this information is not
available from the experiments. However, boundary-layer transition is not uniform
around a body at angle of attack [79], and the author believes the discrepancy be-

179

tween the computations and the experiment are a result of neglecting the azimuthal variation of transition point.

The results from the grid with coarse and refined spacing near the surface are compared in Figure 115. The impact on pressure is small.

The solutions from from the grid refinement study also showed little variation in surface pressure (Figure 116). Only the coarsest angular spacing gave different results. The velocity profiles for the solutions from the grid refinement study showed that prediction of the attached boundary layer does not depend on the angular spacing, over the range of spacing tested. The leeside and windside profiles near the ogive/cylinder-body junction are compared to the experimental data in Figure 117 and Figure 118, respectively.

B.5 Conclusions from Three-dimensional Validation

The implementation of the three-dimensional equations is demonstrated for flow on a tangent-ogive/cylinder forebody at $M_\infty = 2.95$ with $\alpha = 0°$ and $\alpha = 2.9°$. Results for $\alpha = 0°$ agree with previously validated axisymmetric results (shown in Appendix A). Calculations at angle of attack show fairly good agreement with experimental data. Computed surface pressure is within the experimental accuracy and computed boundary-layer velocity profiles are within 10% of experimental. The azimuthal variation of surface pressure is well predicted by the present method. In addition, azimuthal grid refinement is shown not to affect the solution significantly.

The accuracy of the method proposed to handle a nonconformal grid structure is also demonstrated. In general, the separation point and reattachment point for turbulent, Mach 3 flow over a cylinder-flare configuration compares well with computations made using a conformal grid. Also, the pressure within the separated region, and downstream of the attachment point, agrees with the conformal computations.

180
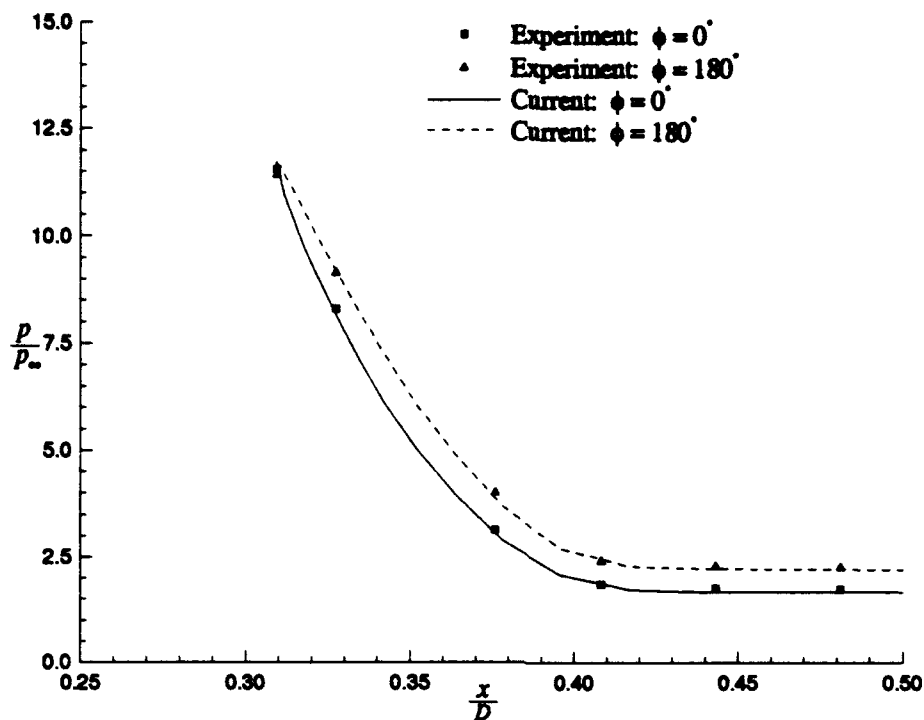
Figure 111. Surface pressure near the nosetip of a tangent-ogive/cylinder in turbulent flow: $M_\infty = 2.95$ and $\alpha = 2.9°$
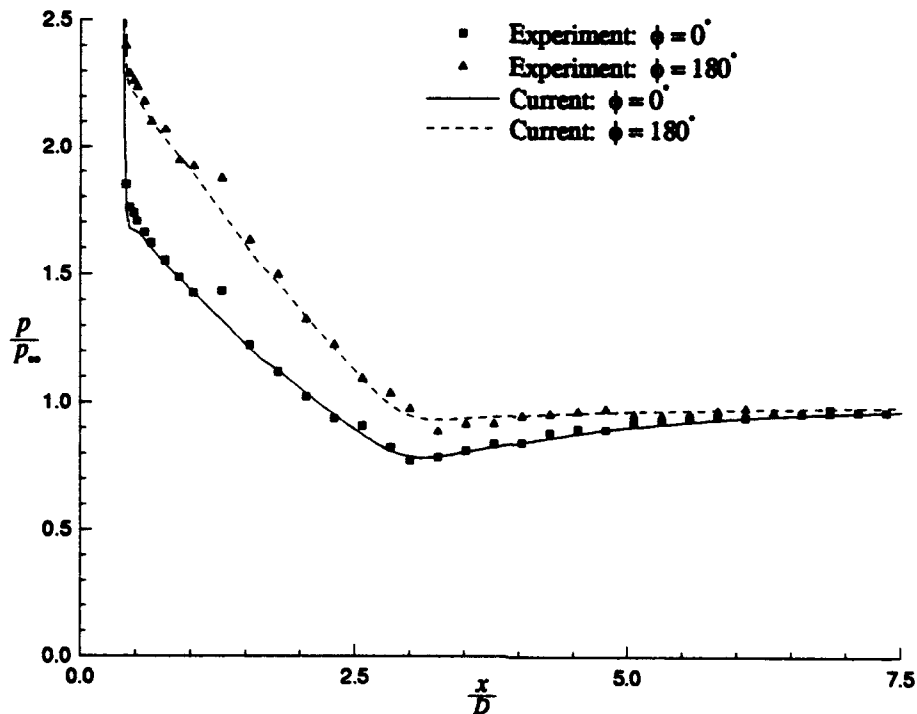
Figure 112. Surface pressure away from the nosetip of a tangent-ogive/cylinder in turbulent flow: $M_\infty = 2.95$ and $\alpha = 2.9°$
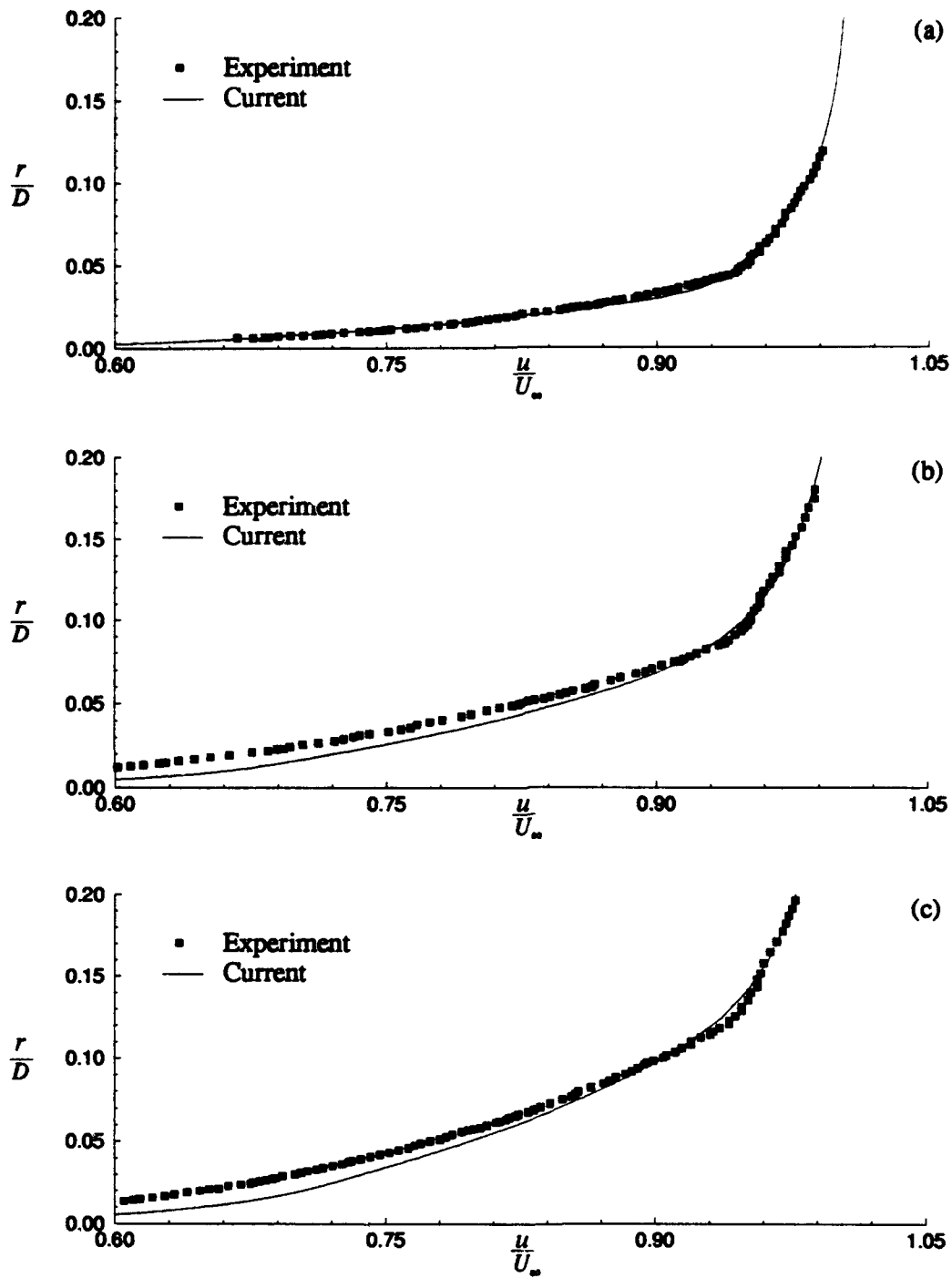
Figure 113. Leeside velocity profiles for a tangent-ogive/cylinder in turbulent flow with $M_\infty = 2.95$ and $\alpha = 2.9°$: (a) $\frac{x}{D} = 3.26$, (b) $\frac{x}{D} = 5.05$, (c) $\frac{x}{D} = 6.33$

182
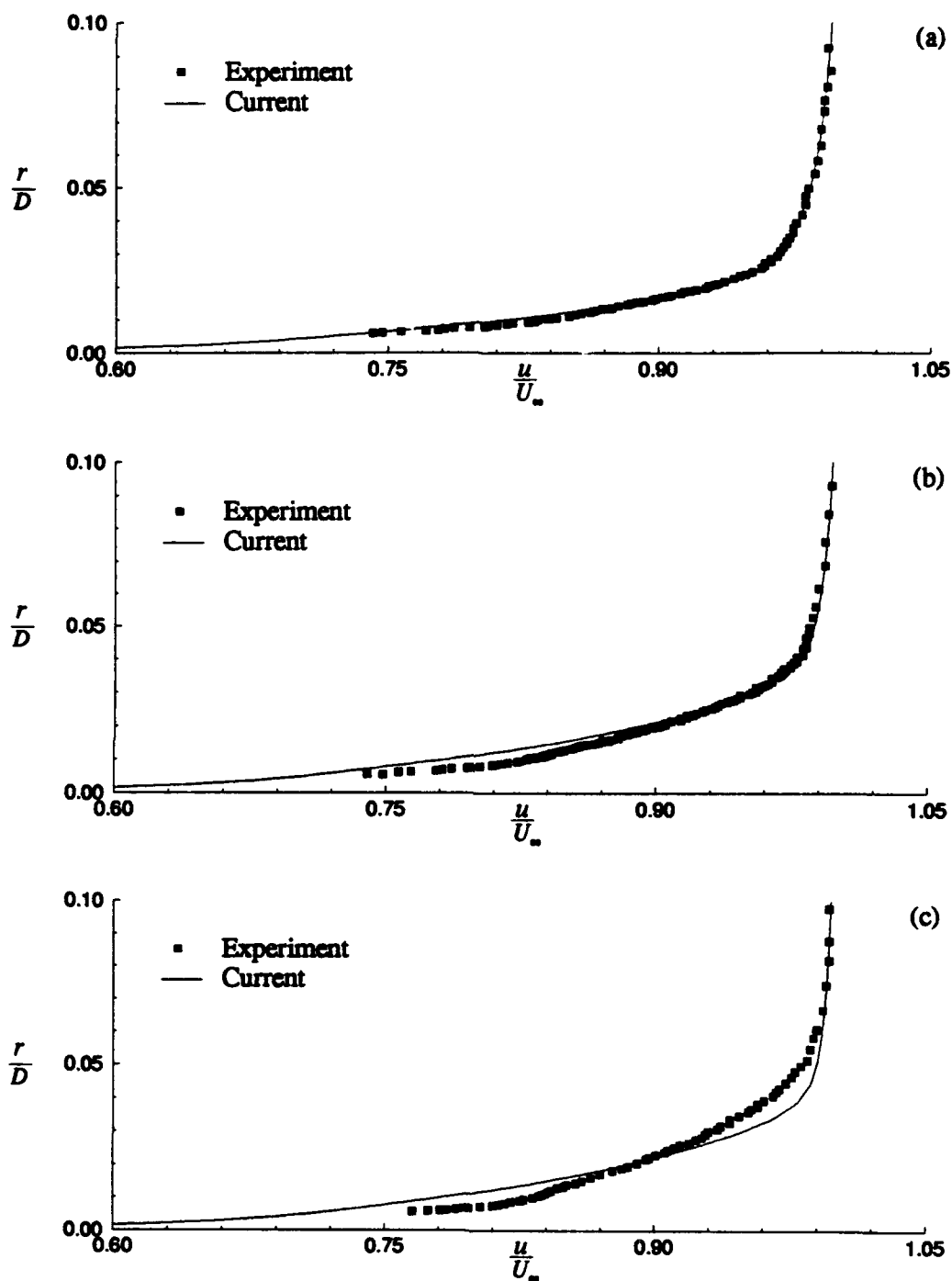
Figure 114.   Windside velocity profiles for a tangent-ogive/cylinder in turbulent flow
with M_∞ = 2.95 and α = 2.9°:   (a) $\frac{x}{D}$ = 3.26, (b) $\frac{x}{D}$ = 5.05, (c)
$\frac{x}{D}$ = 6.33

183
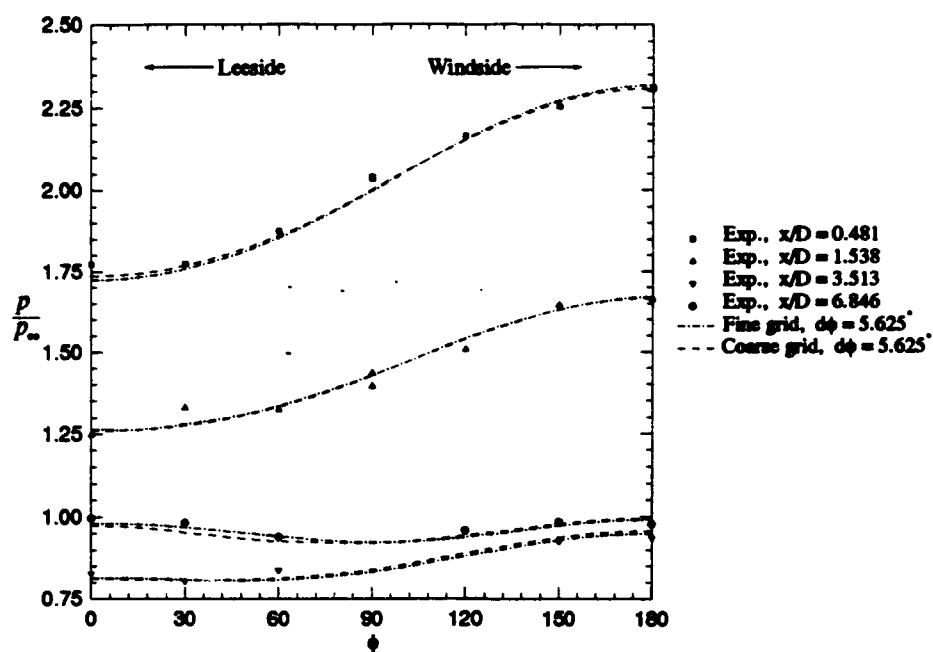
Figure 115.   Comparison of the azimuthal variation of surface pressure using coarse
and refined spacing near the body: $M_\infty = 2.95$ and $\alpha = 2.9°$
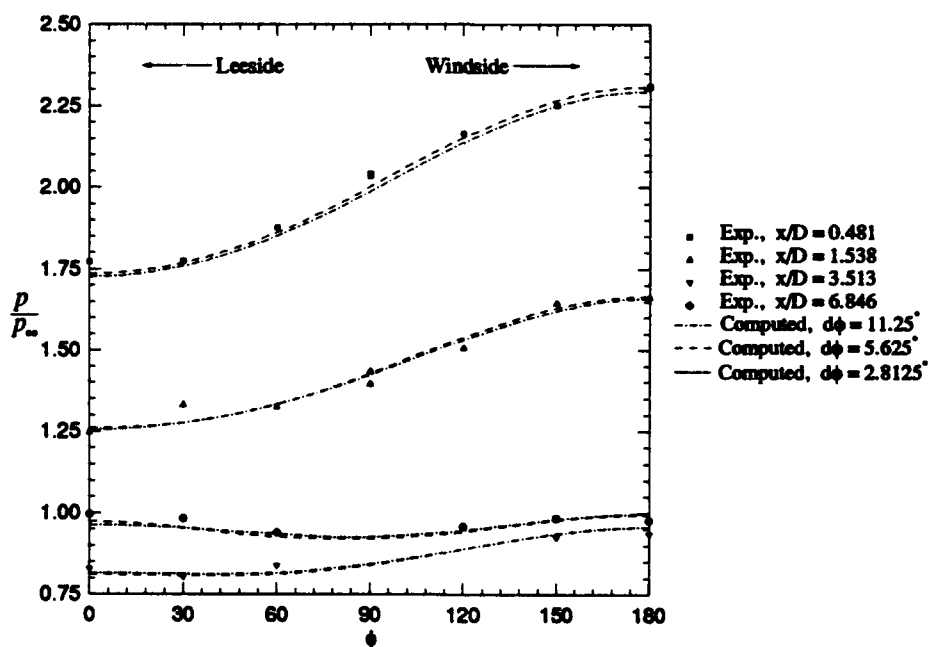
Figure 116.   Comparison of the azimuthal variation of surface pressure for azimuthal
grid refinement: $M_\infty = 2.95$ and $\alpha = 2.9°$

184
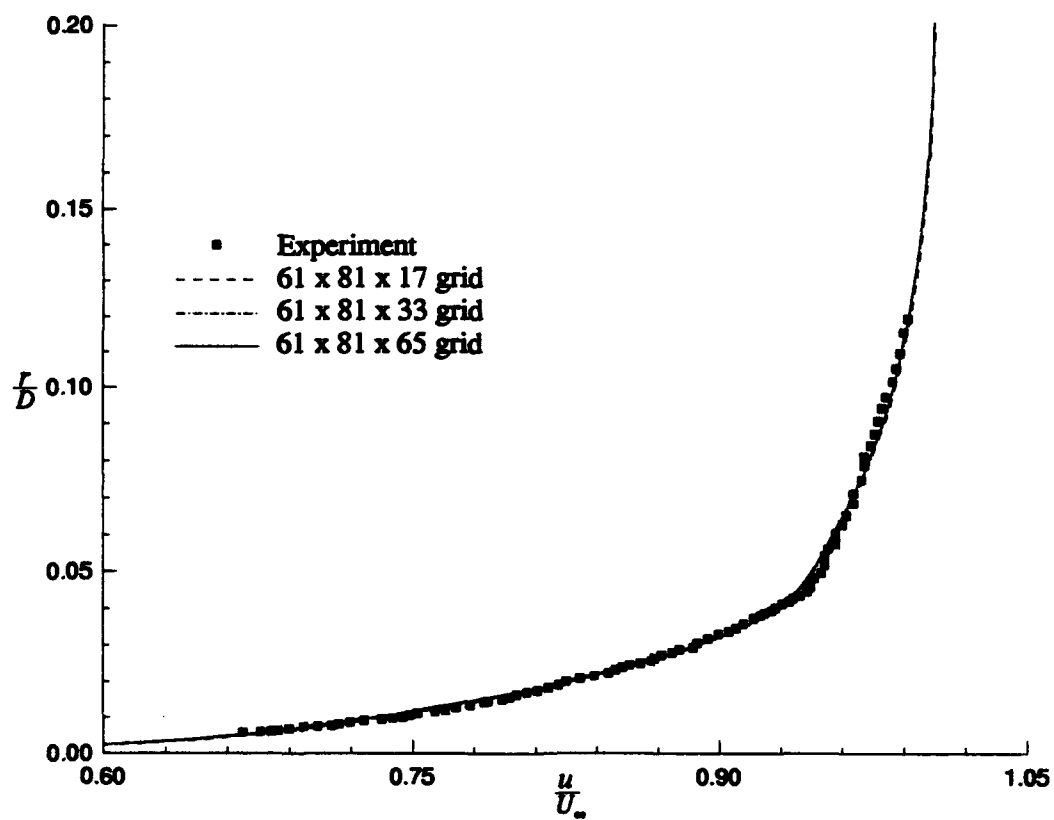
Figure 117. Leeside ($\phi = 0°$) velocity profiles for azimuthal grid refinement: $M_\infty = 2.95$, $\alpha = 2.9°$, and $\frac{x}{D} = 3.26$
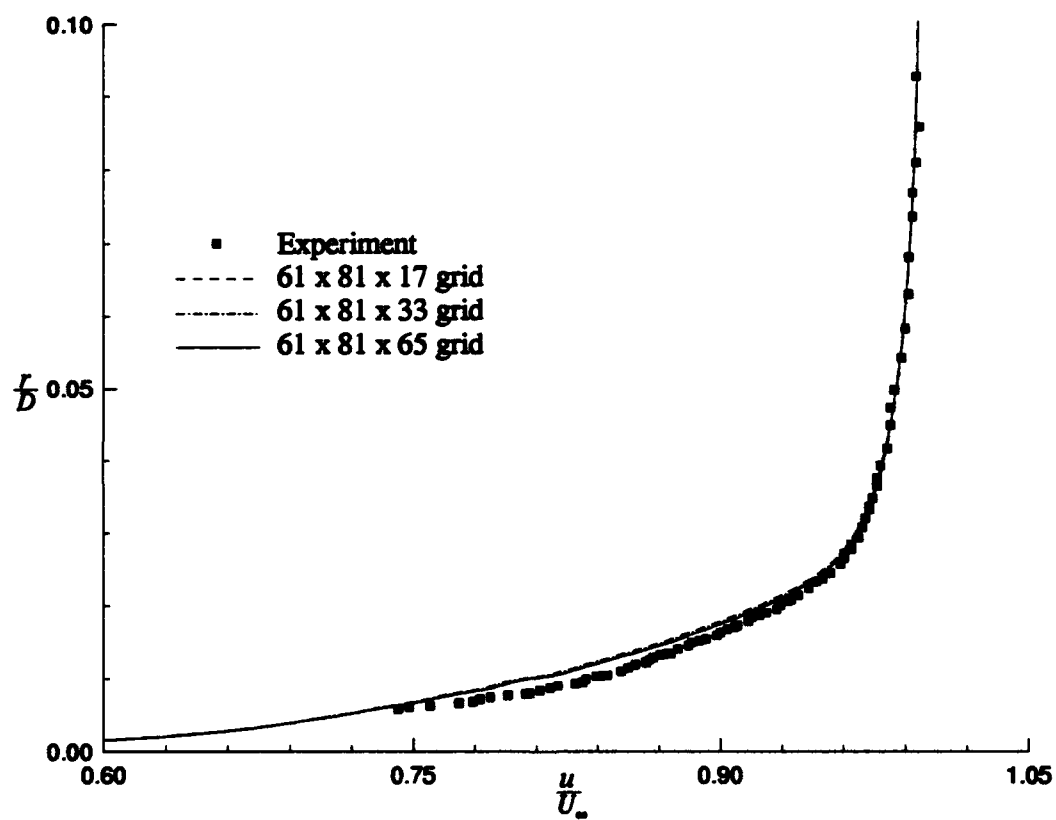
Figure 118. Windside ($\phi = 180°$) velocity profiles for azimuthal grid refinement: $M_\infty = 2.95$, $\alpha = 2.9°$, and $\frac{x}{D} = 3.26$

Appendix C. *Computer Codes and Resources*

The following hardware resources were utilized to perform the computational portions of this dissertation

- AFIT Stardent ST-2000

- AFIT Convex C220

- Cray Y-MP8 (Eglin AFB, FL)

- Cray C-90 (Vicksburg, MS)

The usage of these resources is normalized by Cray Y-MP8 equivalent central processor unit (CPU) hours and summarized in Table 21.

Table 21. Resource utilization.

Computations	Machine	Utilization (CPU hours) (normalized to Cray Y-MP8)
Code Development & Axisymmetric Validation (Appendix A)	AFIT Stardent ST-2000	61
3D Validation & Thin-fin Investigation (Appendix B & Part I)	AFIT Convex C220	226
Thin-fin Investigation (Part I)	Cray Y-MP8	473
Thick-fin Investigation (Part II)	Cray C-90	40

C.1 Software Documentatiion for General Algorithm

This document was prepared using Latex on an AFIT Sun SPARC 10. A short synopsis of the computer codes employed is provided, along with a description of the subroutines contained therein. Three main codes were employed:

1. AFITENS-AXI Version 2.0

2. AFITENS-3D Version 1.0

3. AFITENS-3D Version 1.1

All three codes allow Euler or full Navier-Stokes calculations using upwind differencing of the convective terms and central differencing of the viscous terms. Also, each code encorporates the Baldwin-Lomax turbulence model. AFITENS-AXI Version 2.0 is an axisymmetic code employing a finite-volume methodology, and was used for the validation tests in Appendix A. AFITENS-3D Version 1.0 uses the finite-volume method on a single grid block with an H-H topology for a complete missile configuration. Optional missile fins are modeled with an infinitely thin-fin approximation (i.e., using boundary conditions applied on the interior of the domain). The grid construction and boundary conditions are described in Chapter 3. This version was used for the validation tests in Appendix B and the thin-fin HART missile simulations in Part I. Finally, AFITENS-3D Version 1.1 allows the missile fins to have thickness, again utilizing an H-H grid topology. AFITENS-3D Version 1.1 was used for the thick-fin HART missile simulations in Part II.

A short description of input/output files for the above codes and a short synopsis of the subroutines employed is provided below.

AFITENS-AXI/AFITENS-3D

- **Input Files**

    afitens.drv – input file to specify CFL, Re, M_∞, α, etc.
    grid.dat   – grid file
    restart.dat – restart file for conserved variables

- **Output Files**

    restart.dat – restart file for conserved variables
    forces.dat – lift, drag, and pitching moment

- **Subroutines**

bcaxi – applies boundary conditions at inflow, outflow, farfield, surface for FD grid

bcaxi2 – applies boundary conditions at bisymmetry plane for FD grid

bcaxi3,

bcaxi4 – applies boundary conditions on domain interior for missile fins for FD grid

bcstag – applies boundary conditions at inflow, outflow, farfield, surface for FV grid

bcstag2 – applies boundary conditions at bisymmetry plane for FV grid

bcstag3,

bcstag4 – applies boundary conditions on domain interior for missile fins for FV grid

cd – computes the axial, normal, lift, and drag forces and the pitching moment

efgvect – constructs the inviscid and viscous flux vectors

eigdt – determines the time step using the linearized stability restriction

etasweep – builds the numerical fluxes and performs the operator in the η direction

gradient – computes velocity and temperature gradients

gridaxi – constructs a three-dimensional FD grid

gridstag – constructs a three-dimensional FV grid

lamvisc – computes molecular viscosity

metrics – calculates the geometric terms using a finite-volume method

turbvisc – computes eddy viscosity

xisweepA,

xisweepB – builds the numerical fluxes and performs the operator in the ξ direction

zetasweepA,

zetasweepB,

zetasweepC,

zetasweepD – builds the numerical fluxes and performs the operator in the ζ direction

zl2norm – calculates the residual norm between time steps

The computer codes, and the associated drivers, restart files, and grids, are archived on the AFIT Sun SPARC 10 (enterprise) in the following directories

1. AFITENS-AXI Version 2.0 – /home/fluids/kmoran/AXI

2. AFITENS-3D Version 1.0 – /home/fluids/kmoran/3D/THIN

3. AFITENS-3D Version 1.1 – /home/fluids/kmoran/3D/THICK

C.2 Algorithm Performance and Memory Requirements

The current three-dimensional solver (AFITENS-3D Version 1.0) requires approximately 80 words of core memory per grid point. A comparison of computer code performance is shown in the following tables. Table 22 shows a comparison between the axisymmetric version of the current solver (AFITENS-AXI) versus axisymmetric solvers used by other researchers. The current technique is very efficient in terms of CPU usage.

Table 23 shows the data processing rate of AFITENS-AXI Version 2.0 on several different machines. Resonable computations rates are seen for several AFIT workstations when they are used in a parallel mode.

Table 22. Comparison of computer code performance for axisymmetric solvers.

Developer/ User	Algorithm Type	Machine Type*	DPR**	Comments
BRL	Implicit B/W	Cray X-MP	1.60×10^{-4}	Thin Layer Eqns
WL	Implicit B/W	Cray X-MP	2.50×10^{-5}	$2D$
WL	Explicit FDS-Roe	Cray X-MP	1.15×10^{-4}	MUSCL
AFIT	Implicit B/W	Cray X-MP	1.93×10^{-5}	$2D$
AFIT	Explicit FDS-Roe***	Cray X-MP/216	1.09×10^{-5}	Non-MUSCL

** Data processing rate (DPR) in seconds/iteration/node point
** AFITENS-AXI Version 2.0

Table 23. Comparison of data processing rates for AFITENS-AXI Version 2.0.

Machine Type	DPR*	Factor over Cray-YMP8
Sun SPARC 2	4.32×10^{-4}	81.0
Stardent ST2000**	6.96×10^{-5}	13.0
Titan 3000	4.41×10^{-5}	8.3
Convex C220***	2.92×10^{-5}	5.5
Cray X-MP	1.09×10^{-5}	2.0
Cray 2	7.75×10^{-6}	1.5
Cray Y-MP8	5.34×10^{-6}	1.0

 * Data processing rate (DPR) in seconds/iteration/node point
** Run in parallel using four processors
*** Run in parallel using two processors

191

Finally, Table 24 gives a comparison of the three-dimensional solver developed for this dissertation with those of several other researchers. Again, excellent performance is seen with the current method.

Table 24. Comparison of computer code performance for 3D solvers: full Navier-Stokes and turbulent flow.

Developer/ User	Algorithm Type	Machine Type	DPR*	Comments
BRL	Implicit B/W	Cray 2	1.90×10^{-4}	PNS
WL	Explicit FDS-Roe	Cray Y-MP8	5.40×10^{-5}	MUSCL
WL	Implicit FDS-Roe	Cray Y-MP8	1.00×10^{-4}	MUSCL
NASA Ames	Implicit FDS-Roe	Cray Y-MP8	2.50×10^{-5}	MUSCL, laminar
AFIT	Explicit FDS-Roe**	Cray Y-MP8	1.50×10^{-5}	Non-MUSCL

* Data processing rate (DPR) in seconds/iteration/node point
** AFITENS-3D Version 1.0

Bibliography

1. Anderson, Dale A., John C. Tannehill, and Richard H. Pletcher. *Computational Fluid Mechanics and Heat Transfer*. Series in Computational Methods in Mechanics and Thermal Sciences. New York: Hemisphere Publishing Corporation, 1984.

2. Anderson, John D. *Hypersonic and High Temperature Gas Dynamics*. New York: McGraw-Hill, Inc., 1989.

3. Anderson, W. K. and J. L. Thomas. "A Comparison of Finite Volume Flux Vector Splittings for the Euler Equations," AIAA Paper 85-0122, January 1985.

4. Ashley H. and Landahl, M., *Aerodynamics of Wings and Bodies*, New York: Dover Publications, Inc., 1965.

5. Baldwin B. S. and H. Lomax. "Thin Layer Approximation and Algebraic Model for Separated Turbulent Flow," AIAA Paper 78-0257.

6. Batchelor, G. K. *An Introduction to Fluid Dynamics*. New York: Cambridge University Press, 1967.

7. Beran, Philip S., Assistant Professor. Personal Correspondence. Air Force Institute of Technology, 1992.

8. Blake, D. J. *A Numerical Study of High-Speed Missile Configurations Using a Block-Structured Parallel Algorithm*. MS Thesis, AFIT/GAE/ENY/93D-07. Graduate School of Engineering, Air Force Institute of Technology (AU), Wright-Patterson AFB OH, December 1993.

9. Butler, C. B., Sears, E. S., and Pallas, S. G., "Aerodynamic Characteristics of 2-, 3- and 4-Caliber Tangent-Ogive Cylinders with Nose Bluffness Ratios of 0.00, 0.25, 0.6, and 0.75 at Mach Numbers from 0.6 to 4.0," AFATL-TR-77-8, January 1977.

10. Chapman, Dean R. *An Analysis of Base Pressure at Supersonic Velocities and Comparison with Experiment*, NACA Report 1051, 1951.

11. Cooper, Ralph D., and Robinson, Raymond A. *An Investigation of the Aerodynmic Characteristics of a Series of Cone-Cylinder Configurations at a Mach Numer of 6.86*, NACA Research Memorandum L51J09, 1951.

12. Dolling, D. S. and K. Gray. *Compilation of Wall Pressure and Turbulent Boundary Layer Data for Supersonic High Reynolds Number Flow Over a*

Blunted Tangent Ogive Cylinder at Small Angles of Attack, Mechanical and Aerospace Engineering Dept., Princeton University, Report #1585-MAE, Princeton, NJ, September 1982.

13. Dolling, David S. and W. K. Gray. "Experimental Study of Supersonic Turbulent Flow on a Blunted Axisymmetric Body," *AIAA Journal.* Volume 24, Number 5: 793-799, May 1986.

14. Donaldson, I. S. "The Effects of String Supports on the Base Pressure of a Blunt-Based Body in a Supersonic Stream," *The Aeronautical Quarterly.* 221-229, August 1955.

15. Drew, B. and Jenn, A., "Pressure Drag Calculations on Axisymmetric Bodies of Arbitrary Moldline," AIAA Paper 90-0280, January 1990.

16. Driver, Capt Mark A. *High-Resolution TVD Schemes for the Analysis of I. Inviscid Supersonic and Transonic Flows II. Viscous Flows with Shock-induced Separation and Heat Transfer.* PhD dissertation. School of Engineering, Air Force Institute of Technology (AU), Wright-Patterson AFB OH, December 1991.

17. Dubois, F. and G. Mehlman. "A Non-Parameterized *Entropy Fix* for Roe's Method," *Journal of Aerospatiale*, 1991.

18. Etkin, Bernard. *Dynamics of Atmospheric Flight.* New York: John Wiley & Sons, Inc., 1972.

19. Fischer, M. A., Hathaway, W. H., "Aeroballistic Research Facility Data Analysis System (ARFDAS)," AFATL-TR-88-48, Eglin AFB, FL, September 1988.

20. Gabeaud, A. "Base Pressures at Supersonic Velocities," *Reader's Forum, Journal of the Aeronautical Sciences.* Volume 17 Number 8: 525-526, August 1950.

21. Gaitonde, D., et. al. "A Systematic Comparative Study of Several High Resolution Schemes for Complex Problems in High Speed Flows," AIAA Paper 91-0636, January 1991.

22. Gates, R. S., G. L. Winchenbach, and J. R. Cipolla. "Aerodynamic Test and Analysis of a Slender Generic Missile Configuration," AIAA Paper 89-3368, August 1989.

23. Gnoffo, P. A., "Application of Program LAURA to Three-dimensional AOTV Flowfields," AIAA Paper 86-0565, January 1986.

24. Gnoffo, P. A., McCandless, R. S., and Yee, H. C., "Enhancements to Program LAURA for Computation of Three-Dimensional Hypersonic Flow," AIAA Paper 87-0280, January 1987.

25. Gnoffo, P. A., "An Upwind-Biased, Point-Implicit Relaxation Algorithm for Viscous, Complessible Perfect-Gas Flow," NASA TP-2953, Fegruary 1990.

26. Godunov, S. K. "A Finite Difference Method for the Numerical Computation of Discontinuous Solutions of the Equations of Fluid Dynamics," *Mat. Sb.* Volume 47: 357-393, 1959.

27. Granville, P. S. "Baldwin-Lomax Factors for Turbulent Boundar Layers in Pressure Gradients," *AIAA Journal.* Volume 25, Number 12: 1624,1627, 1987.

28. Granville, P. S. "A Modified Van Driest Formula for the Mising Length of Turbulent Boundary Layers in Pressure Gradients," *Journal of Fluids Engineering.* Volume 111: 94-97, 1989.

29. Guidos, Bernard J., Paul Weinacht, and David S. Dolling. "Comparison of Navier-Stokes Computations and Experiment for Pointed, Spherical and Flat Tipped Shells at Mach 2.95," AIAA Paper 90-0587.

30. Guidos, Bernard J., Paul Weinacht, and David S. Dolling. "Navier-Stokes Computations for Pointed, Spherical, and Flat Tipped Shells at Mach 3," *Journal of Spacecraft and Rockets.* Volume 29, Number 3: 305-311, May-June 1992.

31. Hart, Roger G. *Effects of Stabilizing Fins and a Rear Support Sting on the Base Pressures of a Body of Revolution in Free Flight at Mach Numbers from 0.7 to 1.3,* NACA Research Memorandum L52E06, 1952.

32. Harten, A., J. M. Hyman, and P. D. Lax. "On Finite-Difference Approximations and Entopy Conditions for Shocks," *Communications on Pure and Applied Mathematics,* Volume 24: 297-322, 1976.

33. Harten, A. "High Resolution Schemes for Hyperbolic Conservation Laws," *Journal of Computational Physics.* Volume 49: 357-393, 1983.

34. Harten, A. "On a Class of High Resolution Total-Variation-Stable Finite-Difference Schemes," *SIAM Journal of Numerical Analysis.* Volume 21: 1-23, 1984.

35. Hathaway, W. H., and Whyte, R. H., "Aeroballistic Research Facility Free-Flight Data Analysis Using the Maximum Likelihood Method," AFATL-TR-79-98, Eglin AFB, FL, December 1979.

36. Hathaway, W. H., Whyte, R. H., and Burnett, J. R., "Projectile Design Analysis System (PRODAS)," Presented at the 31st Aeroballistic Range Association Meeting, Pasadena, California, October 1980.

37. Hathaway, W. "HART 1993: Free-flight ARF Test Results," Test Report ARO-WH-94-001, Arrow Tech Associates, South Burlington Vermont, 05403.

195

38. Hill, Freeman K. "Base Pressures at Supersonic Velocities," *Reader's Forum, Journal of the Aeronautical Sciences.* Volume 17 Number 3: 185-187, March 1950.

39. Hung, C. M., and MacCormack, R. W., "Numerical Solution of Three-dimensional Shock Wave and Turbulent Boundary-Layer Interaction," *AIAA Journal,* Volume 16, pp1090-1096, October 1978.

40. Hung, C-M. and Buning, P. G., "Simulation of Blunt-fin-induced Shock-wave and Turbulent Boundary Layer Interaction," *Journal of Fluid Mechanics,* Volume 154, pp153-185, January 1985.

41. Hussain, S., *A Study of the Interaction Between a Glancing Shock Wave and a Turbulent Boundary Layer - the Effects of Leading Edge Bluntness and Sweep.* Cranfield Insitute of Technology, England, November 1985.

42. James, C. S., *Observations of Turbulent-Burst Geometry and Growth in Supersonic Flow,* NACA Technical Note 4235, April 1958.

43. Josyula, E., D. Gaitonde, and S. Shang. "Nonequilibrium Hypersonic Flow Solutions Using the Roe Flux-Difference Split Scheme," AIAA Paper 91-1700, June 1991.

44. Kayser, L. D., "Effects of Small Nose Bluntness on Static Stability and Magnus Characteristics of a Projectile Shape at Mach 0.91 and 3.03," U.S. Army Ballistic Research Laboratory/AMC, BRL-MR-3535, Aberdeen Proving Ground, MD, July 1986.

45. Kittyle, R. L., Packard, J. D., and Winchenbach, G. L., "Description and Capabilities of the Aeroballistic Research Facility," AFATL-TR-87-08, Eglin AFB, FL, May 1987.

46. Knight, D. and Miguel Visbal. "The Baldwin-Lomax Turbulence Model for Two Dimensional Shock-Wave/Boundary-Layer Interactions," *AIAA Journal,* Vol 22, July 1984.

47. Kubota, Toshi. "Investigation of Flow Around Simple Bodies in Hypersonic Flow," Graduate Aeronautical Laboratories California Institure of Technology (GALCIT) Hypersonics Wind Tunnel Memorandum No. 40, Pasadena CA, June 1957.

48. Kubota, H. and Stollery, J.L., "An Experimental Study of the Interaction Between a Glancing Shock Wave and a Turbulent Boundary Layer," *Journal of Fluid Mechanics,* Volume 116, pp431-458, 1982.

49. Laganelli, A. L. and S. M. Dash. *Turbulence Modeling, Interim Report,* SBIR AF91-108. Flight Dynamics Laboratory, Wright Research and Development Center, Wright-Patterson AFB OH, July 1990.

50. Lijewski, L., Cipolla, J., et. al., "Program EAGLE User's Manual, Volume 1 - Introduction and Grid Applications," AFATL-TR-88-117, Volume 1, Eglin AFB, FL, September 1988.

51. Lin, H. "Dissipation Additons to Flux-Difference Splitting," AIAA Paer 91-1544, June 1991.

52. Loth, E., K. Kailasanath, and R. Lohner. "Supersonic Flow Over an Axisymmetric Backward-Facing Step," AIAA Paper 90-1580, June 1990.

53. Love, Eugene S., and O'Donnel, Robert M. *Investigations at Supersonic Speeds of the Base Pressure on Bodies of Revolution With and Without Sweptback Stabilizing Fins*, NACA Research Memorandum L52J21a, 1952.

54. Magagnato, F. "Computation of Axisymmetric Base Flow with Different Turbulence Models," *AGARD Conference Proceedings*. Number 493. April 1990.

55. McMaster, D. L. and Shang, J. S., "A Numerical Study of Three-Dimensional Separated Flows Around a Sweptback Blunt Fin," AIAA Paper 88-0125, January 1988.

56. Mendenhall M. R.(ed), *Tactical Missile Aerodynamics: Prediction Methodology, Second Edition*, Progress in Astronautics and Aeronautics, Volume 142. Washington: American Institute of Aeronautics and Astronautics, 1992.

57. Moran, K. J. *A Comparison of Molecular Vibration Modeling for Thermal Nonequilibrium Airflow*. MS Thesis, AFIT/GAE/ENY/90D-17. School of Engineering, Air Force Institute of Technology (AU), Wright-Patterson AFB OH, December 1990.

58. Moran, K. J. and P. S. Beran. "A Comparison of Molecular Vibration Modeling for Thermal Nonequilibrium Airflow," AIAA Paper 91-1701, June 1991.

59. Moran, K. J. and P. S. Beran. "Navier-Stokes Simulations of Slender Axisymmetric Shapes in Supersonic, Turbulent Flow," *AIAA Journal*, awaiting publication.

60. Mounts, J. S., Belk, D. M., and Whitfield D. L., "Program EAGLE User's Manual, Volume IV - Multiblock Implicit, Steady State Euler Code," AFATL-TR-88-117, Volume 4, Eglin AFB, FL, September 1988.

61. Nichols, R. H. "A Two-Equation Model for Compressible Flows," AIAA Paper 90-0494, Januaray 1990.

62. Oliver, Robert E. "An Experimental investigation of Flow Over Simple Blunt Bodies at a Nominal Mach Number of 5.8," Graduate Aeronautical Laboratories California Institure of Technology (GALCIT) Hypersonics Wind Tunnel Memorandum No. 26, Pasadena CA, June 1955.

63. Palmer, G. and E. Venkatapathy. "Effective Treatments of the Singular Line Boundary Problem for Three Dimensional Grids," AIAA Paper 92-0545, January 1992.

64. Price, A. E. and Stallings, R. L., "Investigation of Turbulent Separated Flows in the Vicinity of Fin Type Protuberances at Supersonic Mach Number," NASA TN D-3804, February 1967.

65. Pulliam, Thomas H. and Joseph L. Steger. "Recent Improvements in Efficiency, Accuracy, and Convergence for Implicit Approximate Factorization Algorithms," *AIAA 23rd Aerospace Sciences Meeting.* AIAA-85-0360. (January 1985).

66. Reller, John O., and Hamaker, Frank M. *An Experimental Investigation of the Base Pressure Characteristics of Nonlifting Bodies of Revolution at Mach Numbers From 2.73 to 4.98,* NACA Research Memorandum A52E20, 1952.

67. Riedelbauch, R. and G. Brenner. "Numerical Simulation of Laminar Hypersonic Flow Past Blunt Bodies Including High Temperature Effects," AIAA Paper 90-1492, June 1990.

68. Riner, W. C., "Aerodynamic Force and Stability Predictions for the HART Missile at High Mach Numbers," Wright Laboratory Armament Directorate, Contractor Report, Contract Number: F08635-91-C-0002, Eglin AFB, FL, October, 1991.

69. Riner, W. C., Private Communication, December 1993.

70. Roache, Patrick J. *Computational Fluid Dynamics.* Albuquerque: Hermosa Publishers, 1972.

71. Roe, P. L. "Approximate Riemann Solvers, Parameter Vectors, and Difference Schemes," *Journal of Computational Physics,* Volume 43: 357-372, 1981.

72. Rose, P. H. and W. I. Stark. "Stagnation Point Heat-Transfer Measurements in Dissociatted Air," *Journal of the Aeronautical Sciences,* Vol. 25, No. 2, February 1958.

73. Shang, J. S., Hankey, W. L., and Petty, J. S., "Three-dimensional Supersonic Interacting Turbulent Flow Along a Corner," *AIAA Journal,* Volume 17, Number 10: pp706-713, July 1979.

74. Shang, J. S. "Numerical Simulation of Wing-Fuselage Aerodynamic Interaction," *AIAA Journal,* Volume 22, Number 10: 1345-1353, October 1984.

75. Shang, J. S., Private Communication, June 1989.

76. Spahr, R. J., and Dickey, R. R. *Effect of Tail Surfaces on the Base Drag of a Body of Revolution at Mach Numbers of 1.5 and 2.0*, NACA Technical Note 2360, 1951.

77. Speziale, C. G. and Tuan Ngo. *Numerical Solution of Turbulent Flow Past a Backward Facing Step Using a Nonlinear $k - \epsilon$ Model.* ICASE Report 87-74. (1987).

78. Steinbrenner, John P., John R. Chawner, and Chris L. Fouts. *The GRIDGEN 3D Multiple Block Grid Generation System, Volume 1: Final Report*, WRDC-TR-90-3022. Flight Dynamics Laboratory, Wright Research and Development Center, Wright-Patterson AFB OH, July 1990.

79. Stetson, K. F., "Hypersonic Boundary-Layer Transition," *The Third Joint Europe/U.S. Short Course in Hypersonics*, University of Aachen, Aachen, Federal Republic of Germany, October 1990.

80. Stollery, J. L., "Glancing Shock-Boundary Layer Interactions," *Special Course on Three-Dimensional Supersonic/Hypersonic Flows Including Separation*, AGARD Report Number 764, January 1990.

81. Sturek, W. B. "Preliminary Surveys of the Three Dimensional Boundary Layer on a Yawed Spinning Body of Revolution," U.S. Army Ballistic Research Laboratory, BRL-MR-2501, Aberdeen Proving Ground, MD, July 1975.

82. Sturek, W. B. and Danberg, J. E., "Experimental Measurements of the Turbulent Boundary Layer on a Yawed Spinning Slender Body," U.S. Army Ballistic Research Laboratory, BRL-R-1954, Aberdeen Proving Ground, MD, January 1977.

83. Sturek, W. B., Guidos, B. J., and Nietubicz, C. J., "Navier-Stokes Computational Study of the Magnus Effect on Shell with Small Bluntness at Supersonic Speeds," AIAA Paper 82-1341, August 1982.

84. Sturek, W. B., Mylin, D. C., Guidos, B. J., and Nietubicz, C. J., "Navier-Stokes Computational Study of the Infulence of Shell Geometry on the Magnus Effect at Supersonic Speeds," U.S. Army Ballistic Research Laboratory/ARRADCOM, ARBRL-TR-02501, Aberdeen Proving Ground, MD, June 1983.

85. Sturek, W. B. "Application of CFD to the Aerodynamics of Spinning Shell," AIAA Paper 84-0323, Januaray 1984.

86. Thompson, J. F., Warsi, Z. U. A., and Mastin, C. W., *Numerical Grid Generation Foundations and Applications.* New York: North-Holland, 1985.

87. Thompson, J. F., and Gatlin, B., "Program EAGLE User's Manual, Volume II - Surface Generation Code," AFATL-TR-88-117, Volume 2, Eglin AFB, FL, September 1988.

88. Thompson, J. F., and Gatlin, B., "Program EAGLE User's Manual, Volume III - Grid Generation Code," AFATL-TR-88-117, Volume 3, Eglin AFB, FL, September 1988.

89. Van Leer, B. "Towards the Ultimate Conservative Difference Scheme V. A Second-Order Sequel to Gudonov's Method," *Journal of Computational Physics*, Vol. 32, 1979.

90. Van Leer, et al. "A Comparison of Numerical Flux Formula for the Euler Equations and Navier-Stokes Equations," AIAA Paer 87-1104, January 1987.

91. Vinokur, M. "An Analysis of Finite-Difference and Finite-Volume Formulations of Conservation Laws," NASA CR 177416, Palo Alto CA, June 1986.

92. Visbal M. *Calculation of Viscous Transonic Flows about a Supercritical Airfoil*, Technical Report, AFWAL, Flight Dynamics Laboratory, WPAFB, OH, AFWAL-TR-86-3013, August 1986.

93. Vitale, H. E., G. L. Winchenbach, and W. C. Riner. "Aerodynamic Test and Ongoing Analysis of a Slender Generic Missile Configuration," AIAA Paper 91-2895.

94. Vukelich, S. R., et. al., "Missile DATCOM VOL I - Final Report," AWAL-TR-86-3091, Volume 1, December 1988.

95. Vukelich, S. R., et. al., "Missile DATCOM VOL II - User's Manual," AWAL-TR-86-3091, Volume 2, December 1988.

96. Wada, Y. and Liou, M., "A Flux Splitting Scheme with High-Resolution and Robustness for Discontinuities," AIAA Paper 94-0083, January 1994.

97. Wardlaw, A. B. and Priolo, F. J., "Applying the ZEUS Code," Naval Surface Warfare Center, TR 86-508, December 1986.

98. Weinacht, P., Guidos, B. J., Kayser, L. D., and Sturek, W. B., "PNS Computations for Spinning and Fin-Stabilized Projectiles at Supersonic Speeds," U.S. Army Ballistic Research Laboratory, ARBRL-MR-3464, Aberdeen Proving Ground, MD, September 1985.

99. Winkelmann, A. E., "Experimental Investigation of a Fin Protuberance Paritally Immersed in a Turbulent Boundary Layer at Mach 5," Naval Ordnance Laboratory Report NOLTR-72-33, January 1972.

100. Whitcomb, R. T. *A Study of the Zero-Lift Drag Rise Characteristics of Wing-Body Combinations Near the Speed of Sound*, NACA Technical Report 1273, 1956.

101. White, Frank M. *Viscous Fluid Flow, Second Edition*. New York: McGraw-Hill, Inc., 1991.

102. Yang, Z. C. and L. C. Zhao. "Analysis of Limit Cycle Flutter of an Airfoil in Incompressible Flow," *Journal of Sound and Vibration*. Vol 123, 1988.

103. Yee, H. C., R. F. Warming, and A. Harten. "Implicit Total Variation Diminishing (TVD) Schemes for Steady-State Calculations," *Journal of Computational Physics*. Volume 57: 327-360 (1985)

104. Yee, H. C. "A Class of High-Resolution Explicit and Implicit Shock-Capturing Methods," NASA TM 101088, Moffett Field California: Ames Research Center, February 1989.

Vita

Captain Kenneth J. Moran was born 21 April 1962 in Shaska, Minnesota. He graduated from Robinson High School in 1980 and attended Virginia Polytechnic Institute and State University, receiving the degree of Bachelor of Aerospace and Ocean Engineering in December 1984. Upon graduation, he received a commission in the USAF through the ROTC Program. After being commissioned, he served as flight test engineer for the 49th Test Squadron, Strategic Air Command, Barksdale Air Force Base, Louisianna, where he flew aboard many different aircraft while conducting operational testing of strategic weapon systems. Following his work at the 49th Test Squadron, he attended Squadron Officer School in 1989, where he was a distinguished graduate. He immediately entered the Graduate School of Engineering, Air Force Institute of Technology in 1989, where as a distinguished graduate, he was awarded the degree of Master of Science in Aeronautical Engineering in December 1990. He entered the doctoral program in January 1991.

Permanent address: 215 Colonial Lane
                       Dayton, Ohio 45429

REPORT DOCUMENTATION PAGE

Public reporting burden for this collection of information is estimated to average 1 hour per response, including the time for reviewing instructions, searching existing data sources, gathering and maintaining the data needed, and completing and reviewing the collection of information. Send comments regarding this burden estimate or any other aspect of this collection of information, including suggestions for reducing this burden, to Washington Headquarters Services, Directorate for Information Operations and Reports, 1215 Jefferson Davis Highway, Suite 1204, Arlington, VA 22202-4302, and to the Office of Management and Budget, Paperwork Reduction Project (0704-0188), Washington, DC 20503.

1. AGENCY USE ONLY (Leave blank)	2. REPORT DATE	3. REPORT TYPE AND DATES COVERED
	April 1994	Dissertation 2 Jan 91 - 30 Apr 94

4. TITLE AND SUBTITLE
An Aerodynamic and Static-Stability Analysis of the
Hypersonic Applied Research Technology Missile

5. FUNDING NUMBERS

6. AUTHOR(S)
Kenneth John Moran, Capt, USAF

7. PERFORMING ORGANIZATION NAME(S) AND ADDRESS(ES)
Graduate School of Engineering
Air Force Institute of Technology
2750 P Street
Wright-Patterson AFB OH 45433

8. PERFORMING ORGANIZATION REPORT NUMBER
AFIT/DS/AA/94-3

9. SPONSORING/MONITORING AGENCY NAME(S) AND ADDRESS(ES)
Dr. Bruce Simpson
Armament Directorate
Wright Laboratory (WL/MNAA)
Eglin AFB FL 32542

10. SPONSORING/MONITORING AGENCY REPORT NUMBER

11. SUPPLEMENTARY NOTES

12a. DISTRIBUTION/AVAILABILITY STATEMENT

Approved for public release; unlimited distribution.

12b. DISTRIBUTION CODE

13. ABSTRACT (Maximum 200 words) The flow about the complete Hypersonic Applied Research Technology (HART) missile is simulated for inviscid, laminar, and turbulent conditions and Mach numbers from 2 to 6. An explicit, second-order-accurate, flux-difference-splitting, algorithm is implemented and employed to solve the Navier-Stokes equations. The equations are solved using a finite-volume methodology. The aerodynamic and static-stability characteristics are investigated to determine if conventional super-sonic missile configurations can be flown at Mach numbers higher than 5. The effects of nosetip blunting and boundary-layer condition are demonstrated. The structure of the flow near the fins is significantly affected by the turbulent transport of momentum in regions of blocked cross flow. Turbulence and the blockage phenomenon cause bleeding around the fin leading edges. Ultimately, this results in lower fin effectiveness and reduced static stability. The aerodynamic characteristics of the HART missile are predicted at Mach numbers beyond the experimental free-flight testing capabilities. The current predictions indicated that the pitching-moment coefficient decreases with increasing Mach number much less than previous numerical computations. The present results also suggest that the clipped-delta-fin configuration is stable beyond Mach 7.

14. SUBJECT TERMS Fin Stabilized, high fineness ratio, Computational Fluid Dynamics, Navier-Stokes equations, turbulence, flux-difference-splitting, finite volume, drag, Hypersonic Applied Research Technology Missile, Stability missile aerodynamics.

15. NUMBER OF PAGES
224

16. PRICE CODE

17. SECURITY CLASSIFICATION OF REPORT	18. SECURITY CLASSIFICATION OF THIS PAGE	19. SECURITY CLASSIFICATION OF ABSTRACT	20. LIMITATION OF ABSTRACT
UNCLASSIFIED	UNCLASSIFIED	UNCLASSIFIED	Unlimited